



HAL
open science

Combined study by Direct Numerical Simulation and optical diagnostics of the flame stabilization in a diesel spray

Fabien Tagliante-Saracino

► **To cite this version:**

Fabien Tagliante-Saracino. Combined study by Direct Numerical Simulation and optical diagnostics of the flame stabilization in a diesel spray. Thermics [physics.class-ph]. Université Paris Saclay (COmUE), 2019. English. NNT: 2019SACLC017 . tel-02094436

HAL Id: tel-02094436

<https://theses.hal.science/tel-02094436>

Submitted on 9 Apr 2019

HAL is a multi-disciplinary open access archive for the deposit and dissemination of scientific research documents, whether they are published or not. The documents may come from teaching and research institutions in France or abroad, or from public or private research centers.

L'archive ouverte pluridisciplinaire **HAL**, est destinée au dépôt et à la diffusion de documents scientifiques de niveau recherche, publiés ou non, émanant des établissements d'enseignement et de recherche français ou étrangers, des laboratoires publics ou privés.

Combined study by direct numerical simulation and optical diagnostics of the flame stabilization in a Diesel spray

Thèse de doctorat de l'Université Paris-Saclay
préparée à CentraleSupélec

École doctorale n°579
Sciences Mécaniques et Energétiques, Matériaux et Géosciences
(SMEMaG)
Spécialité de doctorat : Combustion

Thèse soutenue à Rueil-Malmaison, le 11 Mars 2019, par

Fabien Tagliante-Saracino

Composition du Jury :

Andreas Kempf Professeur, Université Duisburg-Essen	Rapporteur
Jose M. Garcia-Oliver Professeur, Université polytechnique de Valence	Rapporteur
Sébastien Ducruix Directeur de recherche, CentraleSupélec (EM2C)	Président du Jury
Bart Somers Professeur associé, Université de technologie d'Eindhoven	Examineur
Lyle M. Pickett Docteur, Sandia National Laboratories	Examineur
Gilles Bruneaux Docteur, IFP Energies nouvelles	Directeur de thèse
Christian Angelberger Docteur, IFP Energies nouvelles	Co-Directeur de thèse
Louis-Marie Malbec Docteur, IFP Energies nouvelles	Invité

Titre : Etude combinée par simulation numérique direct et diagnostics optiques de la stabilisation de la flamme d'un spray Diesel

Mots clés : Moteurs à Combustion Interne, Stabilisation de la flamme, Diagnostics optiques, Simulation numérique direct.

Résumé : La compréhension du processus de stabilisation des flammes Diesel constitue un défi majeur en raison de son effet sur les émissions de polluants. En effet, la relation étroite entre la distance de lift-off (distance entre la flamme et l'injecteur) et la production de suie est maintenant bien établie. Cependant, différents mécanismes de stabilisation ont été proposés mais sont toujours sujets à discussion. L'objectif de cette thèse est de fournir une contribution expérimentale et numérique pour identifier les mécanismes de stabilisation majeurs.

La combustion d'un spray n-dodécane issu d'un injecteur mono-trou a été étudiée dans une cellule à volume constant en utilisant une combinaison de diagnostics optiques : mesures hautes cadences et simultanées de schlieren, LIF à 355 nm, chimiluminescence haute température ou de chimiluminescence OH*. Des expériences complémentaires sont effectuées au cours desquelles le mélange est allumé entre l'injecteur et le lift-off par plasma induit par laser. L'évolution du lift-off jusqu'à son retour à une position d'équilibre plus en aval est ensuite étudiée pour différentes conditions opératoires. L'analyse de l'évolution du lift-off sans allumage laser révèle deux types principaux de comportement : des sauts brusques en amont et un déplacement plus progressif en aval. Alors que le premier comportement est attribué à des événements d'auto-inflammation, le second est analysé grâce aux résultats obtenus par allumage laser. Il a été constaté que l'emplacement du formaldéhyde avait un impact important sur la vitesse de retour du lift-off.

Une simulation numérique directe (DNS en anglais) bidimensionnelle d'une flamme liftée turbulente se développant spatialement dans les mêmes conditions opératoires que les expériences et reproduisant l'évolution temporelle de la distance de lift-off est proposée. Du fait que les expériences montrent que la flamme se stabilise en aval du spray liquide, la DNS ne couvre qu'une région en aval où

l'écoulement est réduit à un jet gazeux. La chimie de l'n-dodécane est modélisée à l'aide d'un schéma cinétique (28 espèces transportées) prenant en compte les chemins réactionnels basse et haute température.

Comme observé expérimentalement, la stabilisation de la flamme est intermittente : des auto-inflammations se produisent tout d'abord puis se font convecter en aval jusqu'à ce qu'une nouvelle auto-inflammation se produise. Le mécanisme principal de stabilisation est l'auto-inflammation. Toutefois, on observe également à la périphérie du jet diverses topologies de flammes, telles que des flammes triples, qui aident la flamme à se stabiliser en remplissant des réservoirs de gaz brûlés à haute température localisés à la périphérie, ce qui déclenche des auto-inflammations. Toutes ces observations sont résumées dans un modèle conceptuel décrivant la stabilisation de la flamme.

Enfin, un modèle prédisant les fluctuations de la distance du lift-off autour de sa valeur moyenne temporelle est proposé. Ce modèle a été développé sur la base d'observations faites dans l'étude expérimentale et numérique : premièrement, le suivi temporel du lift-off a été décomposé en une succession d'auto-inflammations et d'évolutions en aval. Deuxièmement, la période entre deux auto-inflammations et la vitesse d'évolution en aval ont été modélisées à l'aide de corrélations expérimentales disponibles dans la littérature. Troisièmement, le modèle a été adapté afin de prendre en compte l'effet des réservoirs à haute température sur les fluctuations de la flamme. Et enfin, le modèle a été comparé aux données expérimentales, au cours desquelles des variations de la température ambiante, de la concentration en oxygène et de la pression d'injection ont été effectuées. Dès lors que le modèle a montré une bonne correspondance avec les données expérimentales, il peut être utilisé en complément du modèle prédisant la distance du lift-off moyen afin de mieux décrire la stabilisation d'une flamme Diesel.

Title: Combined study by Direct Numerical Simulation and optical diagnostics of the flame stabilization in a Diesel spray

Keywords : Internal Combustion Engines, Flame stabilization, Optical diagnostics, Direct numerical simulation

Abstract: The understanding of the stabilization process of Diesel spray flames is a key challenge because of its effect on pollutant emissions. In particular, the close relationship between lift-off length and soot production is now well established. However, different stabilization mechanisms have been proposed and are still under debate. The objective of this PhD is to provide an experimental and numerical contribution to the investigation of these governing mechanisms.

Combustion of an n-dodecane spray issued from a single-hole nozzle was studied in a constant-volume precombustion vessel using a combination of optical diagnostic techniques. Simultaneous high frame rate schlieren, 355 LIF (laser-induced fluorescence) and high-temperature chemiluminescence or OH* chemiluminescence are respectively used to follow the evolution of the gaseous jet envelope, formaldehyde location and lift-off position. Additional experiments are performed where the ignition of the mixture is forced at a location upstream of the natural lift-off position by laser-induced plasma ignition. The analysis of the evolution of the lift off position without laser ignition reveals two main types of behaviors: sudden jumps in the upstream direction and more progressive displacement towards the downstream direction. While the former is attributed to auto-ignition events, the latter is studied through the forced laser ignition results. It is found that the location of formaldehyde greatly impacts the return velocity of the lift-off position.

A two-dimensional Direct Numerical Simulation (DNS) of a spatially developing turbulent lifted flame at the same operating conditions than the experiments and reproducing the temporal evolution of the lift-off length is proposed to provide a better understanding of the flame stabilization mechanisms. The DNS only covers a downstream region where the flow can be reduced to a gaseous jet, since experimental

observations have shown that the flame stabilized downstream of the liquid spray. N-dodecane chemistry is modeled using a reduced chemical kinetics scheme (28 species transported) accounting for the low- and high temperature reaction pathways. Similar to what has been observed in the experiments, the flame stabilization is intermittent: flame elements first auto-ignite before being convected downstream until another sudden auto-ignition event occurs closer to the fuel injector. The flame topologies, associated to such events, are discussed in detail, using the DNS results, and a conceptual model summarizing the observations made is proposed. Results show that the main flame stabilization mechanism is auto-ignition. However, multiple reaction zone topologies, such as triple flames, are also observed at the jet periphery of the fuel jet helping the flame to stabilize by filling high-temperature burnt gases reservoirs localized at the periphery, which trigger in its turn auto-ignitions.

Finally, a model predicting the fluctuations of the lift-off length around its time-averaged value is proposed. This model has been developed based on observations made in the experimental and numerical study: first, the lift-off length time-evolution was decomposed into a succession of auto-ignition events and downstream evolutions. Second, the period between two auto-ignition and the velocity of the downstream evolution was modeled using experimental correlations available in the literature. Third, the model has been adapted to take into account the effect of the high-temperature reservoirs on the flame fluctuations. Last, the model was compared to experimental data, where the ambient temperature, oxygen concentration and injection pressure were varied. Since the model showed good agreement with the experimental data, it can be used in addition to the model predicting the time-averaged lift-off length to better describe the Diesel flame stabilization.



Remerciement

Je souhaite tout d'abord remercier les membres de mon jury de thèse, le Professeur Sébastien Ducruix, Président du jury, les Professeurs Andreas Kempf et José M. Garcia-Oliver qui m'ont fait l'honneur d'être rapporteurs, ainsi que le Professeur Bart Somers et le Docteur Lyle M. Pickett pour leur participation en tant qu'examineurs.

Je tiens à remercier chaleureusement mon Directeur et co-Directeur de thèse : Gilles Bruneaux et Christian Angelberger. Vos conseils avisés et votre expérience dans le monde de la recherche m'ont appris énormément d'un point de vue scientifique et rédactionnel (avec plus de douleur). Je n'oublierai sans doute jamais ces bons moments de correction approfondis que vous m'avez offerts lors de l'écriture de ma thèse ou des papiers... Je suis également très reconnaissant envers Louis-Marie Malbec pour son encadrement sans faille et sa disponibilité tout au long de ces 3 années.

Cette thèse n'aurait pas été la même sans l'aide de Maîtres de la combustion notamment Thierry Poinot et Lyle M. Pickett. En effet je souhaite remercier Thierry pour son implication dans ma thèse et pour m'avoir accueilli au CERFACS quelques semaines. Par-delà les océans, les réunions régulières avec Lyle, malgré le décalage horaire, ont été extrêmement enrichissantes. C'est principalement grâce à vous, Gilles, Christian, Louis-Marie, Thierry et Lyle que j'ai pu m'épanouir dans mon travail durant ces 3 années, et pour cela je vous en suis infiniment reconnaissant.

Je souhaite également remercier la team des expérimentateurs de l'IFPEN pour leur soutien technique et leur bonne humeur. Un grand merci à Clément pour son expertise technique sans qui il m'aurait été impossible de mener à bien la partie expérimentale. Je le remercie en outre de m'avoir permis d'intégrer la grande et prestigieuse équipe de foot de l'IFPEN. Je suis également heureux d'avoir pu échanger avec Jérôme, Laurent, Thomas, Francis et Vincent tout au long de ma thèse. Je souhaite enfin exprimer ma gratitude à mes collègues ingénieurs de recherche de l'IFPEN pour leur aide précieuse en réponse à tous types de problèmes.

Cette aventure de trois ans m'a permis d'interagir avec mes collègues doctorants, qui sont ensuite devenus mes amis. Ma première pensée vient à Edouard (Bobbit boo), nos nombreux débats sur la société et le football ont été, pour moi, une bouffée d'air pur durant les longues périodes de rédaction. Je remercie également chaleureusement, Antoine pour son sifflotement, Matthieu pour ses connaissances sportives, Louise pour sa maîtrise du ballon rond, Benoît pour sa bonne humeur à absolument toute épreuve, Alexis pour sa force tranquille et son fromage du Jura, Julien pour son amour des radis, Gorka pour son aide sur AVBP et pour son lancer de type « arbalète » aux fléchettes, Andreas pour sa fougue et sa capacité à oublier des affaires dans le monde entier (que Louise récupère par la suite), Maxime pour ses fameux jeux de mots et sa passion des réacteurs 0D, Hassan pour sa cool altitude, Stéphane pour avoir été faible aux fléchettes, et pour finir, Detlev pour m'avoir fait découvrir la Russie un peu plus chaque jour. Cette fin de thèse est aussi pour moi l'occasion de faire un bilan sur le tournoi international de fléchettes, en effet je

peux dire en tout modestie : j'étais le meilleur.

Il me tient également à cœur de remercier mes encadrants de stage de M2 qui m'ont fait découvrir le monde de la recherche : Bénédetta Franzelli, Philippe Scouflaire et Sébastien Candel. Je vous suis très reconnaissant pour le soutien que vous m'avez apporté tout au long de mon stage et également pour m'avoir aidé à trouver la thèse dans laquelle j'ai pu m'épanouir.

Je voudrais par ailleurs remercier mes chers amis de Paris et de Tournefeuille pour m'avoir permis de garder le contact avec la vie réelle, merci à Zakaria, Victoire, Raphaël et Auriane. Mes derniers remerciements vont à ma famille. Tout d'abord à mes parents et ma sœur qui m'ont toujours soutenu ! Plus spécialement à ma mère qui s'est particulièrement investie dans mes études dès le plus jeune âge. Je ne pouvais pas finir ces remerciements sans un énorme merci à ma douce et tendre épouse. Marie s'est fortement investie dans ce travail de thèse, allant jusqu'à dessiner de sa main la ligne stoechiométrique du modèle conceptuel (Fig. 4.15). Son soutien et son réconfort dans les moments difficiles ont été, pour moi, capitaux dans cette folle aventure qu'est la thèse.

Abstract

The understanding of the stabilization process of Diesel spray flames is a key challenge because of its effect on pollutant emissions. In particular, the close relationship between lift-off length and soot production is now well established. However, different stabilization mechanisms have been proposed and are still under debate. The objective of this PhD is to provide an experimental and numerical contribution to the investigation of these governing mechanisms.

Combustion of an *n*-dodecane spray issued from a single-hole nozzle (90 μm orifice, ECN spray A injector) was studied in a constant-volume precombustion vessel using a combination of optical diagnostic techniques. Simultaneous high frame rate schlieren, 355 LIF (laser-induced fluorescence) and high-temperature chemiluminescence or OH* chemiluminescence are respectively used to follow the evolution of the gaseous jet envelope, formaldehyde location and lift-off position. Additional experiments are performed where the ignition of the mixture is forced at a location upstream of the natural lift-off position by laser-induced plasma ignition. The evolution of the lift-off position until its return to the natural steady-state position is then studied for different ambient temperatures (800 K to 850 K), densities (11 kg/m^3 to 14.8 kg/m^3) and rail pressures (100 MPa to 150 MPa) using the same set of optical diagnostics. The analysis of the evolution of the lift off position without laser ignition reveals two main types of behaviors: sudden jumps in the upstream direction and more progressive displacement towards the downstream direction. While the former is attributed to auto-ignition events, the latter is studied through the forced laser ignition results. It is found that the location of formaldehyde greatly impacts the return velocity of the lift-off position: if laser ignition occurs upstream of the zone where formaldehyde is naturally present, the lift-off position convects rapidly until it reaches the region where formaldehyde is present and then returns more slowly towards its natural position, suggesting that cool-flame greatly assists lift-off stabilization.

A two-dimensional Direct Numerical Simulation (DNS) of a spatially developing turbulent lifted flame at the same operating conditions than the experiments and reproducing the temporal evolution of the lift-off length is proposed to provide a better understanding of the flame stabilization mechanisms. As experimental evidence for the simulated conditions shows a flame stabilization downstream of the zone where the two-phase spray has a major impact on local flow, the DNS only covers a downstream region where the flow can be reduced to a gaseous jet. The inflow conditions for the DNS are imposed based on experimental studies at the considered position. *N*-dodecane chemistry is modeled using a reduced chemical kinetics scheme comprising 28 species and 198 reactions to account for the low- and high temperature reaction pathways, and its predictions have been validated against experimental auto-ignition delays and laminar flame speeds at conditions relevant to the simulated cases. Similar to what has been observed in the experiments, the flame stabilization is intermittent: flame elements first auto-ignite before being convected downstream until another sudden auto-ignition event occurs closer to the fuel injector. The flame topologies, associated to such events, are discussed in detail, using the DNS results, and a conceptual model summarizing the observations made is proposed. Results show

that the main flame stabilization mechanism is auto-ignition. However, multiple reaction zone topologies, such as triple flames, are also observed at the jet periphery of the fuel jet helping the flame to stabilize by filling high-temperature burnt gases reservoirs localized at the periphery, which trigger in its turn auto-ignitions.

Finally, a model predicting the fluctuations of the lift-off length around its time-averaged value is proposed. This model has been developed based on observations made in the experimental and numerical study: first, the lift-off length time-evolution was decomposed into a succession of auto-ignition events and downstream evolutions. Second, the period between two auto-ignition and the velocity of the downstream evolution was modeled using experimental correlations available in the literature. Third, the model has been adapted to take into account the effect of the high-temperature reservoirs on the flame fluctuations. Last, the model was compared to experimental data, where the ambient temperature, oxygen concentration and injection pressure were varied. Since the model showed good agreement with the experimental data, it can be used in addition to the model predicting the time-averaged lift-off length [1, 2] to better describe the Diesel flame stabilization.



Résumé

La compréhension du processus de stabilisation des flammes Diesel constitue un défi majeur en raison de son effet sur les émissions de polluants. En effet, la relation étroite entre la distance de lift-off (distance entre la flamme et l'injecteur) et la production de suie est maintenant bien établie. Cependant, différents mécanismes de stabilisation ont été proposés mais sont toujours sujets à discussion. L'objectif de cette thèse est de fournir une contribution expérimentale et numérique pour identifier les mécanismes de stabilisation majeurs.

La combustion d'un spray *n*-dodécane issu d'un injecteur mono-trou (orifice de 90 μm de diamètre, injecteur ECN spray A) a été étudiée dans une cellule à volume constant en utilisant une combinaison de diagnostics optiques. Des mesures hautes cadences et simultanées de schlieren, LIF à 355 nm, chimiluminescence haute température ou de chimiluminescence OH* sont respectivement utilisées pour suivre l'évolution de l'enveloppe du jet gazeux, la localisation du formaldéhyde et la position de la flamme. Des expériences complémentaires sont effectuées au cours desquelles le mélange est allumé entre l'injecteur et le lift-off par plasma induit par laser. L'évolution du lift-off jusqu'à son retour à une position d'équilibre plus en aval est ensuite étudiée pour différentes températures ambiantes (de 800 à 850 K), densités (11 kg/m^3 à 14,8 kg/m^3) et des pressions d'injections (100 MPa à 150 MPa) en utilisant les mêmes diagnostics optiques. L'analyse de l'évolution du lift-off sans allumage laser révèle deux types principaux de comportement : des sauts brusques en amont et un déplacement plus progressif en aval. Alors que le premier comportement est attribué à des événements d'auto-inflammation, le second est analysé grâce aux résultats obtenus par allumage laser. Il a été constaté que l'emplacement du formaldéhyde avait un impact important sur la vitesse de retour du lift-off : si un allumage laser se produisait en amont de la zone où le formaldéhyde est naturellement présent, le lift-off est convecté rapidement jusqu'à atteindre la région où le formaldéhyde est présent et revient ensuite plus lentement vers sa position naturelle, suggérant que la flamme froide aide grandement à la stabilisation du lift-off.

Une simulation numérique directe (DNS pour Direct Numerical Simulation en anglais) bidimensionnelle d'une flamme liftée turbulente se développant spatialement dans les mêmes conditions opératoires que les expériences et reproduisant l'évolution temporelle de la distance de lift-off est proposée afin de mieux comprendre les mécanismes de stabilisation de la flamme. Du fait que les expériences montrent que la flamme se stabilise en aval de la zone où le spray liquide a un impact majeur sur l'écoulement local, la DNS ne couvre qu'une région en aval où l'écoulement peut être réduit à un jet gazeux. Les conditions d'entrée de la DNS sont imposées sur la base d'études expérimentales. La chimie de l'*n*-dodécane est modélisée à l'aide d'un schéma cinétique réduit comprenant 28 espèces et 198 réactions afin de prendre en compte les chemins réactionnels basse et haute température. Le schéma réduit a été validé en comparant les délais d'auto-inflammation et les vitesses de flamme laminaire de pré-mélange par rapport aux expériences. D'une façon analogue à ce qui a été observé expérimentalement, la stabilisation de la flamme est intermittente : des auto-inflammations se produisent tout d'abord puis se font convecter

en aval jusqu'à ce qu'une nouvelle auto-inflammation se produise plus près de l'injecteur. Les topologies de flammes, associées à de tels événements, sont discutées en détail à l'aide des résultats de la DNS puis un modèle conceptuel résumant les observations est proposé. Les résultats indiquent que le mécanisme principal de stabilisation de la flamme est l'auto-inflammation. Toutefois, on observe également à la périphérie du jet diverses topologies de flammes, telles que des flammes triples, qui aident la flamme à se stabiliser en remplissant des réservoirs de gaz brûlés à haute température localisés à la périphérie, ce qui déclenche des auto-inflammations.

Enfin, un modèle prédisant les fluctuations de la distance du lift-off autour de sa valeur moyenne (moyenne temporelle) est proposé. Ce modèle a été développé sur la base d'observations faites dans l'étude expérimentale et numérique : premièrement, le suivi temporel du lift-off a été décomposé en une succession d'auto-inflammations et d'évolutions en aval. Deuxièmement, la période entre deux auto-inflammations et la vitesse d'évolution en aval ont été modélisées à l'aide de corrélations expérimentales disponibles dans la littérature. Troisièmement, le modèle a été adapté afin de prendre en compte l'effet des réservoirs à haute température sur les fluctuations de la flamme. Et enfin, le modèle a été comparé aux données expérimentales, au cours desquelles des variations de la température ambiante, de la concentration en oxygène et de la pression d'injection ont été effectuées. Dès lors que le modèle a montré une bonne correspondance avec les données expérimentales, il peut être utilisé en complément du modèle prédisant la distance du lift-off moyen [1, 2] afin de mieux décrire la stabilisation d'une flamme Diesel.



Contents

1	Introduction	7
1.1	Environmental context	7
1.2	Diesel engine	8
1.2.1	Basic functioning of a Diesel engine	8
1.2.2	Exhaust after-treatment systems	9
1.3	Soot production in Diesel engines	10
1.4	Objective of the thesis	13
1.5	Structure of the manuscript	15
2	Flame stabilization mechanisms: A literature review	17
2.1	Diesel spray combustion	17
2.1.1	Chemistry of Diesel-type fuels	17
2.1.2	Conceptual models of Diesel spray combustion	19
2.2	Non-premixed gaseous jet flames	22
2.2.1	Stabilization by premixed flame propagation at the flame base	22
2.2.1.1	Stabilization by perfectly premixed flame	22
2.2.1.2	Stabilization by partially premixed flame	24
2.2.2	Impact of scalar dissipation	26
2.2.3	Stabilization by recirculation of burnt gases	28
2.3	Diesel spray flames	29
2.3.1	Stabilization by a premixed flame at the flame base	30
2.3.2	Role of flame extinction	33
2.3.3	Role of auto-ignition	34
2.3.4	Combined role of edge-flames and auto-ignition	36
2.3.4.1	2D-DNS of a laminar mixing layer	36
2.3.4.2	2D-DNS of a turbulent decreasing mixing layer	39
2.3.4.3	DNS of a temporally evolving turbulent mixing layer	40
2.3.4.4	3D-DNS of a spatially developing slot jet flame	41
2.3.5	Stabilization by recirculation of burnt gases	42
2.4	Conclusion	44
3	Experimental study of the stabilization mechanisms of a lifted Diesel-type flame using optical diagnostics and laser plasma ignition	47
3.1	Brief introduction	47
3.2	Experimental details	48
3.2.1	Experimental conditions	48

3.2.2	Optical diagnostics and laser ignition	49
3.2.2.1	Schlieren imaging	50
3.2.2.2	355 LIF	50
3.2.2.3	High-temperature chemiluminescence	52
3.2.2.4	Laser ignition	54
3.3	Results and Discussion	54
3.3.1	Flame structure	55
3.3.2	Results for natural flame evolution	56
3.3.3	Forced laser ignition	58
3.4	Conclusion	65
4	A conceptual model of the flame stabilization mechanisms for a lifted Diesel-type flame based on direct numerical simulation and experiments	67
4.1	Brief introduction	67
4.2	Configuration	69
4.2.1	Simplifying assumptions	69
4.2.2	Numerical set-up	70
4.3	Chemical mechanism	73
4.3.1	Development of the reduced scheme	73
4.3.2	Estimation of the thermal flame thickness	75
4.4	Analysis tools for DNS	76
4.4.1	LOL definition	76
4.4.2	Identification of the reaction zone topologies	76
4.4.2.1	Reaction zone topologies during auto-ignition events	76
4.4.2.2	Reaction zone topologies during continuous evolution of the lift-off	77
4.5	Comparison between DNS and experiments	79
4.6	Analysis of stabilization mechanisms	82
4.6.1	LOL tracking with reaction zone topologies	82
4.6.2	Analysis of Event A	84
4.6.3	Analysis of Evolutions B	86
4.7	Conceptual model of flame stabilization	90
4.8	Conclusion	92
4.8.1	Complementary elements	93
4.8.2	Non-reactive profiles	93
4.8.3	Calculation of the mesh resolution for the DNS	95
4.8.3.1	Criteria to simulate 1D premixed flames under autoignitive conditions	96
4.8.3.2	Grid convergence	97
5	A Lift-Off Length fluctuations model	99
5.1	Motivation	99
5.2	The lift-off length fluctuations model	101
5.2.1	S_a model	102
5.2.2	θ model	103
5.2.3	ΔLOL_{Th} model	104

5.3	Lift-off length fluctuations experimental database	105
5.4	Calibration and validation of the LOL fluctuation model	107
5.5	Conclusion	109
6	Conclusions and perspectives	110
6.1	Summary of main findings	110
6.2	Perspectives	112
6.2.1	Validation of the assumptions and models	112
6.2.2	Lines of research to improve understating of flame stabilization mechanisms	114
6.2.3	Towards a technical solution to reduce the soot emissions	115
A	Criteria to distinguish combustion regimes	116
A.1	Transport budget analysis	116
A.2	Chemical criteria to distinguish auto-ignition and flame propagation . . .	120
B	Regime diagram for the flame stabilization mechanisms	123
C	Impact of a high co-flow on the flame stabilization	126
D	Setup of a "coarse DNS"	129
	Bibliography	140

Chapter 1

Introduction

1.1 Environmental context

Fossil fuels are, nowadays, the main source of energy in all modern societies. The transportation sector is responsible for a significant part of the consumption of these hydrocarbons, which are burnt to produce energy. However, the combustion of hydrocarbons, in Internal Combustion Engines (ICE), is causing two main problems that require improvements in combustion processes.

First, pollutants produced during combustion such as CO , NO , NO_2 and soot particles pose serious public health problems. Among those, soot particles are particularly dangerous for humans. They are 98 % carbon by weight and typically spherical in shape. While most are only around $0.03 \mu\text{m}$ in size, they can aggregate to form larger non-spherical particles of typical sizes of up to $10 \mu\text{m}$. If not oxidized or treated after combustion, they can be inhaled by humans. Numerous studies have shown that this has a number of negative impacts on their health [3].

Second, ICE also contribute to the greenhouse gas (GHG) emissions through the emission of CO_2 , which is identified as the main GHG. Transport is the only domain which increases its contribution to GHG emissions in European Union (EU): between 1990 and 2015, in the transport sector, the GHG emissions went from 15 % to 23 % of the total emissions of GHG (*Eurostat source*).

For these reasons, legislators, all over the world, are imposing continuously more stringent limits to the pollutant emissions of new ICE. Fig. 1.1 shows the evolution of the standards between 1993 and 2015 for the Diesel engines. It clearly appears that the different Euro standards (Euro 1 to 6) have led to drastically decrease the pollutant emissions. Engine manufacturers have invested heavily to reach the objectives imposed by the governments.

Furthermore, the Volkswagen Diesel emissions scandal has revealed that the New European Driving Cycle (NEDC), used to measure the pollutant emissions (designed in the 1980s) is far from the real driving emissions. This is why Europe will introduce a Real Driving Emissions (RDE) test to measure the pollutants emitted by cars driven on the road. RDE serves to confirm NEDC results in real life, thereby ensuring that cars deliver low pollutant emissions, not only in the laboratory but also on the road. The

RDE will require manufacturers to make major investments in developing new vehicles and updating their testing facilities to pass this new test.

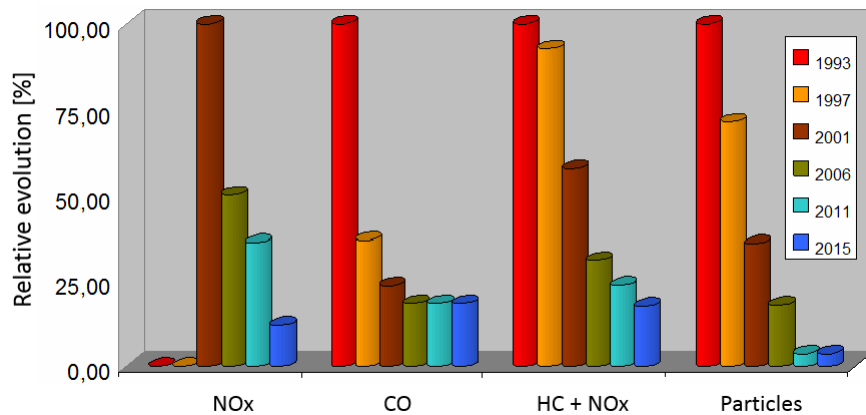


Figure 1.1 – Relative evolution (1993 reference) of the regulatory emissions for Diesel vehicles in Europe from 1993 to 2015 for 4 pollutants: nitrogen oxides NO_x , carbon monoxide CO, the sum of nitrogen oxides NO_x and HC unburned hydrocarbons and finally the particles [4].

In this context, electric cars appear as a promising alternative to ICE. However, although the sales of electric vehicles are in constant expansion, they only represented 1.5% of the new vehicles registrations in 2016. This low percentage of electric cars can be explained by the limited autonomy and high price of this type of vehicles compared to combustion-powered cars. From this perspective and because of the current context of climate change, car manufacturers have no choice but to develop new ICE models and improve their efficiency in terms of pollutant emissions and performance.

1.2 Diesel engine

1.2.1 Basic functioning of a Diesel engine

Most ICE produced in the automotive industry consist in two technologies: compression-ignition (Diesel) engine and spark-ignition (gasoline) engine. They are both designed to convert the chemical energy available in fuel into mechanical energy. This mechanical energy moves pistons up and down inside cylinders (see Fig. 1.2). The pistons are connected to a crankshaft, and the up-and-down motion of the pistons, known as linear motion, creates the rotary motion needed to turn the wheels of a car forward. Both, Diesel engines and gasoline engines, convert fuel into mechanical energy through a series of fast combustions. The major difference between Diesel and gasoline is the way these combustions happen. In a gasoline engine, fuel is mixed with air, compressed by pistons, and ignited by sparks from spark plugs. In a Diesel engine, the air is compressed first, and then the fuel is injected. Because air heats up when it's compressed, the fuel auto-ignites. The Diesel engine uses a four-stroke combustion cycle as shown in Fig. 1.2.

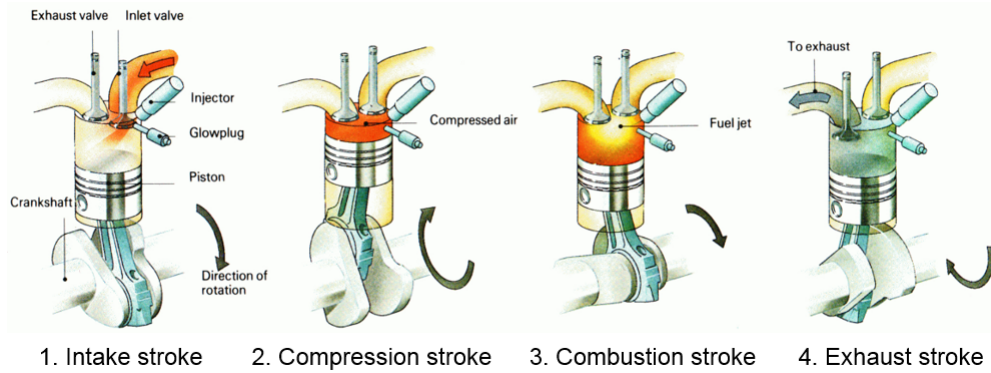


Figure 1.2 – Four-stroke cycle Diesel engine [5].

- Intake stroke: The intake valve opens up, letting in air and moving the piston down. On a recent Diesel engine, a turbocharger increases the density of the gas in order to increase the mass admitted into the combustion chamber.
- Compression stroke: The piston moves back up and compresses the air. Pressure and temperature increase significantly in the cylinder. The temperature can reach 950 K and the pressure 80 bars before the injection.
- Combustion stroke (working stroke): As the piston reaches the top, fuel is injected. The high injection pressure (between 300 and 2500 bar) allows a very fine atomization of the liquid and a high air entrainment rate ensuring rapid evaporation, and on the other hand promotes mixing, the jet being highly turbulent. The combustion is initiated in areas where the mixture is most favorable, then spreads to the entire jet. A direct visualization of the combustion is shown in Fig. 1.3 for 4 instants in a constant volume chamber.

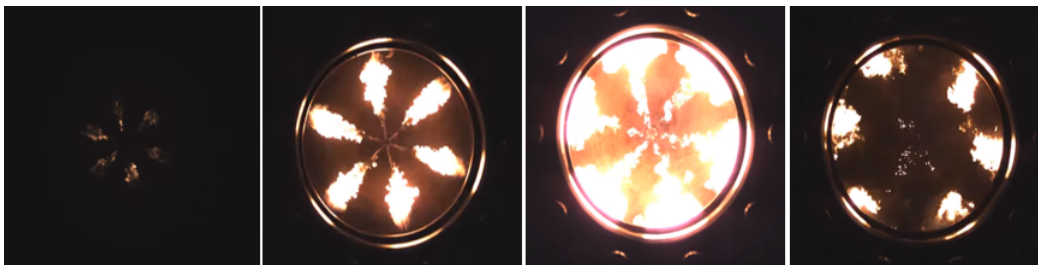


Figure 1.3 – Diesel spray combustion where the injection pressure is 700 bar inside a constant volume combustion chamber at 1100 K [6].

- Exhaust stroke: The piston moves back to the top, pushing out the exhaust gases created from the combustion out of the exhaust valve.

1.2.2 Exhaust after-treatment systems

The two major pollutants emitted after Diesel combustion are nitrogen oxides NO_x and soot particles. In order to reduce these pollutant emissions, two main approaches

have been adopted.

The first technique consists in using a portion of the exhaust gas back to the engine cylinder to reduce the NO_x emissions (technique named EGR for exhaust gas recirculation). The exhaust gas replaces some of the excesses oxygen in the pre-combustion mixture. Because NO_x forms primarily when a mixture of nitrogen and oxygen is subjected to high temperature, the lower combustion chamber temperatures caused by EGR reduces the amount of NO_x the combustion generates.

The second technique is to use exhaust gas after-treatment technologies. The Diesel Oxidation Catalyst (DOC) allows to oxidize NO_x to nitrogen dioxide NO_2 . The NO_x treatment is completed by a Selective Catalytic Reduction (SCR), where NO_2 is needed to support the performance of the SCR. In SCR, urea, a liquid-reductant agent is injected through a catalyst into the exhaust fumes. The urea starts the chemical reaction that produces NO_x into N_2 and H_2O , which is then ejected through the engine exhaust pipe. Finally Diesel Particulate filter (DPF) is used to trap the soot particles. DPF is made of thousands of tiny channels. When exhausts gases pass through these channels, soot is trapped along the walls of the channels. The exhaust gases pass through the porous surface of the ceramic filter. Note that only the big particles are trapped in this filter, while the smallest are released in the environment.

However, all these exhaust gas after-treatment systems, do not allow to avoid the pollutant emissions in the atmosphere on the one hand, and on the other hand they are very expensive and complex. In this context, a deeper and better understanding of the processes occurring during Diesel combustion, and of the driving physical and chemical phenomena, appears as one of the major steps in order to propose a cleaner combustion. By so doing, the pollutant emissions could be minimized from the combustion.

1.3 Soot production in Diesel engines

Fig. 1.4 illustrates the different physical phenomena involved during the Diesel spray combustion.

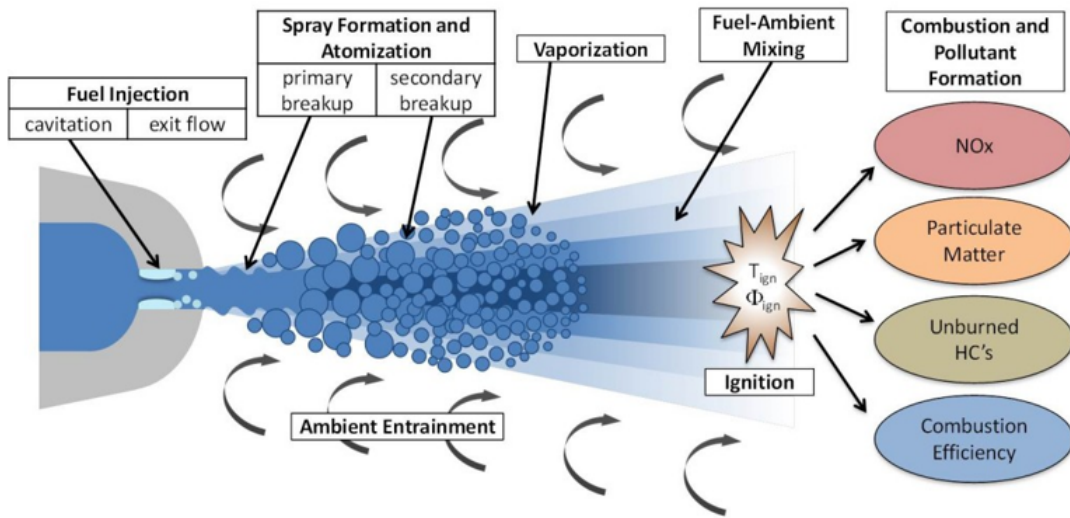


Figure 1.4 – Illustration of the different physical phenomena occurring during Diesel spray combustion. Figure adapted from [7].

First, inside the nozzle, the fuel is ejected at very high injection pressure leading to the formation of vapor cavities in the liquid fuel. This phenomenon is called cavitation and is studied in [8, 9] for Diesel spray. Experimental results have shown that the cavitation within the nozzle modifies the characteristics of the nozzle exit spray, which has an impact on the spray formation and atomization [10, 11].

When the liquid fuel flows out of the injector, a primary breakup regime occurs, where the interaction between the gas and liquid phase causes waves to develop along the liquid surface. Once the wave becomes unstable, it shears off creating elongated ligaments due to the Kelvin-Helmholtz instabilities. These ligaments then further breakdown into large droplets.

Then, the large droplets start to reduce in size due to the Rayleigh-Taylor instabilities and finally vaporize due to the high ambient temperature. The resulting vapor fuel mixes with air, and then auto-ignites (more details are available in Section 2.1.2) leading to a stabilized diffusion flame at a certain distance from the injector. The corresponding axial distance between the injector and the stabilized spray flame is called the Lift-off Length (*LOL*), which is of the order of few tens of millimeters. Fig. 1.5 illustrates an example of *LOL* for a multi-hole injector. During the diffusion combustion, as much as 20 % of the air required to burn the fuel injected is entrained in the zone between the injector tip and the location where the spray flame base is stabilized.

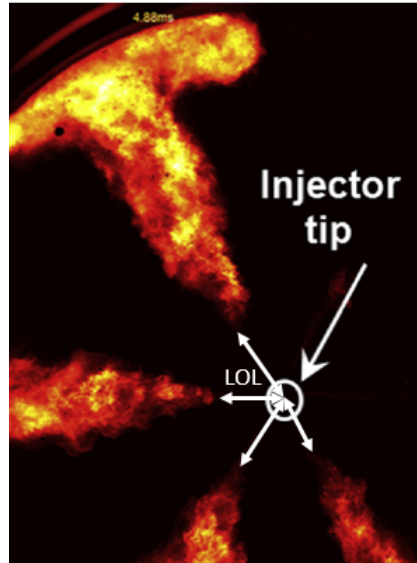


Figure 1.5 – Illustration of the lift-off length (LOL) using broadband luminosity technique in constant volume combustion chamber extracted from [12].

Fig. 1.6 shows the soot production as a function of the inverse of the equivalence ratio at the lift-off ($1/\Phi_{LOL}$, defined as the inverse of the ratio of the fuel-to-oxidizer ratio to the stoichiometric fuel-to-oxidizer ratio) for a Diesel spray in a constant volume vessel for different test conditions. It appears that, the higher the premixing of fuel and air is before it reaches the flame, the leaner it burns and the less soot is produced [13, 14]. According to [15], there is a limit ($1/\Phi_{LOL} > 0.5$) for which the mixture at the lift-off is sufficiently lean so that the soot production is almost non-existent.

Moreover, the arrow on the top of Fig. 1.6 indicates that $1/\Phi_{LOL}$ increases as the LOL increase. For example, when the flame is stabilized close to the injector, the *LOL* is short, the mixture at the lift-off is rich and stratified, thus $1/\Phi_{LOL}$ is low and the level of soot produced is high. Therefore, the order of magnitude of the LOL can be used as an indirect measure for the level of soot particles produced in a Diesel engine.

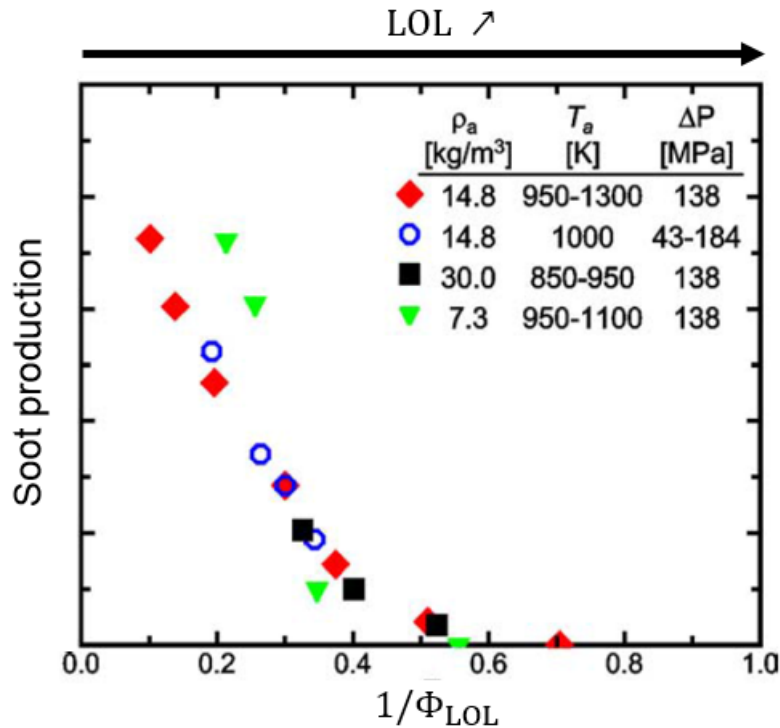


Figure 1.6 – Soot production as a function of the inverse of the equivalence ratio at the lift-off $1/\Phi_{LOL}$ for a Diesel spray in a constant volume vessel and for different ambient temperatures, densities and injection pressure. Figure adapted from [13].

Consequently, there is a very high interest to be able to predict and ultimately control the LOL in order to achieve the desired compromise between soot levels, other emissions and efficiency. However, the flame stabilization is still nowadays poorly understood due to the high-temperature, high-pressure conditions, complex chemistry (e.g. the presence of a cool-flame), very high Reynolds numbers (100,000-200,000 [16]) and two phases flow.

1.4 Objective of the thesis

In this context, the overall objective of the present PhD thesis is to contribute to a better understanding of the stabilization mechanisms of a lifted liquid spray flame under Diesel engine conditions. The expected long-term contribution is to suggest methods for a better prediction and control of the LOL, as a key point of innovative Diesel engine designs.

The proposed research work is based on the extensive experimental and modeling work undertaken in the context of the ECN network [17]. The originality of the present approach is to combine elements from optical diagnostics and Computational Fluid Dynamics (CFD) to overcome the drawbacks of the two approaches. Indeed, experimental measurements do not allow to measure small scale quantities. On the other hand, it is almost impossible to simulate the very constraining Diesel spray conditions without simplifying assumptions. Therefore, combining both approaches allows to measure real quantities using optical diagnostics, and have access to small scale quantities using nu-

merical simulations. In our methodology, the simplifying assumptions of the numerical simulation have been proposed based on experimental observations. This challenging methodology allows to quantify the role and relative importance of the two major stabilization mechanisms proposed so far in the literature:

- Auto-ignition pockets ahead of the lift-off: local auto-ignition spots regularly form ahead of the lift-off and ultimately merge with it, leading to upstream/downstream variations of the flame.
- Premixed flame propagation at the lift-off: Premixed flames could appear at the lift-off located in a zone where fuel and air are premixed stabilizing the flame by premixed flame propagation.

The following points outline the overall research approach taken in the present PhD, relying on a combined usage of optical diagnostics and numerical simulations:

- **Optical diagnostics to explore the stabilization mechanisms:**

Work in this first phase is largely based on the extensive experience acquired at IFPEN, Sandia National Laboratories and other laboratories on the flow and combustion of Diesel spray combustion in a constant volume vessel. The objective in the present PhD is to complement existing measurements in the following way:

- LOL characterization during a long injection duration:

The objective is to apply high temperature chemiluminescence to measure the LOL and its temporal fluctuations for a steady fuel injection rate. These measurements shall be complemented by 355 LIF in order to characterize the formaldehyde zone ahead of the flame basis, and to explore how much formaldehyde could be linked to the auto-ignition pockets. These measurements shall be repeated for different conditions to try and identify the respective impact of key parameters of the studied case.

- Characterize forced auto-ignition and resulting LOL evolution:

Similar to published researches by Pickett et al. [14], a forced ignition of a Diesel spray by means of a laser will be studied. The advantage of this approach is that the point of ignition can be varied. It allows to observe how the local conditions at the ignition points lead to the establishment of a flame, and to quantify the speed with which it will return to a stabilized LOL. The same diagnostics than for the natural ignition shall be employed. The idea is to exploit the observations on the LOL and its speed of evolution towards a stabilized value. In combination with knowledge on the local flow and mixing conditions, this study will explore whether premixed flame propagation phenomena could be a plausible mechanism.

- **Numerical simulation to identify and quantify stabilization mechanisms:**

A second phase of the research work will be to set up, perform and post-process simulations of the same test conditions than studied experimentally. We decided to

perform a Direct Numerical Simulation (DNS) to resolve all space and time scales of the turbulent flow, mixing and chemical reactions. This approach allows to avoid any assumptions on the combustion regime imposed by a combustion model. As a full DNS of such a spray flame is impossible owing to the very high Reynolds numbers, to the complexity of a Diesel-type chemistry and to the complexity of liquid sprays, the aim will be to perform simplified simulations that should nevertheless be representative of real local spray conditions. The methodology will consist in devising a 2D-DNS of a gaseous jet with a reduced chemistry, limited to a domain around the auto-ignition zone and the LOL, and that would be representative of the flow and mixing conditions found in the same zone of the real spray. This will rely on a number of a priori simplifying hypothesis, the justifications of which will a posteriori have to be checked using available experimental evidences from the first phase. The objective will be to post-process the simulation results using existing, or developing new criteria able to distinguish zones exhibiting auto-ignition, premixed flames, or combinations of those. This will allow identifying the relative importance of different stabilization mechanisms.

Finally, the confrontation of the different experimental and numerical results and their analysis is aimed at yielding the expected improved understanding and quantification of the stabilization mechanisms of a lifted Diesel spray flame.

1.5 Structure of the manuscript

This manuscript is organized as follows:

- Chapter 2 proposes a bibliographic review of the flame stabilization mechanisms. First, applied to gaseous turbulent lifted diffusion flame in order to review all the possible flame stabilization mechanisms published. Then, based on this first analysis and considering the difference of Diesel spray combustion, a review of the Diesel flame stabilization mechanisms is proposed.
- Chapter 3 presents an experimental study of the flame stabilization, where simultaneous and time-resolved optical diagnostics are performed to track the cool- and high-temperature flame. This Chapter is also an article published in *Combustion and Flame*:
F. Tagliante, G. Bruneaux, L. M. Malbec, C. Angelberger, L. M. Pickett, Experimental study of the stabilization mechanism of a lifted Diesel-type flame using combined optical diagnostics and laser-induced plasma ignition. *Combustion and Flame* 197 (2018) 215–226.
- Chapter 4 is dedicated to a numerical study proposed in order to develop the observations made during the experimental study thanks to local values. Resulting conceptual model of flame stabilization under Diesel conditions summarizing the observations made. This Chapter is also an extended version (Section 4.8.1 has been added) of an article published in *Combustion and Flame*:
F. Tagliante, T. Poinot, L. M. Pickett, P. Pepiot, L. M. Malbec, G.

Bruneaux, C. Angelberger, A conceptual model of the flame stabilization mechanisms for a lifted Diesel-type flame based on direct numerical simulation and experiments. *Combustion and Flame 201 (2019) 65–77*.

- Chapter 5 proposes a model predicting the fluctuations of the LOL based on the observations made in the previous Chapters. The developed model is then compared to the experimental data.
- Chapter 6 concludes this report and provides perspectives for future works.

Chapter 2

Flame stabilization mechanisms: A literature review

The objective of the present literature review is to discuss the major published mechanism theories of Diesel spray flames. First, a description of the Diesel spray combustion is proposed in Section 2.1 through a description of the chemical characteristics of Diesel-type fuel and different conceptual models describing the stages of combustion from the start of injection to a stabilized lifted flame. Second, since Diesel combustion presents some similarities to gaseous turbulent lifted diffusion flame, Section 2.2 proposes a review of the flame stabilization mechanisms for these flames. This approach allows to take the advantage of decades of studies on atmospheric diffusion flame stabilization, and can be used as a starting point to better understand the Diesel flame stabilization. Finally, based on the flame stabilization theories published for atmospheric flames and considering the difference of Diesel spray combustion, Section 2.3 proposes a review of the Diesel flame stabilization mechanisms.

2.1 Diesel spray combustion

2.1.1 Chemistry of Diesel-type fuels

Unlike many "simple" fuels such as hydrogen, methane or ethylene, combustion of Diesel or Diesel-type fuels (like *n*-dodecane, dimethyl ether (DME)) involves two auto-ignition stages as illustrated in Fig. 2.1 through the temporal evolution of the temperature and heat release. These curves come from a 0D reactor calculation at constant pressure where a homogeneous stoichiometric mixture of *n*-dodecane/air is initialized at 25 bar and 900 K. Two stages of auto-ignition can be distinguished:

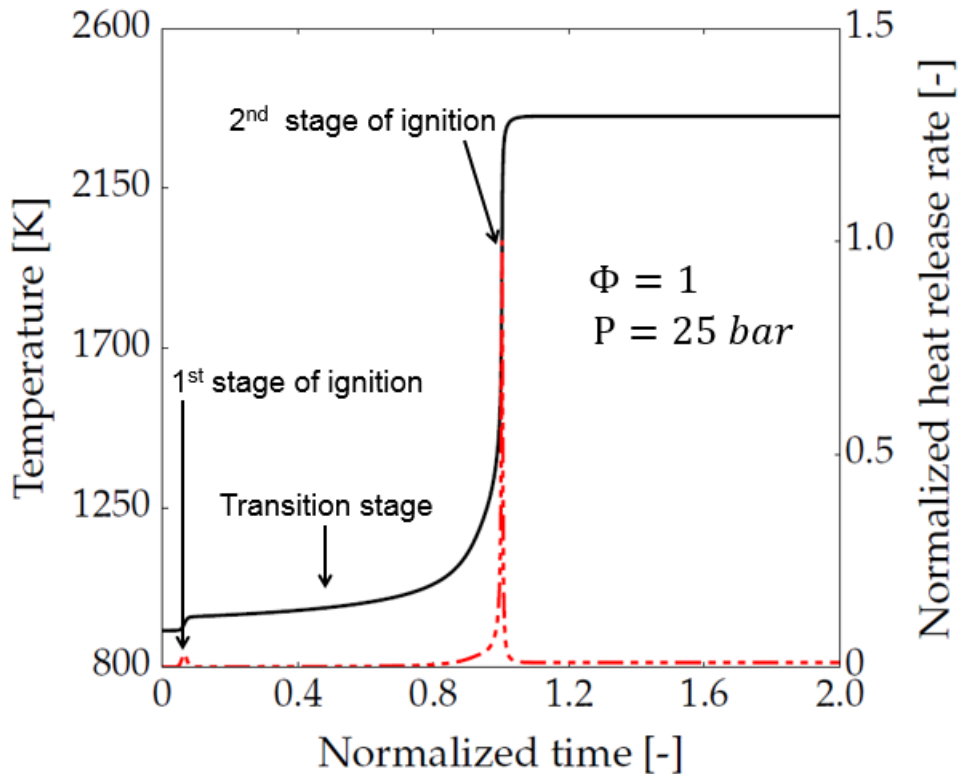


Figure 2.1 – Temporal evolution of temperature (black solid line) and heat release (red dotted line) for a n-dodecane/air mixture computed in 0D homogeneous constant pressure reactor. Figure adapted from [18].

- 1st stage of ignition: a Low-Temperature Heat Release (LTHR) or cool-flame is observed [19]. Kinetically, the cool-flame process is characterized by alkylperoxy radical isomerization, which is the dominant oxidation mechanism in the temperature range 600-950 K [20]. The cool-flame process involves just a few percentage of the total heat release [21]. During this stage, intermediate species such as HCHO can be observed before being consumed [19] in the transition stage.
- Transition stage: as the temperature in the reactor slowly continues to rise, a pool of hydrogen peroxide (H_2O_2) is produced. This region has been reported to lie between 800 and 1100 K for alkanes [20]. Due to the complex chemistry of the Diesel-type fuels, the heat release rate decreases by increasing temperature. This stage is considered as a transition between the cool-flame and the High-Temperature Heat Release (HTHR).
- 2nd stage of ignition: hydrogen peroxide becomes unstable at higher temperatures, and its decomposition into hydroxyl (OH) radicals triggers the exothermic HTHR reactions of the second stage. Most of the heat releases occur in this stage.

One of the key parameters to describe ignition processes is the auto-ignition delay (τ_{AI}). It represents the time for a homogeneous air-fuel mixture to reach the 2nd stage of ignition. Fig. 2.2 shows τ_{AI} for a stoichiometric mixture and for different Diesel-type

fuels in a 0D constant pressure reactor for various initial mixture temperature (T). When the ambient temperature is relatively high (region (a)) or low (region (b)) τ_{AI} decreases as the ambient temperature increases. However, these two regions are separated by a Negative Temperature Coefficient (NTC) region, in which τ_{AI} increases when T increases. This NTC region is the consequence of a competition between the chemical paths of the low- and high-temperature reactions. When the dominant chemical path is the high-temperature reactions, combustion occurs in region (a). Oppositely, combustion occurs in region (b) when the dominant chemical path is the low-temperature reactions.

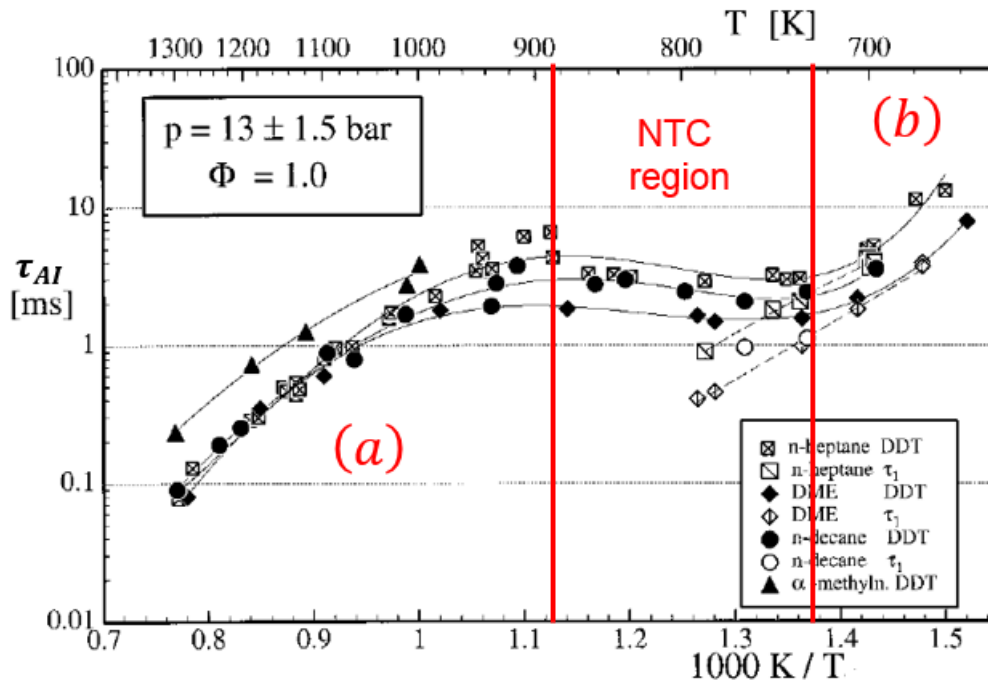


Figure 2.2 – Auto-ignition delay τ_{AI} of various fuels in a 0D constant pressure reactor. Figure adapted from [22].

2.1.2 Conceptual models of Diesel spray combustion

The present study focuses on the flame stabilization mechanisms when the flame anchors at a certain distance from the injector. However, before reaching this state, 4 distinct temporal stages of combustion are observed and will be described below. Pickett et al. [15] have reported that these different stages may have an impact on the high-temperature flame stabilization. Fig. 2.3 shows a conceptual model describing these stages, which has been proposed by Dec [23] and, then, improved by Bruneaux [24].

- Injection – Vaporization: The liquid fuel is injected at high velocity, and atomizes into small droplets as it penetrates into the combustion chamber. The atomized fuel absorbs heat from the surrounding heated compressed air, vaporizes, and mixes with the surrounding high-temperature and high-pressure air. Then, the vapor continues to penetrate in the chamber forming a homogeneous mixing of fuel and air.

- Premixed auto-ignition start (stage 1⁻ Fig. 2.3-bottom): Auto-ignition appears downstream of the liquid jet where the fuel has been vaporized. This stage is identified by formaldehyde pockets, as indication of fuel reaction decomposition at relatively low temperature (cool-flame). The location of auto-ignition corresponds to fuel-rich areas of the jet where the mixture and temperature history are favorable to auto-ignition.
- Premixed auto-ignition extension (stage 1* stage 1⁺): During this stage, an extension of formaldehyde until it reaches a homogeneous cloud is observed. Small regions of OH are observed inside the formaldehyde cloud. OH radicals are a characteristic marker of high temperature combustion, they have been detected by LIF measurements. Therefore, OH LIF detection indicates the set-up of high-temperature reactions: auto-ignition. Then, high temperature reactions region increases consuming the formaldehyde.
- Transition to diffusion combustion (stage 2⁻ and 2*): During the premixed combustion, a diffusion flame grows at the jet periphery. At the same time, the cool-flame is also present upstream of the flame base in a fuel rich premixed zone. Soot precursors, namely Polycyclic Aromatic Hydrocarbons (PAH), are formed in the center of the jet due to mixing of fuel rich pockets with the hot diffusion flame products. Then, formaldehyde is getting consumed at the jet periphery due to the progression of the diffusion flame.
- Stabilized diffusion combustion (stage 2⁺) : The diffusion flame has now consumed all the formaldehyde at the jet periphery. In the centerline, OH radicals are consumed leading to the formation of high concentration of PAH and soot. Large level of OH is observed at the jet periphery. During this stage, there is still some formaldehyde in the centerline upstream of the LOL where the small temperature reactions occur [24].

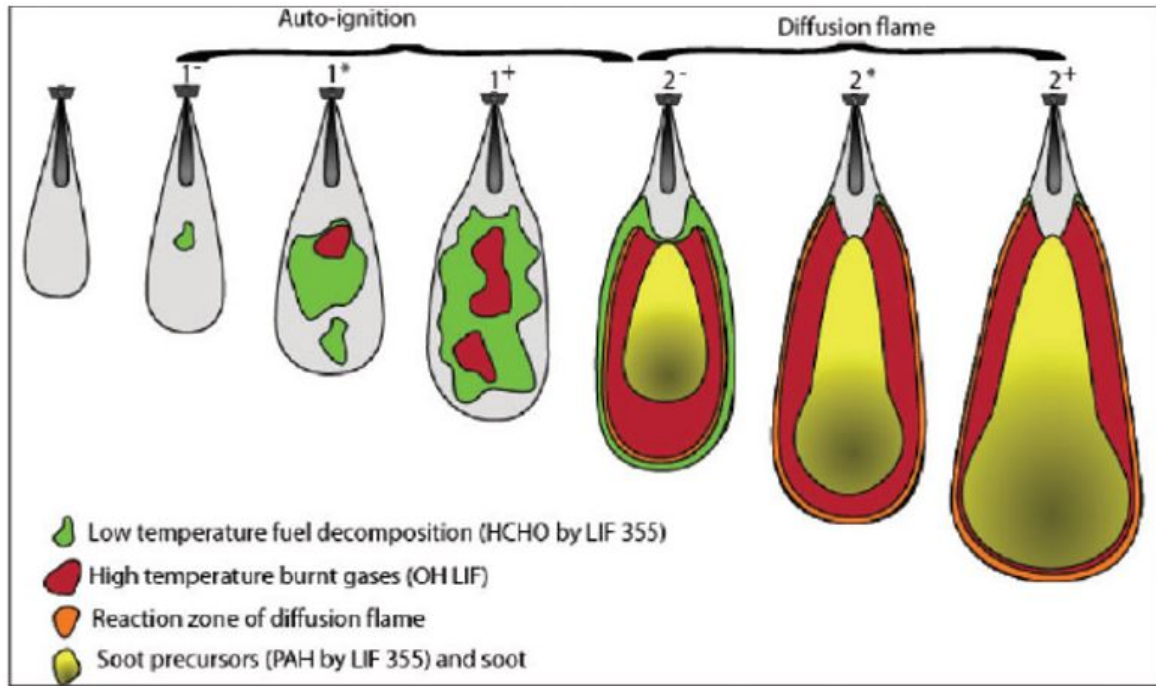


Figure 2.3 – Schematic of a conceptual combustion model describing from the injection to the stabilized diffusion combustion [24].

Fig. 2.4 shows a representation of the stabilized diffusion combustion characterized by a diffusion flame at the jet periphery with a rich-partially premixed area upstream of the lift-off. The lift-off is the most upstream point of the flame and the corresponding axial distance between the injector and the flame is called the Lift-off Length (LOL). Because of the rich-partially premixed area upstream of the lift-off, the Diesel flames are traditionally classified as non-premixed flames [25] similar to those found under atmospheric conditions [26].

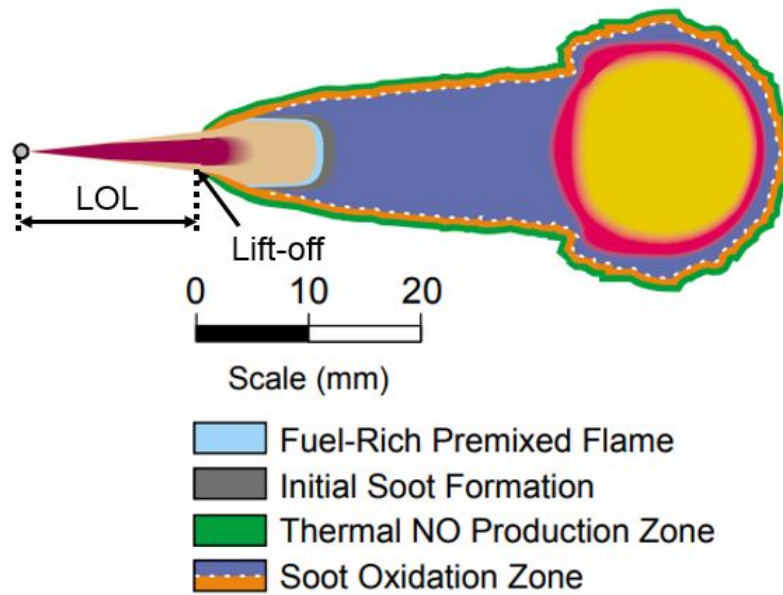


Figure 2.4 – Schematic of a conceptual combustion model during the stabilized diffusion combustion [23].

2.2 Non-premixed gaseous jet flames

Under Diesel conditions two major stabilization mechanisms are proposed so far in the literature (more details in Section 2.3): flame propagation at the flame base and auto-ignition. These two stabilization mechanisms have been widely studied for gaseous non-premixed flames. Therefore, this Section focuses on laminar and turbulent lifted diffusion flame for a gaseous injection.

2.2.1 Stabilization by premixed flame propagation at the flame base

2.2.1.1 Stabilization by perfectly premixed flame

In the case of a lifted diffusion flame (illustrated in Fig. 2.5-left), fuel and oxidizer mix from the injector (or burner) until the lift-off. In this first concept, the mixture at the lift-off is assumed to be perfectly premixed. The flame is stabilized where the mean flow velocity (U_{flow}^{mean}) is equal to the turbulent flame speed (S_T). In this theory, flame stabilization occurs at the contour of the mean stoichiometric mixture. Vanquickenborne and Van Tiggelen [27] have proposed one of the first experimental studies, arguing that the turbulent flame speed equals the gas flow velocity at the base of a lifted diffusion methane flame. They found that lifted diffusion methane flames are stabilized in a region where stoichiometry is reached. A velocity analysis between U_{flow}^{mean} and S_T , is also proposed in Fig. 2.5-right. The flame stabilization point seems to be at the tangency point between U_{flow}^{mean} and S_T . Gautam [28] proposed an adjustment to this concept, in which the turbulent premixed flame speed is related to the turbulence intensity. Later, Lawn

et al. [29] have confirmed that the flame base is stabilized at an equilibrium between the mean flow velocity and the turbulent flame speed.

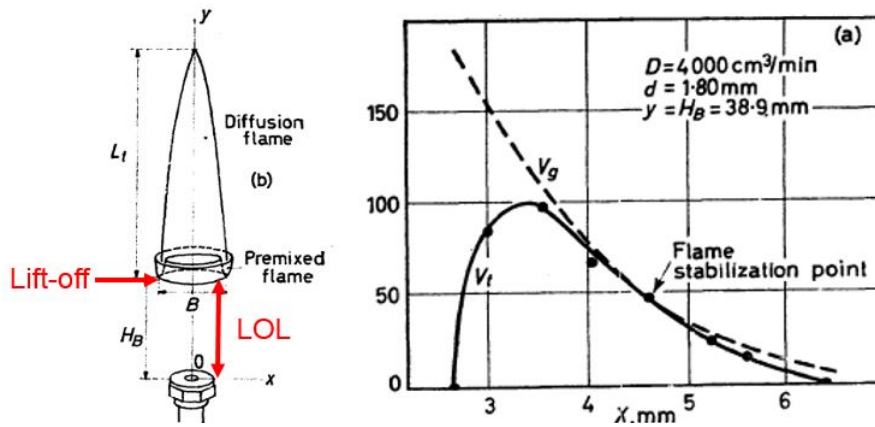


Figure 2.5 – Hypothetical shape of premixed flame (left) and experimental verification of the hypothetical stabilization mechanisms. Figures adapted from [27].

These studies raised the question of the turbulent flame speed estimation. Poinso and Veynante [25] proposed the following definition: S_T is the velocity needed at the inlet of a control volume to keep a turbulent flame stationary in the mean inside this volume. In practice Eq. (2.1) (from [25]) has been used to estimate S_T .

$$S_T = S_L^0 \frac{A_T}{A}, \quad (2.1)$$

where S_L^0 is the laminar planar unstretched propagating flame speed. A representation of the area A and A_T is provided in Fig. 2.6 for greater clarity, where A is the area of a cross section of the control volume and A_T is the total flame area contained in the control volume. The main difficulty to compute S_T according to Eq. (2.1) is the prediction of the ratio A_T/A . Many semi-phenomenological models for S_T can be found in the literature (see [30] for a review and [31, 32] for more details) but both experimental and theoretical results show considerable scatterings. This discrepancy may be due to measurement errors and poor modeling according to Poinso and Veynante [25]. According to [27], S_T ranges from 0.9 to $5S_L^0$ for methane flames and for a Reynolds number ($Re = (\rho \cdot u \cdot d) / \mu$) varying from 1900 to 7600. Numerical simulation of Kaplan [33] indicates that the axial flow velocity at the base of methane flames ($Re=12,500$) ranges from 1.6 to $2.6S_L^0$. These values of velocity are of the same order of magnitude as the estimated S_T in [27], which tends to confirm flame stabilization as an equilibrium between turbulent flame speed and mean jet velocity.

However, Namazian et al. [34] measured the flow velocity at the flame base of a lifted methane flame ($Re=7000$). They reported flow velocity at approx. 5 m/s ($13S_L$) with a peak velocity of 15 m/s ($39S_L$) at the lift-off, which is much higher than the turbulent flame velocity.

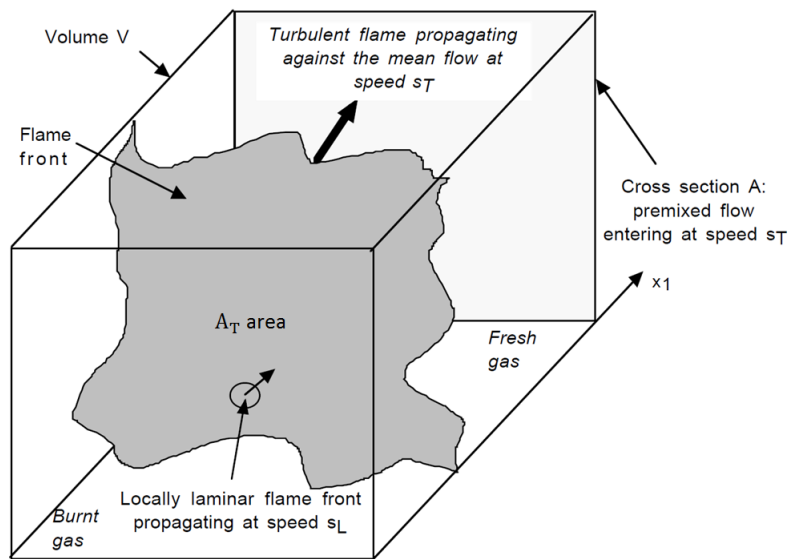


Figure 2.6 – Flame wrinkling by turbulence where A and A_T are displayed. Figure adapted from [25].

2.2.1.2 Stabilization by partially premixed flame

In most configurations where fuel and air are injected separately, the mixing in the flame base region is not perfectly premixed. As a result, the concept developed in the above Section cannot be applied without adaptations. In this context, triple flames (schematic representation in Fig. 2.7-top), also called edge-flames, have been proposed as one of the most convincing approaches to explain the flame stabilization of lifted diffusion flames when the mixture is partially premixed.

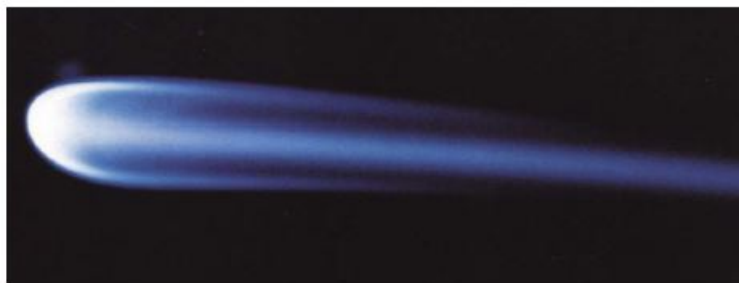
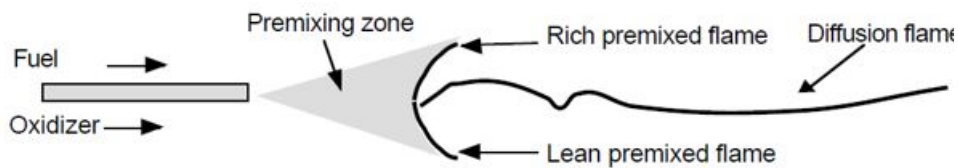


Figure 2.7 – Triple flames structure by [25] (top) and triple flames visualization in a laminar flow by [35] (bottom).

Triple flames have been first observed experimentally by Phillips [36], and photographed by [35], see Fig. 2.7-bottom. They consist of three branches: a rich premixed flame, a lean premixed flame and in-between a third branch, which is a diffusion flame situated on the stoichiometric line.

Fig. 2.8 (extracted from [37] for a laminar flow) presents the ratio u/S_L^0 , where u is the horizontal velocity at the stoichiometric line along the horizontal coordinate. Far upstream from the triple point (in the fresh gas), the flow velocity is higher than S_L^0 . Then, u decreases getting closer to the triple point to finally reach S_L^0 . This observation is different from laminar planar unstretched flame where the flame cannot stabilize if the flow velocity in the fresh gas is larger than S_L^0 . According to the authors, the decrease of u in front of the triple point is due to the flow divergence in front of the flame attributed to the heat release as shown in Fig. 2.8 with the streamlines.

The flow divergence effects also explain the shape of triple flames: the rich and lean branches are curved because the laminar flame speed decreases as the mixture deviates from the stoichiometric line. As a result, they stabilize further downstream where the flow velocity is lower due to dilation effects on the flow.

In order to enrich their study, the authors have introduced the far-field flame speed U_F . This velocity corresponds to the flame front speed of the entire structure relative to the flow and can be estimated as following:

$$U_F \sim S_L^0 \left(\frac{\rho_u}{\rho_b} \right)^{1/2}, \quad (2.2)$$

where ρ_u and ρ_b are the unburnt and burnt gas densities. Since $\rho_u/\rho_b > 1$, Eq. (2.2) demonstrates the importance of triple flames propagation as a stabilization mechanism, which can modify the upstream flow leading to a higher flame speed.

The concept of triple flame has been widely proposed (in experimental and numerical studies) to explain the flame stabilization, first for laminar flows [35–37] and then for turbulent flows [38–41].

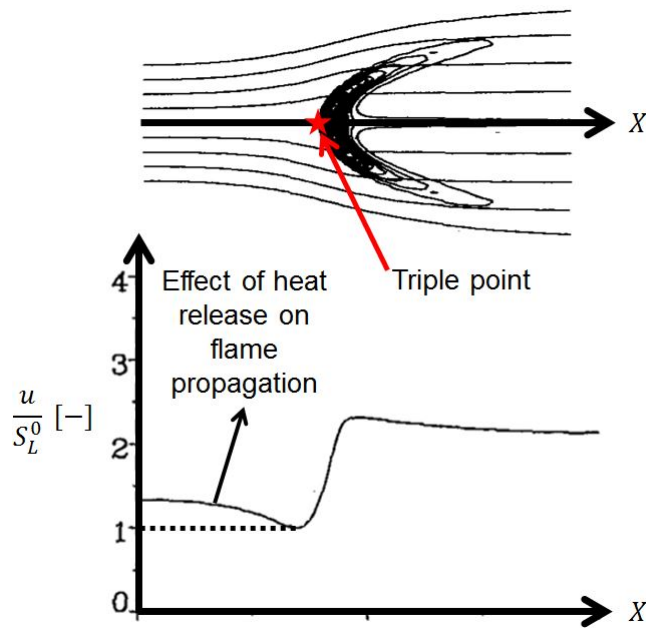


Figure 2.8 – Top: contour lines of the reaction rate showing a triple flame with stream lines. Bottom: ratio u/S_L^0 as a function of the axial coordinate on the stoichiometric line. Figure adapted from [37].

2.2.2 Impact of scalar dissipation

Peters et al. [42] have used the scalar dissipation χ defined in Eq. (2.3), to investigate the flame stabilization of a lifted diffusion methane flame.

$$\chi = 2D \left(\frac{\partial z}{\partial x_i} \right)^2, \quad (2.3)$$

where D is the diffusion coefficient, z the mixture fraction ($z=1$ for fuel and $z=0$ for oxidizer) and $x_{i=1,2,3}$ are the spatial coordinates. In this theory, the flame is stabilized because it cannot move further upstream due to too high levels of χ .

As illustrated in Fig. 2.9, χ_{st} decreases as the distance from the injector increases. The authors argued that the lift-off is localized where $\chi_{st} = \chi_{qu}$, χ_{qu} being a critical value of the scalar dissipation rate. Indeed, if $\chi_{st} > \chi_{qu}$ the flame is quenched, caused by a mixing time scale too high in comparison to the chemical time scale. In the work of Peters et al. [42], χ_{qu} is given by Linan [43] who analyzed the structure and extinction of counterflow diffusion flames.

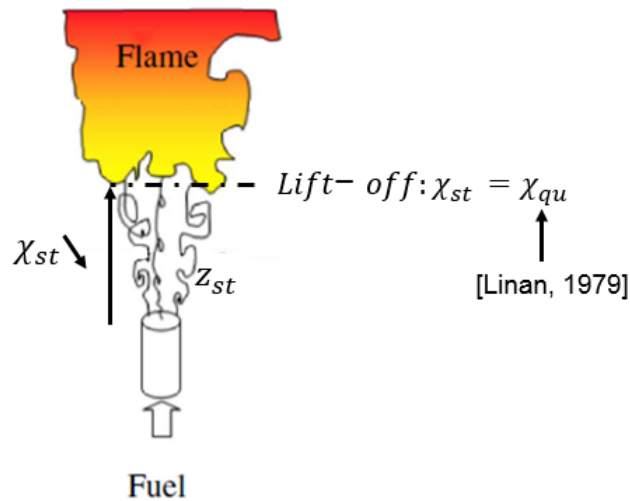


Figure 2.9 – Flame stabilization by critical scalar dissipation rate according to Peters et al. [42].

Fig. 2.10 shows a comparison between the experimental measurement of the lift-off length (or h for lift-off height) (solid line) and theoretical estimations based on the methodology described above (dotted curves). Three theoretical estimations of the LOL are proposed (Th_1 , Th_2 and Th_3), they come from different methods for the calculation of the diffusion term D and $\left(\frac{\partial z_{st}}{\partial x_i}\right)^2$ in the estimation of χ_{st} . For Th_3 , a good agreement between the estimated and the measured LOL is observed, indicating that the critical dissipation theory may explain the flame stabilization.

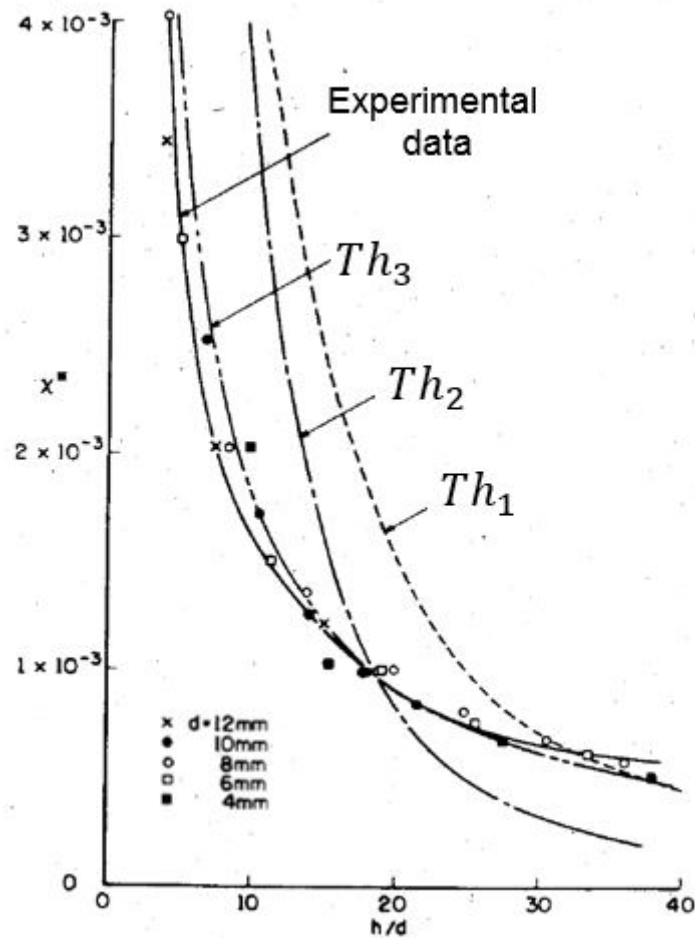


Figure 2.10 – Nondimensional scalar dissipation rate as a function of the ratio of the lift-off height (h) to the jet diameter (d) for a turbulent methane diffusion flame. Figure adapted from [42].

More recently, Everest et al. [44] found that χ , at the lift-off, exceeds the predicted value by a factor of sixty. Similarly, Schefer et al. [45] for turbulent diffusion flames, found the value of χ considerably below the critical value in the lift-off area. Moreover, flame quenching can only explain the lack of flame. For that reason, this theory cannot, alone, fully explain the stabilization mechanisms of a turbulent lifted-flame. However, Lawn [29] suggests that the role of scalar dissipation rate in the flame stabilization cannot be totally excluded.

2.2.3 Stabilization by recirculation of burnt gases

Based on the analysis of turbulent diffusion flames, Broadwell et al. [46] proposed a theory (illustrated in Fig. 2.11) where large-scale turbulent structures lead to an upstream recirculation of hot combustion products which can allow auto-igniting the fresh gases mixture.

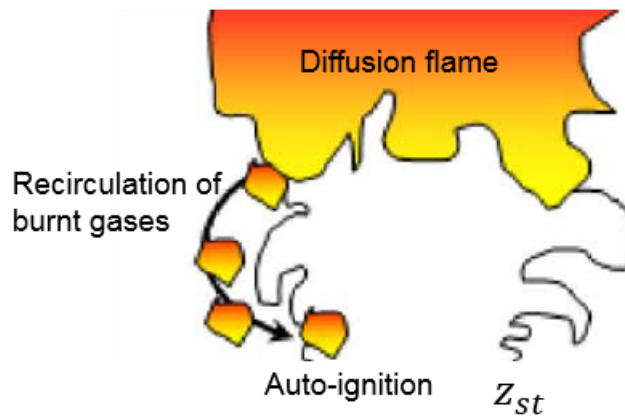


Figure 2.11 – Flame stabilization by recirculation of burnt gases according to Broadwell et al.[46]. Figure adapted from Karami et al. [47].

In this stabilization mechanism, the flame is blown out when the recirculating hot reaction products are mixed so rapidly with the fresh gas that there is not enough time for ignition. Therefore, their blowout criterion is that the ratio of the local mixing time t_d , to a characteristic chemical time t_c is lower than a critical value of ε as defined in Eq. (2.4):

$$\varepsilon = \frac{t_d}{t_c} = d S_L^2 \Psi^2 \frac{(\rho_{fuel}/\rho_{air})^{1/2}}{u_b \kappa}, \quad (2.4)$$

where d is the nozzle diameter, Ψ is the stoichiometric air to fuel ratio, κ is the thermal conductivity, ρ_{fuel} and ρ_{air} are the fuel and air density. A critical value of the blowout parameters, ε has been explored for different fuels (methane, propane, ethylene, acetylene, hydrogen and butane). The authors have found an average critical value of $\varepsilon = 4.8$ for all of the fuels studied. It is important to note that this critical value has not been used to quantify the LOL. Nevertheless, they have proposed the following relationship to estimate it:

$$LOL \sim [u d (\rho_{fuel}/\rho_{air})^{1/2} \kappa / S_L^2]^{1/2}, \quad (2.5)$$

where u is the jet velocity. However, no comparison with experimental observations has been made. This stabilization mechanism has been rarely used for gaseous flame thereafter, mainly because triple flames have become widely accepted as the major elements contributing to the stabilization of a lifted diffusion flame.

2.3 Diesel spray flames

Fig. 2.12 shows a comparison between a gaseous diffusion flame, as studied in the previous Section (left), and a Diesel spray flame (right). Under Diesel conditions, the stabilization mechanisms may be different from gaseous diffusion flames because of high-temperature, high-pressure conditions, complex chemistry (e.g. the presence of a cool-flame), very high Reynolds number (100,000-200,000 [16]) and liquid fuel injection. However, they both remain turbulent diffusion flames with a partially premixed area upstream

the lift-off. Thus, some of the previous stabilization mechanisms may be also involved in the diesel combustion.

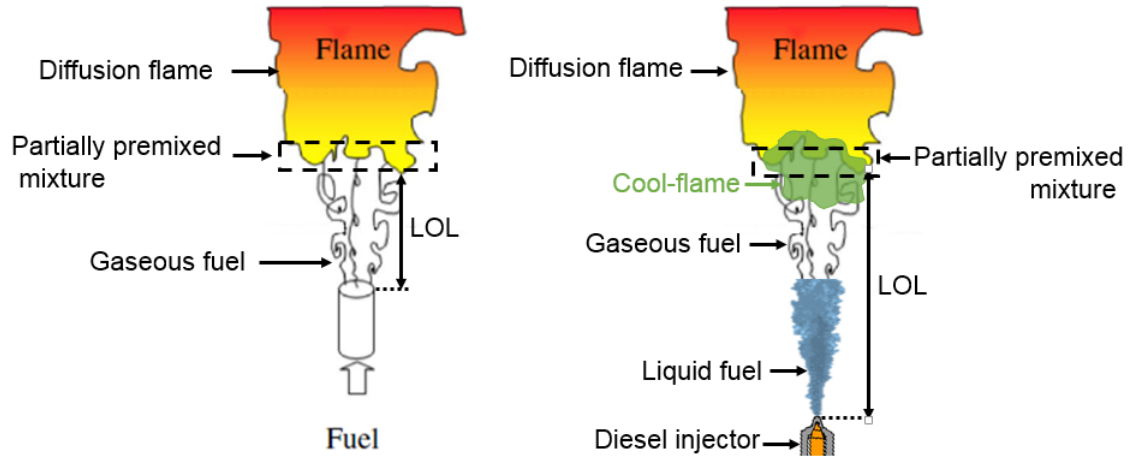


Figure 2.12 – Illustration of a turbulent gaseous diffusion flame (left) and a Diesel spray flame (right).

2.3.1 Stabilization by a premixed flame at the flame base

One of the first comprehensive studies of LOL under Diesel conditions was conducted by Siebers and Higgins [1], focusing on the impact of injector hole diameter, injection pressure, ambient temperature and density variations on the flame stabilization. This study was completed by an analysis of the impact of oxygen concentration on the LOL [2], and by the work presented in [48] and [49] analyzing the relation between the LOL and soot production. Fig. 2.13 summarizes the trends obtained when test conditions are varied.

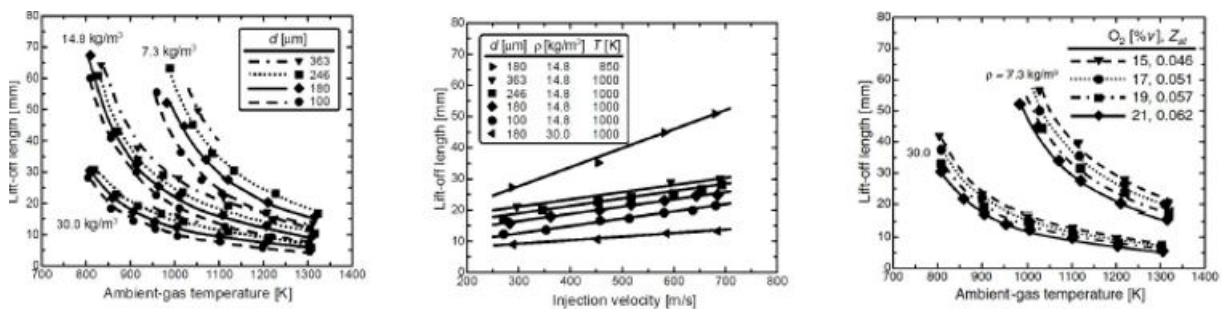


Figure 2.13 – LOL variation versus ambient temperature (left) [1], injection velocity (middle) [1] and oxygen concentration (right) [2].

The dependence of the LOL on the different parameters was found to be [1, 2]:

- Ambient temperature : $LOL \sim T_a^{-3.74}$
- Ambient density : $LOL \sim \rho^{-0.85}$

- Diameter of the injector hole : $LOL \sim d^{0.34}$
- Dioxygen concentration (proportional to z_{st} [2]) : $LOL \sim z_{st}^{-1}$
- Injection velocity : $LOL \sim U_0$

Combining these dependencies, Siebers, Higgins and Pickett [1, 2] proposed an experimental correlation which predicts the time-averaged LOL when the flame is stabilized:

$$LOL \sim U_0 T_a^{-3.74} \rho^{-0.85} d^{0.34} z_{st}^{-1}. \quad (2.6)$$

Siebers et al. [2] have, then, compared the experimental correlation (Eq. 2.6) to the following relationship:

$$LOL \sim U_0 \frac{\kappa}{S_L^2(z_{st})} z_{st}, \quad (2.7)$$

which has been proposed by Peters [50] assuming a flame stabilization based on premixed flame propagation as detailed in Section 2.2.1.1. In Eq. 2.7, κ is the thermal diffusivity and $S_L(z_{st})$ is the laminar flame speed at stoichiometry. The similarities and differences between the predictions by Eq. 2.6 and Eq. 2.7 can be summarized as follows:

- **Temperature effect:** In Eq. 2.7, two parameters are function of temperature: the thermal diffusivity κ and the laminar flame speed $S_L(z_{st})$. Metghalchi and Keck [51] have proposed the following relation to predict the flame speed as a function of temperature and pressure:

$$S_L \sim T^a P^b. \quad (2.8)$$

Higgins and Siebers [52] have chosen the value of a and b for gasoline ($a = 2.1$ and $b = -0.36$). According to [53], a and b should not change with Diesel. Using Eq. 2.8 along an iso-density profile (constant pressure) gives:

$$S_L \sim T^{2.1}. \quad (2.9)$$

Moreover, the thermal diffusivity of a gas increases with the square root of the temperature:

$$\kappa \sim T^{0.5}. \quad (2.10)$$

Injecting Eq. 2.9 and Eq. 2.10 in Eq. 2.7, we obtain:

$$LOL \sim \frac{\kappa}{S_L^2(Z_{st})} \sim \frac{T^{0.5}}{T^{2.1*2}} \sim T^{-3.7}. \quad (2.11)$$

Eq. 2.11 shows that the temperature dependence between the theoretical ($T^{-3.7}$) formulation and the experimental correlation ($T^{-3.74}$) is in excellent agreement.

- **Density effect:** Following the same logic than for ambient temperature, Eq. 2.7 can be written as a function of density assuming the thermal diffusivity κ is inversely proportional to density and $S_L \sim \rho_a^{-0.2}$ according to [54]:

$$LOL \sim \frac{\kappa}{S_L^2(z_{st})} = \frac{\rho^{-1}}{\rho^{-0.2*2}} = \rho_a^{-0.6}. \quad (2.12)$$

This relation is different from the experimental correlation ($LOL \sim \rho_a^{-0.85}$), but it is without taking into account the spreading angle of the spray which depends on the ambient density [55]. After correction of the vapor angle, the new correlation binding LOL and density is:

$$LOL \sim \rho_a^{-0.8}, \quad (2.13)$$

which is very close from the experimental measurement ($LOL \sim \rho_a^{-0.85}$) according to [2].

- **Diameter of the injector hole:** Eq. 2.7 does not take into account the diameter of the injector hole, whereas it has been experimentally observed that it has an impact on the lift-off stabilization (proportional to $d^{0.34}$). According to [52], this weak dependency can be explained by the fact that Eq. 2.6 is obtained from a flame spray while Eq. 2.7 is proposed for a gaseous jet flame.
- **Dioxygen concentration effect:** Dugger et al. [56] proposed that the laminar flame speed is proportional to the dioxygen concentration. Thus, only considering the dioxygen concentration, Eq. 2.7 can be expressed as follows:

$$LOL \sim \frac{z_{st}}{S_L^2(z_{st})} \sim \frac{z_{st}}{z_{st}^{-2}} = z_{st}^{-1}, \quad (2.14)$$

Therefore, Eq. 2.14 presents the same proportionality relation than Eq. 2.6 varying dioxygen concentration.

- **Injection velocity effect:** Eq. 2.7 presents a linear dependence of the LOL with the injection velocity. This dependence has been validated by experiments as shown in Fig. 2.13.

The experimental correlation (Eq. 2.6) seems to be in good agreement with the theory. However, other experiments performed at Sandia [15, 57–59] seem to indicate the limit of this theory: Fig. 2.14 shows the time-averaged LOL of Diesel-type spray flame as a function of the ambient temperature for different fuels (with different Cetane numbers, 42, 60 and 80). It clearly shows some significant differences of the LOL varying the fuel, especially for low temperature conditions. This strong dependence of the fuel type on the prediction of the LOL was not expected in Eq. 2.7. This lack of prediction highlights the fact that Eq. 2.7, based on premixed flame propagation does not fully explain the

flame stabilization. Therefore, other physical and chemical phenomena must be taken into account to correctly predict the LOL.

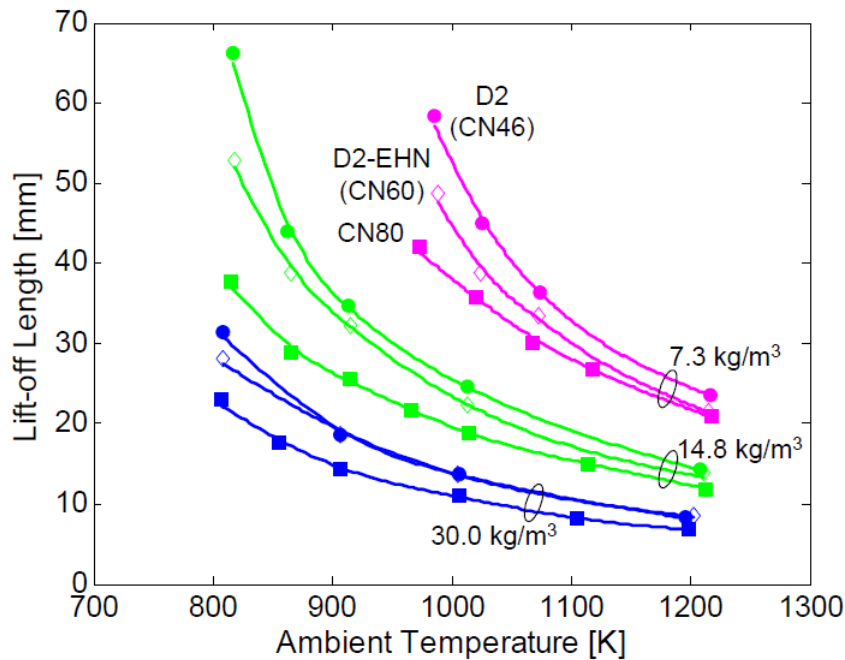


Figure 2.14 – LOL for three fuels and ambient densities. Labels are given by the symbol used for each fuel. The experimental conditions were: 180 μm orifice, 1380 bar pressure drop, fuel at 373 K, and 21 % ambient oxygen [15].

2.3.2 Role of flame extinction

More recently, Venugopal and Abraham [60], based on Reynolds Averaged Navier-Stokes (RANS), have proposed a study of Diesel flame stabilization. In this work [60], lift-off is modeled to result from flame extinction in the near-field of the jet. Thus, for Venugopal and Abraham [60], the flame is stabilized for a critical value of χ like for gaseous diffusion flames. Authors have carried test conditions variations (keeping constant the diameter of the injector hole) in order to propose the following power law estimating a time-averaged LOL under Diesel conditions:

$$LOL \sim U_0^{0.72} T_a^{-2.78} \rho_a^{-0.76} Z_{st}^{-0.82}. \quad (2.15)$$

Comparing this numerically estimated power law to the experimental correlation (Eq. 2.6, based on premixed flame propagation) in Table 2.1, it appears that the coefficients attributed to ρ_a and Z_{st} are in good agreement with the experiments while the coefficients U_0 and T_a are underpredicted.

Table 2.1 – Comparison of the coefficients predicting the time-averaged LOL between experiments and simulations (RANS). The experiments assumed a flame stabilization by premixed flame at the flame base while the RANS estimated the LOL by flame extinction.

	$LOL \sim U_0^a T_a^b \rho_a^c d^d Z_{st}^e$				
	a	b	c	d	e
Siebers et al. [2] (experiments)	1	-3.74	-0.85	0.34	-1
Venugopal and Abraham [60] (RANS)	0.72	-2.78	-0.76	not addressed	-0.82

In conclusion, Venugopal and Abraham [60] argued that the flame seems to stabilize in the region where the local scalar dissipation reaches a critical extinction value, since the coefficients of the power law found by the authors (last line Table 2.1) are fairly close to the experimental coefficients (penultimate line Table 2.1). However, the authors also stated that it would be inappropriate to conclude that, locally, high scalar dissipation rates are the only factor explaining the flame stabilization.

2.3.3 Role of auto-ignition

Pauls et al. [61] have proposed an experimental and numerical study to evaluate the relative importance of auto-ignition and flame propagation in the stabilization of different Diesel fuels and ambient test conditions. The measurements have been performed by OH chemiluminescence. The Unsteady Reynolds Averaged Navier-Stokes-URANS approach was chosen for the numerical study. The URANS were run using G-equation coupled with the Multiple Representative Interactive Flamelet (G-MRIF model described in [61]) which predicts both auto-ignition and flame propagation. The combination of these two techniques allowed the authors to propose a new concept illustrated in Fig. 2.15.

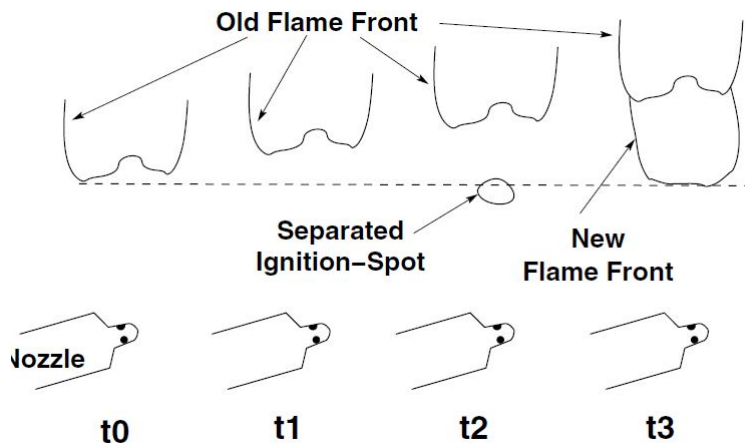


Figure 2.15 – Stabilization of the flame-front by auto-ignition and flame propagation [61].

Between t_0 and t_1 , the flame is convected downstream due to the high flow velocity. Because of relatively slow flame propagation speed (compared to the jet velocity), a slow downstream drift of the flame can be observed (also named as a downstream propagation). At t_2 , a separated ignition-spot occurs. Fig. 2.16 shows a visualization of such event for

a bio-Diesel spray flame (see properties of the fuel in Table of [61]). At t_3 , the separated ignition-spot merges the main flame creating a new flame front, which is then convected downstream until a new auto-ignition occurs.

For the authors, the main flame stabilization mechanism is auto-ignition. Nevertheless, flame propagation is also playing a (minor) role in the downstream propagation.

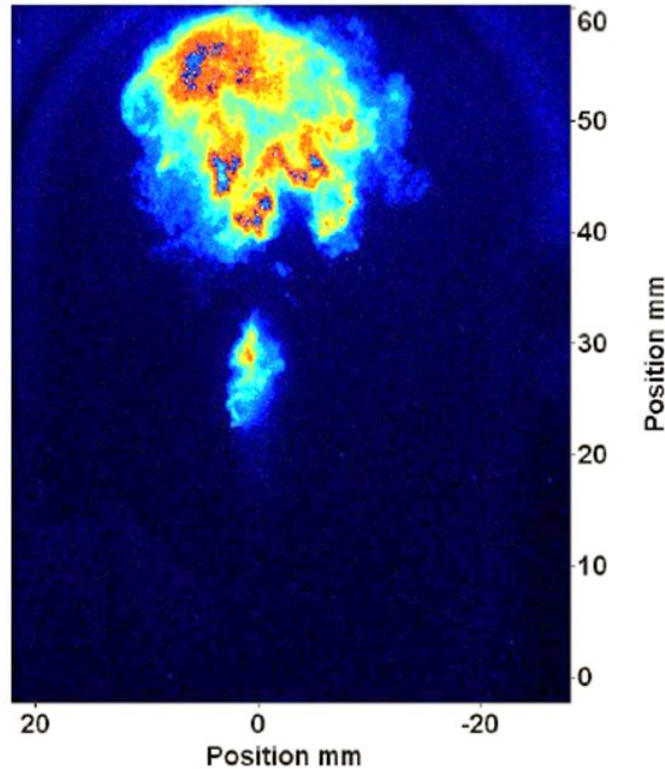


Figure 2.16 – Typical OH chemiluminescence single-shot showing a separated ignition spot [61].

Pickett et al. [15] have investigated the effect of cool-flame on the Diesel-type flame stabilization. Fig. 2.17 shows the cool-flame shortly before the auto-ignition delay and the corresponding LOL, for different fuels. It appears that a fuel leading to a short distance between the injector and the cool-flame base leads to a short LOL, or *vice versa*. Thus, the authors argued that the location of the cool-flame has some bearings on the flame stabilization. Many studies have focused on the interactions between the cool- and the high-temperature flame [18, 62–66]. However, to the best of our knowledge, no studies have clearly shown how the cool-flame can help the high-temperature flame to stabilize. Therefore, the importance of the cool-flame upstream the high-temperature flame will be investigated in Chapter 4.

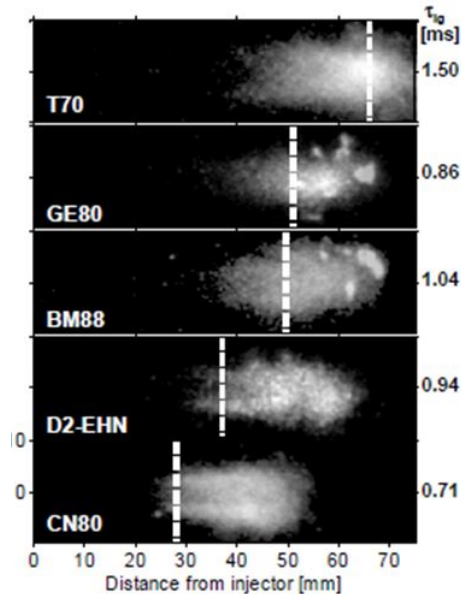


Figure 2.17 – Cool-flame chemiluminescence images shortly before auto-ignition. The fuel is given on the lower left corner and on the right side the auto-ignition delay is displayed. Quasi-steady LOL is shown as a vertical dashed white line [15].

2.3.4 Combined role of edge-flames and auto-ignition

Since 2015, with the work of Krisman et al. [67], many DNS have shown the presence of edge-flames under Diesel conditions, which plays a role in the flame stabilization. DNS allow to resolve all space and time scales of the turbulent flow, mixing and chemical reactions without any simplifying assumption on the interactions between flow and chemical reactions. However, because of the prohibitive computational cost of performing 3D-DNS of the full spray flame (mesh resolution in the range of few micrometers due to very fine flame thickness), simplified DNS (detailed in the four sub-sections below) have been run to analyze the interactions between edge-flames and auto-ignition:

- 2D-DNS of a spatially stabilized flame in a laminar mixing layer
- 2D-DNS of a temporally evolving mixing layer subject to decaying isotropic turbulence
- 2D and 3D-DNS of a temporally evolving turbulent mixing layer where ignition takes place in a reference frame traveling at the mean speed of the two streams
- 3D-DNS of a spatially developing gaseous slot jet flame

2.3.4.1 2D-DNS of a laminar mixing layer

Krisman et al. [67] have performed a 2D-DNS under near-diesel conditions. The domain was initialized with a mixing layer between a pure oxidizer (air) and a pure fuel (DME) according to a hyperbolic tangent profile at a pressure of 40 atmospheres. A fixed uniform velocity is imposed in the x direction (see Fig. 2.18), while the transverse

velocity, in the y direction, is set to zero. The composition and temperature inlet profiles are convected at uniform velocity U_X . This study has been conducted with a reduced mechanism including 30 species, taking into account auto-ignition, cool-flame chemistry and NTC. They have simulated different test conditions (different oxidizer temperatures and flow velocities) to analyze the flame stabilization mechanisms.

Fig. 2.18 shows the heat-release rate for the different test conditions. The stabilization mechanism was found to be temperature dependent:

- For ambient oxidizer temperature at 700 K, we can recognize a triple flame shape. In this case, the flame is stabilized where the flow velocity is equal to the triple flame displacement speed.
- At 900 K, in addition to the main triple flame, there is an upstream fourth branch due to the low-temperature chemistry. This leads to call this flame a quadruple flame. However, even with this extra branch, the authors argued that the flame is stabilized by premixed flame propagation.
- At 1100 and 1300 K, the flame keeps the same structure downstream but, upstream, there are two more branches (due to low-temperature chemistry), leading to call this flame a quintuple flame. In these cases, the flames are stabilized by auto-ignition.
- At 1500 K, the flame reverts to a quadruple flame stabilized by auto-ignition.

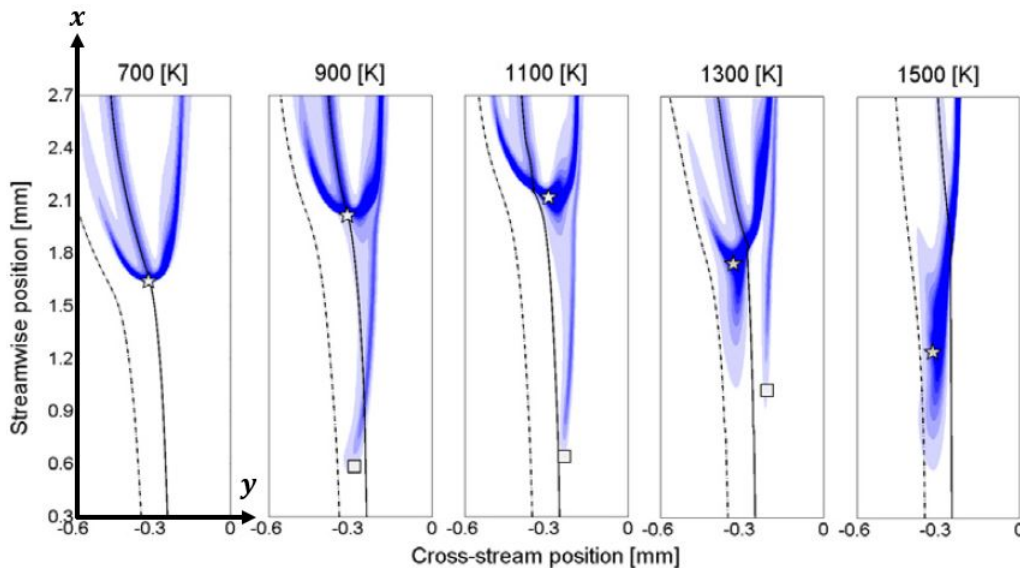


Figure 2.18 – The color shows the edge-flames through heat release rate fields, the solid line indicates the z_{st} contour, the star marker indicates the flame base position and the square marker indicates the closer distance to the injector of the cool-flame [67].

Following the same methodology than proposed by Krisman et al. [67], Deng et al. [68, 69] have also simulated a 2D-DNS of a laminar mixing layer using DME as fuel. They

have varied the oxidizer (air) temperature between 700 and 1100 K [68], then, in [69] they have varied the uniform inlet flow velocities between 2.4 and 8 m/s. In both cases ([68] and [69]), the ambient pressure was 30 atmospheres. The same flame structures than observed in [67] were found.

The authors [68, 69] proposed a qualitative regime diagram for the flame stabilization mechanisms as the boundary temperature and the inlet velocity vary (Fig. 2.19) based on a Chemical Explosive Mode Analysis (CEMA) [70, 71], (briefly described in Appendix A.1) and on a Lagrangian Flamelet Analysis (LFA) (described in [72]).

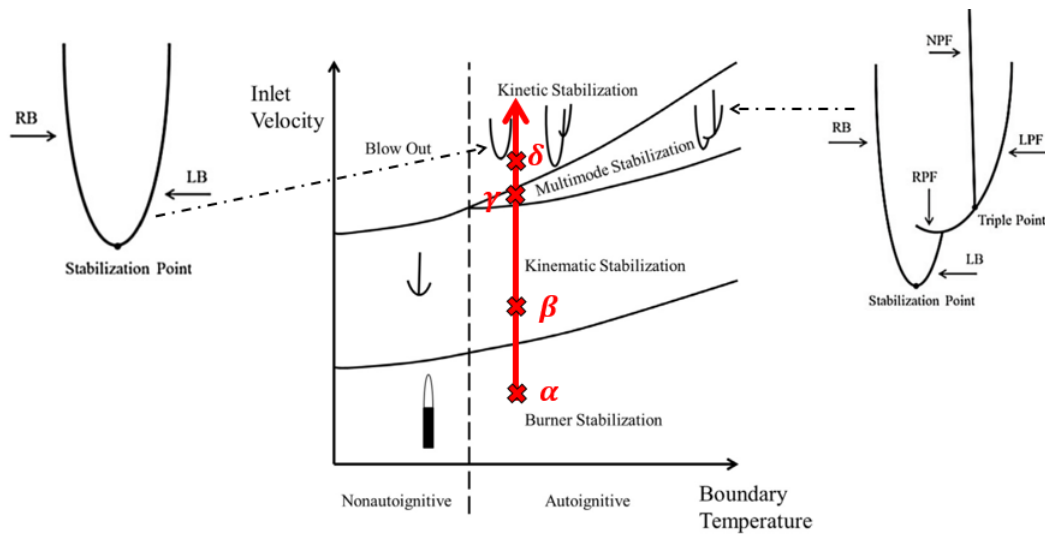


Figure 2.19 – Qualitative regime diagram for the stabilization mechanisms as the boundary temperature and inlet velocity vary. The left cartoon is a zoom of a flame topology during the "kinetic" stabilization mode while the right cartoon shows an edge-flame during the "multi-mode" stabilization. The meaning of the acronyms is: RB: Rich Branch, LB: Lean Branch, RPF: Rich Premixed Flame, LPF: Lean Premixed Flame, NPF: Non-Premixed Flame. Figure adapted from [69].

Fig. 2.19 is described following the vertical arrow in the middle of the figure from α to δ :

- α : When the inlet flow velocity is below a certain threshold value, the flame is attached to the burner in both autoignitive and non-autoignitive conditions (noted as α).
- β : Increasing the inlet velocity while keeping constant the boundary temperature, the flame stabilization mechanism transits from a burner stabilization to a kinematic balance between flame speed and incoming flow velocity.
- γ : Then, a multi-mode stabilization is observed, where the flame is stabilized by both flame propagation and auto-ignition as reported in [67].

- δ : Finally, increasing the inlet velocity leads to kinetic stabilization governed by auto-ignition. In this mode, auto-ignition and NTC chemistry play a major role in the flame stabilization.

Very recently, Dalakoti et al. [63] have simulated a 2D-DNS of a laminar mixing layer similarly to [67–69]. However, in this recent work, the fuel was *n*-dodecane and the ambient pressure was 60 bar in order to come closer to the ECN spray A conditions [17].

The influence of inlet flow velocity and scalar dissipation rate (χ) on the edge-flame structure and the flame stabilization has been investigated. A negative correlation of the high-temperature flame speed with χ was observed (increasing χ decreases the flame propagation speed) as observed for triple flames under non-autoignitive conditions [73, 74]. Moreover, the low-temperature chemistry branch causes a flow divergence upstream of the triple point leading to reduce the χ . The low-temperature chemistry thus makes the high-temperature flame more resilient to variations of χ and, therefore, helps the high-temperature flame stabilization.

These 2D-DNS of a laminar mixing layer [63, 67–69] found an interesting coupling (flame propagation/auto-ignition) to explain the flame stabilization. However, these works present some large differences compared to a real diesel injection which may change the conclusion on flame stabilization.

2.3.4.2 2D-DNS of a turbulent decreasing mixing layer

Krisman et al. [64, 75] have performed 2D DNS of an igniting turbulent mixing layer subject to a decaying isotropic turbulence. Fig. 2.20 shows the computational domain where the mixing layer was composed of DME and air with a spectrum of isotropic turbulence imposed as an initial condition in order to match the Damkholer number estimated at the flame base of a diesel jet. The thermochemical conditions were identical to the 900 K case from the laminar edge-flame study [67]. Unlike the DNS shown in Section 2.3.4.1, such approach allows to analyze turbulence/auto-ignition/edge-flame interaction.

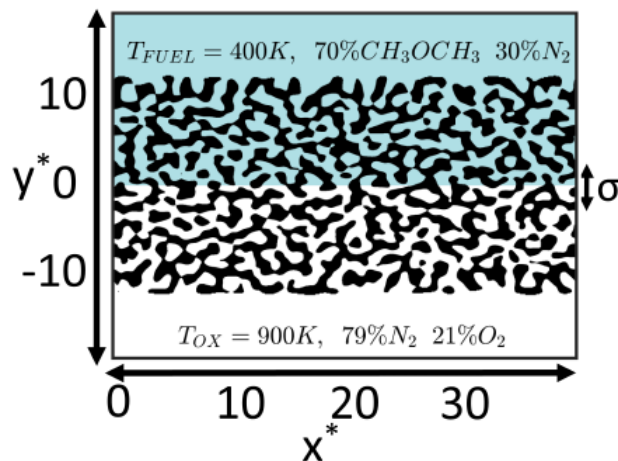


Figure 2.20 – “Initial domain configuration. Black shading pattern shows high vorticity regions. Grey/blue shading in top of figure represents the fuel and the white shading in the bottom represents the oxidiser.” [65].

Fig. 2.21 shows heat release rate fields at different instants: $t^* = t/\tau_{mr}$, where t is the time and τ_{MR} is the ignition delay of the most reactive mixture fraction. For $t^* = 1.2$, the authors [75] show an auto-ignition kernel close to the stoichiometric line. At $t^* = 1.4$, this kernel has created two edge-flames propagating in opposite directions. This observation, added to previous studies in laminar configurations, shows a temporal transition between auto-ignition and edge-flame propagation.

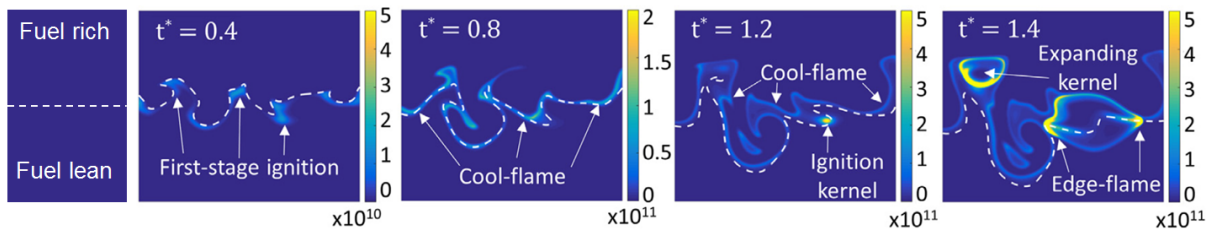


Figure 2.21 – Heat release rate for a fixed window in the domain. The dashed line is z_{st} . Figure adapted from [75].

2.3.4.3 DNS of a temporally evolving turbulent mixing layer

More recent studies [18, 65] have investigated turbulence/auto-ignition/edge-flame interactions through temporally evolving planar jet (computational domain illustrated in Fig. 2.22). As a first step [65] used *n*-heptane as fuel with a chemistry model which did not take into account the NTC. Then, in [18], used *n*-dodecane with a 35-species reduced mechanism which included both low- and high- temperature reaction pathways. In [18, 65], a deeper analysis of the edge-flame speed, χ and the classification of Diesel combustion modes is proposed. They found that the propagation speed of the edge-flames in regions with low χ ranges between $1.9 S_L$ and $3.4 S_L$. An analysis of χ shows that

ignition, both in low- and high-temperature sense, is delayed by intense χ . Following ignition, low values of χ promote faster spatial growth of ignition kernels.

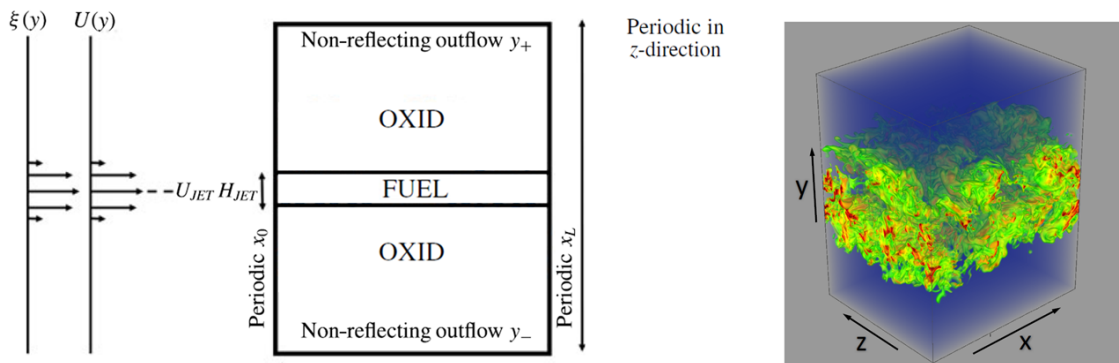


Figure 2.22 – Left (adapted figure from [65]): computational domain including specification of the boundary conditions. Right (figure from [18]): "volumetric rendering of H_2O_2 mass fraction, $Y_{H_2O_2}$ at $t = 0.45$ ms. The green color corresponds to $Y_{H_2O_2} = 10^{-3}$, and the red color to $Y_{H_2O_2} = 3 \times 10^{-3}$ ".

2.3.4.4 3D-DNS of a spatially developing slot jet flame

Minamoto and Chen [76] conducted a 3D-DNS study of a turbulent lifted gaseous DME flame. In order to reduce the computational cost of the simulation, a partially reacted mixture was imposed at the inlet to represent the products of the LTC reactions. This approach reduced the residence time (and hence domain size) requirements, which made the use of DNS possible. Moreover, the jet Reynolds number has been reduced to 5,400, which is considerably below the values found in real Diesel spray ($Re = 100,000$ – $200,000$ [16]).

The result obtained by Minamoto and Chen [76] is illustrated in Fig. 2.23 using the same marker of LTC and HTC than in [64]: $Y_{CH_3OCH_2O_2}$ and Y_{OH} . The authors [76] characterized the flame stabilization predominantly as propagating deflagration fronts with significant contributions from molecular diffusion, rather than as auto-ignition fronts.

This observation has been confirmed by Shin et al. [77] post-processing the DNS from Minamoto and Chen [76] based on fluid age analysis. The overall idea of this methodology is to track the residence time or age of fluid at different points within the flow to estimate when and where a mixture will reach its ignition delay and auto-ignite [78, 79]. Shin et al. [77] found low values of fluid age at the LOL (approximately one order of magnitude shorter than the second stage ignition delay time) indicating that the flame stabilization is predominantly governed by propagation through a mixture that has undergone first-stage ignition. Therefore, the flame propagation speed at the flame base appears to be enhanced significantly by the presence of the partially-reacted mixture produced by the first-stage ignition. Chemical activity is also significant in the mixture upstream of the flame base, with conditional statistics revealing bands of heat release consistent with the upstream branches of polybrachial flame structures observed in laminar flames at similar thermochemical conditions [67].

However, they did not mention the presence of auto-ignition spots occurring upstream the main high-temperature flame as observed in many experimental studies [14, 15, 61]. Therefore, it appears doubtful that this DNS can fully explain the flame stabilization mechanisms without discussing the contribution of auto-ignition spots.

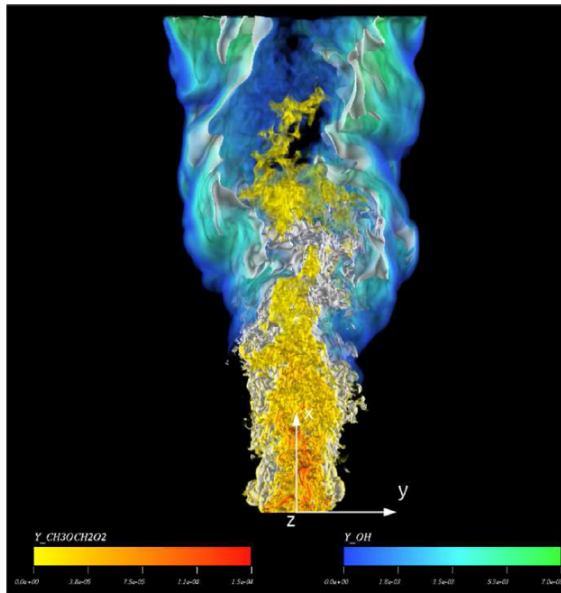


Figure 2.23 – Turbulent DME lifted jet flame showing a low-temperature heat release marker, $Y_{CH_3OCH_2O_2}$ and a high-temperature flame marker Y_{OH} [76].

These DNS studies have highlighted the fact that edge-flames and auto-ignition co-exist under Diesel conditions. Thus, different numerical studies, summarized in Appendix A, have been focused on criteria to distinguish auto-ignition and flame propagation at the flame base based on transport budget analysis or reaction rate analysis of key species. However, to the best of our knowledge, no fully resolved studies exist that would include both Diesel engine relevant thermochemical conditions (leading to two-stage ignition) and a realistic turbulence. On the experimental side, this is due to the extreme challenge of obtaining well resolved measurements at Diesel engine conditions of local phenomena such as triple flames. Therefore, more work is needed on both sides (experimental and numerical) to have a better understanding of the exact impact of edge-flames on the flame stabilization.

2.3.5 Stabilization by recirculation of burnt gases

Pickett et al. [14] have performed high-speed high-temperature chemiluminescence of a Diesel spray flame in an optically accessible constant-volume chamber. The originality of this study is that a laser-induced plasma was used to ignite the mixture between the injector and the high-temperature flame when it had reached a quasi-steady state.

Fig. 2.24 shows a chemiluminescence image sequence with a laser ignition at 3.9 ms. An ignited kernel is created at the jet axis. After 0.25 ms, the ignited kernel merges to

the main flame body. Then, the new formed flame returns to its previous (before the forced ignition) position, at approx. 40 mm from the injector, after 5 ms.

This long period of time (5ms), until the flame reaches its original position (approx. 40 mm), has been one of the main topics of discussion. The authors have estimated the axial flow velocity at the flame base location at approx. 100 m/s. Therefore, based on this assumption, it is impossible to explain the slow downstream LOL evolution by premixed flame, propagating against 100 m/s.

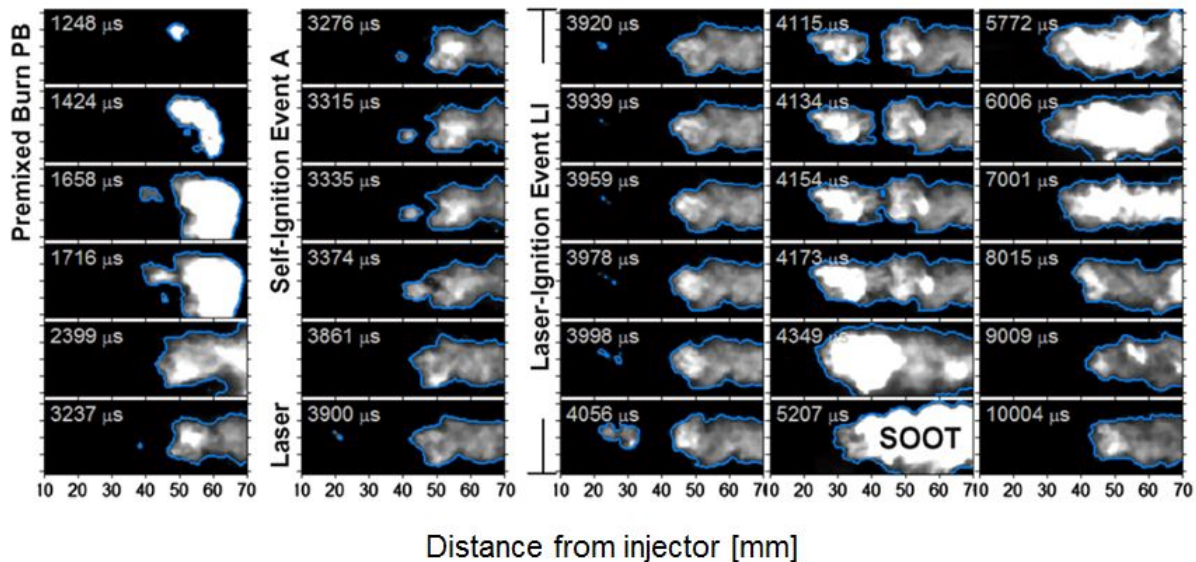


Figure 2.24 – Chemiluminescence image sequence with laser ignition at 3.9 ms [14].

Based on the assumption that flame propagation cannot fully explain the downstream evolution after forced laser ignition, they have proposed a stabilization mechanism coupling premixed flame, auto-ignition and large-scale turbulent structure. According to the authors, large scale turbulence carries burnt gases localized at the jet periphery (named high-temperature products reservoirs) and triggers auto-ignition upstream of the flame base. This theory could possibly explain the long return duration of the flame after laser ignition due to a succession of auto-ignition. Note that, flame propagation is also involved in this mechanism to fill the combustion products reservoirs at the jet edges.

However, we can make one possible objection to this analysis: this experimental study has been performed with one camera providing 3D signal projected into a 2D plane meaning that it is impossible to know where is radially located the ignited kernel. In Fig. 2.24, the kernel seems to be in the centerline but it can be located at the jet periphery where flow velocities are much smaller on average. Taking into account that the mixture is more favorable to combustion at the jet periphery (z_{st} or z_{mr}), it is highly possible that the kernel is positioned at the jet periphery, which thus changes the velocity balance between premixed flame and flow velocity, making plausible a stabilization by flame propagation.

The idea to perform forced laser ignition upstream the flame base has been followed by Gong et al. [80] performing a URANS trying to reproduce the experiment proposed by

Pickett et al. [15]. In order to investigate the stabilization mechanisms, they studied the budget term of the diffusion transport term and the reaction rate term in the transport equation for the mass fraction of CO_2 . This methodology is described in Appendix A.1. Gong et al. [80] argued that the displacement speed of the reaction front was smaller but comparable to the local jet velocity which is consistent with a stabilization by flame propagation. Thus, for the authors [80], the dominant flame stabilization mechanism after forced ignition is flame propagation which is different from the conclusion of Pickett et al. [14]. It is important to note that for Gong et al. [80] the stabilization mechanism without forced ignition is due to auto-ignition like agreed in [14, 15, 61, 67].

2.4 Conclusion

The flame stabilization mechanisms of gaseous turbulent diffusion flames have been widely discussed for the past four decades. Different theories have been proposed to explain flame stabilization based on experimental and numerical studies and are summarized in review articles [29, 40, 47, 81]. Triple flames have become widely accepted as the main elements contributing to the stabilization of lifted diffusion flames.

Under Diesel conditions, no single stabilization mechanism could be identified. However, because of the diffusion flame structure of a Diesel flame with partially premixed mixture upstream the flame base, the stabilization mechanisms for gas jets have been used as a starting point to propose new flame stabilization mechanisms. Fig. 2.25 proposes a summary of the five possible flame stabilization mechanisms identified in the literature.

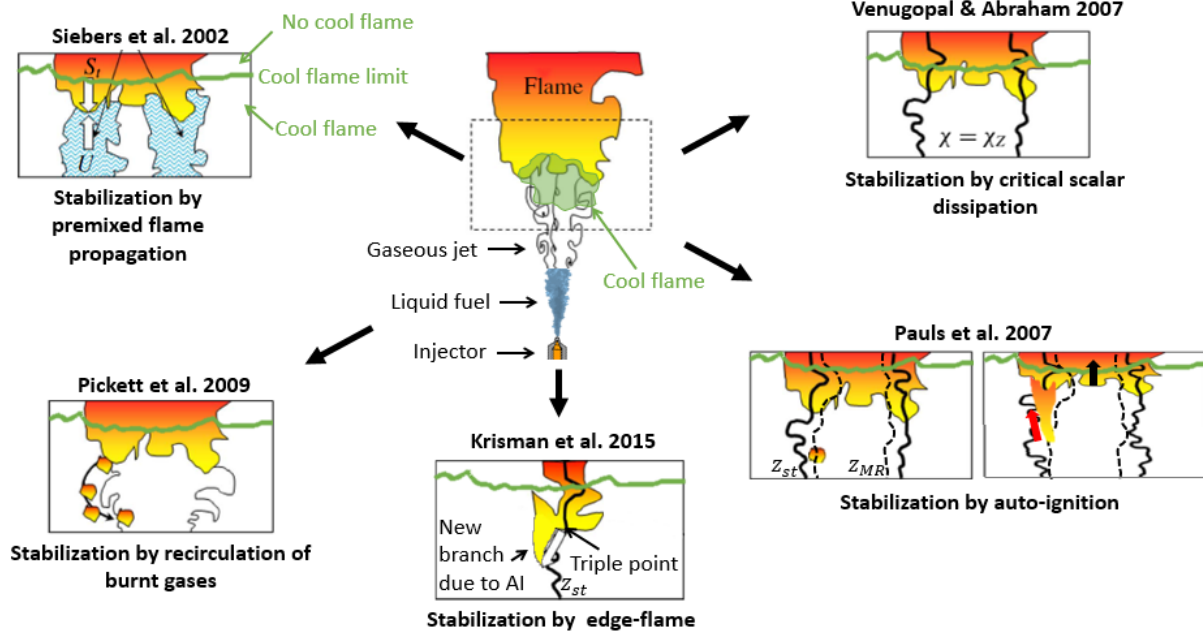


Figure 2.25 – Schematic of a lifted spray flame under Diesel conditions (center), and different theories for the stabilization. Authors, associated to the flame stabilization theories, are noted in bold character above the illustrations. The flame cartoons are adapted from [47], which have been originally used to illustrate the stabilization mechanisms of atmospheric lifted diffusion flame.

- **Stabilization by premixed flame propagation (Section 2.3.1)**: the Lift-Off-Length (LOL) is defined by an equilibrium between turbulent flame speed and local flow velocity.
- **Stabilization by critical scalar dissipation (Section 2.3.2)**: the flame is stabilized because it cannot move further upstream due to a too high level of scalar dissipation rate (i.e. too high species gradients).
- **Stabilization by auto-ignition (Section 2.3.3)**: an auto-ignition kernel appears upstream the main flame. The upstream part of this kernel stays stable, while the downstream part propagates toward the main flame (localized further downstream). The large flame resulting from this merging is stabilized further upstream, compared to before the auto-ignition. Because the flow velocity is very high at the flame base, it is convected until another auto-ignition occurs.
- **Stabilization by edge-flame (Section 2.3.4)**: similarly to gaseous lifted diffusion flames, edge-flames stabilize the Diesel spray flame where the local flow velocity equals the edge-flame displacement speed. Unlike edge-flames under non-autoignitive conditions, they have other branches due to the high reactivity of the mixture upstream the triple point. However, it is still unclear how these extra branches affect the edge-flames.
- **Stabilization by recirculation of burnt gases (Section 2.3.5)**: pockets of hot

burnt products are recirculated upstream and ignite the fuel/air mixture. In this theory, premixed flame helps to generate hot burnt products.

Many experimental and numerical studies have been performed allowing to identify these different stabilization mechanisms. As argued by Venugopal and Abraham [16], the answer is most likely a combination of the theories proposed in Fig. 2.25. However, since 2007 almost all the works published identify edge-flames (based on DNS) or auto-ignition (mainly driven by experimental observations) as having a major impact in the flame stabilization. Therefore, considering the complexity of this problematic, we propose to combine elements from optical diagnostics and DNS in order to quantify the relative importance of each stabilization mechanism.

Chapter 3

Experimental study of the stabilization mechanisms of a lifted Diesel-type flame using optical diagnostics and laser plasma ignition

Based on the extensive experience acquired at IFPEN, Sandia and other laboratories on the flow and combustion of Diesel-type spray in a constant volume vessel, we first propose an experimental study to investigate the flame stabilization mechanisms.

Section 3.2, first presents a sophisticated setup allowing simultaneous and time-resolved optical measurement of the cool- and high-temperature flame base dynamic. Additionally, forced laser ignition is performed upstream the flame base in order to observe the flame dynamic when it returns to a more stable position downstream as proposed in [14]. In Section 3.3, an analysis of the cool-flame and the LOL is proposed for a long injection duration (10 ms), as a first step without laser ignition and in a second step with laser ignition.

This experimental study is presented here as an adapted version for the thesis manuscript of an article entitled "Experimental study of the stabilization mechanisms of a lifted Diesel-type flame using combined optical diagnostics and laser-induced plasma ignition", published in the journal *Combustion and Flame* [82]. The abstract, present in the original paper, is removed and the introduction has been modified to avoid repetitions with Chapter 2.

3.1 Brief introduction

Despite the numerous studies on the flame stabilization mechanisms, there is still a need of further investigations to better understand the stabilization mechanisms of lift-off for Diesel sprays. The objective of the work presented in this paper is to contribute to this understanding effort by performing an experimental investigation of the Diesel lift off stabilization process using advanced high-speed diagnostics. In particular, compared to previous experimental studies, the present work provide additional information on the effect of the low temperature chemistry on the stabilization process. Therefore, as a first step, simultaneous and time-resolved optical diagnostics are used to follow the evolution

of low-temperature and high-temperature chemical activity around the lift-off length location. In a second step, using the same experimental setup than for the first step, forced laser ignitions upstream the LOL have been performed following the same methodology than [14], since the latter has proved to be a pertinent approach for providing relevant information on the stabilization process. Thus, the low- and high-temperature flame are spatially and temporally tracked after a forced ignition to investigate the stabilization mechanisms. The results are discussed to provide new information on the stabilization process of Diesel spray flames.

3.2 Experimental details

3.2.1 Experimental conditions

Experiments were conducted in an optically-accessible constant-volume combustion vessel. The vessel geometry and operation have already been extensively described in previous work [83], therefore only the main features will be recalled here. It has a cubical combustion chamber (125 mm per side) with five optical accesses provided by sapphire windows (120 mm diameter) providing a 80 mm optical access. Pressure and temperature are increased by the combustion of a flammable mixture, and injection is triggered during the cool-down process following the combustion, when the desired temperature is reached.

A single-hole Diesel Bosch injector (90 μm orifice, ECN spray A injector [17]) is horizontally mounted on the vessel. Long injection durations (10 ms) are performed in ambient gases simulating Diesel engine thermodynamic conditions. These long injections allow for the flame to reach and stay in a steady-state regime. Specifications for the injector and ambient operating conditions are given in Table 3.1. The ambient oxygen percentage (volumetric) is 16 %. Variations of ambient temperature, density and injection pressure have been tested and are summarized in Table 3.2, where the reference case is condition α . The fuel is *n*-dodecane. The injection setup respects ECN recommendations.

Table 3.1 – Operating condition.

Common rail fuel injector	Bosh solenoid-activated, generation 2.2
Injector serial #	306.22
Fuel injector nominal nozzle outlet diameter	90 μm
Nozzle K factor	$K = (d_{inlet} - d_{outlet})/10[\mu\text{m}] = 1.5$
Nozzle shaping	Hydro-eroded
Mini-sac volume	0.2 mm^3
Discharge coefficient	$C_d=0.86$
Spray full include angle	0°
Fuel	<i>n</i> -dodecane
Fuel temperature at nozzle	363 K (90°)
Common rail volume/length	22 $\text{cm}^3/28 \text{ cm}$
Distance from the injector inlet to common rail	24 cm
Fuel pressure measurement	7 cm from injector inlet

Table 3.2 – The different test conditions. The parameters that change compared to the reference case α are in bold characters.

Test condition name	α	α'	β	γ	δ
Ambient temperature [K]	800	850	800	850	800
Ambient density [kg/m ³]	14.8	14.8	12	11	14.8
Injection pressure [MPa]	150	150	150	150	100
Ambient gas oxygen (by volume) [%]			16		
Effective injection duration [ms]			10		

3.2.2 Optical diagnostics and laser ignition

The experimental setup presented in Figure 3.1 simultaneously tracks the evolution of the gaseous jet envelope, the formaldehyde location, and the lift-off position, with and without a forced laser ignition event during injection. The characteristics of the light excitation and collection are detailed in Table 3.3 and are also developed in the next sub-sections.

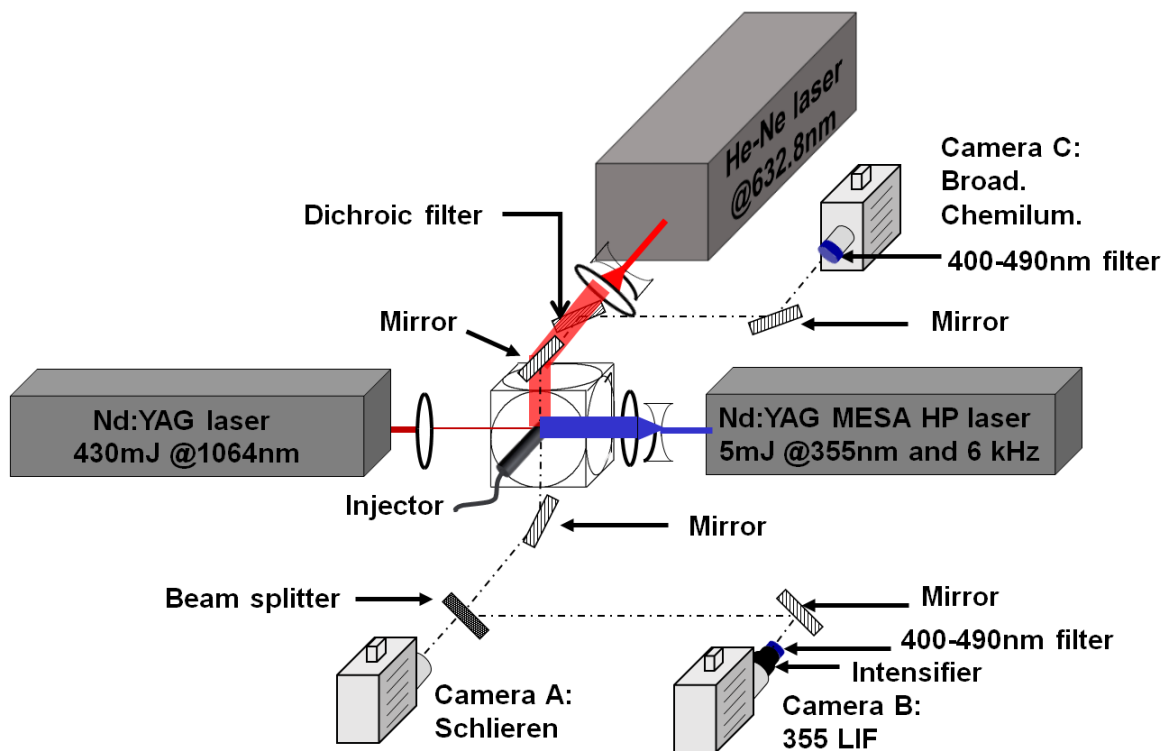


Figure 3.1 – Experimental setup for simultaneous schlieren, 355 LIF and broadband chemiluminescence images with forced laser ignition.

Table 3.3 – Laser and imaging parameters.

355 LIF High-speed	Extinction	Continum MESA HP Nd:YAG laser 5 mJ at 355 nm and 6 kHz
	Detection	Photron SA-Z camera + intensifier at 6 kfps 445 nm filter FWHM 45 nm
355 LIF High-energy	Extinction	Quanta-Ray Nd:YAG laser 5 mJ at 355 nm and 6 kHz
	Detection	Photron SA-Z camera + intensifier (one frame) 445 nm filter filter FWHM 45 nm
Schlieren	Laser	Melles Griot He-Ne laser continuous at 632.8 nm
	Detection	Photron SA-1 camera at 30 kfps
Broadband Chemilu.	Detection	Photron SA-Z camera at 30 kfps 445 nm filter FWHM 45 nm
OH*	Detection	Photron SA-Z camera + intensifier at 60 kfps 315 nm filter FWHM 15 nm

3.2.2.1 Schlieren imaging

A bright-field schlieren setup (camera A and He-Ne laser in Figure 3.1) was used to image the gaseous envelope of the spray. Schlieren imaging (a description of the schlieren imaging methodology is proposed in [84]) was performed using a He-Ne laser light source at 632 nm. The laser beam was expanded ($\times 10$) then diverged through a diverging lens (focal -35 mm). The laser-expanded beam covered 58 mm of the spray. The beam is next collimated with a converging lens (focal 600 mm), passed through the chamber, and then re-focused with a converging lens (focal 600 mm). A diaphragm of 0.5 mm diameter is used as spatial filter. The signal collection is performed with a high-speed Photron FASTCAM SA-1 CMOS camera equipped with a 100-mm lens. The camera was operated at a resolution of 448×384 pixels (58.2×49.9 mm), allowing for framing periods of $33.3 \mu\text{s}$ with an exposure duration of $5.6 \mu\text{s}$. It allows sufficient temporal resolution to visualize the unsteady spray according to previous Sandia and IFPEN research [85].

3.2.2.2 355 LIF

The 355 LIF technique is described in [86]. It allows the localization of formaldehyde species (HCHO), hence of low-temperature reactions occurring during the first reactions of fuel decomposition [24]. It also detects poly-aromatic hydrocarbon (PAH) molecules that are formed in high-temperature fuel-rich areas downstream of the jet [24]. But, because of different spatial locations, it is possible to discriminate between HCHO and PAH in such sprays. Here, high-speed 355 LIF is implemented in order to provide a temporal tracking of the formaldehyde cloud during Diesel injections (camera B and Nd:YAG laser in Figure 3.1).

High-speed 355 LIF was performed using the third harmonic of a Continuum MESA HP Nd:YAG laser generating a 355 nm pulsed beam up to 40kHz. The laser sheet measuring 35 mm long and 1 mm thick (starting at 13 mm from the injector), has been created by a collection of three lenses. The first one is a diverging lens (focal -76.2 mm), then the beam went through two converging lenses, (focal 300 mm and 500 mm) to create the final laser sheet. The signal was collected by a high-speed Photron FASTCAM SA-Z CMOS camera coupled with a Lambert Instruments HiCATT intensifier, gain set to 850. The camera was operated at a resolution of 1024×256 pixels (152.7×38.1 mm) with an 85 mm f/1.4 lens and a 455 nm filter (FWHM 45 nm). This wavelength range has been chosen to collect the spectral bands of formaldehyde in the range 410-440 nm after a 355 nm excitation [24]. A compromise has to be found between the laser repetition rate and the energy per pulse, which must be high enough to obtain enough LIF signal, which will be detailed in the Results section. To the best of our knowledge, high-speed 355 LIF has not yet been proposed in a similar configuration, thus no recommendations can be found in the literature on the minimum energy level. Therefore, conventional single-shot LIF is proposed as the reference optical diagnostics to measure formaldehyde. For that purpose, single-shot 355 LIF was performed using a Quanta-Ray Nd:YAG laser generating a 100 mJ laser beam at 355 nm and 10 Hz (one pulse per injection event). The same lenses combination as for the high-speed 355 LIF technique has been used, resulting in wider laser sheet (45 mm instead of 35 mm). The laser sheet starts at 8 mm and finishes at 53 mm from the injector. Because of the higher fluence of the laser, a gain of 750 (instead of 850) for the intensifier was sufficient to collect enough signal while increasing the signal/noise ratio. Only one frame per injection is acquired, 4 ms After the Start of Injection (ASI) during the quasi-steady state of the combustion. For each technique, 10 injections have been performed in order to compare ensemble-averaged images. The signals are integrated along the radial direction to obtain an average axial profile, which is then normalized by its maximum value. The results obtained with a repetition rate of 6 kHz (i.e. 5mJ per pulse) and for test condition α are presented in Figure 3.2. The two images on the top and in the middle are normalized by the maximum intensity of a square pixel area made of 9 pixels. The profiles are the integration of the normalized intensity along the radial axis. First of all, the spatial location of the collected signal, which is upstream of high-temperature, soot forming regions, leads to the assumption that this signal comes only from formaldehyde fluorescence and not from PAH. Indeed, previous results published in [86] for comparable ambient conditions show that it is very unlikely to collect PAH fluorescence signal for axial distances below 35 mm. Therefore, as a first step, we assumed that the acquired images are not contaminated with PAH fluorescence.

The global spatial locations of the formaldehyde clouds are similar between the two setups. However, it appears that the single-shot 355 LIF (high-energy LIF) allows a better detection of the HCHO for axial distances below approx. 25mm. To go further, the normalized average 355 LIF profiles (Figure 3.2 - bottom) are compared. Similar to the lift-off length defined for the high-temperature flame, a formaldehyde lift-off length LOLHCHO can be computed. This is defined as the most upstream axial position where the normalized profile reaches 10% of the maximum signal. For the α test condition presented in Figure 3.2, it leads to a position of 22 mm for the single shot 355 LIF and 25 mm for the high-speed 355 LIF. Increasing the repetition rate of the high-speed 355 nm

laser (and thus decreasing the energy per pulse) would lead to a further deterioration of the collected fluorescence signal. Test at 10 kHz and 2.2 mJ per pulses have shown a very bad signal-to-noise ratio and have been discarded. A decrease in the repetition rate would allow to increase the energy per pulse, but that would be to the detriment of temporal resolution. Therefore, a good compromise between temporal resolution and signal collected is obtained at 6 kHz and 5 mJ per pulse. However, in the following analysis, this lack of sensitivity for axial positions below 25 mm where there is low formaldehyde concentration must be kept in mind.

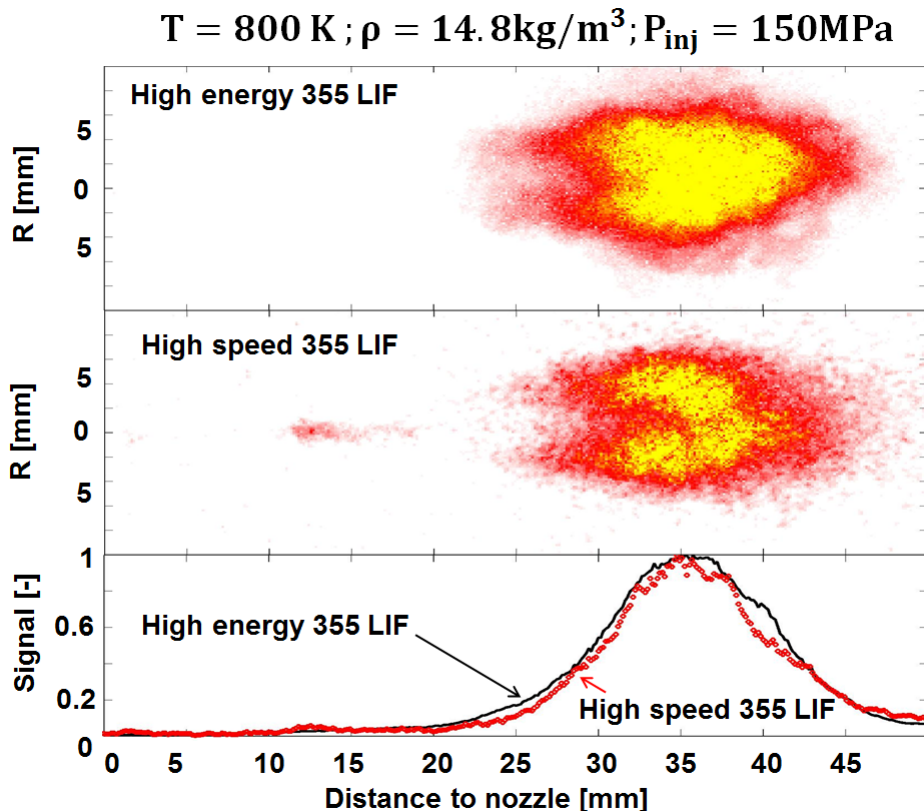


Figure 3.2 – Average formaldehyde cloud from 355 LIF at 100 mJ (top image) and 5 mJ (middle image), normalized average 355 LIF profiles integrated radially (bottom image).

3.2.2.3 High-temperature chemiluminescence

Two different techniques have been used to track the high-temperature flame: OH^* and broadband chemiluminescence. The former is the recommended technique, in particular within the ECN framework, because UV-range imaging minimizes contamination by soot incandescence, but it requires the use of a high-speed UV-sensitive camera (intensifier). Since only one high-speed intensifier was available for the experiments, when the latter was required for another diagnostic (high-speed 355 LIF), broadband chemiluminescence was used to determine the LOL position.

The OH^* signal has been collected with a high-speed Photron FASTCAM SA-Z CMOS

camera at 60 kfps coupled with a high-speed intensifier (same intensifier as for the 355 LIF). The camera was equipped with an ultraviolet transmitting lens (UV-Cerco 100-mm, f/2.8) and with a 315 nm filter (FWHM 10 nm), as recommended setup [52, 87]. The resolution was 1024×256 pixels (117.5×29.3 mm) and the exposure time was 10 μ s.

Broadband chemiluminescence has been collected with a high-speed FASTCAM SA-Z CMOS camera at 30 kfps, equipped with a 85mm f/1.8 lens and a 455 nm filter (FWHM 45 nm) collecting around the CH* radical band, while rejecting the strongest emission from soot incandescence. The exposure duration was 25 μ s and the resolution was 1024×384 pixels (113.7×42.6 mm).

Since broadband chemiluminescence may lack of sensitivity near the flame base and could also be polluted by soot natural incandescence signal [1, 52, 87], a detailed comparison of the two techniques was performed. OH* and broadband chemiluminescence have been collected simultaneously though not at the same frame-rate. Figure 3.3 shows a comparison between the broadband and the OH* chemiluminescence images for 8 different timings. First, an auto-ignited kernel appears, then, this kernel merges the main flame while being convected downstream by the flow. These two techniques show good agreement, since the observed flame structures are similar. Especially, broadband chemiluminescence is able to catch the signal from the kernel appearing upstream of the flame base. However, the signal is weaker with the Broadband chemiluminescence setup, and some information can be lost in the very upstream locations of the flame. For example, at 7967 μ s ASI an auto-ignited kernel appears on the OH* images whereas this kernel is not yet observed on the broadband images. However 66 μ s after, the kernel is observed on both diagnostics. Therefore, high-speed OH* chemiluminescence is the preferred technique to obtain quantitative information on LOL because of its higher time and spatial resolution. A Previous study [88] performing simultaneously single-shot images of OH and formaldehyde PLIF has shown that formaldehyde is disappearing at the same position where the high-temperature flame is measured. The formaldehyde is mainly localized at the center of jet as shown in Figure 3.2, while OH PLIF identifies the high-temperature flame at the jet periphery. A more detailed description of the interaction between formaldehyde and the high-temperature flame is proposed in Section 3.3.

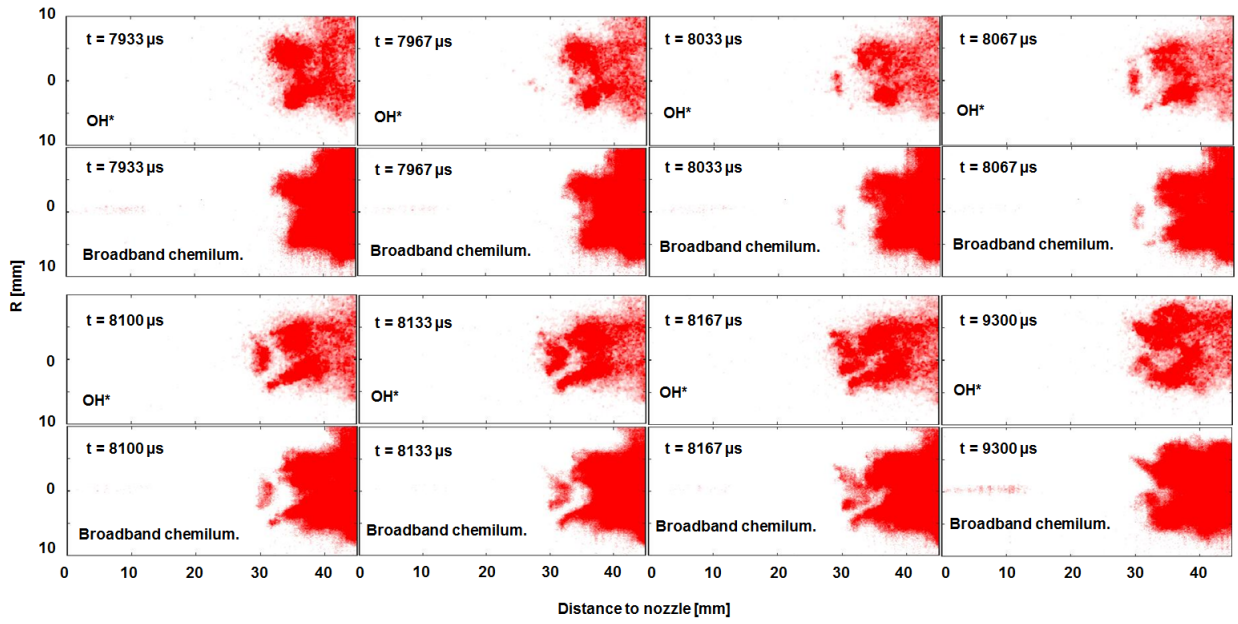


Figure 3.3 – Instantaneous frames from OH^* and broadband chemiluminescence at 30 kfps for the α test condition. The time is expressed in terms of time ASI.

3.2.2.4 Laser ignition

The ignition was accomplished focusing a 1064 nm beam produced by a Quanta-Ray Nd:YAG laser through a spherical 100 mm converging lens. The beam diameter before the lens was 1 cm with an energy of 430 mJ per pulse, and a pulse duration of 8 ns. The beam diameter at the focal point has been estimated at $38 \mu\text{m}$ through equation Eq. (3.1) [89]:

$$d = M^2 \frac{4\lambda f}{\pi D}, \quad (3.1)$$

where, d is the laser ignition beam diameter at focal point, M^2 is the beam quality factor of the beam ($M^2 = 2.8$), λ is the laser wavelength, f is the focal length and D is the beam diameter before the focal lens. Note that Eq. (3.1) can only provide a rough estimation of the beam diameter because it does not take into account all the optical effects like the beam-steering. Due to the high-energy density (about $38 \text{ kJ}/\text{cm}^2$), plasma formation occurs [14, 90], thereby igniting the air-fuel mixture. This focalization point is located on the spray axis, as confirmed by generating a plasma in pure nitrogen, as proposed in [90]. The forced laser ignitions were performed for two axial positions, the closest to the injector at 17 mm, upstream the formaldehyde cloud, and the other one at 26 mm from the injector, within the formaldehyde cloud.

3.3 Results and Discussion

The results are presented and analyzed with the following steps. After an analysis of the flame structure, the evolution of the low- (LOL_{HCHO}) and high- (LOL) temperature

flame base locations are first analyzed without forced laser ignition, hereafter referred as “natural evolution” of the flame. Then, simultaneous observations of the gaseous jet envelope, formaldehyde location and flame position after forced laser ignition are discussed.

3.3.1 Flame structure

Figure 3.4 presents the superposition of the gas envelope of the spray (gray, schlieren), an iso-contour of the formaldehyde cloud (green, high-speed 355 LIF) and the high-temperature flame (red, broadband chemiluminescence). The two locations where the ignition laser is focused are also indicated. In the region of the formaldehyde cloud, the schlieren signal gets weaker as shown in the area pointed by the labeled arrow (a). This can be explained by the increase of the temperature caused by the cool flame that induce a decrease of the (refractive index) gradients [91, 92]. Further downstream, the spray expansion and the apparition of the high-temperature flame are located in similar areas. However, the vapor envelope of the jet appears larger than the flame because hot burnt gases are present at the periphery of the flame as indicated with the labeled arrows(b). This description confirms the presence of high-temperature products localized at the jet periphery which would tend to stabilize the flame according to [14]. Therefore, Figure 3.4 confirms previous results [91, 92] showing that the schlieren images can be used to provide a general view of the formaldehyde location and the LOL, and that burned gases exist outside the flame. In the rest of the paper, the flame stabilization mechanisms are investigated through high-temperature or OH^* chemiluminescence and 355 LIF.

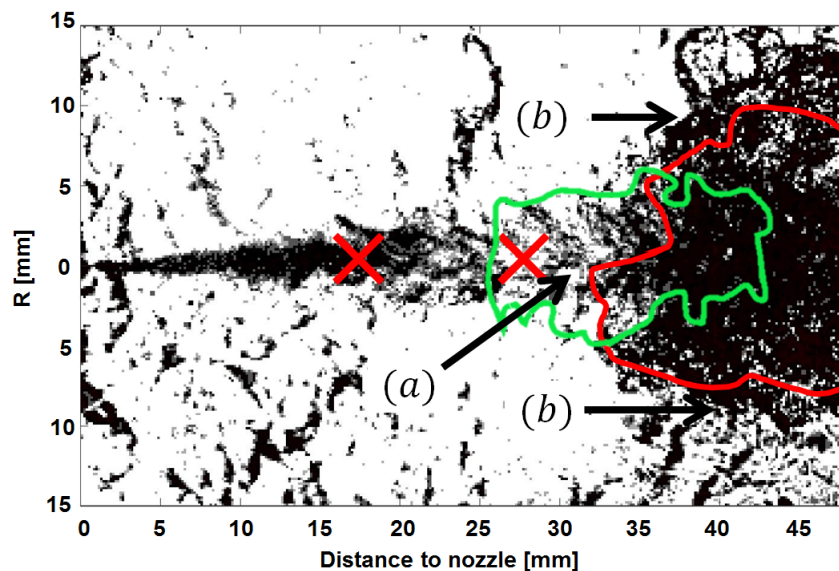


Figure 3.4 – Superposition of an instantaneous frame from simultaneous schlieren imaging (30kfps) on an iso-contour of 355 LIF (6kfps, green line) and broadband chemiluminescence (30kfps, red line) for the α condition. The two red crosses show the location where the ignition laser is focused.

3.3.2 Results for natural flame evolution

LOL and LOL_{HCHO} evolutions have been compared for all the test conditions without laser ignition. The results are presented in Table 3.4. HCHO results, obtained with both high-speed and low-speed techniques, are presented, while the high-temperature chemiluminescence results are provided through high-speed OH* chemiluminescence imaging. In the following, ensemble averages are noted $\langle X \rangle$ while time averages are noted \overline{X} . Time and ensemble averages are noted $\langle \overline{X} \rangle$. The standard deviation of X is noted $\sigma(X)$. The High-Speed 355 LIF is indexed as follows X^{HS} while the High-Energy 355 LIF is noted X^{HE} .

Table 3.4 – LOL and LOL_{HCHO} averages for the different test conditions.

Test condition name	α	β	γ	δ
$\langle \overline{LOL_{OH^*}} \rangle$ [mm]	35.5	49.1	44.9	31.6
$\sigma(\langle \overline{LOL_{OH^*}} \rangle)$ [mm]	2.5	3.5	4.3	3.1
$\langle LOL_{HCHO} \rangle^{HE}$ [mm]	22.7	24.1	22.6	20.0
$\sigma(\langle LOL_{HCHO} \rangle^{HE})$ [mm]	0.3	0.4	0.9	0.9
$\langle LOL_{HCHO} \rangle^{HS}$ [mm]	24.5	24.0	22.7	22.7
$\sigma(\langle LOL_{HCHO} \rangle^{HS})$ [mm]	0.8	0.3	0.8	1.2

$\langle \overline{LOL_{OH^*}} \rangle$ is the average LOL during a 1.65 ms steady period (between 1.35 and 3 ms ASI) from 10 realizations collected by high-speed OH* chemiluminescence imaging at 60 kHz. $\langle LOL_{HCHO} \rangle^{HE}$ is the ensemble average of LOL_{HCHO} at high-energy. Images were acquired at 2.8 ms ASI. $\langle LOL_{HCHO} \rangle^{HS}$ is the results of ensemble average formaldehyde location $\langle LOL_{HCHO} \rangle$ obtained from 10 realizations of high-speed 355 LIF. Note that none of these three diagnostics have been performed simultaneously.

As described in Section 3.2.2.2, the high-speed 355 LIF presents a lack of sensitivity upstream the formaldehyde cloud caused by the lower energy level of the excitation. Comparing the HE and the HS LIF, for test condition α and δ confirm this lack of sensitivity while conditions β and γ (with higher $\langle \overline{LOL_{OH^*}} \rangle$) show a good agreement between the high-speed and the high-energy setup. It is not straightforward why test conditions presenting a short LOL (α and δ) present a lack of signal detection upstream the formaldehyde measured with the high-speed 355 LIF in comparison to the high energy LIF setup. The standard deviation results of $\langle LOL_{HCHO} \rangle^{HS}$ and $\langle LOL_{HCHO} \rangle^{HE}$ are of the same order of magnitude, with the latter being 24% higher. It shows that the high-speed 355 LIF reasonably detects the LOL_{HCHO} fluctuations, even if not perfectly.

The standard deviation results shown for OH* and HE LIF show that on average $\sigma(\langle \overline{LOL_{OH^*}} \rangle)$ is 3 to 4 times greater than $\sigma(\langle LOL_{HCHO} \rangle^{HE})$ hence, the upstream position of the formaldehyde cloud is much more stable than that of the high-temperature flame. In addition the fact that the standard deviations of $\langle LOL_{HCHO} \rangle^{HE}$ is low shows that the average position of the formaldehyde cloud, detected with the high-energy 355 LIF, can

be used to correctly define the instantaneous upstream position of the formaldehyde cloud.

Figure 3.5 presents LOL temporal evolutions provided by OH* chemiluminescence for two different conditions (800 K, 850 K). From a general point of view, comparing the different test conditions shows that the higher the temperature, the shorter the LOL and the weaker the absolute dispersion around the mean LOL. More specifically, two types of characteristic evolutions are observed: event A (red rectangle) and evolution B (red line).

- Event A is characterized by very rapid upstream displacements of the LOL: in some cases, the LOL can decrease by 5 mm in less than 50 μ s. These displacements are very probably caused by auto-ignitions events and will be called "large scale" auto-ignitions in the following. This evolution can be observed on Figure 3 7967 μ s ASI for the α condition and also in Figure 3.5 (right) 5233 μ s ASI for the α' condition. In both cases an isolated auto-ignited kernel appears upstream the main flame resulting in an upstream jump of the LOL.
- Evolution B is usually observed just after event A when, following a "large scale" auto-ignition event, a progressive downstream evolution is observed for a given period of time. Figure 3.5 (right) illustrates this downstream evolution through two images taken at 5333 and 6000 μ s ASI where the LOL progressively increase. Figure 3 also shows evolution B after a "large scale" auto-ignition. Another "large scale" auto-ignition event often occurs ending phase B, significantly decreasing the LOL. The characteristic time of this evolution is approx. 0.25 ms to 1 ms.

Event A is more often observed at 800 K than at 850 K, the same remark also stands for evolution B. Indeed, the more the flame is stabilized downstream, the more auto-ignitions are detached far from the main flame, and thus the longer evolution B is. Interestingly, these auto-ignition sites are always located in the formaldehyde cloud for the reference case α . Figure 3.5 (for the α condition) shows that auto-ignitions can reduce the LOL up to 28 mm from the injector. Moreover, it has been shown in Table 3.4 that $\langle LOL_{HCHO} \rangle^{HE}$ stays relatively stable at 22.7 mm from the injector. From all the realizations performed in this study, no auto-ignitions have been detected upstream the formaldehyde cloud. It is not possible to perform the same analysis for the α' case since no formaldehyde measurement have been performed in this cases.

The natural flame stabilization seems to be mainly governed by an alternation of event A and evolution B. The rest of the paper focuses on the analysis of the mechanisms governing the evolution B with the aim to discriminate between different potential mechanisms, in particular flame propagation, auto-ignition, or others.

Assuming a constant speed during evolution B, as illustrated by the solid lines in Figure 3.5, the average absolute flame front speed \overline{S}_a relative to a fixed reference can be determined using Eq. (3.2)

$$\overline{S}_a = \frac{\Delta LOL}{\Delta t}, \quad (3.2)$$

where ΔLOL and Δt are the LOL and time variation during phase B. For condition α , \overline{S}_a is found equal to 6.6 m/s in average with a standard deviation of 2.8 m/s based on

the eight evolutions B displayed in Figure 3.5. However, as can be seen on Figure 3.5, the apparition of phases A and B are random, which makes a systematic analysis of these phenomena on a large number of injections, or for varied ambient conditions, difficult. Forced laser ignition, whose setup is described in Section 3.3.3, is therefore used to have reproducible and controlled apparitions of evolution B. It also allows a forcing of the ignition either in the formaldehyde cloud, or upstream of this cloud.

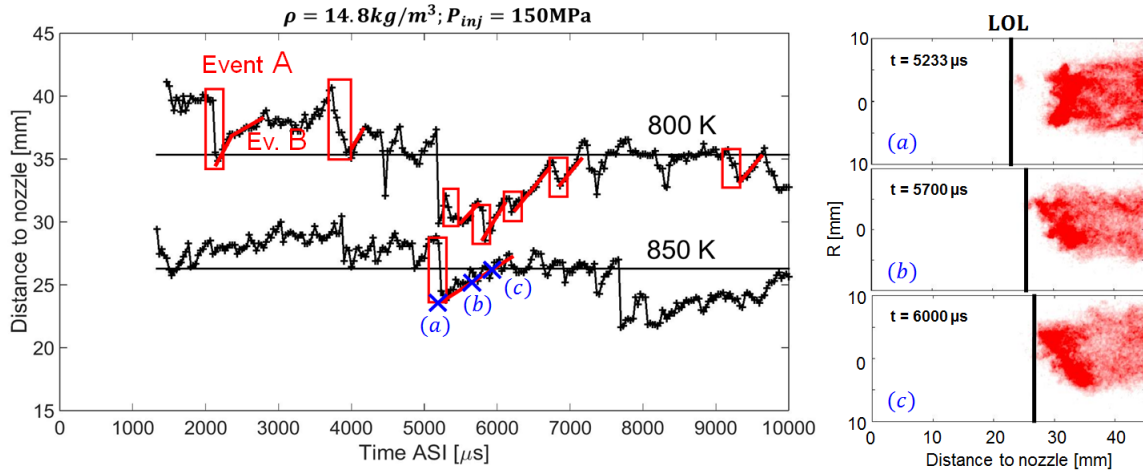


Figure 3.5 – Left: LOL time tracking using OH^* chemiluminescence imaging for ambient temperatures of 800 K and 850 K, respectively named α and α' conditions. Events A are shown as red rectangles and evolutions B as red lines for the α conditions. Right: snapshot of OH^* images illustrating event A and evolution B.

3.3.3 Forced laser ignition

Forced laser-induced plasma ignition was used to perform a systematic analysis of phase B (downstream propagation). Indeed the advantage of laser-induced plasma ignition is that it enables to set the LOL in a location upstream of its natural position, where the conditions for natural ignition are not present and therefore where large scale auto-ignition is unlikely to occur, hence enabling to focus on the study of phase B. Laser ignition was triggered 3 ms after the effective start of injection, hence when the natural LOL is already stabilized. As detailed in the experimental setup section, two axial positions have been selected for the forced ignition as shown in Figure 3.4: upstream the formaldehyde cloud (17 mm downstream the orifice), and within the formaldehyde cloud (26 mm downstream the orifice).

A broadband chemiluminescence sequence at 30 kfps, showing the first 400 μs transient lift-off after a forced laser ignition is shown in Figure 3.6 for condition α . High-speed formaldehyde imaging is not available at such frame rate and therefore formaldehyde LIF is not shown in the Figure 3.6. The case shown in Figure 3.6 corresponds to a forced ignition at 26 mm from the nozzle orifice, hence upstream of the natural mean LOL ($\langle LOL_{HCHO} \rangle = 22 \text{ mm}$).

After laser ignition, the broadband chemiluminescence images present a saturation (non convected signal at the plasma location for more than 1 ms) on the top of the images. This saturation is attributed to the high plasma emission collected by the camera with a large gate width (25 μs). In comparison, OH* chemiluminescence, with a shorter gate width (10 μs), presents this saturation for less than 150 μs due to less plasma emission collected. Therefore, the saturation is ignored for the LOL detection.

The ignited kernel, created just after laser ignition, can split into two parts for analysis: the upstream part of the kernel and the downstream part. The downstream part which propagates towards the main flame in the same observation was made in [14], where it was proposed that this downwards propagation occurs in premixed flame mode. The upstream part of the kernel remains at a fixed position then after starts a slow downstream evolution. This slow downstream evolution is analyzed in more detail later in the paper using high-speed OH* chemiluminescence (60 kfps).

Interestingly, a statistical analysis, in which the radial position of the ignition location has been measured for all the test conditions, shows that although the laser beam is focused on the spray axis forced ignition occurs at a radial position between 3 and 4 mm from the jet axis. This is very probably the result of the balance between laser local fluence and local mixture ignitability. A 1D spray model [55, 93] used to calculate the average mixture fraction field showed that the stoichiometric line, corresponding to a mixture fraction $z_{st} = 0.048$, is 2.85 mm from the centerline at this axial position. So, laser ignition occurs on the lean side of the average stoichiometric line. To further analyze this, most reactive mixture fractions have been computed with Cantera [94] using a 53-species skeletal model for n-dodecane oxidation [95] in a constant pressure reactor. The initial temperature is determined from the stoichiometric mixture fraction assuming an adiabatic mixing process. The computed most reactive mixture fractions are 0.048 at 800 K, and 0.054 for at 850 K, corresponding to a range from stoichiometric to rich mixtures. This is not consistent with the observed locations of the forced ignition, on the lean side of the average stoichiometric line. Therefore it seems that laser ignition has no requirement that it be near a preferred self-ignition zone. The high-temperature kernels detected just after forced ignition are probably governed by plasma dynamics in a stratified mixture. Plasma breakdown begins when there is enough hydrogen, but does not mandate that this is lean or rich of stoichiometric. Once plasma forms, it becomes optically thick and absorbs the next laser radiation, which can bias the energy deposition to the lean side. Then the flame is sustained at the jet periphery for mixture near z_{st} .

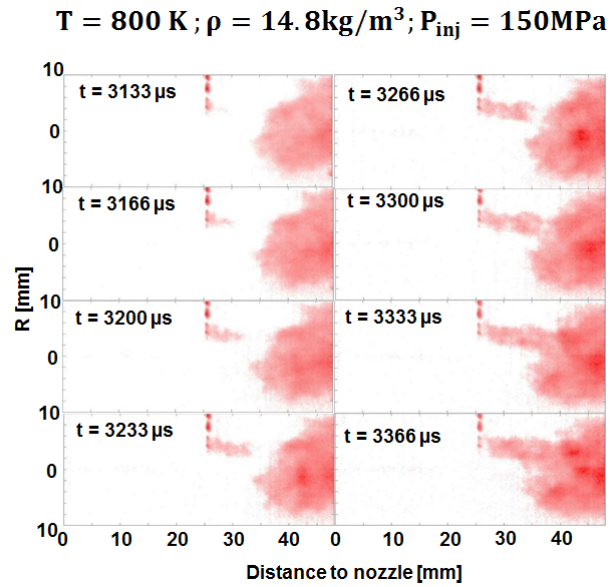


Figure 3.6 – Broadband chemiluminescence image sequence after the laser ignition ($3000 \mu\text{s}$ ASI) at 26 mm from the injector. The laser propagation is top to bottom.

Following the analysis of the very first instants after laser ignition in Figure 3.6, Figure 3.7 displays the later evolution of the flame when the ignition kernel and the main flame are already connected. Figure 3.7 shows a 6 kfps images sequence with simultaneous visualization of formaldehyde (green) and high-temperature flame (red). An asymmetric high-temperature flame starts at 26 mm from the injector, where the forced laser ignition occurs. The LOL increases progressively until it returns to its natural position 35 mm from the orifice, as it is shown at $4366 \mu\text{s}$ ASI.

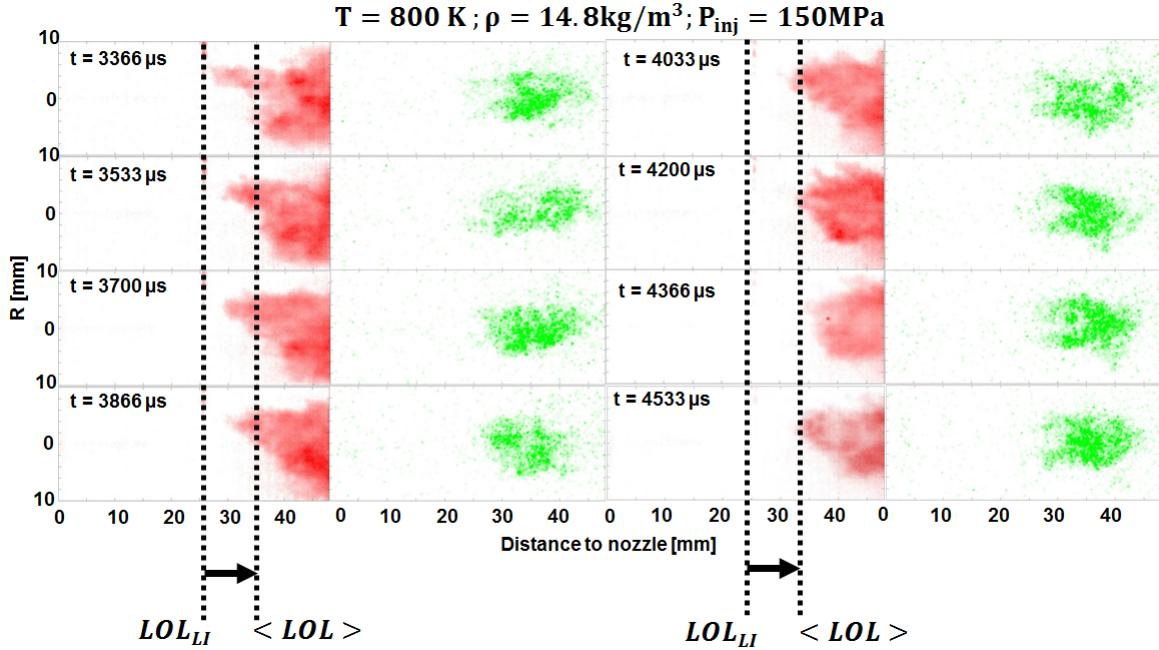


Figure 3.7 – Broadband chemiluminescence (red, first and third columns) and 355 LIF (green, second and fourth columns) image sequence after the laser ignition ($3000 \mu\text{s}$ ASI) at 26 mm from the injector, for condition α . The two dotted lines show the LOL just after the laser ignition (left line) and the average position of the “natural” LOL.

Under the limiting factor that signal to noise ratio of 355 LIF imaging is low, the formaldehyde location does not seem to be significantly affected by the ignition kernel, ignited inside the formaldehyde as shown in Figure 3.7. In order to further analyze the evolution of the formaldehyde cloud, Figure 3.8 (two top images) shows ensemble (10 realizations) and time (500 μs before and after forced ignition) averaged images provided by high-speed 355 LIF. The time is expressed in terms of time After Laser Ignition (ALI): $t_{ALI} < 0$ before the laser ignition and $t_{ALI} > 0$ after the laser ignition. In addition Figure 3.8 (bottom image) displays different timings of high-speed 355 LIF signal integrated along the radial direction. The left column is for laser ignition at 17 mm, upstream the formaldehyde cloud, the right column is for laser ignition at 26 mm, inside the formaldehyde cloud. The ensemble and time averaged images show a weak decrease of the LIF signal after laser ignition ($t_{ALI} > 0$), in the upper part of the formaldehyde cloud at approx. 35 mm from the injector, for both locations of laser ignition. Laser ignition also occurs in the upper part of the spray. This decrease of signal is presumably due to the formaldehyde consumption by the larger high-temperature flame generate after forced ignition like shown in Figure 3.7. However, 355 LIF is a planar measurement while high-temperature chemiluminescence is a line-of-sight technique. Therefore, the collected signal from broadband chemiluminescence is not necessarily located in the same plane as the formaldehyde cloud. The integrated intensity profiles shown on the bottom part of Figure 3.8 show that the most upstream location of the formaldehyde cloud is not affected by laser ignition. The zoomed plots shown on Figure 3.8 indicate that the rise of the formaldehyde signal appears at the same axial distance before and after the laser ignition, thus proving that LOLHCHO is not modified by laser ignition. The small bump

appearing $33 \mu\text{s}$ after laser ignition (green curve on the zoomed image on the bottom left) is attributed to the plasma created by the laser.

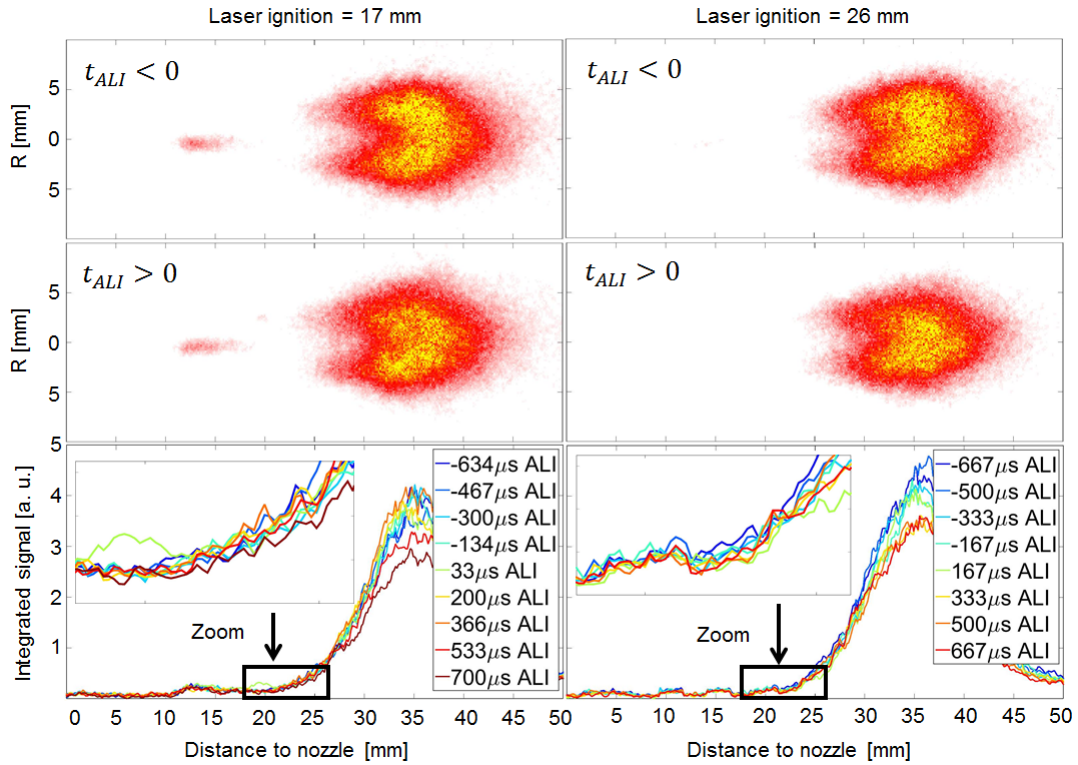


Figure 3.8 – Ensemble and time averaged images of high-speed 355 LIF $500 \mu\text{s}$ before (first pair of images) and after (second pair of images) laser ignition. Bottom plots: ensemble averaged of high-speed 355 LIF integrated over R for different timings.

To analyze in more detail the evolution of LOL, high-speed OH^* chemiluminescence measurements at 60 kfps were performed (for laser ignition upstream the formaldehyde cloud) and the corresponding evolutions are presented in Figure 3.9 for 16 injection events.

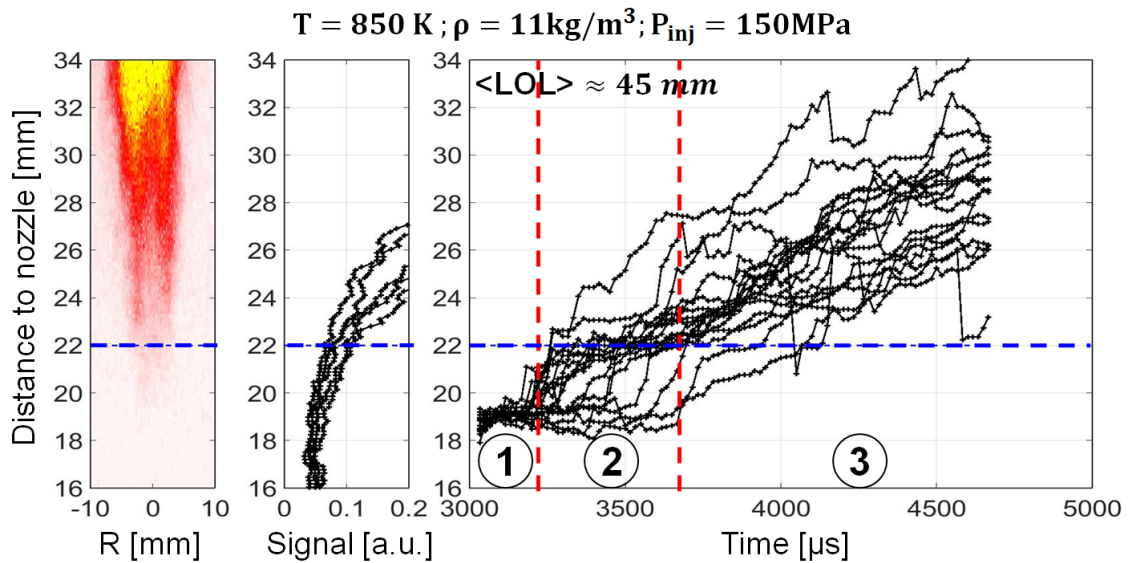


Figure 3.9 – Averaged high-energy 355 LIF image (first column), instantaneous high-energy 355 LIF profiles integrated over R (second column), instantaneous LOL evolution after laser ignition (at 17 mm and 3000 μs) performed by OH^* measurement (third column) for different injection events. The horizontal dotted blue line stands for the rising of HCHO signal at 22 mm from the injector. The two dotted vertical red lines delimit the three different stages observed after a forced laser ignition.

Figure 3.9 also presents an ensemble-averaged HCHO image (from high-energy 355 LIF) corresponding to 5 injections events (reported in Table 3.4), as well as the corresponding intensity profiles, in order to compare the LOL evolution with the formaldehyde location. Three different stages are identified.

- During the first stage, the upstream position of the ignition kernel remains fixed for 100 to 600 μs after laser ignition, near the laser ignition area. A large dispersion of the duration of this stage is observed, but it is seen systematically, and for all the test conditions.
- During the second stage, the LOL shows, in most cases, a very rapid increase up to a position around 22 mm corresponding to the value of $\langle \text{LOL}_{\text{HCHO}} \rangle^{\text{HE}}$.
- The third and last stage, shows the same type of evolution as evolution B in Figure 5, with progressive increase at an almost constant speed.

The mechanisms explaining why LOL remains fixed for a given time after laser ignition (phase 1) are not straightforward. It seems that the propagation speed of the flame kernel ignited by the laser is able for some time to balance the flow velocity. Another possibility would be that the flow is affected by the laser plasma. In any case this mechanism have not been further investigated here since the authors consider that it is beyond the scope of this study. Phase 1 is very probably closely related to plasma ignition effects while the scope of the study is the evolution of the LOL after ignition, hence the following phases. In Figure 3.9, the transition between stages 2 and 3 seems to be closely related

to the location of formaldehyde. To confirm this observation, an analysis of the axial position corresponding to transition between stages 2 and 3 has been repeated for the other conditions and is summarized in Table 3.5. For laser ignition at 17 mm from the injector, the α , β and γ test conditions mostly show the 3 stages, however 40 % of the δ case exhibits only the first stage and, then, directly starts a progressive evolution without showing the second stage. Table 3.5 also displays an ensemble average of the transition position between the second and the third stage. Comparing these results to $\langle LOL_{HCHO} \rangle^{HE}$ in Table 3.4, it appears that the turning point between the second and the last stage corresponds to the beginning of the formaldehyde cloud. Indeed, the maximum difference between $\langle LOL_{HCHO} \rangle^{HE}$ and the transition point given in Table 3.5 is 5 % for the δ case. The fact that only 60 % of the realizations of the δ case shows the 3 stages is attributed to the close distance between the laser ignition and the formaldehyde cloud. Even if the laser is focused at 17 mm, due to turbulence, the ignited kernel can start growing further downstream. Additionally, regarding the standard deviation of $\langle LOL_{HCHO} \rangle^{HE}$ (0.9 mm), for the δ condition, laser ignition inside the formaldehyde cloud can be statistically considered for this condition and thus, can explain the 40 % of realizations not showing the 3 stages. This hypothesis is confirmed by performing laser ignition within the formaldehyde cloud for the α condition. In this case, neither of the realizations show the 3 stages. When laser ignition occurs within the formaldehyde region, there is no rapid LOL increase stage, and the evolution of the LOL is more progressive, as can be observed during stage 3 (Figure 3.9). These results emphasize the role of the low temperature reaction region on the LOL progression speed. Upstream of the formaldehyde cloud, rapid evolutions are observed and inside the formaldehyde cloud systematic slower progression of the LOL location is observed. The mechanisms explaining the effect of the presence of formaldehyde on the LOL progression requires further analysis, but the results obtained here show that the cool flame products appear to play an important role in the LOL stabilization process.

Table 3.5 – Statistical analysis of the three different stages identified for laser ignition at 17 mm from the injector. Standard deviations are noted in parenthesis.

Test condition name	α	β	γ	δ
Percentage of realizations showing the 3 stages [%]	83	72	75	60
Ensemble average of the transition position between stages 2 and 3 [mm]	22.4(2.3)	23.1(2.4)	22.0(0.9)	21.0(1.4)
Ensemble average of $\overline{S_a}$ during stage 3 [m/s]	5.0(1.5)	7.3(2.1)	6.5(2.2)	3.6(1.5)

The fairly linear return to the natural lift-off position (stage 3) is analyzed through Eq. (3.2) to determine if there are compelling observations that govern this phase for all conditions. A statistical analysis of the near-constant absolute downstream velocities ($\overline{S_a}$) measured during stage 3 for all the test conditions are summarized in last line Table 3.5. Table 3.5 is illustrated by Figure 10, where each curve was selected as being representative of the position of the transition stage 2/3 and the downstream evolution during stage 3 under the corresponding condition.

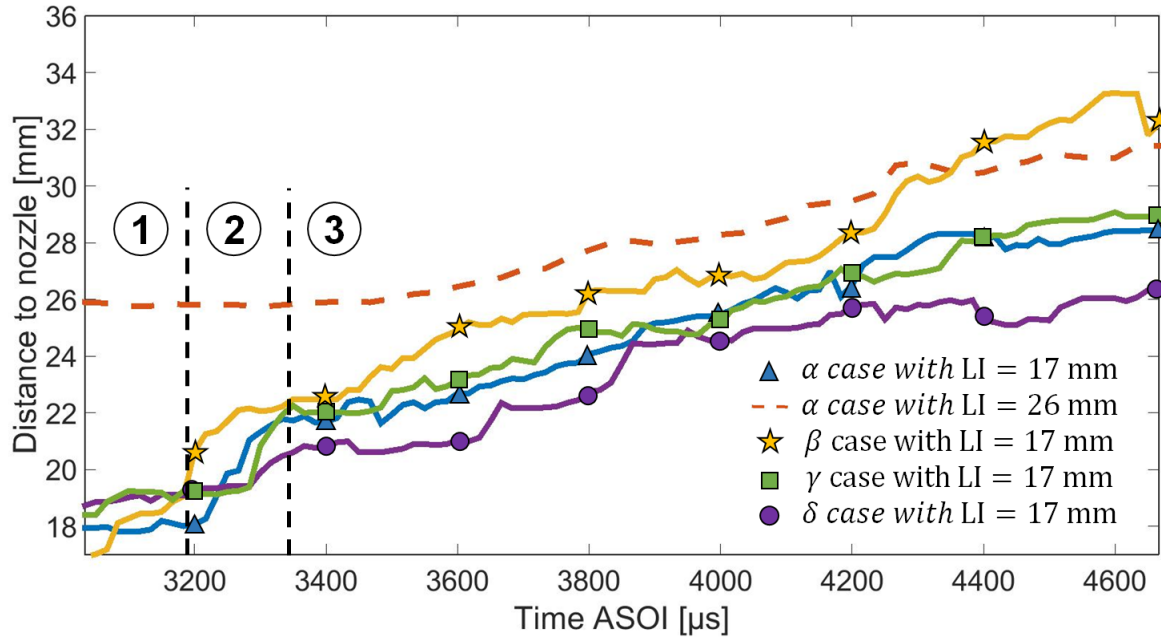


Figure 3.10 – Instantaneous LOL tracking performed by OH^* measurement (60 kfps) for the α , β , γ and δ test conditions and for laser ignition focused at 17 mm from the injector. The LOL tracking is performed by broadband chemiluminescence (30 kfps) for laser ignition at 26 mm (α test condition). When laser ignition occurs inside the formaldehyde cloud the LOL evolution are displayed with dotted lines, otherwise the LOL evolutions are plotted in solid lines.

Interestingly, \overline{S}_a after forced ignition for the α condition is in the same range as $\overline{S}_a = 6.6$ m/s observed after a “natural” auto-ignition as shown on Figure 3.5, suggesting that the mechanisms governing the LOL evolution are similar when considering forced ignition or natural evolution. An attempt to compare the evolution of the absolute downstream velocities \overline{S}_a with the flow velocity at the LOL was performed in order to investigate the role of the latter on the mechanisms governing the downstream evolution. Since no experimental velocity measurements were performed in this study, the 1D spray model [55, 93] was used to provide estimations of the average velocity fields. However, no clear correlation was found between the absolute downstream velocities \overline{S}_a and the average flow velocity at the LOL when taking into account the measurement uncertainties. This result shows that information on local quantities for flame structure and flow velocity are needed for such an analysis.

3.4 Conclusion

Combined optical diagnostics and laser-induced plasma ignition have been performed to study the stabilization mechanism of a lifted Diesel-type flame. High-temperature chemiluminescence and 355 LIF have provided the temporal evolution of the high and cool-temperature flames without and with laser ignition.

The natural LOL and LOL_{HCHO} evolutions were first analyzed. The formaldehyde cloud has been found to be much more stable than the high-temperature flame location. Auto-ignited detached kernels have always been localized inside the formaldehyde cloud and lead to a rapid decrease in the LOL while the LOL_{HCHO} remains stable. The “natural” LOL temporal evolution was analyzed for different test conditions and two typical features have been identified:

- Very rapid upstream displacement of the LOL very probably linked to auto-ignition and called “large scale” auto-ignition indicated by detached kernel upstream the main high-temperature flame
- A progressive downstream evolution of the LOL for a given period of time until another “large scale” auto-ignition occurs

The natural high-temperature flame seems to be driven by an alternation of the two above evolutions. Forced laser ignition was performed to highlight the “natural” downstream evolution occurring after a “large scale” auto-ignition and, consequently, to investigate the main stabilization mechanism during this stage. The laser ignition was performed upstream and inside the formaldehyde cloud, demonstrating the leading role of low-temperature reaction on the downstream evolution. Upstream the formaldehyde, rapid LOL temporal evolutions are observed whereas inside the formaldehyde cloud systematic slower progression is observed.

Finally, the stabilization mechanism seems to be governed by an alternation of “large scale” auto-ignition and downstream evolution which can be governed by “small scale” auto-ignition or/and flame propagation. Moreover, the impact of the flow velocity on the possible auto-ignition fronts or/and premixed flame needs to be investigated during this downstream evolution. More investigations are needed to clarify these points and to discriminate between the propagation and auto-ignition processes.

Chapter 4

A conceptual model of the flame stabilization mechanisms for a lifted Diesel-type flame based on direct numerical simulation and experiments

This Chapter proposes to use the results from a DNS in combination with the observations made in the experimental study to complete our understanding of the flame stabilization mechanisms under Diesel conditions. Section 4.2 first presents the numerical setup of the DNS. Then, a description of the chemical mechanism is proposed in Section 4.3. Section 4.4 describes the different tools developed to analyze the local reaction zone topologies at the flame base. In Section 4.5, a comparison between the DNS and the experiments is proposed. Based on the tools developed in Section 4.4, Section 4.6 presents an analysis of the flame stabilization mechanisms. Finally, Section 4.7 shows a conceptual model of the flame stabilization mechanisms for a lifted Diesel-type flame.

This study is presented here as an adapted version for the thesis manuscript of an article entitled "A conceptual model of the flame stabilization mechanisms for a lifted Diesel-type flame based on direct numerical simulation and experiments", published in the journal *Combustion and Flame* [96]. The abstract, present in the original paper, is removed and the introduction has been modified to avoid repetitions with Chapter 2. Furthermore, Section 4.8.1 has been added to provide complementary elements.

4.1 Brief introduction

The objective of the present work was to perform a DNS study of the spatial and temporal evolution of a Diesel-type spray previously studied experimentally [82] in order to explore in detail the phenomena contributing to the spray-flame stabilization.

Ideally, such a DNS would have to simulate the full spray, including in particular the liquid fuel spray originated from the injector nozzle. A DNS including the latter

would be a challenge in itself and has not been addressed by published research due to its inherent complexity and extreme requirements in terms of spatial and temporal resolution. Published DNS have therefore restricted the computational domain to the gaseous part of the spray where chemical reactions essentially take place. A first approach was to perform temporal DNS of the turbulent mixing layer created downstream of the liquid part of the spray [18, 64, 65, 75]. While this allowed addressing realistic Damköhler numbers, it may not account for spatial recirculation of hot burnt gases that have been found to possibly be of importance for the flame stabilization of ACDF [14]. Another type of DNS simulated a spatially stabilized gaseous flame set up to be as representative as possible to Diesel-spray conditions [76]. While this allowed addressing Damköhler numbers under Diesel-spray conditions, the studied Reynolds numbers were considerably smaller than that of a Diesel spray.

In the present work, we chose to perform a DNS of the spatial evolution of the gaseous part of the spray studied in [82] (α condition), in order to account both for realistic Reynolds and Damköhler numbers, and to address in particular the recirculation of burnt gases and their suspected impact on flame stabilization. To limit the computational cost of such an approach, the simulations were restricted to 2D, which allowed ensuring a sufficient resolution of the small spatial scales of premixed flames under the studied conditions.¹

Unlike many turbulent flames, which can be computed with simplified chemical descriptions [97, 98], the simulation of ACDF requires more complex chemical kinetics. The LOL time evolution is a discontinuous quantity, characterized by frequent jumps when the flame auto-ignites. Experiments reveal that these auto-ignition events (called “Events A” in [82]) are followed by the formation and the downstream convection of flames (called “Evolution B” [82]) before a new auto-ignition event occurs upstream and brings the flame back closer to the injector. Low-temperature chemistry has been shown to play an important role in that dynamic process [82]. Reproducing these low-temperature chemistry phenomena, especially in the NTC (Negative Temperature Coefficient) regime, is impossible with global schemes [65] and requires more complex chemistry descriptions.

In the present DNS, chemistry was modelled using an ARC (Analytically Reduced Chemistry) scheme [99–103] adapted for n-dodecane / air flames at 3.4 MPa.

The paper is organized as follows: the computational domain and numerical method employed in the DNS of the ACDF configuration is described in Section 4.2, followed by the chemical scheme reduction methodology and its validation in Section 4.3. The analysis tools, used to identify the instantaneous LOL as well as the local reaction zone topologies around it, are detailed in Section 4.4. Then, Section 4.5 presents a comparison between experiments [82] and the performed DNS in order to validate the strong hypothesis and in particular those related to a 2D simulation and a synthetic simplified turbulence at the inflow of the gas jet allow realistic predictions. In Section 4.6, each discrete instantaneous lift-off predicted by the DNS is identified to be either of the Event A or Evolution B types following the definitions proposed in [82]. Furthermore, the developed automatic tools analysis are used to identify the local reaction zone topologies around discrete instanta-

¹Care was taken to base the 2D DNS of the gaseous part of the spray on a sufficiently realistic chemical mechanism including low-temperature chemistry.

neous lift-off positions. Finally, a conceptual model for flame stabilization in ACDF-type configurations is proposed in Section 4.7 based on the performed analyses and resulting observations.

4.2 Configuration

The case simulated in the present work had previously been studied experimentally. Details on the employed techniques and obtained results can be found in [82], where it is referred to as the α condition.

The configuration consists of a *n*-dodecane liquid fuel injected into a large constant volume vessel containing a mixture with a 16% (by volume) oxygen concentration, at an initial pressure of 3.4 MPa and temperature of 800 K.

4.2.1 Simplifying assumptions

Performing a 3D DNS of the full liquid spray, and its combustion under such Diesel engine-like conditions, would require a very fine spatial and temporal discretization in order to capture the smallest scales. An estimation of the resulting necessary computational effort indicated that the cost of performing such a 3D DNS would be prohibitive.

In order to define an affordable computational framework able to reproduce essential aspects of ACDF flame stabilization, the following simplifying assumptions were made:

- The simulation was simplified to be two-dimensional. Despite the related limitations, in terms of an accurate reproduction of all features of a turbulent flow, comparisons with experimental findings indicated that this strong simplification allowed capturing key features at a fraction of the cost of a 3D DNS. It also simplified the analysis of the reaction zone dynamics significantly.
- As experimental observations for the simulated condition showed a flame stabilization downstream of the zone where the liquid spray impacts the local flow dynamics, the liquid injection was not included in the simulations. As shown in Fig. 4.1, the computational domain was therefore started 20 mm downstream the injector outlet, i.e. downstream of the liquid length that was estimated to be 18 mm [104].
- The computational domain was chosen to include an area of interest axially situated between 25 mm and 50 mm downstream of the injector. As illustrated in Fig. 4.1 (top), experimental findings [82] indicate that this well-resolved area of interest includes the spatially relatively stable low-temperature-chemistry (e.g. formaldehyde), as well as the region situated axially between 26 and 45 mm downstream the injector in which the LOL varies. In the radial direction, the area of interest encompasses a region containing high-temperature products localized at the jet periphery, which, according to [14], may contribute to the flame stabilization.
- Inflow boundary conditions imposed in the central part of the jet were not chosen to reproduce the complex turbulent multi-species and possibly reactive flow found at that axial position 20 mm downstream the injector. These complex flow conditions are not known from published research, and would indeed require performing a full

DNS of the spray. The inflow boundary conditions were thus strongly simplified to only reproduce the mean mass flow rate and a very approximate level of velocity fluctuations. Temperature fluctuations were neglected, and only a non-reactive mixture of fuel and air was fed into the domain. Such inflow conditions are very crude approximations, but the flow can develop between the inflow and the beginning of the area of interest at 25 mm, where we observed a qualitatively realistic turbulent reactive flow. This was checked quantitatively in a posteriori way by comparing DNS predictions with experimental findings, as will be exposed in Section 4.5. In this sense, the inflow boundary conditions should be viewed only as a crude simplification resulting from the absence of detailed knowledge, and chosen to allow for realistic flow conditions in the area of interest to which all analysis presented below were restricted.

- Only the "quasi-steady" state reached once the spray flame has auto-ignited was studied [23]. This phase is characterized by a constant mean fuel flow rate.

In Section 4.5, the DNS will be compared to experimental findings in order to a posteriori assess the validity of these assumptions.

4.2.2 Numerical set-up

The present DNS were performed with the AVBP code co-developed by CERFACS and IFPEN [105]. AVBP solves the compressible reactive Navier-Stokes equations for momentum, total energy, and species mass fractions on unstructured grids. The Lax-Wendroff scheme [106] (second-order accurate in space and time) was used.

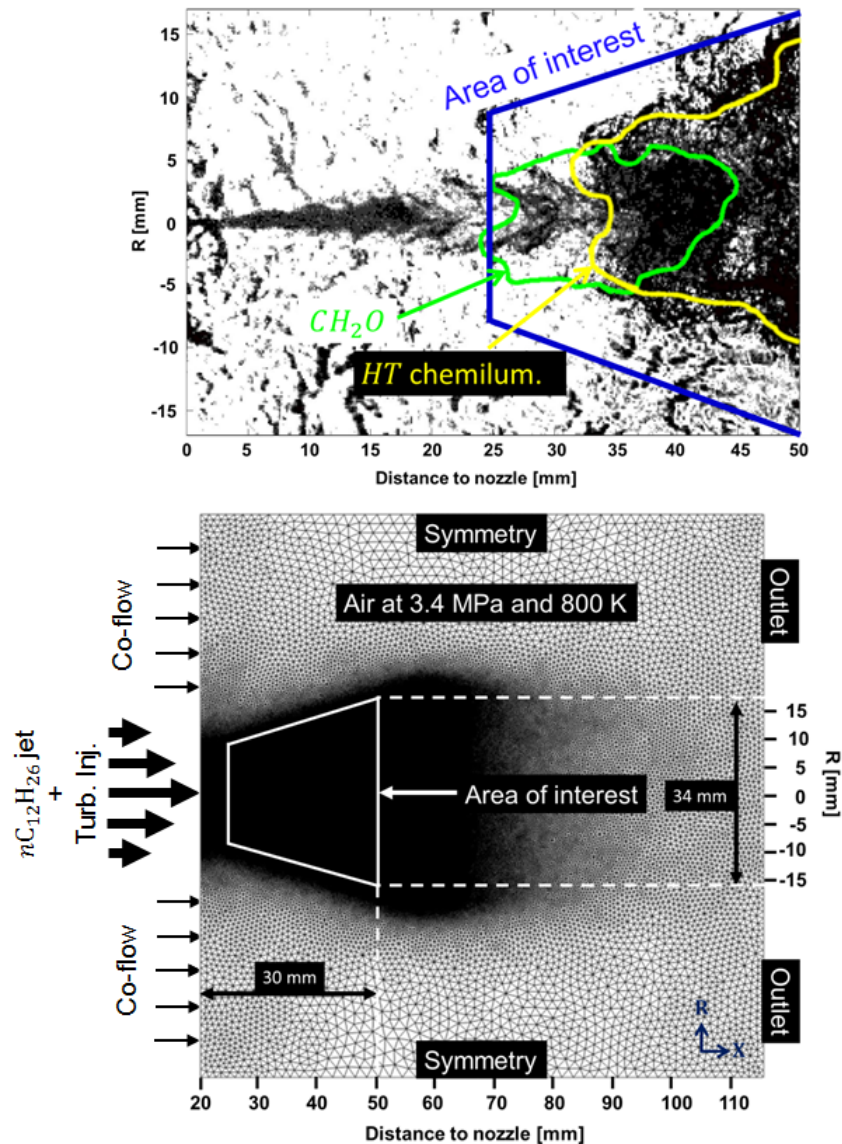


Figure 4.1 – Top: Superposition of the gas envelope of the spray (Schlieren imaging) on an iso-contour of the formaldehyde cloud (green line, high-speed 355 LIF), and the high-temperature flame (yellow line, broadband chemiluminescence). This image was obtained from the experimental setup presented in [82]. Bottom: Computational domain showing the used tetrahedral grid which is refined in the area of interest to capture combustion phenomena.

Fig. 4.1 (bottom) shows the 2D square computation domain. Spatial discretization is based on an unstructured tetrahedral mesh. The highest spatial resolution of $6\ \mu\text{m}$ is imposed in the area of interest that covers the region where key mechanisms of flame stabilization take place and were analyzed. This cell size was chosen to achieve a sufficient resolution of the estimated premixed flame thickness under the simulated conditions, as outlined in Section 4.3.2. The cell size is progressively coarsened laterally and downstream of the area of interest in order to impose lateral and downstream boundary conditions far enough to mimic the large size of the real constant volume vessel used in the experiments.

The resulting mesh comprises 33.7 million nodes. The time-step was 1.9 ns to satisfy the acoustic Courant-Friedrichs-Lewy (CFL) condition of the explicit time advancement.

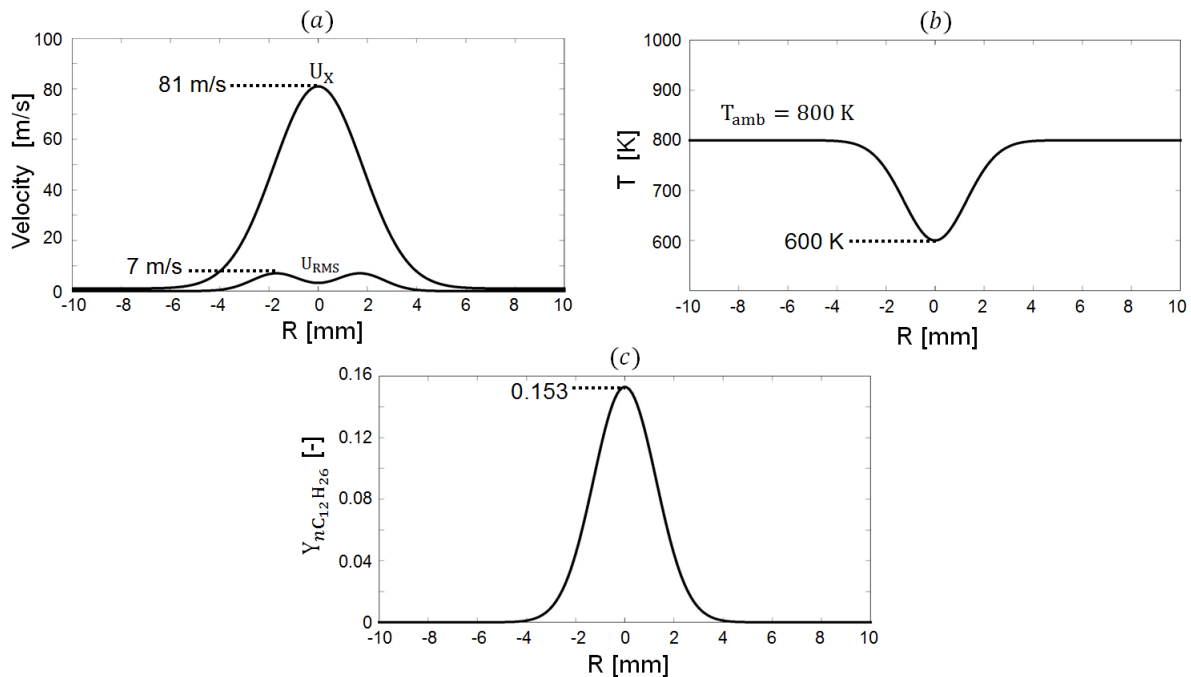


Figure 4.2 – All of the graphs show radial profiles imposed at the inlet boundary condition. (a): Axial flow velocity (U_X) and axial velocity fluctuation (U_{RMS}), (b): temperature, (c): n-dodecane mass fraction.

Lateral symmetric boundary conditions are used. The inlet and outlet boundary conditions are imposed using the Navier-Stokes characteristic boundary condition (NSCBC) [107]. At the outflow, a relaxation method is used to impose the vessel pressure of 3.4 MPa while minimizing spurious wave reflections.

In the central part of the inflow boundary, an relaxation method is used to impose the mean profiles of axial velocity (U_X), temperature (T) and species mass fractions (Y_k). These profiles, shown in Fig. 4.2 (and detailed in Appendix 1), impose the constant mean gas flow entering the computational domain as a result of the not simulated upstream liquid spray during quasi-steady state.

In order to roughly approximate the turbulence entering the domain as a result of the upstream spray, temporal fluctuations (following the Taylor hypothesis), proportional to the U_{RMS} profile (shown in Fig. 4.2), are added to the axial in-flow velocity using the Celik method [108] and following the Passot Pouquet spectrum [109] as detailed in Appendix 1.

A co-flow of $U_{coflow} = 1$ m/s is imposed laterally of the central inflow to avoid negative axial velocities on the inlet, which could cause numerical difficulties. This small velocity is assumed to have a negligible impact on the stabilization mechanism.

The random perturbations, added to the mean axial inflow velocity, were selected to achieve a satisfactory opening angle of the jet in the area of interest. This was checked

by performing a non-reactive simulation and comparing time-averaged radial profiles of velocity, temperature, and fuel mass fraction obtained by post-processing instantaneous DNS fields with profiles given by experimentally established correlations. This allowed (shown in Section 4.8.2) to check that the imposed boundary conditions yielded satisfactory mean profiles in the area of interest where flame stabilization mechanisms were studied. Therefore, the chosen inflow boundary conditions allow to investigate the flame stabilization mechanisms, unlike temporally developing jets created by a mixing layer between fuel and air [18, 64, 65, 75].

The initial condition for the DNS was a flow at rest at the initial temperature, pressure and composition known from the experiments. The initial mass fractions of N_2 , O_2 , CO_2 , and H_2O are imposed to be spatially homogeneous and equal to the values given in Table 4.1. The CO_2 and H_2O species are products of the lean pre-combustion used in the experiments to bring the vessel to its initial conditions at the start of injection.

Table 4.1 – Initial species mass fractions in the vessel.

Species	N_2	O_2	CO_2	H_2O	$nC_{12}H_{26}$
Mass fraction [-]	0.7016	0.1746	0.1001	0.0237	0

The simulated physical time was 12 ms. A first initial phase of 3 ms was necessary to have the flame ignite and for the flow to reach a stabilized state in the mean. Flame stabilization was only analyzed after this initial stage.

The computational cost was 120,000 CPU hours per simulated physical millisecond. AVBP allowed achieving a return time of approximately 24h per simulated millisecond on 4992 cores.

4.3 Chemical mechanism

The reference chemical kinetics scheme used in this work is the 54-species skeletal model for n-dodecane oxidation developed by Yao et al. [95], itself based on the detailed kinetic scheme for a variety of alkanes by Sarathy et al. [110].

4.3.1 Development of the reduced scheme

This reference mechanism is further reduced for the conditions relevant to the DNS presented here using the YARC reduction tools [99]. The resulting analytically reduced chemistry (ARC) model is then validated against experimental and simulation data obtained using Yao’s model. Comparison are shown in Fig. 4.3 for laminar flame speed (left column) and auto-ignition delay (right column). Laminar premixed flame values were obtained for equivalence ratios in the range 0.7-1.3 for atmospheric and high pressure (3.5 MPa). Auto-ignition delays are checked for pressures of 2.0-5.0 MPa, equivalence ratios of 0.5-1.2, and initial temperatures of 700-1200 K. The first step of the reduction methodology is to identify species and reactions which can be removed without affecting the laminar flame speed and the auto-ignition delay using the directed relation graph method with error propagation [100]. At the end of this stage, 7 species are removed.

Species for which a Quasi-Steady State Approximation (QSSA) can be used are, then, chosen using the Level Of Importance criterion [111]. The resulting ARC scheme is composed of 28 transported species, 19 QSS species (Table 4.2) and 198 reactions. As shown in Fig. 4.3, the 28-species reduced scheme correctly reproduces the laminar flame speeds and the auto-ignition delays over the selected range of conditions, also capturing the NTC region for a fixed composition with varying temperature.

Table 4.2 – Summary of the reduced mechanism (28 ARC): transported (left) and Quasi Steady State (QSS) (right) species.

Transported species (28)	QSS species (19)
N ₂ , O, H ₂ ,	CH ₂ , HCO, CH ₂ [*] ,
H, OH, H ₂ O,	CH ₃ O, C ₂ H ₃ , CH ₂ CHO,
H ₂ O ₂ , O ₂ , HO ₂ ,	C ₂ H ₅ , a-C ₃ H ₅ , C ₂ H ₃ CHO,
CH ₂ O, CO ₂ , CH ₃ ,	n-C ₃ H ₇ , C ₄ H ₇ , p-C ₄ H ₉ ,
CO, C ₂ H ₆ , CH ₄ ,	p-C ₅ H ₁₁ , p-C ₇ H ₁₅ , p-C ₁₂ H ₂₅ ,
C ₂ H ₄ , C ₂ H ₂ , C ₃ H ₆ ,	s ₃ -C ₁₂ H ₂₅ , s-C ₁₂ H ₂₅ , C ₁₂ OOH,
C ₄ H ₈ , C ₅ H ₁₀ , C ₆ H ₁₂ ,	O ₂ C ₁₂ H ₂₄ OOH
C ₇ H ₁₄ , C ₈ H ₁₆ , C ₉ H ₁₈ ,	
C ₁₀ H ₂₀ , C ₁₂ H ₂₅ O ₂ , n-C ₁₂ H ₂₆ ,	
OC ₁₂ H ₂₃ OOH	

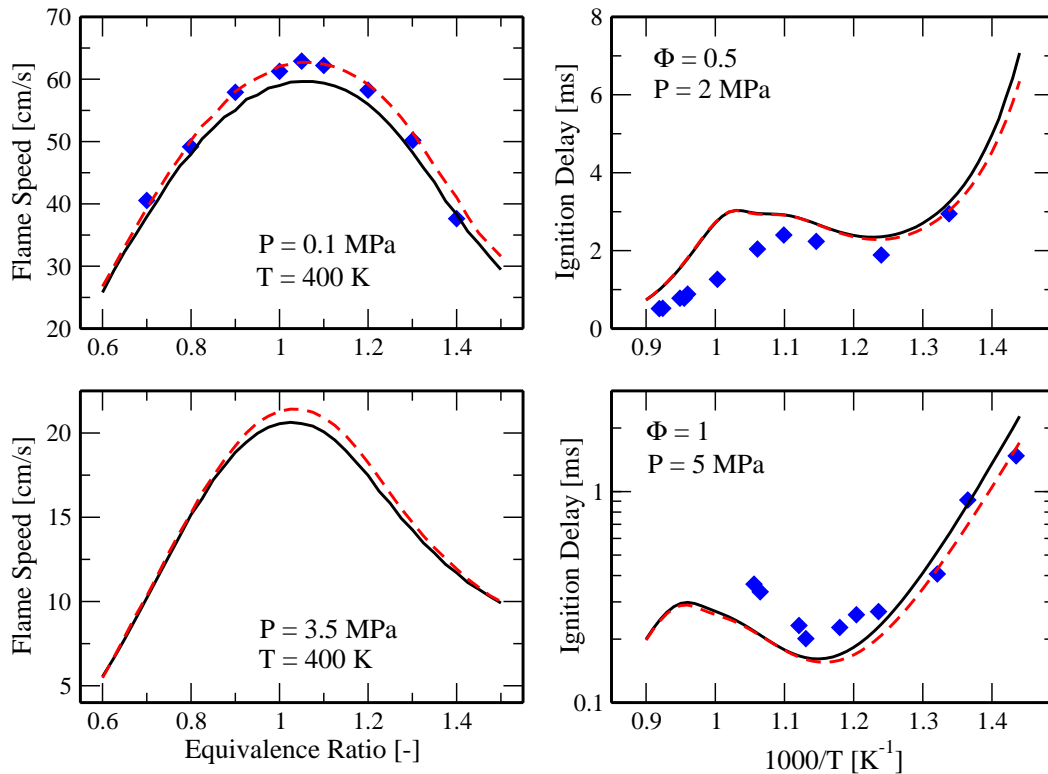


Figure 4.3 – Comparison between the reference mechanism of Yao et al. (solid black lines, [95]) the ARC model derived in the work (dotted red line), and experimental data (symbols, [22, 112, 113]). Left: laminar flame speeds, right: ignition delay times.

4.3.2 Estimation of the thermal flame thickness

The reduced scheme was used to estimate the necessary spatial resolution in the area of interest of the computational domain. To this purpose, a 1D premixed flame is first calculated using Cantera [94] for a stoichiometric mixture (computed using Bilger’s definition [114]) at the initial pressure and temperature of the studied spray. The length of the 1D domain is 0.2 mm allowing to stabilize the 1D premixed flame in the middle of the domain without interactions with auto-ignitions ahead of it as discussed in [66] (this problem is also known as the ”cold boundary problem” [115]). The thermal flame thickness was hereby found to be 32 μm .

In a second step, the same 1D flame simulation was performed with AVBP using different spatial resolutions. This allowed to show that a spatial resolution of 6 μm was sufficient to solve for all species present in the ARC scheme and to reproduce the CANTERA findings.

For more details concerning the definition of the spatial resolution of the DNS, the

reader can refer to Section 4.8.3.

4.4 Analysis tools for DNS

An important issue to analyze the stabilization mechanisms is to build adapted post-processing tools for the DNS results. To this purpose, we first developed a method for tracking the temporal variations of LOL, which then exploited for identifying four different reaction zone topologies of importance for the flame stabilization.

4.4.1 LOL definition

For each instantaneous DNS solution, two distinct LOL are identified: the LOL for the flame base located above ($R > 0$, see Fig. 4.1) and below ($R < 0$) the injector. This decomposition was possible because the upper flame branch interacts weakly with the lower one, and presented the advantage of increasing the number of lift-off tracked. Here, we chose to track the lift-off according to a double criterion: First, the local heat release rate needs to exceed a threshold value of $\dot{\omega}_{T,crit} = 4 \times 10^{11} W/m^3$, corresponding to 83 % of the maximum $\dot{\omega}_T$ reached in the corresponding premixed stoichiometric laminar flame. Second, if the first criterion is met, the temperature must exceed a value of $T_{crit} = 1900K$ in a region of 0.15 mm around the point closest to the injector for which the first criterion is met. This double criterion is required to eliminate events where heat release peaks occur for a short period of time, but for which the kernel fails to grow, indicating that a minimum flame radius is not reached. The lift-off is then defined as the closest point to the nozzle, meeting this double criterion, and allows to compute the LOL, which is the distance between the lift-off and the fuel injector. Following the methodology proposed in [82], the LOL are tracked between 3 and 12 ms After the Start of Injection (ASI) with a time resolution of 0.01 ms leading to 1,802 (901×2) LOL.

4.4.2 Identification of the reaction zone topologies

Once the tracking of the evolution of the lift-off is made possible, an analysis of the local reaction zone structure in its neighborhood allows identifying different events linked to the stabilization.

4.4.2.1 Reaction zone topologies during auto-ignition events

Auto-ignition is identified by a discontinuity of the LOL time-tracking leading to very rapid upstream displacements of the LOL, as observed in a previous experimental study [82]. Therefore, in this paper, auto-ignition is defined by the following expression: $-\Delta LOL / \Delta t > 80$ m/s, where ΔLOL and Δt are the LOL and time variation between two instants (here, Δt is set to 0.01 ms). We found that the identification process is fairly insensitive to the value of the threshold. In the following, a value of 80 m/s has been chosen.

In order to provide a deeper understanding of the auto-ignition events, two types of auto-ignitions were identified: isolated auto-ignition (AI-I), and auto-ignition assisted by burnt gases (AI-BG). An AI-I is identified as an auto-ignition event occurring in

fresh gases, so without being affected by any surrounding burnt gases. The appellation “isolated” is given if the temperature is below T_{crit} within the edge (0.04 mm thick) of a square box of 3.8×3.8 mm centered at the lift-off. Otherwise, (if $T_{crit} > 1900K$) the appellation “assisted by burnt gases” is given, which corresponds to an auto-ignition event close to a high-temperature zone.

4.4.2.2 Reaction zone topologies during continuous evolution of the lift-off

In the absence of auto-ignition events or flame extinctions, the lift-off has been divided into two reaction zone topologies: Triple Flames (TF) and Lean/Rich Reaction Zones (L/R RZ).

TF can be identified for certain LOL, as shown in Fig. 4.4, where a zoom on the flame base reveals the existence of the conventional branches of a TF [37, 116]: branch A is a lean premixed flame, branch B designates a rich premixed flame, and branch C, a diffusion flame. The TF are detected by post-processing the mixture fraction, temperature, and heat release rate fields within a square area of 0.3×0.3 mm² around the flame base location. The conditions used to detect a TF are:

- The TF must have two intersection points between z_{st} and $\dot{\omega}_{T,crit}$.
- The TF must propagate towards fresh gases on the stoichiometric line where $T < T_{crit}$, while the downstream branch C is defined as a stoichiometric line where $T > T_{crit}$.
- One branch of the reaction zone must be on the lean side ($z_{branchA} < z_{st}$), while the other branch needs to be on the rich side ($z_{branchB} > z_{st}$).

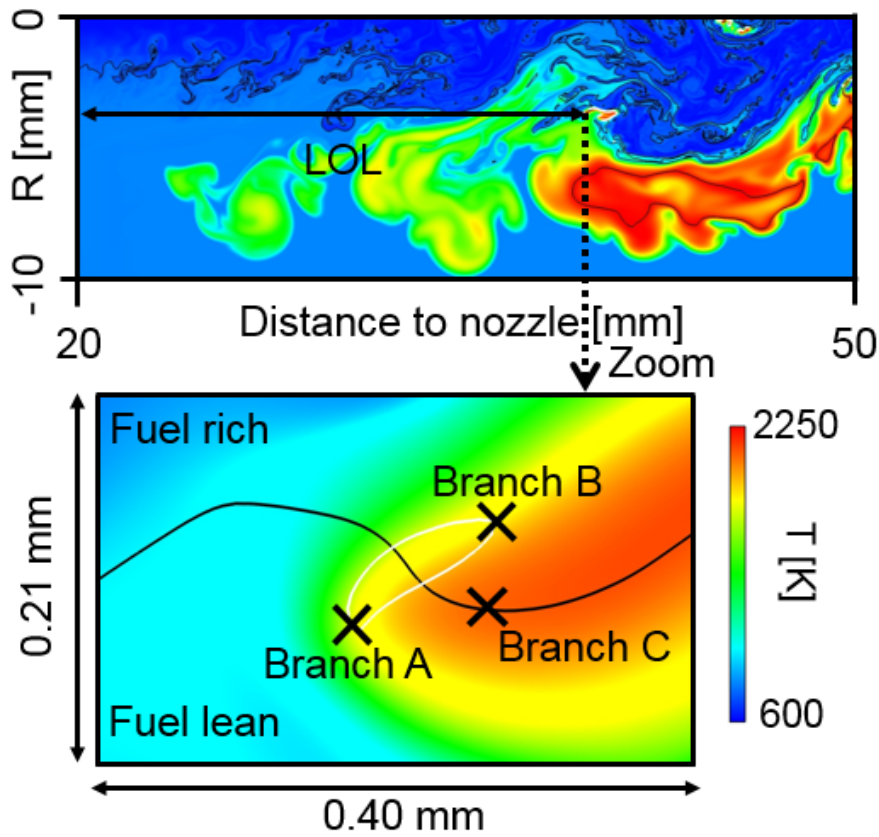


Figure 4.4 – Instantaneous temperature profile of the stabilized flame (above the injector: $R < 0$) showing a triple flame. The bottom image is a zoom around the lift-off found in the upper image. The black line represents the stoichiometric line. The white line shows $4 \times 10^{11} \text{W}/\text{m}^3$ iso-contour of heat release rate.

L/R RZ is the name given to the reaction zones which are not triple flames during continuous evolutions of the LOL. These zones can be identified just after a jump of the LOL attributed to an AI-I. In this case, the lift-off is first detected on the fuel rich side as shown in Fig. 4.5-(a). Similar results have been shown in [117] by performing unsteady Reynolds averaged Navier-Stokes simulations of Diesel spray flames, where the ambient pressures are 42 bar and 85 bar. The authors have found that the high-temperature flame first appears on the fuel rich side in the region where the scalar dissipation rate is low and the residence time is long. In the present DNS, these regions are mixture pockets observed at the jet periphery, where the flow velocity is relatively low. Due to thermal expansion, the heat release rate threshold then moves on the fuel lean side as shown in (a'). Lastly, L/R RZ is also found after TF events when the reaction zone leaves the stoichiometric line as displayed in (b) with the arrows indicating the displacement of the TF out of the stoichiometric line, resulting in a lean reaction zone (b').

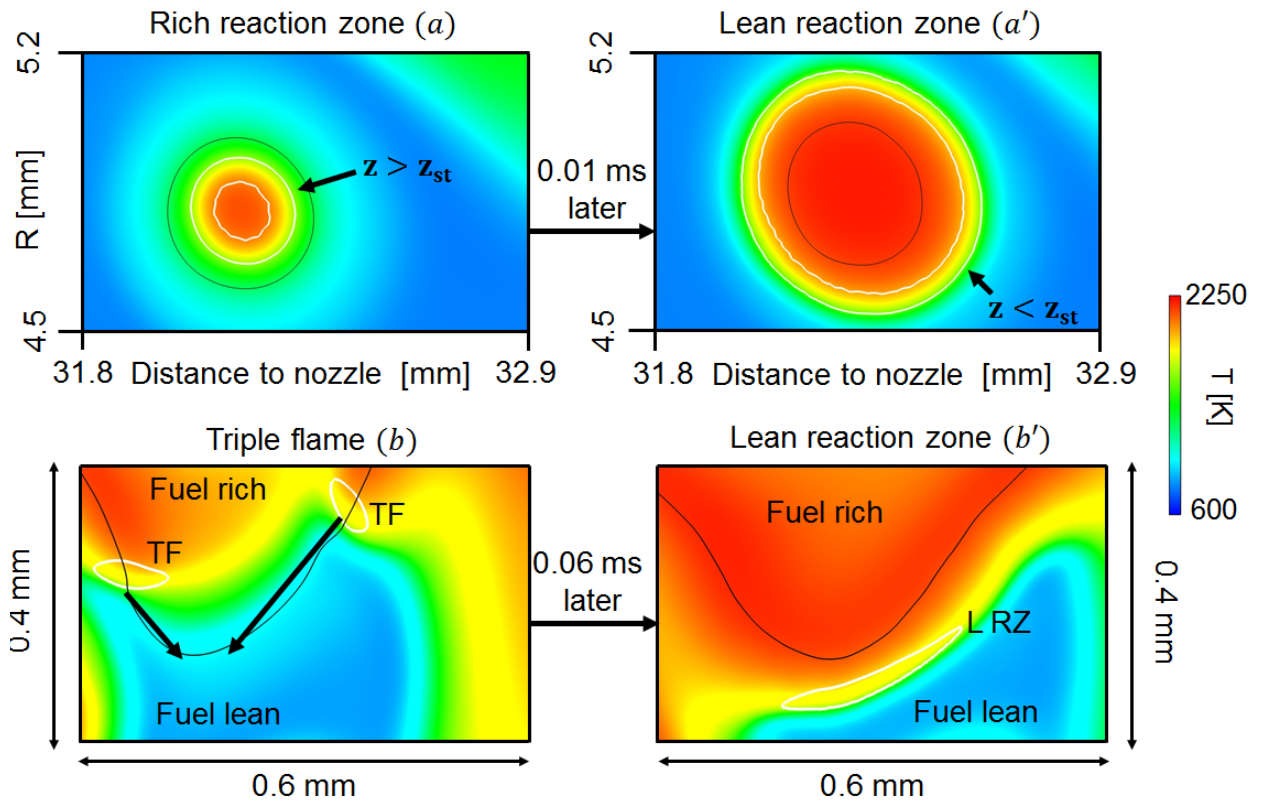


Figure 4.5 – (a) and (a'): two different instantaneous views illustrating a rich reaction zone (a) and a lean reaction zone (a') after an auto-ignition event. (b) and (b'): time sequence showing triple flames leaving the stoichiometric line. The black line represents the stoichiometric line. The white line shows the contour of heat release rate of $4 \times 10^{11} W/m^3$.

4.5 Comparison between DNS and experiments

In order to assess the accuracy/validity of the DNS, a comparison between experiments and the DNS when the flame has reached a quasi-steady state is proposed. Fig. 4.6 shows a snapshot of mixture fraction (z) and formaldehyde mass fraction (Y_{CH_2O}) fields at 3.53 ms ASI. The high-temperature flame can be visualized through the iso-lines of temperature (Fig. 4.6-top) or OH mass fraction (Fig. 4.6-bottom). As in the experiments (Fig. 4.1-top), the flame is lifted between 30 and 40 mm from the injector. Fig. 4.6, for $R > 0$, shows a detached auto-ignited kernel upstream of the main flame which suddenly decreases the LOL as observed experimentally [14, 15, 61, 82]. Moreover, as observed in [82, 86, 88], DNS predicts formaldehyde upstream the high-temperature reaction zone.

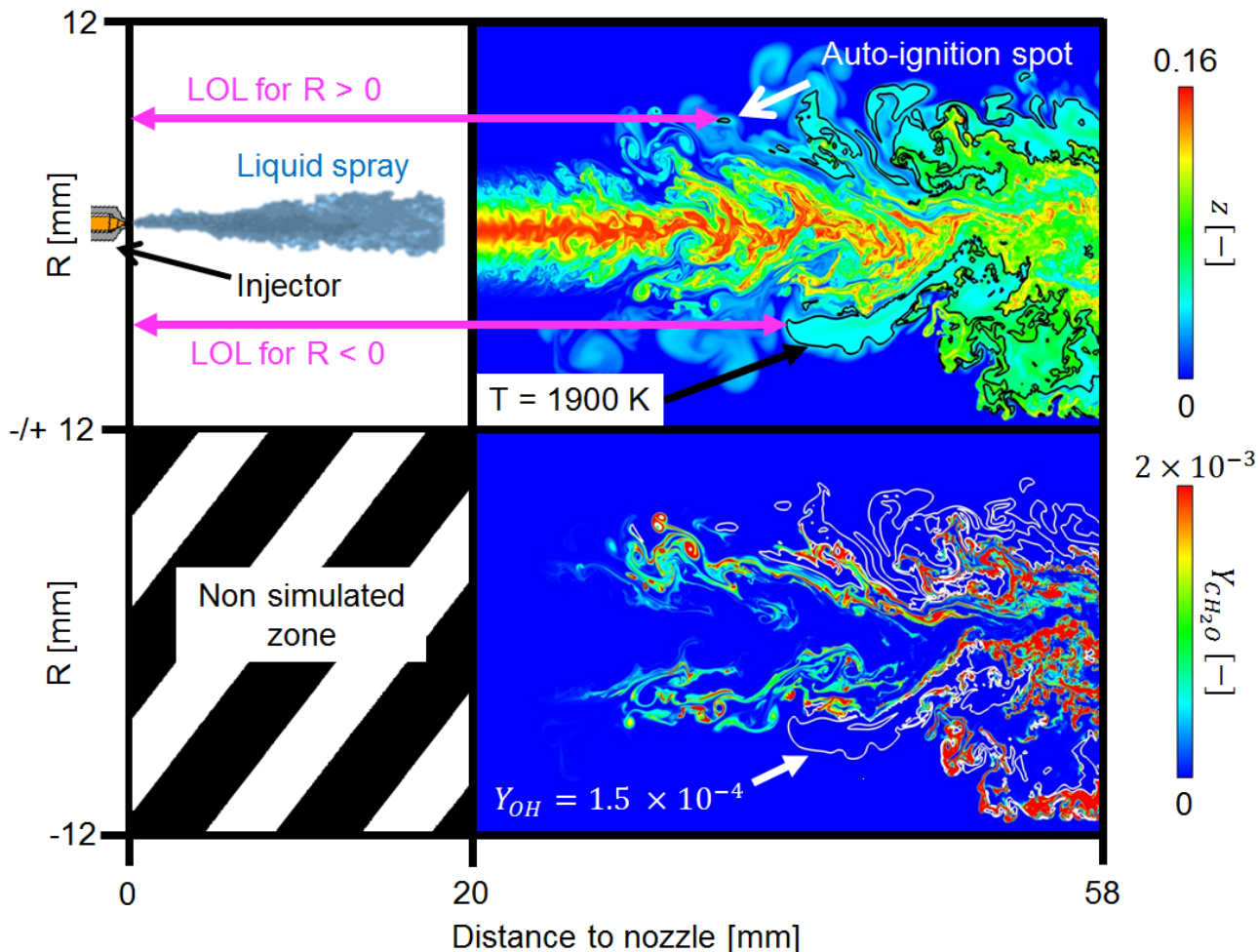


Figure 4.6 – DNS fields at 3.53 ms After the Start of Injection (ASI). Top image: mixture fraction field with an iso-line of temperature at 1900 K (black line). Bottom image: formaldehyde field with an iso-line of OH mass fraction at 1.5×10^{-4} in white.

Additionally, a comparison of the cool-flame structure (identified by CH_2O) between experiments and DNS is proposed through averaged images in Fig. 4.7-(a). CH_2O is experimentally measured with 355 LIF (laser generating a 100 mJ laser beam at 355 nm and collected between 400 and 490 nm). The experimental CH_2O averaged image is built by averaging 10 images collected at 4 ms, when the flame has reached a "quasi-steady" state. The DNS field of Y_{CH_2O} is averaged between 3 and 12 ms. A comparison between experiments and DNS shows that the upstream location of the stabilized cool-flame is similar. However, the DNS CH_2O levels are lower than experimental levels in the center jet of the DNS. Nevertheless, the lack of CH_2O in the center jet is expected not to have a strong impact on the stabilization mechanisms since the high-temperature flame is stabilized at the jet periphery, where CH_2O is correctly predicted.

Fig. 4.7-(b) also shows a comparison of the high-temperature flame between experiments (OH^*) and DNS (OH). The OH^* image is generated by temporal (between 1.35 and 3 ms) and ensemble (10 realizations) averaging using data, collected by high-speed OH^* chemiluminescence imaging at 60 kHz. The DNS field of Y_{OH} is averaged between

3 and 12 ms. Regarding the high-temperature flames, the difference of signal collected in the center jet between the experiments and the DNS is attributed to the line of sight 3D collection of OH^* chemiluminescence. Indeed, OH PLIF has shown OH species at the jet periphery [88] as observed in the DNS. OH^* chemiluminescence image allows to visualize the average LOL of the high temperature flame, which corresponds to the DNS results.

In conclusion, even if differences between experiments and DNS exist, the simulation reproduces the main features observed experimentally:

- The upstream position of the low- and high-temperature flame, in the DNS, is similar to the experiments.
- The DNS reproduces the presence of auto-ignited kernels upstream of the high-temperature flame. Such events are responsible for high LOL variation, which have been identified as a capital parameter in the flame stabilization [82].

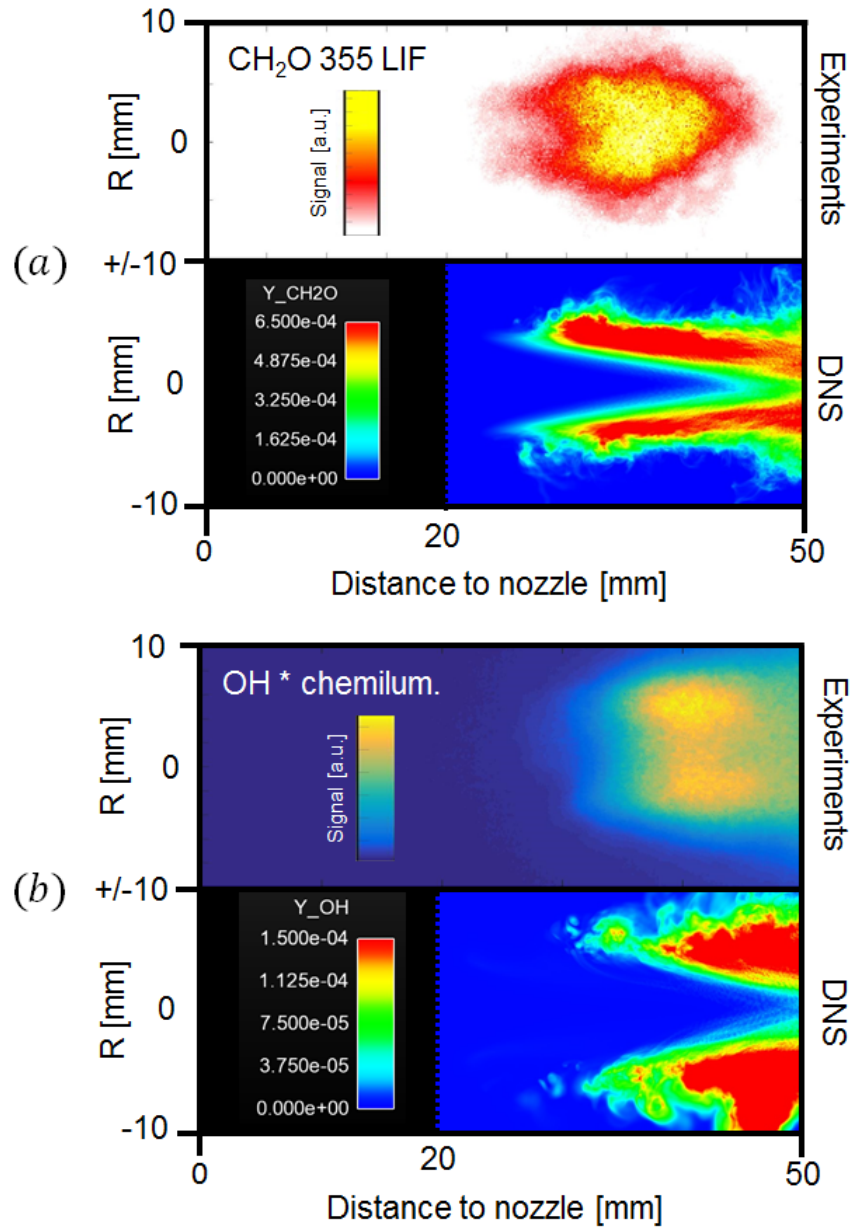


Figure 4.7 – (a): Average images of the high-temperature flame visualized by OH^* and OH species. (b): Average images of the cool-flame visualized by CH_2O species. The experimental data are generated using the experimental setup presented in [82].

4.6 Analysis of stabilization mechanisms

4.6.1 LOL tracking with reaction zone topologies

A description of the flame stabilization mechanisms is proposed using the time-tracking of the different reaction zone topologies identified at the lift-off defined in Section 4.4.2. Fig. 4.8 presents the LOL evolutions where, for the sake of clarity, only 3 ms are displayed, but the full physical time simulated is 12 ms. Each discrete point in time, obtained from

analyzing the DNS every 0.01 ms, is identified by a specific symbol for each of the four topologies defined in Section 4.4.2.

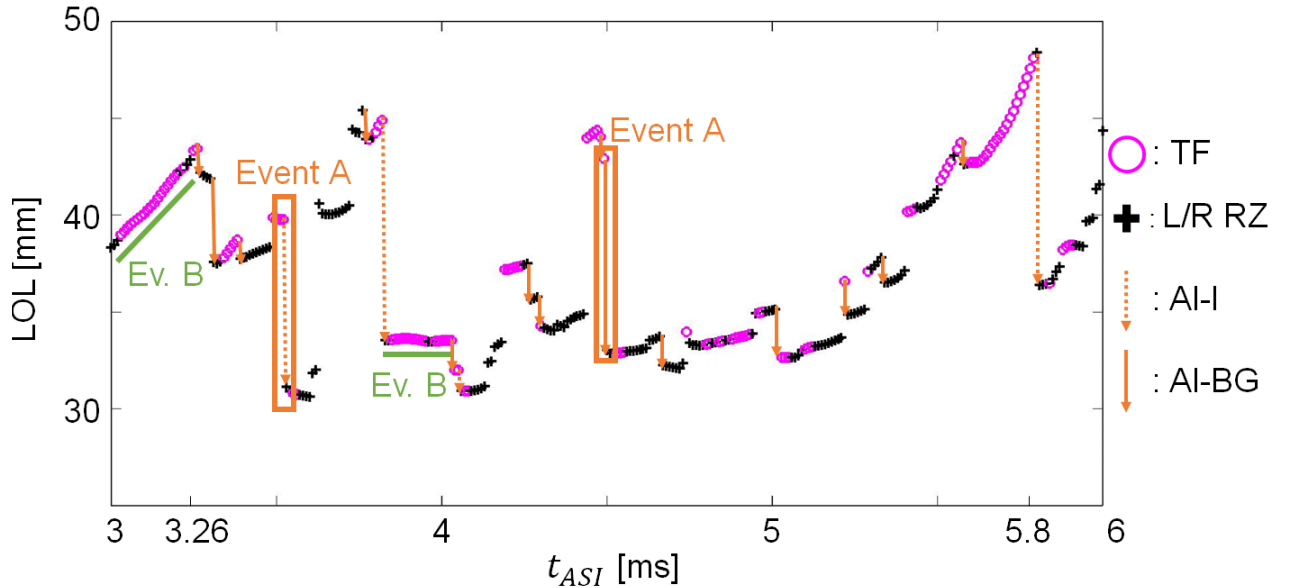


Figure 4.8 – LOL time-tracking with the detection of Triple Flames (TF), Lean/Rich Reaction Zones (L/R RZ), Isolated Auto-Ignitions (AI-I) and Auto-Ignitions Assisted by Burnt Gases (AI-BG) at the lift-off for $R > 0$.

The same two main characteristic behaviors, observed experimentally in [82] (Figure 5), are also reproduced in the DNS: auto-ignition events (also named Event A) and continuous evolutions of the LOL, which are mainly downstream evolutions of the lift-off named Evolutions B.

Fig. 4.9-(a) allows to illustrate the LOL time-tracking during an auto-ignition event. At t_0 , the flame is stabilized far from the injector, then, at t_1 , an auto-ignition occurs (AI-I or AI-BG), which brutally decreases the LOL. As shown in Fig. 4.8, at 4.5 ms (AI-BG) or at 4.5 ms (AI-I), auto-ignitions can decrease the LOL by 10 mm in 0.01 ms, and quasi-systematically Evolution B starts after these events.

Fig. 4.9-(b) illustrates Evolution B, where at t_1 , the flame has been convected downstream. An example of downstream evolution is proposed in Fig. 4.8, between 3 and 3.26 ms, where the lift-off is mainly identified as TF.

This decomposition into auto-ignition and downstream evolution implies that, if no new auto-ignition occurs, bringing the flame closer to the injector, the flame cannot sustain the flow and is, therefore, blown.

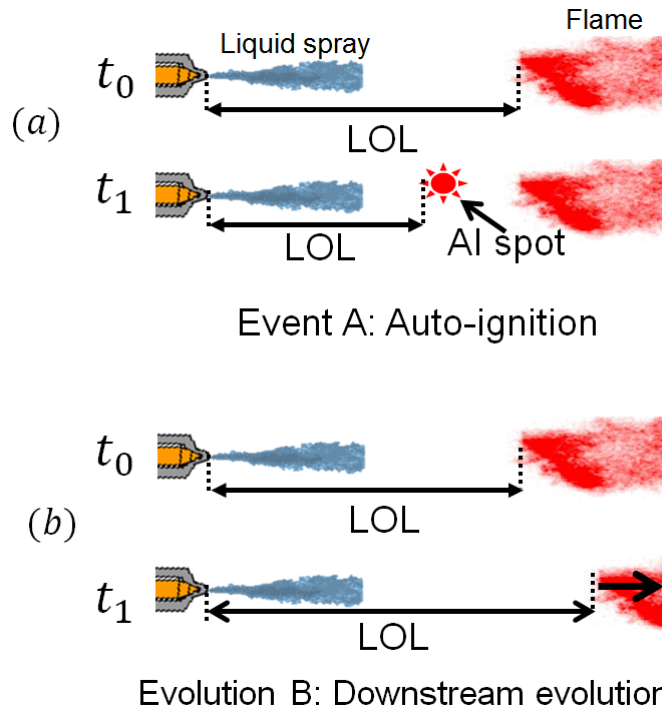


Figure 4.9 – (a): auto-ignition event, also named Event A, occurring at t_1 . (b): downstream evolution, between t_0 and t_1 , also named Evolution B.

4.6.2 Analysis of Event A

Focusing on Event A, a statistical analysis at the lift-off (between 3 and 12 ms) shows that 69 % of the auto-ignition events come from AI-BG (thus 31 % from AI-I). This demonstrates the leading role of high temperature burnt gases, which can trigger auto-ignitions and help to stabilize the flame. This observation confirms the hypothesis of Pickett et al. [14] that high temperature burnt gases reservoirs at the jet periphery could be an important factor in the flame stabilization.

First, focusing on AI-I, Fig. 4.10 shows a sequence of a stoichiometric pocket convected at the jet periphery (radially between 3.5 and 5.0 mm from the center line). It starts 0.19 ms before the AI-I and finishes when the AI-I is detected. It has been constructed starting from the third image (corresponding to the time at which an AI-I occurs, named t_{AI-I}), and exploring the DNS backward in time to see where this event actually starts. The three plots under the images represent the CH_2O and OH mass fraction profiles along the red dotted line (1 mm long) for different timings. At, 0.19 ms before AI-I, Y_{CH_2O} is very small and Y_{OH} almost inexistent. At, 0.12 ms before AI-I, Y_{OH} is still almost inexistent. However, Y_{CH_2O} raises to a maximum of 8×10^{-3} (compared to 1.8×10^{-3} in a stoichiometric premixed flame). According to [18], $t_{AI-I} - 0.12$ ms corresponds to the time between the 1st and the 2nd stage of ignition because of the large amount CH_2O , the significant rise of temperature and the lack of OH. At t_{AI-I} , an AI-I is detected, Y_{OH} has risen up to 1.5×10^{-3} at the center of the stoichiometric pocket, where the temperature is maximum, and CH_2O is totally consumed. This instant corresponds to the 2nd stage of ignition, where heat release and temperature become high enough to define the lift-off,

according to our double criterion (described in Section 4.4.1). In conclusion, the different stages, shown between $t_{AI-I} - 0.19$ ms and t_{AI-I} , follow the same well-known steps than auto-ignition in 0D homogenous reactor configurations.

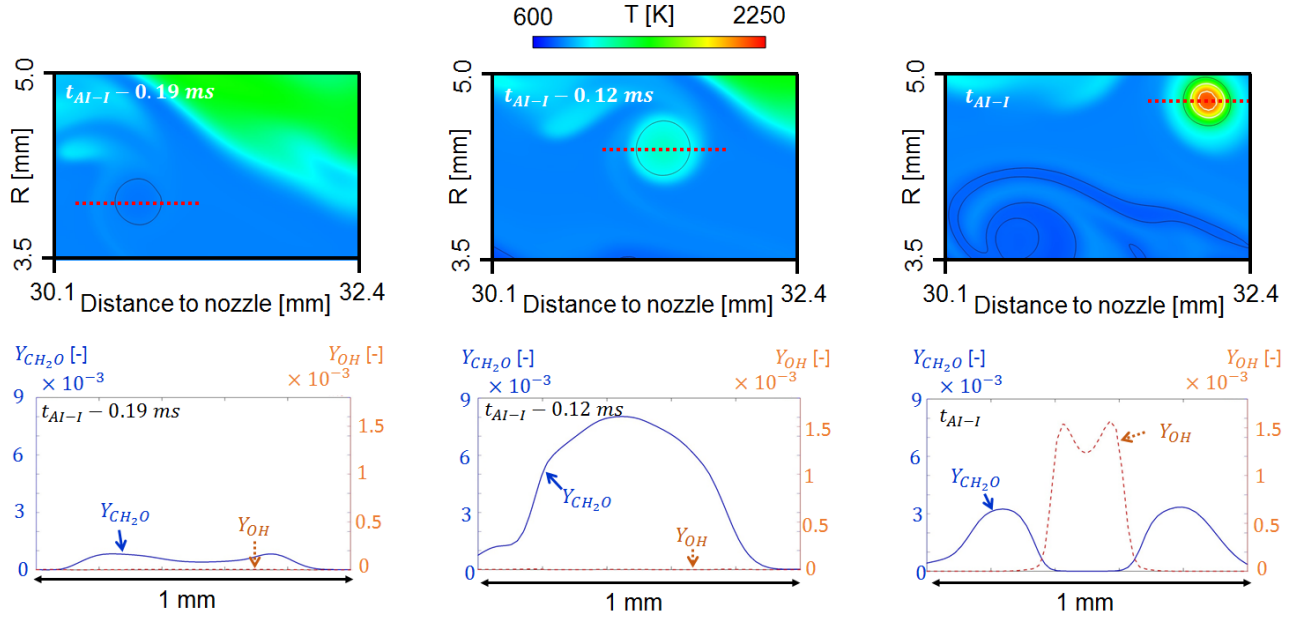


Figure 4.10 – Image sequence illustrating an isolated auto-ignition (AI-I) at the lift-off. The black line represents the stoichiometric line and the white line shows the contour of heat release rate of $4 \times 10^{11} W/m^3$ (top images). The three bottom plots show OH and CH_2O mass fraction profiles along the red dotted line (measuring 1 mm long) shown on the top image sequence.

Fig. 4.11 illustrates an AI-BG event, where combustion starts near a zone of hot gases: auto-ignition occurs between the stoichiometric line and a burnt gases pocket, without presenting the two stages observed for AI-I. In this case, burnt gases pockets move, due to the flow convection, and when they are close enough to the stoichiometric line, they trigger AI-BG.

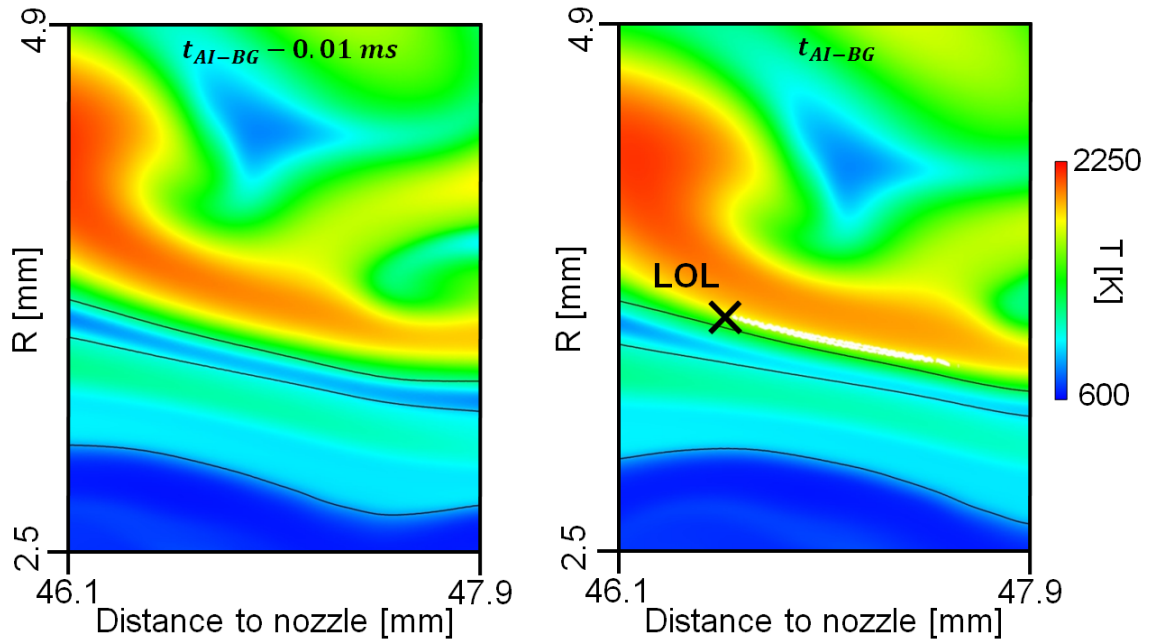


Figure 4.11 – Image sequence leading to an AI-BG event. The black line represents the stoichiometric line. The white line shows $4 \times 10^{11} \text{W}/\text{m}^3$ iso-contour of heat release rate.

4.6.3 Analysis of Evolutions B

An illustration of Evolution B is proposed in Fig. 4.12. At 3.03 ms ASI, a TF is detected at the lift-off, then 0.23 ms later, the LOL has increased by 4.4 mm (still defined as a TF) showing that this flame is convected downstream. The proportion of TF, L/R RZ is almost the same during Evolution B: 45 % TF and 55 % L/R RZ. It indicates that edge-flames must be taken into account to correctly model spray combustion under Diesel conditions as suggested in [18, 64, 65, 67, 75, 76].

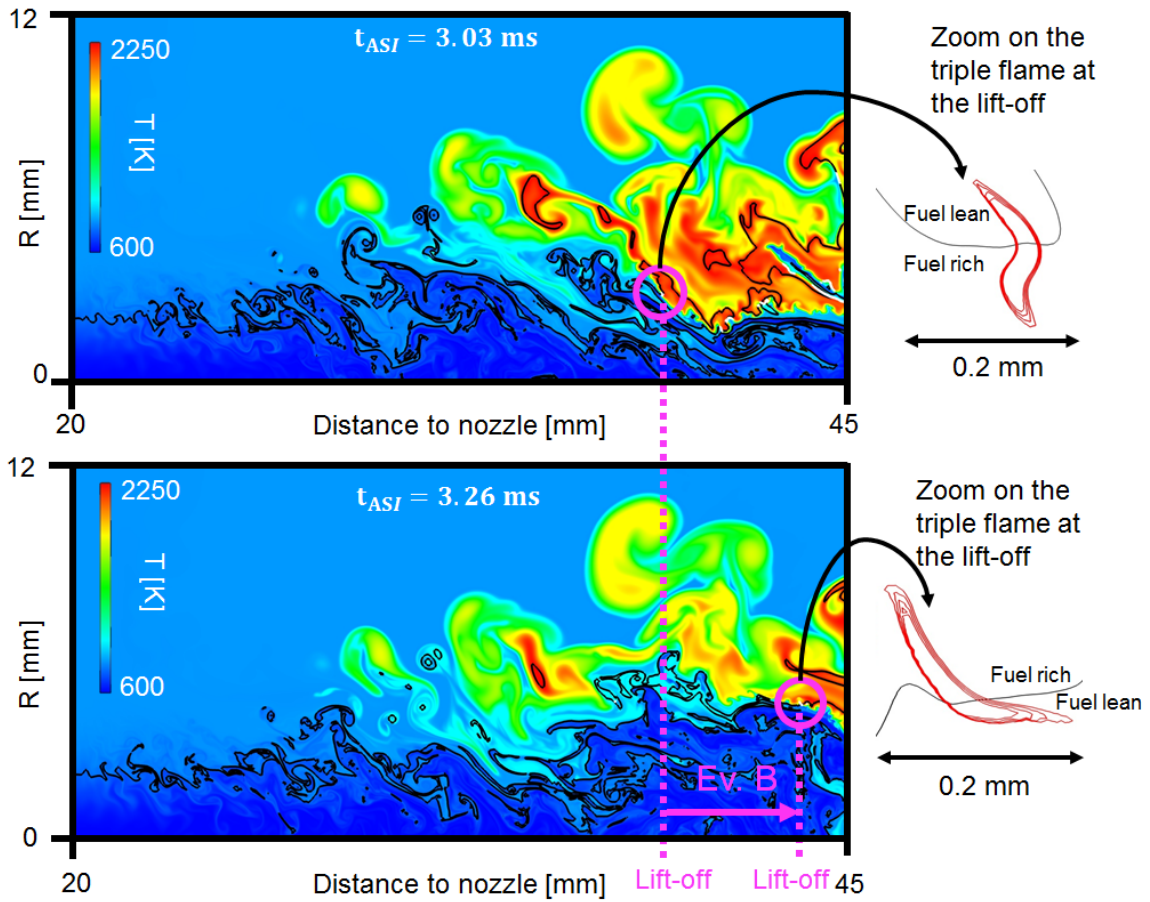


Figure 4.12 – Instantaneous temperature fields showing Evolution B between 3.03 and 3.26 ms ASI. Black line: stoichiometric line. The triple flames detected at the lift-off are zoomed, and displayed on the right of the images. Iso-lines of heat release rate between $3.7 \times 10^{11} W/m^3$ and $4.3 \times 10^{11} W/m^3$ are displayed in red on the zoomed images.

In our case, the edge-flames of interest are TF located at the lift-off. The question is to assess whether or not the TF propagation is balancing the flow. An analysis consists in a comparison between the orientation of the TF propagation and, first, the spray axis, then, the local flow. Fig. 4.13-(a) shows the definition of the instantaneous angle θ_{TF} and θ_{flow} used to compare these directions against the axis. Fig. 4.13-(b) shows two series of angles observed in the DNS: one above the injector (marked by the + exponent), the other below (marked by the - exponent). In both cases, the TF are mainly oriented towards the center line. None of these two histograms show a preferential direction around 180° , which indicates that statistically, TF do not propagate upstream. Naming the angular difference between the TF propagation direction and the upstream flow $\theta_{TF,flow}$ (as shown in Fig. 4.13-(a)), an histogram can be built and is shown in Fig. 4.13-(c). The dispersed distribution of $\theta_{TF,flow}^+$ and $\theta_{TF,flow}^-$ shows the TF do not have a preferential propagation direction with respect to the flow.

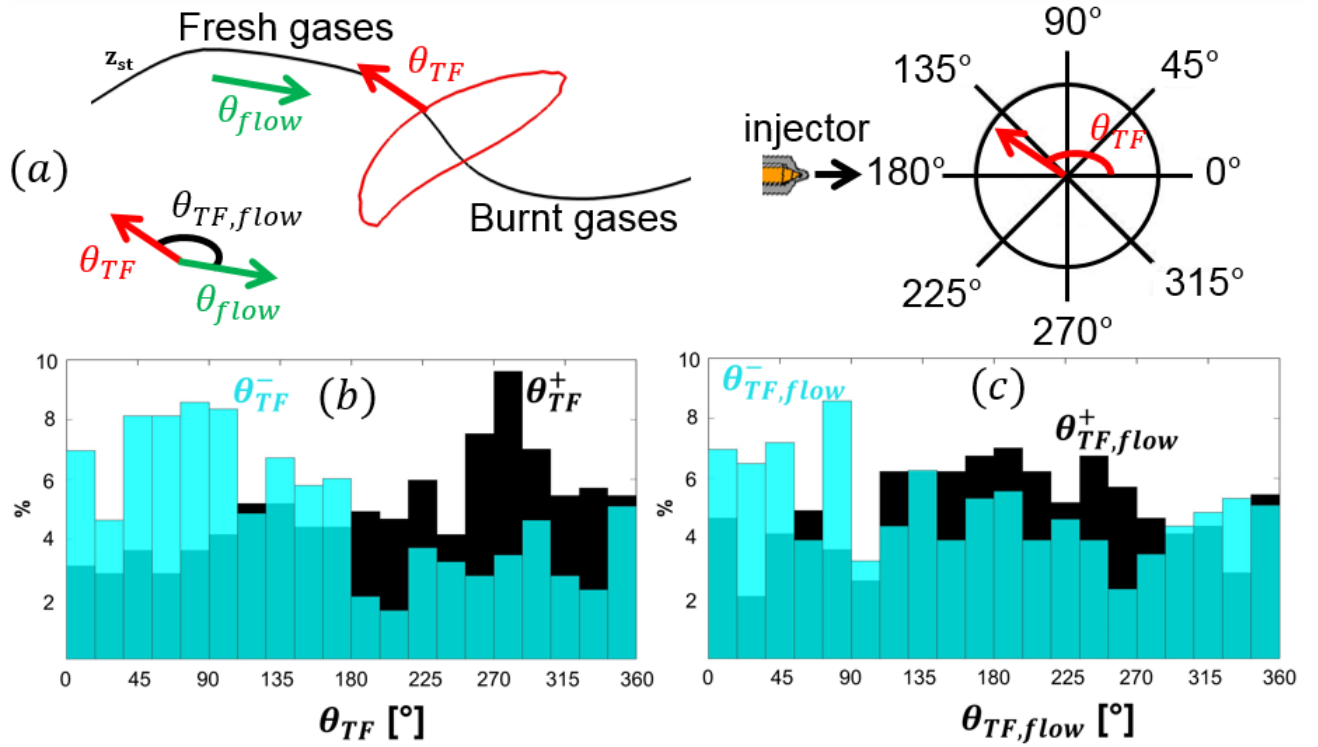


Figure 4.13 – (a): cartoon of a triple flame propagating along z_{st} . The red solid line represents the $\dot{\omega}_{T,crit} = 4 \times 10^{11} W/m^3$ iso-line. The red arrow shows the triple flame propagation direction (θ_{TF}) while the green arrow shows the flow direction (θ_{flow}). (b): histograms of θ_{TF}^+ and θ_{TF}^- . (c): histograms of $\theta_{TF,flow}^+$ and $\theta_{TF,flow}^-$ (right).

Since the flame stabilization is defined by axial displacement of the flame, a comparison between the axial flow velocity at the lift-off ($U_{X,flow,LO}$) and the absolute axial flame front speed relative to a fixed reference (S_a) is proposed through the ratio $U_{X,flow,LO}/S_a$. S_a is defined as the temporal variation of LOL. In order to eliminate spurious behaviors, only triplets of consecutive LOL values with correlation coefficient $r^2 > 0.98$ are considered. $U_{X,flow,LO}$ are computed by averaging the corresponding three instantaneous axial flow velocities at the lift-off.

Fig. 4.14-(a) shows a histogram of the ratio $U_{X,flow,LO}/S_a$ computed between 3 and 12 ms for both positive and negative radial coordinates of TF at the lift-off. The mean value of this distribution is 0.83, which indicates that S_a is statistically the same order of magnitude than $U_{X,flow,LO}$, and thus that the flow controls the evolution of the LOL. However, this analysis can be further detailed. The ratio $U_{X,flow,LO}/S_a$ is plotted as a function of $U_{X,flow,LO}$ in Fig. 4.14-(b). It appears that for $U_{X,flow,LO} > 15$, the ratio is very close to 1, meaning that S_a is governed by the flow. In order to interpret the points corresponding to $U_{X,flow,LO} < 15$, DNS of flames under Diesel-like conditions [18, 76] have indicated that the order of magnitude of the TF displacement speed S_d is between 1 and 2 m/s. Assuming $S_d = 1.5$ m/s, these TF should, therefore, correspond to a curve $U_{X,flow,LO}/(U_{X,flow,LO} - 1.5)$. Fig. 4.14-(b) indeed shows that the points corresponding to $U_{X,flow,LO} < 15$ lie very close to this curve.

Thus, there are regions where the flow velocity is of the same order of magnitude

than S_d , i.e. regions where the TF can resist to the convection by the fresh gases flow. However, in most regions of the jet, the flow has a much higher velocity than S_d , and therefore Evolution B is governed by the local flow velocity. This conclusion is different from what is observed for lifted diffusion flames under non-autoignitive conditions [35–38, 116], for which the flame is locally stabilized by an equilibrium between flow velocity and S_d .

Not shown here, plotting a similar histogram to the one, shown in Fig. 4.14-(a) for the L/R RZ, shows that Evolution B for these zones is also governed by the local flow velocity.

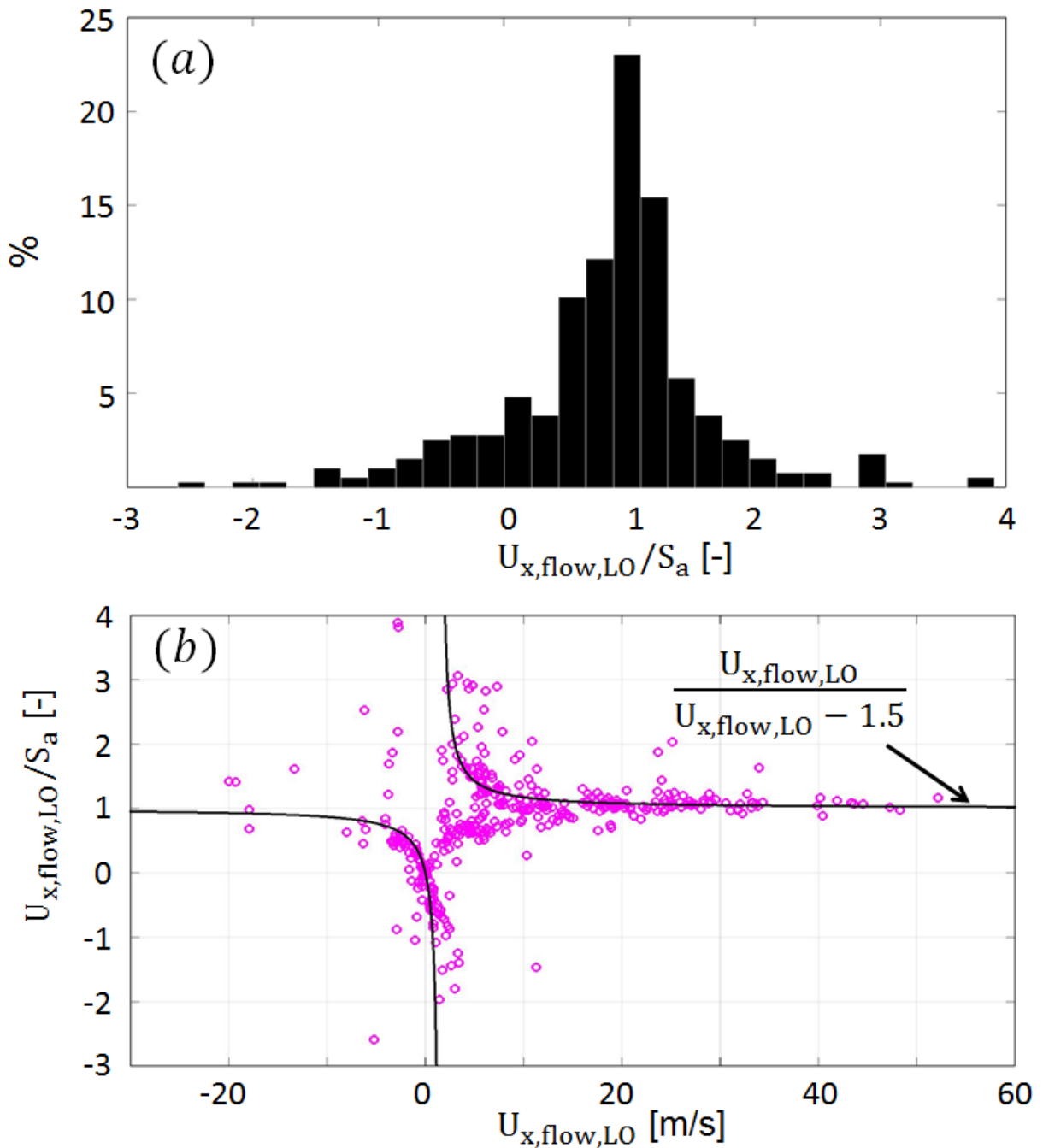


Figure 4.14 – Both graphics have been constructed from triple flames data at the lift-off for $R > 0$ and $R < 0$. (a): Histogram of the ratio $U_{X,flow,LO}/S_a$. (b): symbols show $U_{X,flow,LO}/S_a$ as a function of $U_{X,flow,LO}$, while the black curve displays $U_{X,flow,LO}/(U_{X,flow,LO} - 1.5)$ as a function of $U_{X,flow,LO}$.

4.7 Conceptual model of flame stabilization

The findings from the presented simulations and from optical diagnostics allow proposing a conceptual model for the stabilization of a Diesel-type ACDF flame. To this purpose,

Fig. 4.15 shows an idealized cross-sectional slice through the mid plane of a spray flame. Only the top branch of the jet is displayed ($R > 0$). Labelled (a) to (f), six basic local reaction zone topologies are shown on relation to an idealized instantaneous stoichiometric line in the downstream gaseous part of the jet.

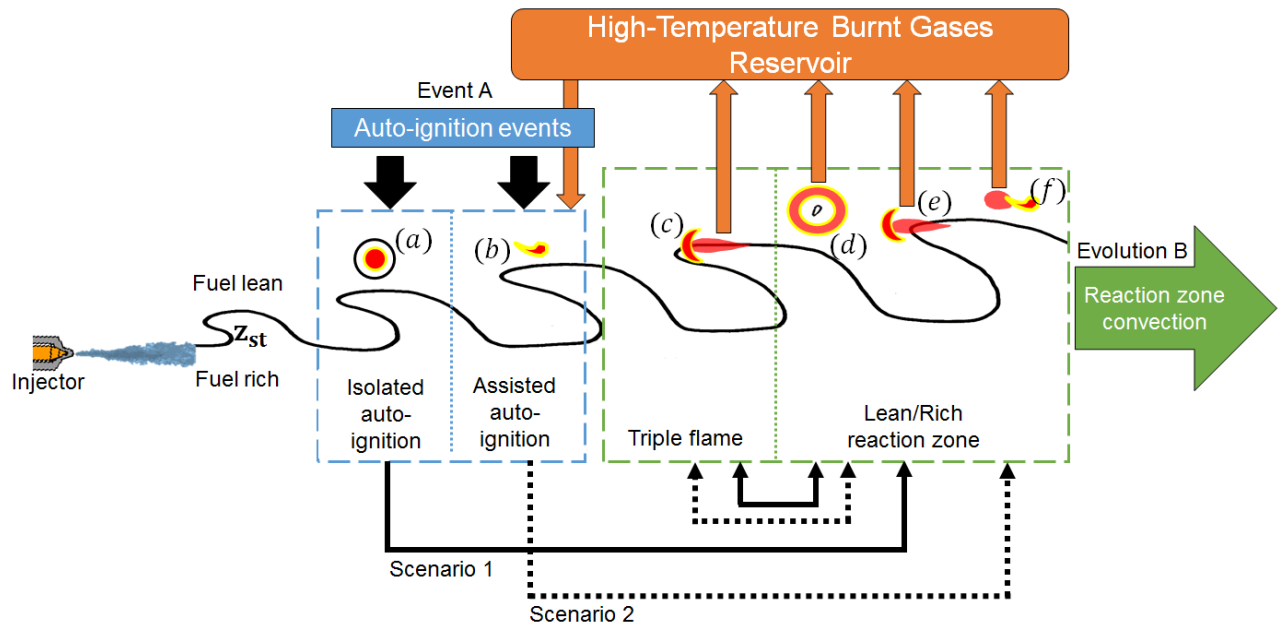


Figure 4.15 – Sketch illustrating the conceptual model of flame stabilization under Diesel condition derived from optical diagnostics and DNS.

As found above, the key necessary stabilization mechanism is auto-ignition. Two different types of auto-ignition can be found, both pertaining to Event A introduced above: isolated spontaneous auto-ignition, leading to the local topology (a); and auto-ignition assisted by burnt gases, corresponding to the local topology (b). Depending on whether an (a) or (b) topology creates an Event A, two different stabilization scenarios can be distinguished in Fig. 4.15:

Scenario 1 starts with an isolated auto-ignition spot (a) localized in a stoichiometric pocket detached from the main jet. This results in an upstream jump of LOL as seen in Fig. 4.8 (dotted arrows). The lift-off is first detected on the fuel-rich side of the local mixture pocket for a few microseconds as displayed in Fig. 4.5-(a). The resulting reaction zone grows in size, and as a result of thermal expansion, the LOL is detected on the fuel-lean side of the mixture pocket as shown in Fig. 4.5-(a'), corresponding to a local topology of type (d) in Fig. 4.15. During the transition from (a) to (d), the lift-off axially remains relatively stable due to thermal expansion that opposes to convection by the flow [118]. At the same time, the resulting burnt gases feed high-temperature reservoirs situated in external low-velocity or recirculation regions of the jet. Such burnt gases reservoirs remain axially quite stable, and can ultimately lead to topologies (b) at the origin of scenario 2 (see below). Topologies of type (d) can then either extinguish, or reach the stoichiometric line, leading to the appearance of a TF corresponding to topology (c). According to Section 4.6.3, the absolute flame speed of the TF is mainly governed by the flow velocity,

and the TF is convected downstream resulting in Evolution B. During this evolution, the TF also feeds burnt gases to the high-temperature reservoirs because of the displacement of their diffusion flame branch.

Finally, a TF can deviate from the stoichiometric line, leading to the appearance of a topology of type (*e*), corresponding to a lean or rich reaction zone as shown in Fig. 4.5-(*b'*). Transitions between topologies (*e*) and (*c*) can happen in both directions until a new auto-ignition occurs or local extinction is encountered.

Scenario 2 starts with a topology of type (*b*), i.e. an assisted auto-ignition by burnt gases coming from high-temperature reservoirs that are fed by the topologies (*c*)-(*f*). Topology (*b*) mainly transitions to (*f*) which corresponds to fuel-lean reaction zones as illustrated in Fig. 4.11. Unlike topology (*d*), the reaction zones of topology (*f*) are surrounded by burnt gases which limit the thermal expansion. They are thus growing slower, and are convected downstream by the flow following Evolution B. During this evolution, they feed burnt gases to the high-temperature reservoirs, which, thus, potentially facilitating the appearance of future scenarios 2. Topologies (*f*) can also reach a stoichiometric line and form TF corresponding to topology (*c*). The latter also feeds burnt gases to the high-temperature reservoirs, and follows an Evolution B.

In summary, auto-ignition is indispensable for allowing to stabilize a spray flame under Diesel-like conditions. Auto-ignition events appear intermittently in the upstream part of the jet, leading to the strong discontinuities in LOL observed in experiments and simulations. In-between such auto-ignitions, the leading edge of the reaction zones that can have any of the four topologies (*c*) - (*f*) are convected downstream by the strong velocities resulting from the high-pressure liquid jet. Even if these secondary topologies are ultimately blown, they allow sustaining combustion by feeding burnt gases to high-temperature reservoirs situated at the periphery of the jet. These reservoirs, indeed, facilitate the appearance of upstream auto-ignition by burnt gases, which combined with spontaneous auto-ignition allows intermittent strong reductions of the LOL, which ultimately allows an overall stabilization of the flame.

The flame stabilization mechanism is a coupling between the main mechanism auto-ignition and secondary mechanisms linked to the downstream convection of reaction zones. The two mechanisms are linked by the high temperature burnt gases reservoirs at the jet periphery, confirming the hypothesis proposed in [14].

4.8 Conclusion

This joint experimental/numerical study focused on the stabilization mechanisms of Autoignitive Conditions Diffusion Flames (ACDF) created when a high speed fuel jet was injected into hot air. Starting from experimental observations of *n*-dodecane jets into hot air, a specific DNS was built to elucidate mechanisms which control the LOL (Lift-Off Length). The analysis of the DNS showed that two types of mechanisms control the flame stabilization: auto-ignition events, where the LOL jumped rapidly to small values, followed by evolutions where the flames, created by auto-ignition events, were convected downstream by the flow without significant flame propagation effects. To obtain these results, a post-processing methodology to extract information, from DNS fields, was derived. The main conclusion is that auto-ignition was the key stabilization mechanism, while triple flames, even if they exist, had insufficient propagation speeds to contribute to

the flame stabilization. These flames were visible in multiple points of the flame brush, but they cannot be expected to provide a stabilization mechanism. Future studies should further explore the behavior of the presented conceptual model according to test condition variations (e.g. ambient temperature, and injection pressure variation). Finally, a Diesel engine environment is wall bounded and characterized by jet-jet interactions in the context of a swirling flow [119, 120]. These differences with the presently studied unbounded isolated spray could impact the stabilization mechanisms and their interactions. This would have to be explored in future experimental and simulation work.

Appendix 1

The inlet NSCBC [107] boundary condition (left edge of the computational domain) is addressed imposing radial profiles of mean axial velocity (Eq. 4.1), temperature (Eq. 4.2), mass fraction species (Eq. 4.3) and synthetic isotropic turbulence (Eq. 4.4):

$$\begin{cases} U_X(R) = U_X^{max} \exp(-R^2/2\sigma_1^2) + U_{coflow} \\ U_X^{max} = 80 \text{ m/s} \end{cases} \quad (4.1)$$

$$T(R) = T_{amb} + (600 - T_{amb}) \exp(-R^2/\sigma_1^2) \quad (4.2)$$

$$\begin{cases} Y_{nC_{12}H_{26}}(R) = 0.153 \exp(-R^2/\sigma_1^2) \\ Y_k(R) = (1 - Y_{nC_{12}H_{26}})Y_k^0 \quad \text{with } k = N_2, O_2, CO_2, H_2O \end{cases} \quad (4.3)$$

$$\begin{cases} U_{RMS}(R) = U_{RMS}^{max} \exp(-(R - \mu)^2/\sigma_2^2) + U_{RMS}^{max} \exp(-(R + \mu)^2/\sigma_2^2), \\ U_{RMS}^{max} = 7 \text{ m/s} \end{cases} \quad (4.4)$$

where:

- R is the radial coordinate
- σ_1 , σ_2 and μ are constant respectively equal to 1.8, 1.4 and 1.7 mm
- U_{coflow} is a co-flow used to avoid negative axial velocity on the inlet boundary condition set to 1 m/s
- T_{amb} is the ambient temperature (800 K)
- $Y_{N_2}^0$, $Y_{O_2}^0$, $Y_{CO_2}^0$, $Y_{H_2O}^0$ are given in Table 4.1

4.8.1 Complementary elements

4.8.2 Non-reactive profiles

This section presents the methodology adopted to compare the characteristics of the mixing between the DNS and the experiments.

First, a non-reactive DNS is performed from 0 to 10 ms. In this simulation, the numerical setup is identical to the reactive DNS. The only difference between the two

simulations is that all the sources terms are imposed to 0 to avoid the chemical reactions in the non-reactive DNS. Once the non-reactive simulation is performed, time-averaged (between 2 and 10 ms) fields of axial flow velocity (U_X), temperature (T) and n-dodecane mass fraction ($Y_{C_{12}H_{26}}$) are computed. Based on these averaged fields, radial profiles of U_X , T and $Y_{C_{12}H_{26}}$ are extracted between 30 and 50 mm from the injector (Fig. 4.16 thick red line). This range of positions corresponds to the axial coordinates where the high-temperature flame fluctuates.

Second, a 1D spray model [55, 93], validated against experiments, is used to provide averaged profiles of U_X , T and $Y_{C_{12}H_{26}}$ (Fig. 4.16 thin black line) at 30 and 50 mm from the injector.

Comparing the DNS averaged profiles and the profiles given by the 1D spray model in Fig. 4.16, some differences are observed. The largest difference is observed for U_X . Indeed, the decrease and the spreading of U_X , when the axial position increases, is underestimated in the DNS compared to the 1D spray model. This difference indicates that the profiles imposed at the inlet boundary conditions (Eq. 4.1 to 4.4) could have been tuned more accurately. Nevertheless, even with a very thorough tuning, there is no guaranty that DNS would have match the experiments since a 2D simulation cannot capture all the complex physical phenomena involved in 3D such as the 3D dissipation of the vortexes.

In conclusion, even if differences are observed between the DNS and the 1D spray model, there are judged fairly low. Therefore, it is considered that the imposed boundary conditions provide acceptable mean profiles in the area where the flame stabilization mechanisms were studied.

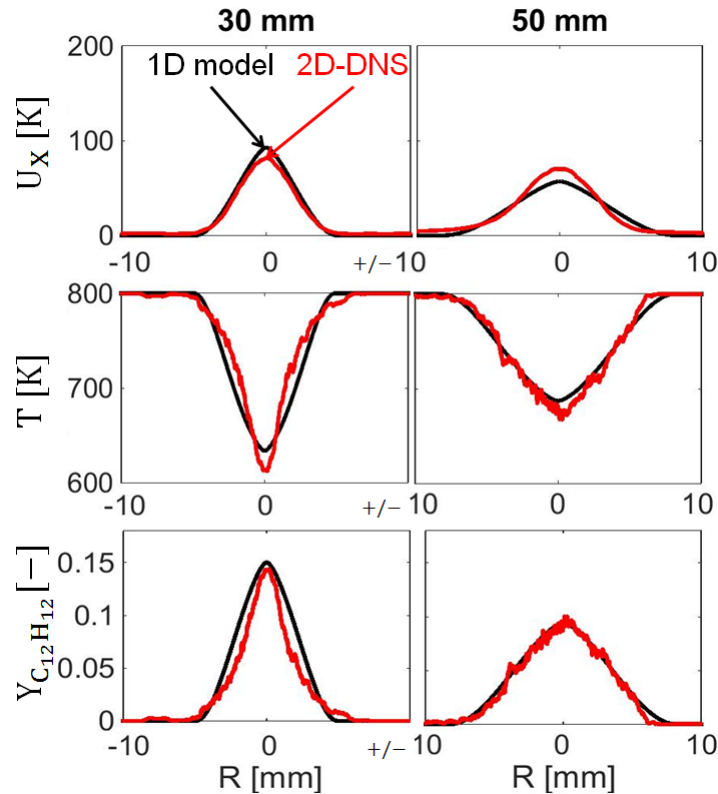


Figure 4.16 – Radial profiles comparison between time-average non-reactive DNS jet and a 1D spray model [55, 93]. Left column shows radial profiles at an axial distance of 30 mm from the injector. Right column shows radial profiles at 50 mm from the injector.

4.8.3 Calculation of the mesh resolution for the DNS

The 28-species ARC scheme was used to estimate the necessary spatial resolution in the area of interest of the computational domain in the DNS. For this purpose, a grid convergence is realized simulating 1D premixed flames.

The imposed inlet temperature, species mass fraction and ambient pressure of the 1D premixed flame are described in Section 4.3.2 and summarized in Table 4.3. As reported in [66], performing 1D premixed flames under autoignitive conditions requires great cautions due to the high temperature of the reactant mixture which can auto-ignite in the computational domain leading to domain size dependent solutions. Therefore, before performing a grid convergence to define the mesh resolution for the DNS, we propose two criteria allowing to compute a 1D premixed flame without interactions with auto-ignition.

Table 4.3 – 1D premixed flame initial conditions.

Inlet temperature [K]	739
Inlet Y_{N_2} [-]	0.668
Inlet Y_{O_2} [-]	0.166
Inlet Y_{CO_2} [-]	0.095
Inlet $Y_{C_{12}H_{26}}$ [-]	0.048
Inlet Y_{H_2O} [-]	0.023
Pressure [bar]	34

4.8.3.1 Criteria to simulate 1D premixed flames under autoignitive conditions

For a 1D premixed flame the mixture is convected at U_I in the fresh gas. This velocity is equal to the laminar premixed flame velocity if the flame is stabilized. However, when the inlet temperature and ambient pressure are high enough, the mixture can auto-ignite before the premixed flame front.

In such case, illustrated in Fig. 4.17, there is a gradual increase in temperature before the flame front. This rise of temperature is attributed to the low-temperature chemical reactions. Then the high-temperature flame stabilized by auto-ignition at approx. $U_I \times \tau_{AI}$, where τ_{AI} is the auto-ignition delay of the mixture.

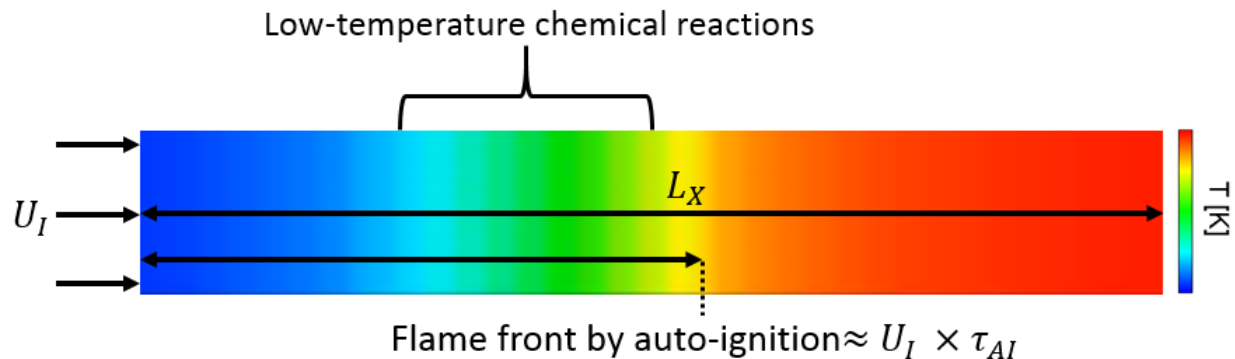


Figure 4.17 – Illustration of 1D flame stabilized by auto-ignition.

The methodology to avoid auto-ignition in the 1D computational domain consists in reducing the length of domain (L_X , see Fig. 4.17). So that, the residence time of the mixture is too low to auto-ignite in the domain. For this purpose, the following parameter is defined:

$$C_{AI} = \frac{\min(\tau_{AI}, \tau_{AI, coolflame}) \cdot U_I}{L_X}, \quad (4.5)$$

where, $\tau_{AI, coolflame}$ and τ_{AI} are the delays corresponding to the 1st and 2nd stage ignition [18, 62] computed in a 0D constant pressure reactor. We consider that if the criterion $C_{AI} > 1$ is met, the cool-flame and the auto-ignition front is localized outside of the computational domain.

Taking into account only the above criterion would lead to infinitely reduce the length of the domain. However, the length of the domain needs to be large enough to correctly model the diffusion phenomena in a 1D premixed flame. Therefore, the following parameter is defined:

$$C_{\delta_T} = \frac{\delta_T}{L_f}, \quad (4.6)$$

where, δ_T is the thermal thickness [25] and L_f is the distance between the inlet boundary conditions and the front flame. In the case where the flame is stabilized in the middle of the domain $L_f = L_X/2$. Verifying $C_{\delta_T} < 0.5$ is judged to be acceptable to properly resolve the 1D premixed flame.

A 1D premixed flame is computed using Cantera with the 28-species ARC scheme for the conditions shown in Table 4.3. The length of the domain is 0.2 mm and the flame front is localized in the middle of the domain ($L_f = 0.1$ mm). Table 4.4 shows the values of C_{AI} and C_{δ_T} . As the two criteria are both satisfied ($C_{AI} > 1$ and $C_{\delta_T} < 0.5$), the mesh resolution can be varied in order to define mesh resolution in the area of interest of the DNS.

Table 4.4 – 1D premixed flame characteristics.

C_{AI} [-]	1.7
δ_T [μm]	32
C_{δ_T} [-]	0.32
$U_I = S_L$ [m/s]	0.34

4.8.3.2 Grid convergence

In a second step, 1D premixed flame simulations are performed with AVBP for different spatial resolutions. They are all simulated in a computational domain with a length of 0.2 mm and for the conditions described in Table 4.3. Fig. 4.18 shows four grids resolutions tested: 1, 5, 6 and 7 μm . The first three (1, 5 and 6 μm) cases present a flame stabilized. However, the 7 μm case shows two curves because the flame is not able to stabilize and oscillates between two positions for t_1 and t_2 . Therefore, the area of interest for the DNS is set to 6 μm since we assume that this resolution is sufficient to correctly resolve the flame front.

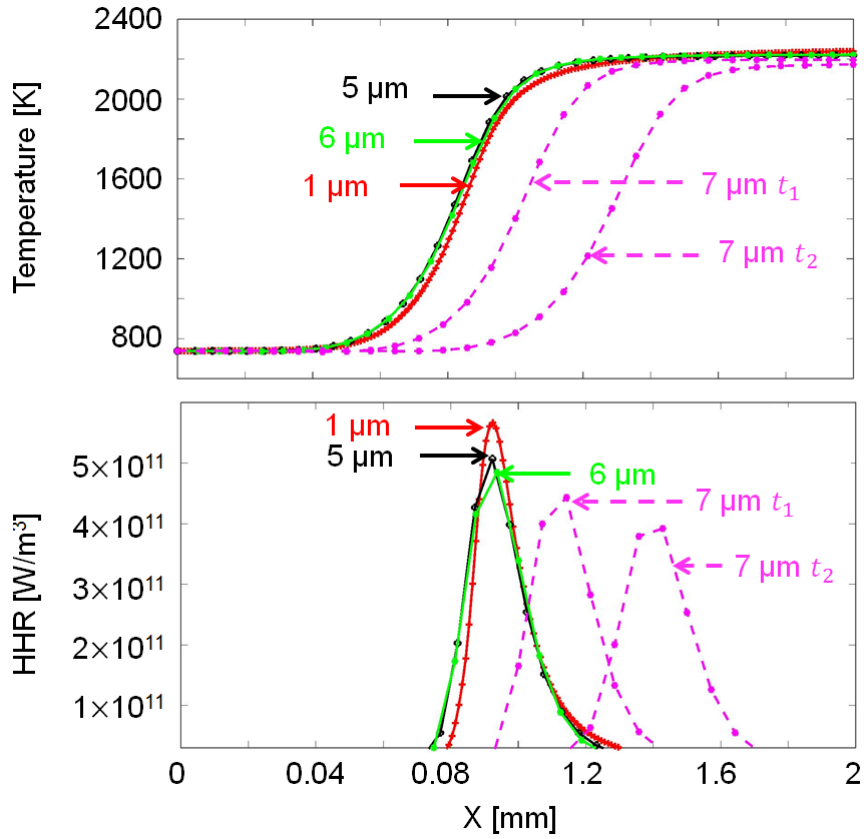


Figure 4.18 – Grid convergence for 1D premixed flames at the stoichiometric mixture fraction. Temperature (top) and heat release rate (bottom) profiles are plotted for a spatial resolution varying between 1 and 7 μm .

Chapter 5

A Lift-Off Length fluctuations model

Experimental correlations such as the one proposed by Siebers et al. [1, 2] or by Venugopal and Abraham [60] aim at predicting the time-averaged LOL when the flame is stabilized (see Eq. 2.6 and Eq. 2.15). They are very useful and are widely used but, since they predict the time-averaged LOL, they do not account for the spatial fluctuations of that value. It has been shown in the previous Chapters that the high-temperature flame can significantly fluctuate around the time-averaged LOL. These spatial fluctuations lead to fluctuations of the local mixing at the lift-off, which may result in significant fluctuations of soot production, since it was shown in Bardi et al. [121] that the latter is highly sensitive to small variations of the LOL. In the previous chapters, a detailed investigation of the mechanisms responsible for the LOL stabilization process lead to the proposal of a conceptual model. The objective of this Chapter is to take advantage of this new knowledge to propose a numerical model that aims at predicting the LOL fluctuations around the time-averaged value.

The motivations for such a LOL fluctuations model are first detailed (Section 5.1) before deriving an expression of the fluctuations of the LOL based on the understanding of the stabilization mechanisms acquired during this work (Section 5.2). Then, a database of LOL fluctuations measurements for various test conditions is presented (Section 5.3). The latter has been acquired in a previous experimental campaign [121]. Finally, in Section 5.4, the theoretical LOL fluctuations model is compared to the experimental LOL fluctuations database in order to analyze the performance of the model.

5.1 Motivation

Experimental results available in the literature [13] show that the soot level evolves linearly with the inverse of the equivalence ratio at the time-averaged LOL, and that it is reduced to zero for an equivalence ratio lower than a threshold. Fig. 5.1 is reproduced from [13] and illustrates this result. It displays the density-normalized peak of the optical thickness (KL) (used as a representation of relative soot level in a fuel jet) as a function of the inverse of the equivalence ratio at the time-averaged LOL ($1/\overline{\Phi_{LOL}}$).

When the flame is stabilized close enough to the injector, the local mixture at the lift-off is fuel-rich (equivalence ratio between 2 and 10) resulting in soot formation. However,

when the flame is stabilized far enough from the injector, in regions where the equivalence ratio is below 2 (above $1/\overline{\Phi}_{LOL} = 0.5$), no soot are produced.

In order to illustrate the interest of predicting the LOL fluctuations, we take here the example of a case where the LOL is stabilized such that the equivalence ratio is 1.82 (i.e. the inverse of the equivalence ratio is 0.55). This latter value is illustrated by a red star in Fig. 5.1. The outcome of this latter figure shows that the soot production is supposed to be negligible in this case. But this is the result of an average representation that does not take into account fluctuations of the LOL. Indeed, experimental and numerical results presented in Chapter 3 and 4 have shown high fluctuations around the averaged LOL, mainly attributed to auto-ignition processes. For convenience, we note ΔLOL the magnitude of the LOL fluctuations around the time-averaged LOL. A double arrow indicating the magnitude of equivalence ratio fluctuations corresponding to ΔLOL and set to an arbitrary value is displayed in Fig. 5.1. It illustrates this fluctuation of the LOL position and their effect on the equivalence ratio at the lift-off. This illustration shows that although soot production is zero in average, the LOL can fluctuate in regions where the equivalence ratio is higher and therefore one can expect that soot are generated as illustrated by the dashed area. This case clearly illustrates the interest of taking into account LOL position fluctuations and therefore of having a model able to predict these fluctuations. Having clearly demonstrated the interest of predicting LOL fluctuations, the objective of the next sections will be to propose and validate such a lift-off length fluctuations model.

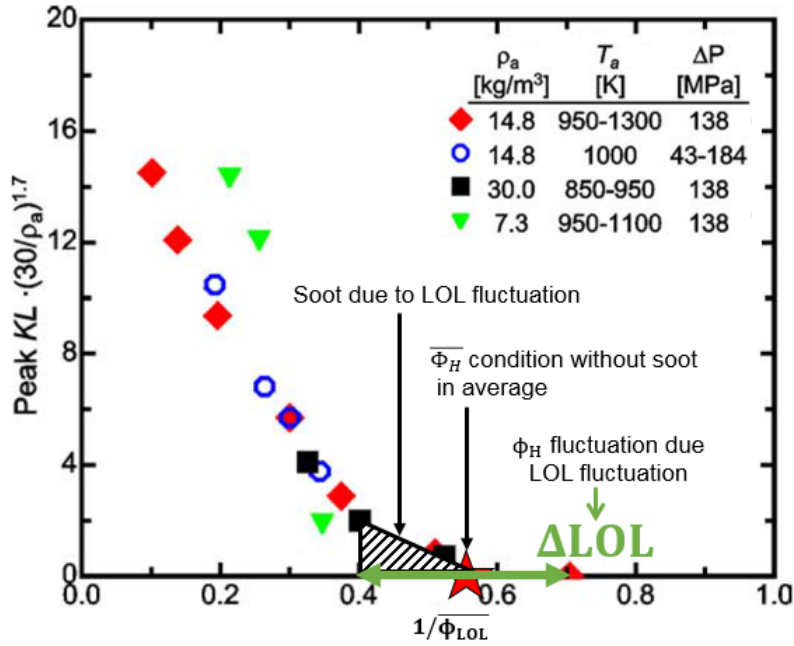


Figure 5.1 – Peak optical thickness (KL) values from the averaged axial profiles of KL measured for each set of conditions considered, versus the inverse of the averaged equivalence ratio at the lift-off. The legend gives the range of experimental conditions considered. Adapted figure from [13]. A red star indicating the case chosen for illustration, the corresponding arbitrary value of equivalence ratio fluctuations related to LOL fluctuations and an area of corresponding soot production are added for illustration to the original figure.

5.2 The lift-off length fluctuations model

Based on the observations made in Chapter 3 and 4, the LOL time evolution can be modeled as a succession of Event A and Evolution B as shown in Fig. 5.2. According to this schematic representation, the magnitude of the LOL fluctuations is attributed to auto-ignition processes and is modeled as the product of the velocity of the Evolution B event times the period between two Event A:

$$\Delta LOL_{Th} \sim S_a \cdot \theta, \quad (5.1)$$

where, S_a is the absolute velocity (relative to a fix reference) of the lift-off and θ is the period between two auto-ignition events as shown in Fig. 5.2.

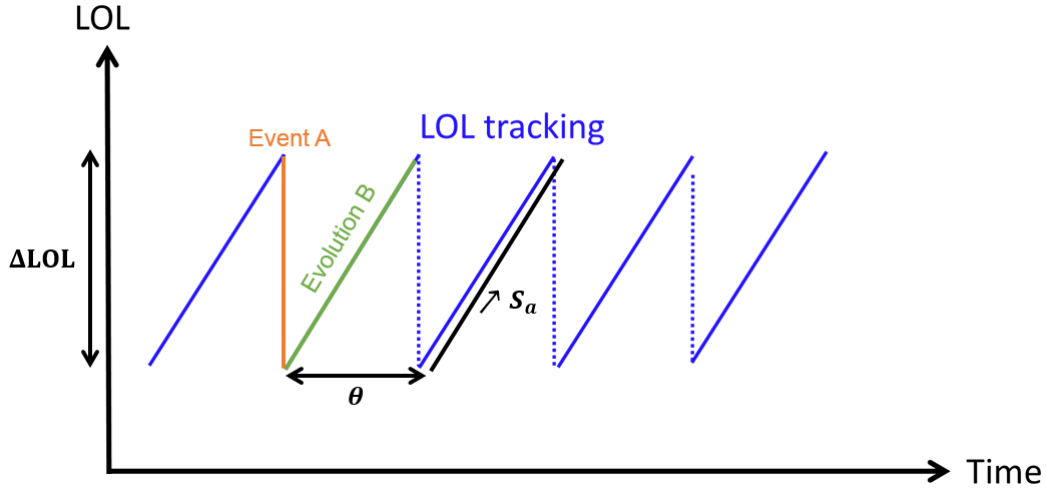


Figure 5.2 – Schematic representation of the Lift-off length as a function of time.

Once this primary expression of the LOL fluctuations is proposed, a modeling of S_a and θ are required. The latter is proposed in the next sections using the knowledge of the lift-off stabilization mechanisms acquired in Chapter 3 and 4.

5.2.1 S_a model

According to the results obtained in Chapter 4, and illustrated by the conceptual model, the flow velocity governs the downstream evolution of the LOL (evolution B). Therefore we assume:

$$S_a \approx u_{LO}, \quad (5.2)$$

where u_{LO} is the flow velocity at the lift-off. In order to derive an expression for u_{LO} , we assume that it varies proportionally to the axial flow velocity in the center of the jet, $U_{X;R=0}$. The latter can be derived using a 1D spray model [55, 93]. Fig. 5.3 displays the result of this model and shows how $U_{X;R=0}$ evolves as a function of the axial position (X) for the α test condition (see Chapter 3 for the definition of α). At $X = 0$, the flow velocity is U_0 , then $U_{X;R=0}$ decays as a function of $1/X$. Thus, assuming that the flow velocity at the lift-off follows the same $1/X$ trend, we obtain: $u_{LO} \sim U_0/LOL$. Furthermore according to the conservation of momentum [55, 93] the flow velocity at the lift-off also depends on the fuel and air density (ρ_f and ρ_a) and the nozzle diameter (d_0). Therefore it leads to the following relationship:

$$u_{LO} \sim \frac{U_0}{LOL} \cdot d_0 \cdot \left(\frac{\rho_f}{\rho_a} \right)^{0.5} \quad (5.3)$$

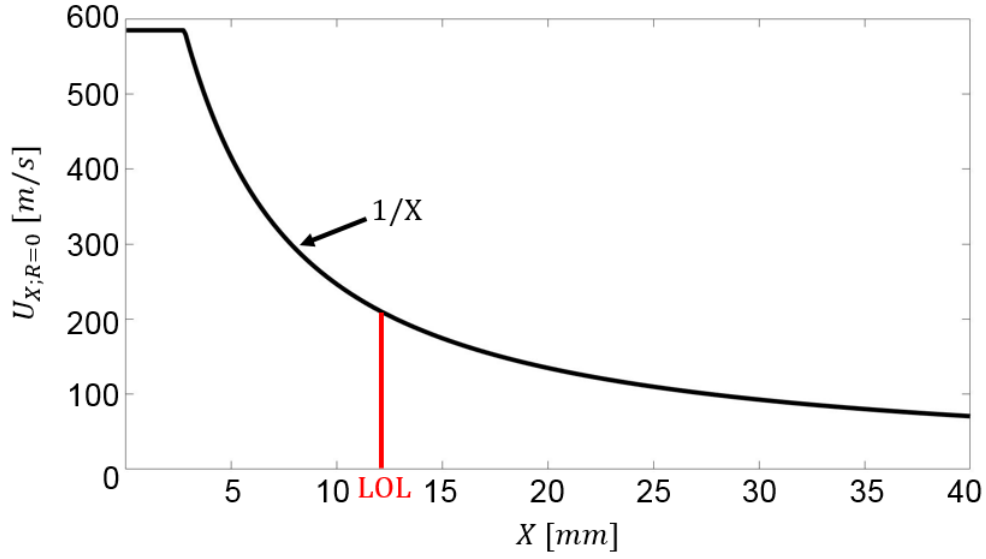


Figure 5.3 – Averaged axial flow velocity in the center of the jet ($U_{X;R=0}$) as a function of the axial position (X) for the α test condition, computed with a 1D spray model [55, 93]. The LOL is also displayed in red to illustrate the assumption that the velocity at the lift off follows the same trend.

Combining Eq. 5.3 with the experimental correlation developed by Siebers et al. [1, 2] for the time-averaged LOL, we obtain:

$$u_{LO} \sim \frac{U_0}{LOL} \cdot d_0 \cdot \left(\frac{\rho_f}{\rho_a}\right)^{0.5} \sim \frac{U_0}{U_0 \cdot T_a^{-3.74} \cdot \rho_a^{-0.85} \cdot d_0^{0.34} \cdot z_{st}^{-1}} \cdot d_0 \cdot \left(\frac{\rho_f}{\rho_a}\right)^{0.5} \sim T_a^{3.74} \cdot \rho_a^{1.35} \cdot d_0^{0.66} \cdot z_{st} \cdot \rho_f^{0.5} \quad (5.4)$$

Finally, combining Eq. 5.4 with Eq. 5.2 yields the following expression for S_a :

$$S_a \sim T_a^{3.74} \cdot \rho_a^{1.35} \cdot d_0^{0.66} \cdot z_{st} \cdot \rho_f^{0.5} \quad (5.5)$$

5.2.2 θ model

The period between two auto-ignition events, θ , is a stochastic event, that in a first step, can be assumed to be proportional to the auto-ignition delay of the spray flame ($\tau_{AI,turb}$). Pickett et al. [15], Malbec et al. [122] and Bardi et al. [123] have proposed an experimental correlation for the latter:

$$\theta \sim \tau_{AI,turb} \sim \exp(A/T_a) \cdot \rho^B \cdot z_{st}^C, \quad (5.6)$$

where, A , B and C , are fitting constants. Different values of these constants are available in the literature, we use here the averaged values derived from references [15, 122, 123]: $A = 6298$, $B = 1.3$ and $C = -1$. Also approximating the exponential term in Eq. 5.6 with a power law it simplifies to:

$$\theta \sim \tau_{AI,turb} \sim T_a^{-7.0} \cdot \rho^{1.3} \cdot z_{st}^{-1} \quad (5.7)$$

The results of Chapter 3 and 4 demonstrate that in addition to isolated auto-ignition, High-Temperature Reservoirs (HTR) have a significant effect on the LOL stabilization process by enabling auto-ignition assisted by burnt gases. This mechanism is not taken into account in Eq. 5.6, therefore a second modeling step is proposed.

Based on the results of Chapter 3 and 4, two parameters are found to have a significant effect on the mechanism of auto-ignition assisted by burnt gases: ambient temperature and injection velocity.

Indeed, the HTR are filled by burnt gases formed after an auto-ignition or a premixed flame. Increasing the ambient temperature leads to increase the temperature of fresh gases locally before an auto-ignition event and in front of a triple flame. This leads to an increase of the temperature of the burnt gases in both cases. As a result, it is likely that increasing the temperature of the HTR facilitates assisted auto-ignition, therefore decreasing the time between two auto-ignition events.

Also, the injection velocity is expected to modify the flow field surrounding the spray and therefore the ability of the HTR to remain at the jet periphery. In particular, we can expect that if the injection velocity is high the probability of the HTR to be blown off is higher. Finally, no corrections are proposed for the density and the mixture fraction terms since no influence of these parameters has been observed in the previous chapters. Based on these observations, the following modifications are proposed to Eq. 5.7:

$$\theta \sim \tau_{AI,turb} \sim T_a^{-7.0+a} \cdot \rho^{1.3} \cdot z_{st}^{-1} \cdot U_0^b, \quad (5.8)$$

where a is a negative coefficient to take into account the fact that increasing T_a facilitates assisted auto-ignition and therefore reduces time between two auto-ignition events, and b is a positive coefficient taking into account the fact that with higher velocity, the probability of the HTR to be blown off is higher hence increasing the time between two auto-ignition events. The value of these coefficients has to be determined based on experimental correlation, this is the purpose on the next sections.

5.2.3 ΔLOL_{Th} model

Combining the modeled expressions of S_a (Eq. 5.5) and θ (Eq. 5.8) with Eq. 5.1, we finally propose the following expression of the LOL fluctuations:

$$\Delta LOL_{Th} \sim T_a^{-3.26+a} \cdot \rho_a^{2.65} \cdot d_0^{0.66} \cdot U_0^b \cdot \rho_f^{0.5} \quad (5.9)$$

The results obtained with this LOL fluctuations model are compared to an experimental database in the next sections for validation purpose and to calibrate the coefficient a and b .

5.3 Lift-off length fluctuations experimental database

In order to calibrate and validate the LOL fluctuations model, an experimental database already available has been used. The latter was performed within the ASMAPE ¹ project at IFPEN. Detailed information on this database are available in [121]. Therefore, only a brief description, relevant in the context of the present work is presented here.

The constant volume pre-burn facility, used for the database, is the same than the one described in Chapter 3. The fuel injector also presents the same characteristics than the one in Chapter 3 even if the injector is different: injector # 306.15 in this section (injector # 306.22 in Chapter 3).

The high-speed OH* chemiluminescence technique is used to track the LOL over time in order to analyze its fluctuations noted ΔLOL_{expe} . Similarly to Chapter 3, a high-speed intensifier (Lambert Instruments - HiCATT) is coupled to a high-speed camera (Photron SA-Z) enabling low-noise high-speed image acquisition. The flame radiation was filtered using a band-pass filter (315 ± 15 nm), and collected using a 100 mm UV lens between 1.5 and 5.5 ms after the start of injection. The details of the high-speed OH* chemiluminescence setup are presented in Table 5.1.

Fig. 5.4 shows the time evolution of LOL_{expe} for conditions similar to spray A [17], but with a lower (800 K) ambient temperature. Similarly to the results described in Chapter 3, the LOL_{expe} time evolution ($LOL_{expe}(t)$) can be decomposed into auto-ignition events (Event A) and downstream evolution (Evolution B). The fluctuations of LOL_{expe} (shown with an orange double arrow) are derived from the standard deviation of the LOL time-tracking, $\sigma(LOL_{expe}(t))$, as illustrated in the figure with the blue double arrow and according to the following equation:

$$\Delta LOL_{expe} \sim \sigma(LOL_{expe}(t)) \quad (5.10)$$

¹Advanced Soot Models for Aeronautic and Piston Engines

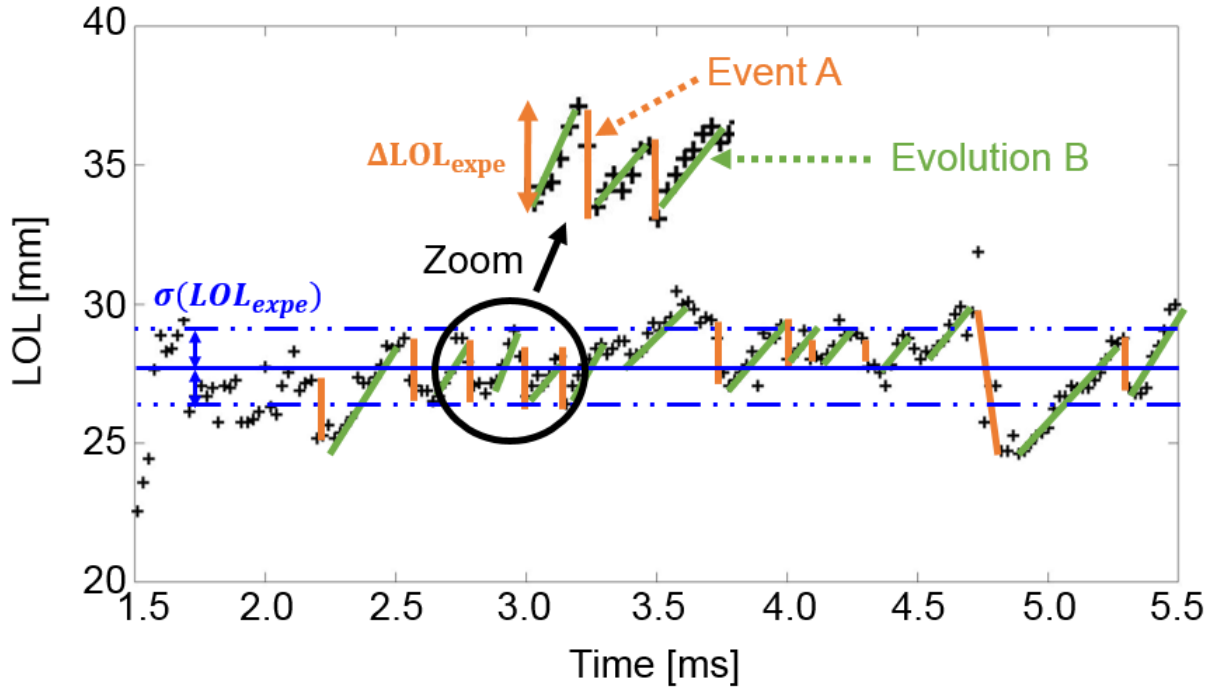


Figure 5.4 – LOL time evolution using OH* chemiluminescence imaging. Test conditions are: $P_{inj} = 150MPa$, $Prct_{O_2} = 15\%$, $T_{amb} = 800K$ and $\rho_{amb} = 22.8kg/m^3$.

Table 5.2 presents the different test conditions available in the database. Variations of ambient temperature, injection pressure and ambient oxygen concentration were carried out and are available to observe the variations of ΔLOL_{expe} when test conditions change. Table 5.3 shows the number of realizations for each parametric variation. For every realization, the LOL time tracking is performed (as shown in Fig. 5.4), resulting in a calculation of $\sigma(LOL_{expe}(t))$ for each realization.

Table 5.1 – High-speed OH* chemiluminescence optical setup.

Camera	Photron SA-Z camera + HS intensifier
Lens	UV 100 mm -f/2.8
Filter	315 ± 15 nm
Shutter time	$5 \mu s$ (gate time)
Frame rate	47.2 kHz

Table 5.2 – Test conditions.

Fuel	<i>n</i> -dodecane					
Fuel temperature at nozzle [K]	363					
Injection duration [ms]	6					
Ambient density [kg/m ³]	22.8					
Ambient temperature [K]	800	815	850	900	950	1000
Injection pressure [MPa]	600 1000 1500					
Ambient gas oxygen (by volume) [%]	13 15 18 21					

Table 5.3 – Number of realizations for the different test conditions performed.

$P_{inj} = 150$ MPa and $Prct_{O_2} = 15$ %						
Ambient temperature [K]	800	815	850	900	950	1000
Number of realizations [-]	27	6	14	51	14	14
$T_{amb} = 900$ K and $Prct_{O_2} = 15$ %						
Injection pressure [MPa]	600		1000		1500	
Number of realizations [-]	14		7		51	
$T_{amb} = 900$ K and $P_{inj} = 150$ MPa						
Ambient gas oxygen (by volume) [%]	13		15	18	21	
Number of realizations [-]	7		51	7	7	

5.4 Calibration and validation of the LOL fluctuation model

In order to calibrate and validate the fluctuations model, its results are compared to the experimental database. Fig. 5.5 presents the results of this comparison, based on the quantities defined below:

- $\langle \sigma(LOL_{expe}(t)) \rangle$ and $\sigma[\sigma(LOL_{expe}(t))]/\sqrt{n}$ are respectively the ensemble average and the measurement uncertainty of $\sigma(LOL_{expe}(t))$ computed for each parametric variation.
- A power law fit of ΔLOL_{expe} is calculated and plotted in order to better compare with ΔLOL_{Th} , and to determine the power coefficient.
- In order to evaluate the effect of the modeling of the HTR, the results using the expression of Eq. 5.9, with a and b coefficient set to 0 (hence without taking into account the HTR effect), are also plotted as ΔLOL_{Th}^* .

The upper left graph of Fig. 5.5 presents a comparison for the ambient temperature variations. When the HTR effect is not taken into account, ΔLOL_{Th}^* reproduces the experimental trend, but with a lower negative power coefficient. With a coefficient a set to -0.80, the evolution of ΔLOL_{Th} and the ΔLOL_{expe} fit match perfectly. This value will therefore be chosen for the final expression of the model.

The upper right graph presents a comparison for the oxygen concentration variations. It shows that ΔLOL_{Th}^* is not affected by oxygen concentration. A different evolution for the ΔLOL_{expe} fit is found. Indeed, the latter is constant for oxygen concentration between 15 and 21 %, but it is higher in the 13 % of oxygen case. Such a behavior is not straightforward to explain and requires more investigation. This is beyond the scope of the present work.

Finally, the lower left graph presents a comparison for the injection pressure variations. ΔLOL_{expe} clearly shows an increase when the injection pressure is increased. When HTR effects are not taken into account, ΔLOL_{Th}^* does not reproduce this trend, therefore showing the necessity to take these effects into account. Adjusting the coefficient b to 0.54 (0.27×2) enables to correctly follow the experimentally observed trend.

The results displayed in Fig. 5.5 demonstrate that the LOL fluctuations model available in Eq. 5.9 well reproduces the variations of the LOL fluctuations observed experimentally, once the a and b coefficients are calibrated. Taking the latter into account, the final expression of the model is:

$$\boxed{\Delta LOL_{Th} \sim T_a^{-4.06} \cdot \rho_a^{2.65} \cdot d^{0.66} \cdot U_0^{0.54} \cdot \rho_f^{0.50}} \quad (5.11)$$

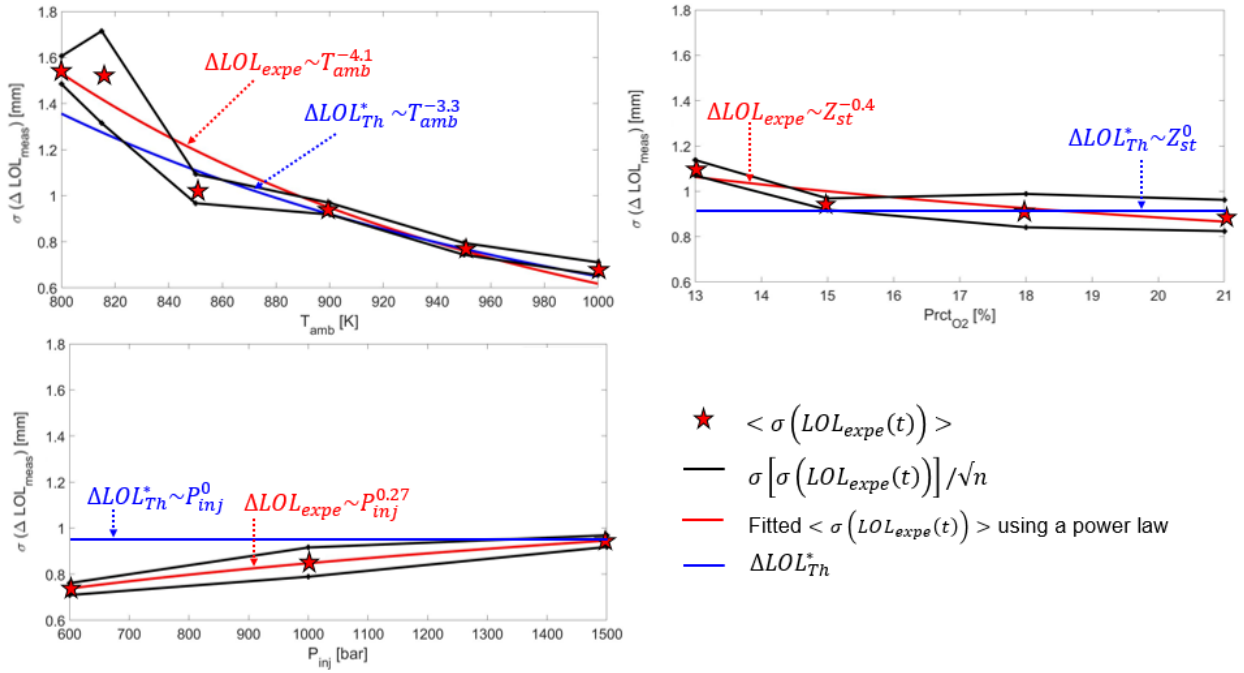


Figure 5.5 – Plot of the experimental and theoretical magnitude of the LOL fluctuations according to ambient temperature (T_{amb}), oxygen concentration ($Prct_{O_2}$) and injection pressure (P_{inj}) variations.

5.5 Conclusion

A model predicting the variations of the LOL fluctuations (ΔLOL) has been proposed and is available in Eq. 5.9. This model was derived from observations made in Chapter 3 and 4, where it was found that the LOL time evolution is characterized by auto-ignition events and downstream evolution. The auto-ignition period and the velocity of the downstream evolution were modeled using experimental correlations available in the literature. Moreover, the role of high-temperature reservoirs on the flame stabilization process, demonstrated in Chapter 4, is taken into account through additional coefficients for ambient temperature and injection velocity.

The resulting model has been compared to an experimental database, where the ambient temperature, oxygen concentration and injection pressure were varied. The trends of the variations of LOL experimentally measured were in good agreement with the model developed in Eq. 5.9. Moreover, the experimental data allowed to calibrate the coefficients proposed for the effect of high temperature reservoirs. The final expression of the model available in Eq. 5.11, based on the conceptual model shown Fig. 4.15, correctly reproduces the experimental measurements.

Chapter 6

Conclusions and perspectives

6.1 Summary of main findings

The overall objective of the present PhD thesis was to contribute to a better understanding of the stabilization mechanisms of a lifted liquid spray flame under diesel engine conditions. This investigation has been conducted because the stabilization process of diesel spray flames has a strong link to the soot production. However, the fundamental nature of the stabilization mechanisms is still a subject of research.

The bibliographic review presented in Chapter 2 has shown two main candidates to explain the flame stabilization under diesel conditions: auto-ignition and premixed flame propagation. The proposed research combined a experimental and numerical approach in order to quantify the role and relative importance of these two stabilization mechanisms, and to identify other phenomena possibly implicated in the spray flame stabilization.

In Chapter 3, the stabilization processes were experimentally studied using long *n*-dodecane injection duration (10 ms) under conditions close to the ECN spray A [17]. High-temperature chemiluminescence and 355 LIF have confirmed the existence of a formaldehyde cloud upstream of the lift-off. Moreover, the formaldehyde cloud was found to be stable in comparison to the high-temperature flame zone which on the contrary exhibits large lift-off length (LOL) fluctuations. The latter are due to the sporadic appearance of auto-ignition spots upstream the stabilized lift-off. The temporal variations of the LOL presented two typical features: very rapid upstream evolution events linked to auto-ignition, and more progressive downstream evolution, both of them occurring within the formaldehyde cloud.

In order to investigate the stabilization mechanisms involved during the downstream evolution stage, a forced ignition at different positions upstream the lift-off using laser-induced plasma was performed. This allowed to emphasize the role of low-temperature reactions on the downstream evolution: when located upstream the formaldehyde cloud, rapid LOL temporal evolutions was observed, whereas inside the formaldehyde cloud a systematic slower progression was observed. This lead to the conclusion that, the stabilization mechanism was governed by an alternation of auto-ignition and downstream evolution, in which the low-temperature reactions play a leading role.

In order to provide a better understanding of the local instantaneous flame stabilization mechanisms, a two-dimensional Direct Numerical Simulation (DNS) of a spatially developing turbulent lifted gaseous flame was presented in Chapter 4. This DNS yielded local conditions similar to those found for the α test conditions experimentally studied in Chapter 3. The DNS only covers a downstream region where the flow can be reduced to a gaseous jet, since experimental observations have shown that the flame stabilized downstream of the liquid spray. The inflow conditions for the DNS were imposed based on experimental studies. The chemistry was modeled using a reduced chemical kinetics scheme comprising 28 species and 198 reactions. This scheme was formulated to account for the low- and high temperature reaction pathways, and its predictions have been validated against experimental auto-ignition delays and laminar flame speeds at conditions relevant to the simulated cases.

The analysis of DNS results showed the same two types of mechanisms controlling the flame stabilization than observed experimentally: auto-ignition events, where the lift-off jumped rapidly to smaller values, followed by downstream evolution of the lift-off. However, the analysis of local values of velocities, gas composition and chemical reaction conditions in the lift-off zone allowed to further detail these mechanisms:

- Auto-ignition events have been subdivided into two types:
 - Isolated auto-ignitions (AI-I) appearing in fresh gasses regions
 - Auto-ignition assisted by burned gases (AI-BG), appearing in regions where combustion products were in contact with fuel and fresh gasses. This proves that high-temperature reservoirs, as hypothesized in [14], play a leading role in the stabilization of the lift-off.
- Downstream evolutions have also been divided into two types, depending on the nature of the reaction zone at lift-off:
 - Triple flames (TF), presenting the same characteristics than the TF observed for non-autoignitive flame (Section 2.2.1.2).
 - Lean/Rich reaction zones (L/R RZ) was the name given to the reaction zones which were not triple flames during continuous evolutions of the LOL. These zones have been identified just after a jump of the LOL attributed to an AI-I.

An analysis of the local velocities at the lift-off showed that downstream evolution was mainly governed by the flow velocity. The flame propagation speed had only a minor contribution. Therefore, auto-ignition was the key mechanism allowing to stabilize the flame, that would otherwise be blown away by the flow. These observations were summarized in a conceptual model at the end of Chapter 4.

The fluctuations of LOL have been observed and explained in Chapter 3 and 4. In terms of soot emissions, these fluctuations are of great importance because they mean that a flame can alternatively be non-sooting (when the LOL moves downstream) or sooting (when the LOL moves upstream). Based on the results of Chapter 3 and 4, a scaling-law estimating the amplitude of these fluctuations was proposed in Chapter 5. It accounted

for the isolated and assisted auto-ignitions mechanisms, and for the flow velocity that governs downstream evolution. This scaling law had been validated against an experimental database and the comparison showed that ambient temperature and injection pressure effects were correctly modeled, while oxygen concentration effect still needs a better understanding.

In conclusion, the two main results of this thesis were: a conceptual model for the flame stabilization and a model predicting the fluctuations of the LOL. These results present a significant advance toward a better understanding of the Diesel flame stabilization. However, a lot of work is still needed to fully understand the Diesel flame stabilization, particularly under real engine conditions. Moreover, several assumptions have been made in this thesis and need to be validated.

6.2 Perspectives

Based on the results presented in this thesis, we can distinguish several types of perspectives: those aimed at confirming and reinforcing the results obtained (Section 6.2.1), those aimed at improving understanding of flame stabilization mechanisms (Section 6.2.2) and finally those proposing ideas for the elaboration of a technical solution to reduce the soot emissions (Section 6.2.3).

6.2.1 Validation of the assumptions and models

Performing a DNS under Diesel conditions, several simplifying assumptions have been proposed (see Section 4.2.1):

- The DNS were run on a 2D mesh, where real turbulence cannot be simulated.
- A pure gaseous mixture was injected where the inlet boundary condition was axially shifted by 20 mm from the injector without taking into account the chemical reactions between 0 and 20 mm.
- The chemical reactions were modeled with a reduced chemical mechanism (28 species transported).

Consequently, differences between the experiments and the DNS were observed, such as the lack of formaldehyde in the center jet in the DNS. Therefore, new numerical studies are needed to confirm the main results presented in Chapter 4. These studies could be LES simulating the full spray, 2D-DNS of a Diesel-type flame with a more accurate chemical mechanism or even 3D-DNS of a Diesel-type flame with a reduced Reynolds number (performing a 3D-DNS of the full spray is not practicable). It would be interesting to observe if these different types of simulations (each with different assumptions) can confirm our conceptual model of flame stabilization.

The developed conceptual model showed that the high-temperature reservoirs (HTR), located at the jet periphery, played a leading role in the flame stabilization by triggering auto-ignition assisted by burnt gases (AI-BG). However, to the best of our knowledge,

no experimental study has shown interactions between HTR and auto-ignition. Pickett et al. [14] have proposed to combine high-temperature chemiluminescence and schlieren imaging to observe the HTR. Therefore, we propose to use high-speed high-temperature chemiluminescence and schlieren imaging (available data in this thesis) to observe the HTR over time, and observe if these HTR can be associated to auto-ignition events.

Furthermore, in the conceptual model, the lift-off evolution was governed by the flow velocity between two auto-ignition events. This observation could be experimentally verified by performing high-speed PIV measurements in addition to high-speed OH LIF in the same plane. It would allow to compare the flow velocity and the absolute velocity of the high-temperature flame resulting from its spatial fluctuations.

In Chapter 3, the flame stabilization mechanisms were studied by performing a laser ignition between the injector and the high-temperature flame. This methodology allowed us to highlight the leading role of the cool-flame on the flame stabilization. However, when tracking the LOL just after laser ignition some questions remain open:

- The LOL remained fixed for a certain period of time just after laser ignition. The physical phenomena involved in such case are not clearly identified. It could be a balance between the flow velocity and the propagation speed of the ignited kernel in regions where the flow velocity is very low (at the jet periphery), or the flow could be affected by the laser plasma. In order to clarify this point, time-resolved tomographic OH LIF (as performed in [124]) could be envisaged to study the spatial and temporal evolution of the ignited kernel.
- The LOL time-evolution was different when the lift-off propagates upstream or within the formaldehyde cloud. This change of evolution could be explained by auto-ignition events (a priori not possible outside the formaldehyde) occurring at the jet periphery as suggested in the DNS results. This point could be clarified by performing simultaneous and time-resolved tracking of the cool- and high-temperature flame, but with some improvements compared to the measurements performed in this thesis. First, increase the 355 LIF signal used to track the cool-flame. Indeed, the high-speed 355 LIF (5 mJ at 6 kHz), in this thesis, presented a lack of signal upstream of the cool-flame compared to high-energy 355 LIF (100 mJ at 10 Hz). Second, increase the time resolution of the 355 LIF in order to gain a better visualization of the kernel when it enters in the formaldehyde cloud. Third, perform high-speed OH LIF in the same plane as the 355 LIF. It will allow to track the ignited kernel in the same plane unlike the OH* chemiluminescence technique.

The change of the absolute speed of the lift-off when it enters in the formaldehyde could also be investigated by numerical simulations. The main advantage of this approach is the access to local values. However, it requires a simulation which reproduces the flow, mixing and the chemistry (low- and high-temperature chemical reactions) upstream of the formaldehyde cloud, which was not the case of the DNS in this thesis.

In Chapter 5 we proposed a model estimating the amplitude of the LOL fluctuations. This model was tuned, and then validated, based on a limited range of experimental test

conditions. Therefore, more test conditions variations (e. g. ambient density variations), are needed to confirm the model in a wider range of operating conditions. Moreover, the model has shown some discrepancies with the experiments for oxygen concentration variations, thus more measurements need to be performed to observe if this tendency is confirmed.

6.2.2 Lines of research to improve understating of flame stabilization mechanisms

This work has shown that auto-ignition (mainly) and partially premixed flames (secondly) played a role in the flame stabilization processes, for the test conditions studied. However, it is likely that the relative importance of auto-ignition and partially premixed flames, on the flame stabilization, changes depending on the operating test conditions. Therefore, we suggest to build a regime diagram for diffusion flame stabilization allowing to identify the main stabilization mechanisms according to the operating conditions. As a first step, we decided to focus on the Diesel-type flames. To build such a diagram, we propose to perform many DNS varying the operating conditions, such as the ambient temperature or the injection pressure. Then, we suggest to use the same post-processing methodology than developed in Chapter 4 to investigate the stabilization mechanisms for each simulation:

- A LOL time-tracking with the identification of four reaction zone topologies in order to observe the distribution of the different topologies according to test conditions variations.
- A velocity analysis at the lift-off between the flow velocity and the displacement speed of the lift-off in order to observe the importance of the premixed flames propagation on the flame stabilization.

However, performing many DNS, even 2D-DNS, is very expensive in term of CPU cost (1.4 million CPU.hrs for one simulation with a mesh resolution of $6\mu\text{m}$). Thus, we propose to run "coarse DNS" with a decreased mesh resolution to reduce the CPU cost. Nevertheless, the "coarse DNS" need to be validated against reference DNS following the methodology proposed in Appendix D whenever the ambient temperature changes (because the flame thickness changes).

Appendix B presents a qualitative regime diagram for the flame stabilization mechanisms based on the different observations made using optical diagnostics and numerical simulations. This graph is a first step toward a quantitative graph and needs to be completed by many DNS especially in the Autoignitive Conditions Diffusion Flames (ACDF) region.

Focusing of the ACDF region, we propose to use the LOL fluctuations model in combination with the models predicting the time-averaged LOL in order to find optimal parameters (e.g. ambient temperature or injection pressure) leading to a non-sooting flame. Since the soot production is linked to the equivalence ratio at the lift-off, the average position and the fluctuations of the lift-off first need to be expressed in term of equivalence ratio. Then, the objective is to find operating test conditions, which allows to

reduce the equivalence ratio at the lift-off in average, and also minimizes the fluctuations of the lift-off in fuel-rich regions.

Finally, the Diesel-type flames investigated in this thesis are isolated sprays in constant volume cells, which avoids wall/flame interactions. Whereas, a Diesel engine environment is wall bounded and characterized by jet-jet interactions in the context of a swirling flow [119, 120]. Therefore, the influence of these differences on the flame stabilization needs to be explored in future experimental and simulation works.

6.2.3 Towards a technical solution to reduce the soot emissions

The DNS results showed that 69 % of the auto-ignition were assisted by burnt gases. Therefore, it is clear that the high-temperature reservoirs (HTR) help the flame to stabilize in fuel-rich regions, leading to a high level of soot produced.

In order to reduce the soot emissions, we propose to impose a co-flow of air. It would lead to blow out the HTR and consequently stabilize the flame further downstream in more homogeneous and leaner regions.

Appendix C presents a DNS in which a co-flow of air is imposed at 8 m/s. Comparing the α test conditions with and without high co-flow, it appears that the lift-off, in the high co-flow case, is convected faster and fluctuates further downstream.

Based on this observation, blowing a co-flow of air at the jet periphery seems to be a promising approach to reduce the soot production. Therefore, future works could be envisaged in this direction by working on a technical solution to reduce the soot emissions by blowing the HTR.

Appendix A

Criteria to distinguish combustion regimes

The need to distinguish combustion regimes such as premixed and diffusion flame is not a recent research endeavor topic. Yamashita et al. [125] have defined the flame index (also known as the Takeno index), based on the fuel and oxidizer mass fraction profile variations, as written in Eq. (A.1):

$$FI = \nabla Y_F \cdot \nabla Y_O, \quad (\text{A.1})$$

where Y_F and Y_O are the fuel and oxidizer mass fractions. If the flame index is superior to zero, the authors concluded to premixed flame regime because fuel and oxidizer are coming from the same way and are both decreasing during the combustion. If this index is inferior to zero the authors proposed a diffusion regime. This criterion is one of the first indexes allowing to catch premixed regime. However, this index is not appropriated when considering complex chemistry where the fuel is decomposed into many species which react together. Moreover, it does not allow to distinguish auto-ignition and flame propagation.

Numerical simulations are able to provide turbulent local values which make possible to define a criterion to distinguish flame propagation and auto-ignition. Two main approaches are proposed to distinguish auto-ignition and flame propagation in this section: transport budget analysis and reaction rate analysis of key species.

A.1 Transport budget analysis

Examining the contribution of transport and reaction in species continuity equations (Eq. (A.2)) provides a measure of the relative importance of auto-ignition versus premixed flame propagation. This analysis is performed by evaluating and comparing the terms in the transport equation for species k :

$$\frac{\partial \rho Y_k}{\partial t} + \frac{\partial(\rho u_i Y_k)}{\partial x_i} = \frac{\partial}{\partial x_i}(\rho D_k \frac{\partial}{\partial x_i}(Y_k)) + \dot{\omega}_k, \quad (\text{A.2})$$

where

- ρ is the density and Y_k is the specie mass fraction of k

- the term $\frac{\partial(\rho u_i Y_k)}{\partial x_i}$ describes the convection of k where, $x_{i=1,2,3}$ is the three dimensions and u_i is the three dimensional velocity field
- the term $\frac{\partial}{\partial x_i}(\rho D_k \frac{\partial}{\partial x_i}(Y_k))$ describes the diffusion contribution of k , where D_k is the specie molecular diffusion coefficient
- $\dot{\omega}_k$ is the reaction rate of k

In this approach, the budget contribution of diffusion and chemistry is in the same order of magnitude for premixed flame propagation while auto-ignition is identified by a high chemical activity and a negligible molecular transport [126–128].

Many studies have performed transport budget analysis of OH specie [64, 67, 75, 129]. Fig. A.1 (from Krisman et al. [64]) shows an example of transport budget analysis for Y_{OH} , as well the scalar dissipation rate χ . The evaluations are performed along lines normal to the reaction front. Lines marked from **A** to **F** are fully described in the paper [64], only a brief description of the key observations is proposed here. The authors identified an auto-ignition event labeled **A** and premixed flame at **B**, **E** and **F**. Plot showing the contribution of the reaction and the diffusion term on line **A** (Fig. A.1) clearly shows that the diffusion term is much smaller than the reaction term and also the χ is very low, as expected for auto-ignition. Event **B** shows an expending flame front following the formation of an auto-ignited kernel. The same structure is found in event **E** which is evaluated through the rich premixed branch of the nearby edge-flame identified as event **F**. In these three cases, a balance between the reaction and the diffusion term is observed. Moreover, significant peaks in χ are shown which is consistent with the premixed flame regime.

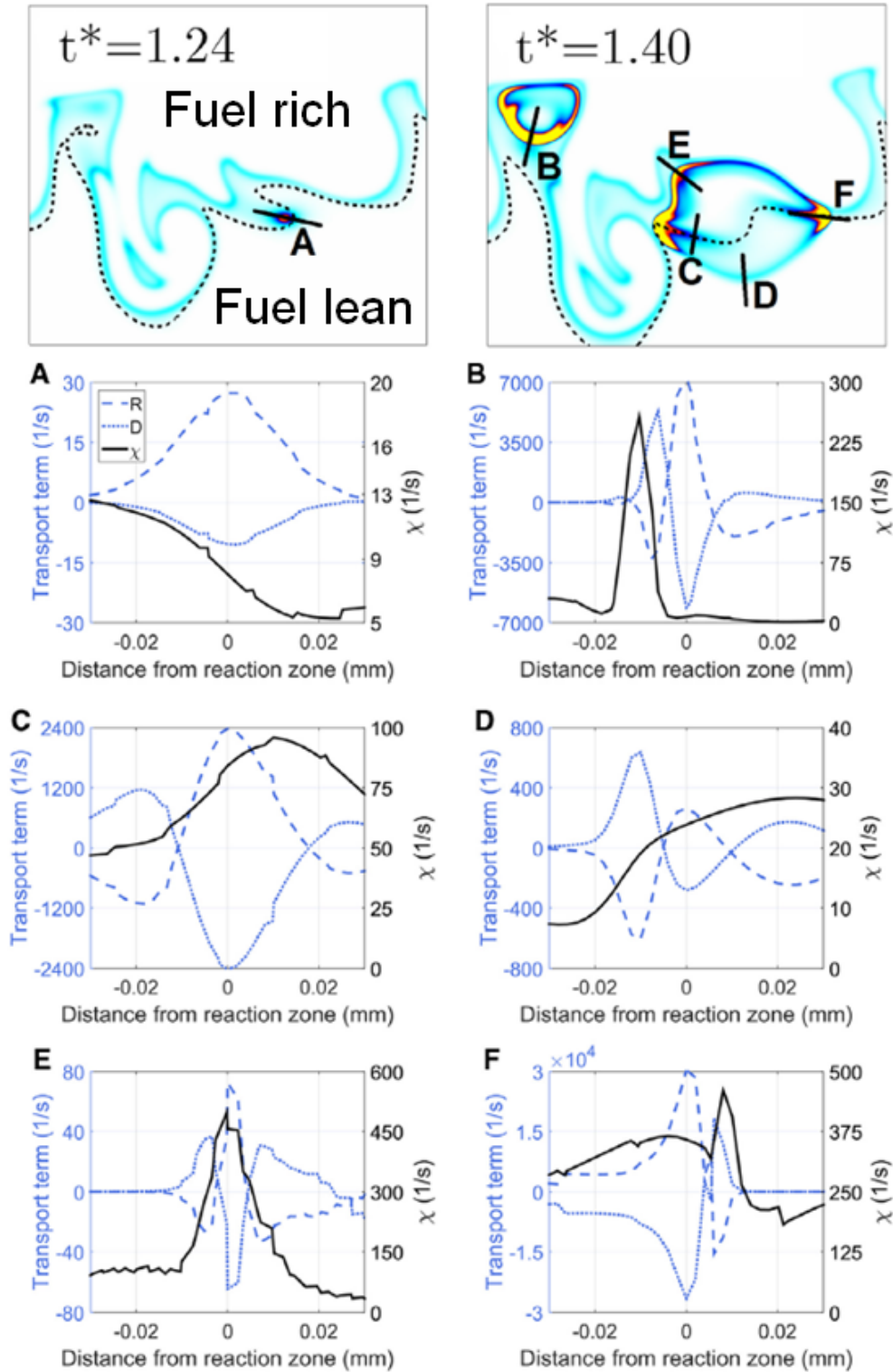


Figure A.1 – The two top images show heat release rate fields for two different instants ($t^* = t/\tau_{MR}$ defined in Section 2.3.4) where the dashed black lines are z_{st} . The plot labeled from A to F represents the evaluation of the diffusion term (D), reaction term (R) and χ along lines indicated on the top figures. Figure adapted from [64].

Using the same approach, Gong et al. [80] compared the reaction and the diffusion term of CO_2 specie. The authors propose to study the ratio of the diffusion term to the reaction rate at the flame front. If this ratio is under a critical value, auto-ignition is proposed as the stabilization mechanism otherwise it is flame propagation. Fig. A.2 shows an application of this index after a forced laser ignition. Between 4 and 7 ms (during the downstream evolution after forced ignition) they concluded as flame propagation stabilization. After 7 ms, when LOL stop increasing, the ratio fluctuates around 0.1 leading to stabilization in an auto-ignition mode.

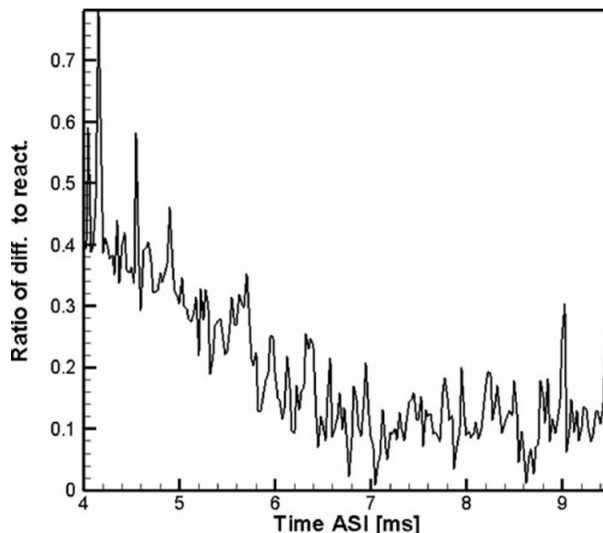


Figure A.2 – Ratio of the diffusion term to the reaction rate of CO_2 after a forced laser ignition [80].

Transport budget analysis has also been conducted for low-temperature reaction front using OCH_2OCHO as marker for LTC with DME [64, 75] and $OC_{12}H_{23}OOH$ for n -dodecane [18]. At least four studies [18, 62, 64, 75] confirm the propagation of a cool-flame. According to Krisman et al. [75], the cool-flame propagates rapidly up the mixture fraction gradient into richer gradient. However, none of these studies have estimated a cool-flame speed due to autoignitive characteristics of the mixture during this stage of combustion. Thus, more work is required on this topic to have a better understanding of the interaction between the cool-flame propagation and the high-temperature flame stabilization.

In addition to the analysis based on selected species profiles, Chemical Explosive Mode Analysis (CEMA) [70, 71] has been proposed to identify the controlling chemistry in complex reacting flows. Briefly, the eigenvalues of the Jacobian matrix of the chemical source term, based on the local species concentrations and temperature, are evaluated and determined as the chemical modes. More details on this diagnostic are available in [70, 71]. Improving the CEMA, Aditya et al. [129] have built a quantitative parameter named α indicating how important the diffusion source term is compared to the chemical source term. According to the authors:

A.2. CHEMICAL CRITERIA TO DISTINGUISH AUTO-IGNITION AND FLAME PROPAGATION

- $\alpha > 1$ is named assisted-ignition by the authors [129] and corresponds to a premixed flame regime which occurs where diffusion significantly promotes reactions
- $-1 < \alpha < 1$ corresponds to auto-ignition when chemistry plays a dominant role
- $\alpha < -1$ corresponds to a local flame extinction occurring when diffusion dominates chemistry and suppresses ignition

Fig. A.3 allows to illustrate α for a reheat gas turbine combustor configuration. First, a snapshot of the temperature field is displayed (Fig. A.3-left) where the α parameter (Fig. A.3-right) shows auto-ignition as the major combustion mode, mainly in the center jet, even if premixed flame and local flame extinction occur near the wall. It would be interesting to apply this very new criterion for lifted-Diesel flame to observe the different combustion modes on the flame stabilization.

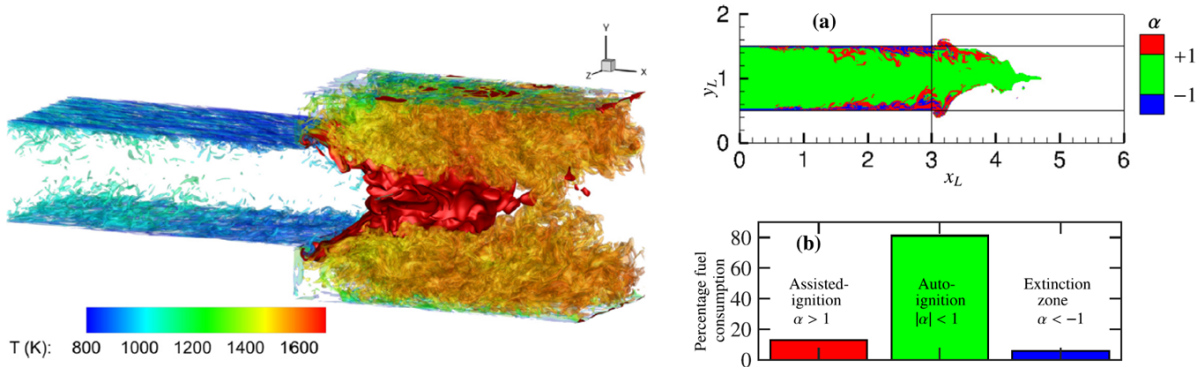


Figure A.3 – Left: ”Illustration of instantaneous flow field represented by iso-surfaces of vorticity magnitude at 300,000 1/s colored by the enclosed temperature scale. The flame shape and location within the combustion chamber is illustrated by the red iso-surface of a representative value of heat release rate.” Right: ”(a) Iso-contours of the instantaneous field of α delineating the combustion modes. (b) Bar chart quantifying the fraction of H_2 fuel consumption (reaction rate) due to each mode.” [129].

A.2 Chemical criteria to distinguish auto-ignition and flame propagation

A second approach consists in defining criteria only based on the chemical reactions. Schulz et al. [101] have defined an auto-ignition index (AI) in a Cabra flame (lifted methane-air jet flame well experimentally described). This index is built on the reaction rate flux analysis proposed by Yoo et al. [130], who identified the dominant role of auto-ignition at the flame base of an hydrogen jet flame by analyzing the chemistry of hydroperoxyl (HO_2) and hydroxyl (OH). Starting from this statement, Schulz et al. [101] have performed 1D simulations with a chemical solver (CANTERA [94]) to define the auto-ignition index based on the consumption of HO_2 through the following reactions:



Fig. A.4 shows the HO_2 reaction rate flux difference for reference cases of a 1D pre-mixed flame stabilized by flame propagation (left) and a 1D flame stabilized by auto-ignition flame front (right). The propagation regime clearly shows a decrease of $R8$ compared to $R6$ and *vice versa* for the auto-ignition regime. Based on this observation, the authors [101] have derived an auto-ignition index:

$$AI = \left| \frac{R8_{HO_2}}{R8_{HO_2} + R6_{HO_2}} \right| \quad (A.3)$$

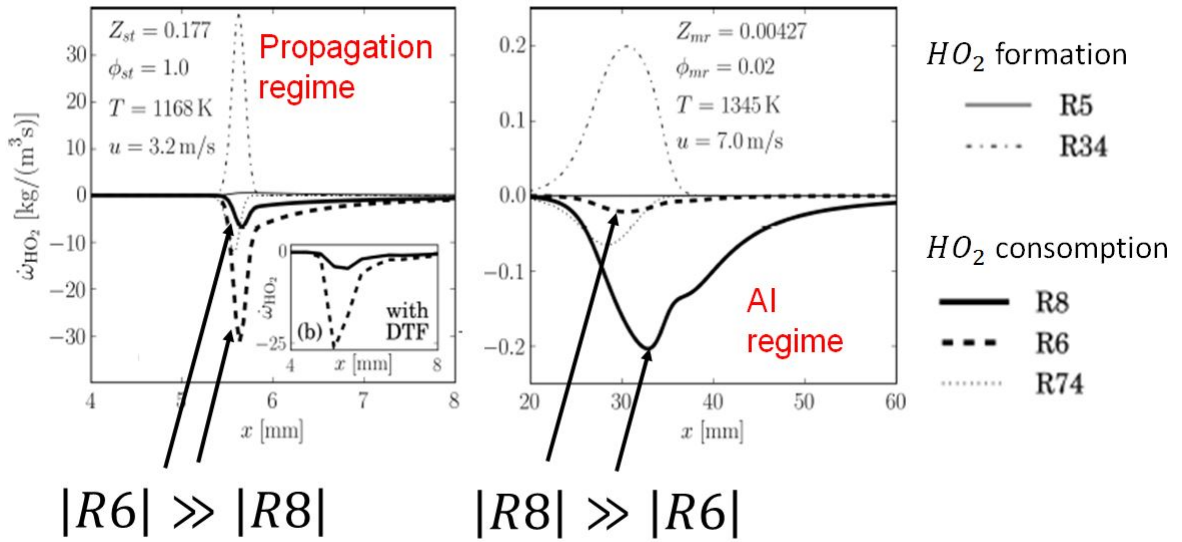


Figure A.4 – The propagation regime is given for a premixed propagation flame at the stoichiometry z_{st} (left plot) and auto-ignition flame is at the most reactive mixture fraction z_{mr} (right plot) [101].

Thanks to the flame and auto-ignition index (FI and AI), Schulz et al. [101] are able to distinguish two areas: cut A (Fig. A.5) and cut B (Fig. A.5). For A, premixed flame is the main stabilization mechanism while for B this is auto-ignition. Fig. A.5 also shows z_{mr} and z_{st} iso-line in the two last columns ((e) and (f)). On the one hand, high value (near 1) of auto-ignition index matches with the most reactive isolines. On the other hand, high positive value (near 1) of the flame index corresponds with the stoichiometric isolines. This study confirms that even in lifted atmospheric methane-air jet flame, auto-ignition can still play a role in the upstream stabilization process.

However, it seems doubtful that the auto-ignition index can be used for Diesel combustion because of different species and reactions for Diesel-type fuel. Nevertheless, the 1D chemistry methodology proposed by the authors is a relevant technique which can be tested under Diesel conditions.

A.2. CHEMICAL CRITERIA TO DISTINGUISH AUTO-IGNITION AND FLAME PROPAGATION

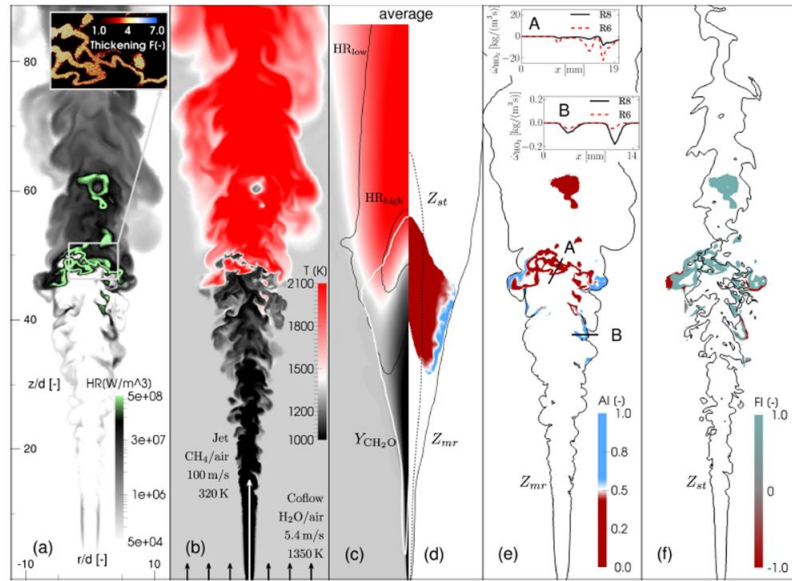


Figure A.5 – Snapshots of (a) heat release rate, (b) temperature, (c) mean temperature field, (d) mean *AI* (Auto-Ignition) index field, (e) instantaneous *AI* index field + most reactive mixture fraction (z_{mr}) iso-lines, and (f) instantaneous *FI* (Flame Index) field + stoichiometric mixture fraction (z_{st}) iso-lines. Insets A and B show the local contribution of *R8* and *R6* to HO_2 consumption [101].

Appendix B

Regime diagram for the flame stabilization mechanisms

Based on different observations made using optical diagnostics and numerical simulations, Fig. B.1 proposes a qualitative regime diagram for the flame stabilization. This diagram can be used for all type of diffusion flames, since the inputs of the diagram are: the auto-ignition delay of the most reactive mixture ($\tau_{AI,mr}$) and the flow velocity on the stoichiometric line at the flame base (U_{st}). The diagram comprises 5 different regions, which are delimited by the average flow velocity at the lift-off ($\overline{u_{LO}}$), the displacement speed of the flame (S_d) and a quantity C (defined in Eq. B.1).

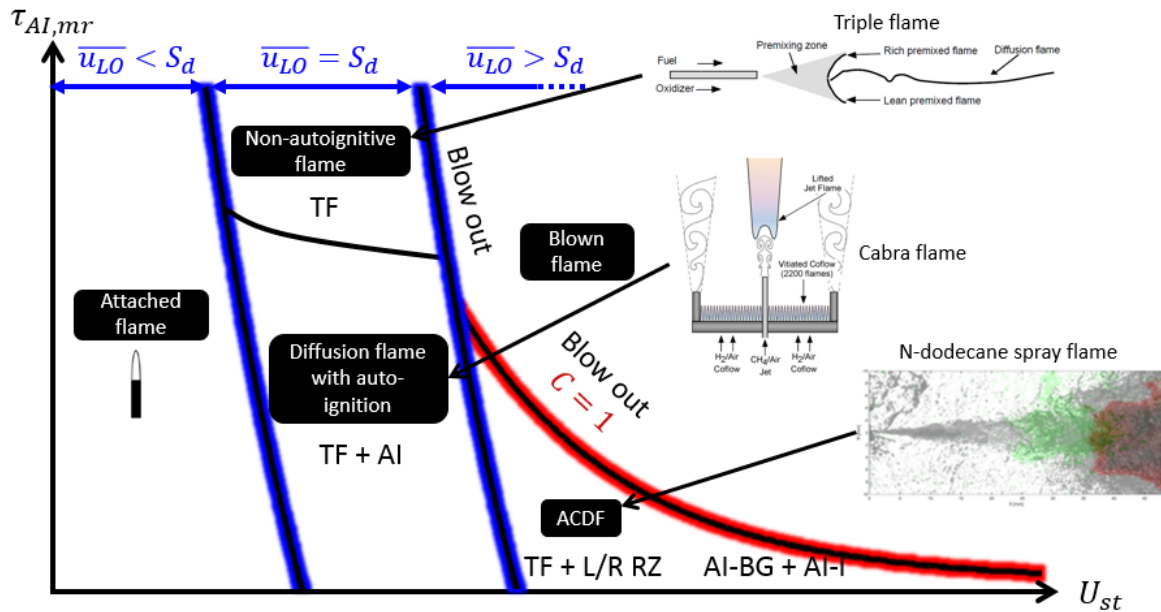


Figure B.1 – Qualitative regime diagram for the flame stabilization as the most reactive mixture fraction ($\tau_{AI,mr}$) and the axial flow velocity on the stoichiometric line (U_{st}) vary. The triple flame image is extracted from [25], the Cabra flame from [131], the burner flame stabilized from [68], while the n-dodecane spray flame image is obtained with the experimental setup presented in Section 3.2.2.

-
- **Attached flame** ($\overline{u_{LO}} < S_d$): As reported in many works [25, 50, 69], when $\overline{u_{LO}}$ is lower than S_d , the flame is anchored to the burner.
 - **Non-autoignitive flame** ($\overline{u_{LO}} = S_d$ and high $\tau_{AI,mr}$): Increasing U_{st} , while keeping a high $\tau_{AI,mr}$ leads to stabilize a lifted diffusion flame with a partially premixed and not auto-ignited mixture upstream of the flame base. In this configuration, triple flames have become widely accepted to explain the flame stabilization as detailed in Section 2.2.
 - **Diffusion flame with auto-ignition** ($\overline{u_{LO}} = S_d$ and low $\tau_{AI,mr}$): This region corresponds to test conditions where $\tau_{AI,mr}$ is low enough to auto-ignite the mixture. The flames are stabilized by triple flames in regions where the flow velocity is low. However, auto-ignition also appears as a driving mechanism for the flame stabilization in the high velocity flow regions as reported by Schulz et al. [101] for the methane-air Cabra jet flame [131]. In the present diagram, this transition zone is illustrated by the Cabra flame (see illustration on the right of the figure). In this configuration, $\tau_{AI,mr}$ is reduced by a hot vitiated co-flow.
 - **ACDF** ($\overline{u_{LO}} > S_d$ and $C < 1$): Keeping a low $\tau_{AI,mr}$ and increasing U_{st} leads to enter in the ACDF region as illustrated with the n-dodecane spray flame at the right of the diagram. In the ACDF region, the flame stabilization is decomposed into auto-ignition (isolated auto-ignition (AI-I) and auto-ignition assisted by burnt gases (AI-BG)) and downstream evolution of the lift-off (triple flames (TF) and lean/rich reaction zones (L/R RZ)). In average, the flow velocity at the lift-off is higher than the displacement speed of the partially premixed flame. Thus, contrary to the other regions in the diagram, the main stabilization mechanism is auto-ignition. As a result, for ACDF, the blow out limit is no longer a speed equilibrium between u_{LO} and U_{st} .

For these ACDF, we propose to estimate the blow out limit through the following parameter, based on auto-ignition:

$$C = \frac{\tau_{AI,mr}\overline{u_{LO}}}{L - LL}, \quad (\text{B.1})$$

where $\tau_{AI,mr}$ has been estimated using Eq. 5.6, L corresponds to the distance between the fuel injector and the opposite wall of the combustion chamber, LL is the liquid length, which can be estimated through the expression provided in [122]. In Eq. B.1 we assume that the auto-igniting mixture is convected at a constant speed $\overline{u_{LO}}$ along the stoichiometric line and can stabilize the flame by auto-ignition before reaching the limit of the combustion chamber. The assumption of $\overline{u_{LO}}$ constant is only realistic far enough from the injector. Therefore, C is computed in the vapor phase. For that reason, LL is subtracted from L in Eq. B.1.

Taking the example of the reference cases (α) studied in Chapter 3 and 4, we can estimate C for the α operating conditions. The auto-ignition delay of the spray flame is 1.1 ms. The axial flow velocity at the lift-off (at 35 mm from the injector) is 26 m/s according to the 1D spray model [55, 93]. The distance between the

injector and the opposite wall is 125 mm and the liquid length is 18 mm. Therefore, C is equal to 0.3, which is inferior to 1 as expected, since the flame is stabilized.

- **Blown flame ($\overline{u_{LO}} > S_d$ and $C > 1$):** Under non-autoignitive conditions the flame is blown out when $u_{LO} > S_d$. However, we assume that the ACDF is blown out if C is higher than 1. In such case, the mixture is convected too fast or is not reactive enough and thus, cannot stabilize the flame by auto-ignition within the combustion chamber.

Appendix C

Impact of a high co-flow on the flame stabilization

In order to have a better understanding of the importance of the high-temperature burnt gases reservoirs on the flame stabilization, we propose to artificially considerably decrease these reservoirs by imposing a high co-flow of air for the α test conditions. Thus, a new simulation named α_{coflow} has been run from 0 to 12 ms after the start of injection imposing a co-flow of 8 m/s. Note that the only difference between α and α_{coflow} is the co-flow at the inlet boundary condition, the maximum axial flow velocity ($U_{X,max}$) and U_{RMS} are the same.

However, because of the very high computational cost of performing DNS with a very fine spatial mesh resolution, the α and α_{coflow} cases have been simulated on a coarse mesh (highest spatial resolution set to 20 μm instead of 6 μm in Chapter 4). The simulations with a poor resolution are referred as "coarse DNS" and have been compared to the reference DNS and experimental data in Appendix D. Since the "coarse DNS" shows good agreement with reference DNS, all the results presented below come from the "coarse DNS".

Fig. C.1 shows a comparison of instantaneous temperature fields between cases α and α_{coflow} . It clearly appears that the high-temperature reservoirs are considerably reduced with a high co-flow. Consequently, the number of auto-ignition assisted by burnt gases (AI-BG) is reduced by 39 % in case α_{coflow} compared to α .

Fig. C.2 shows the LOL time-tracking for α and α_{coflow} with the four different reaction zone topologies. It appears that when the AI-BG are reduced, the lift-off is convected faster and fluctuates further downstream. In case α_{coflow} 39 % of the instantaneous lift-off are located outside the area of interest. This result demonstrates that the high-temperature reservoirs, triggering AI-BG, considerably help the flame to stabilize.

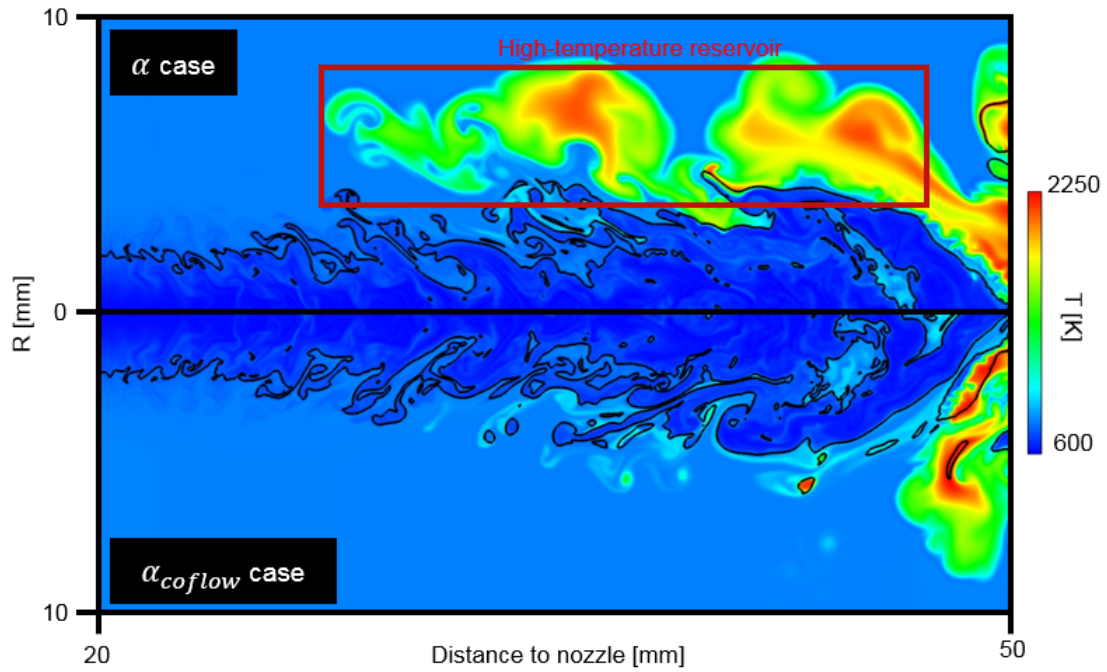


Figure C.1 – Instantaneous temperature fields for case α and α_{coflow} , both of these images are displayed at 3.26 ms ASI for $R > 0$. The black line represents the stoichiometric line. (The bottom image has been rotated to provide a symmetrical comparison with the top image).

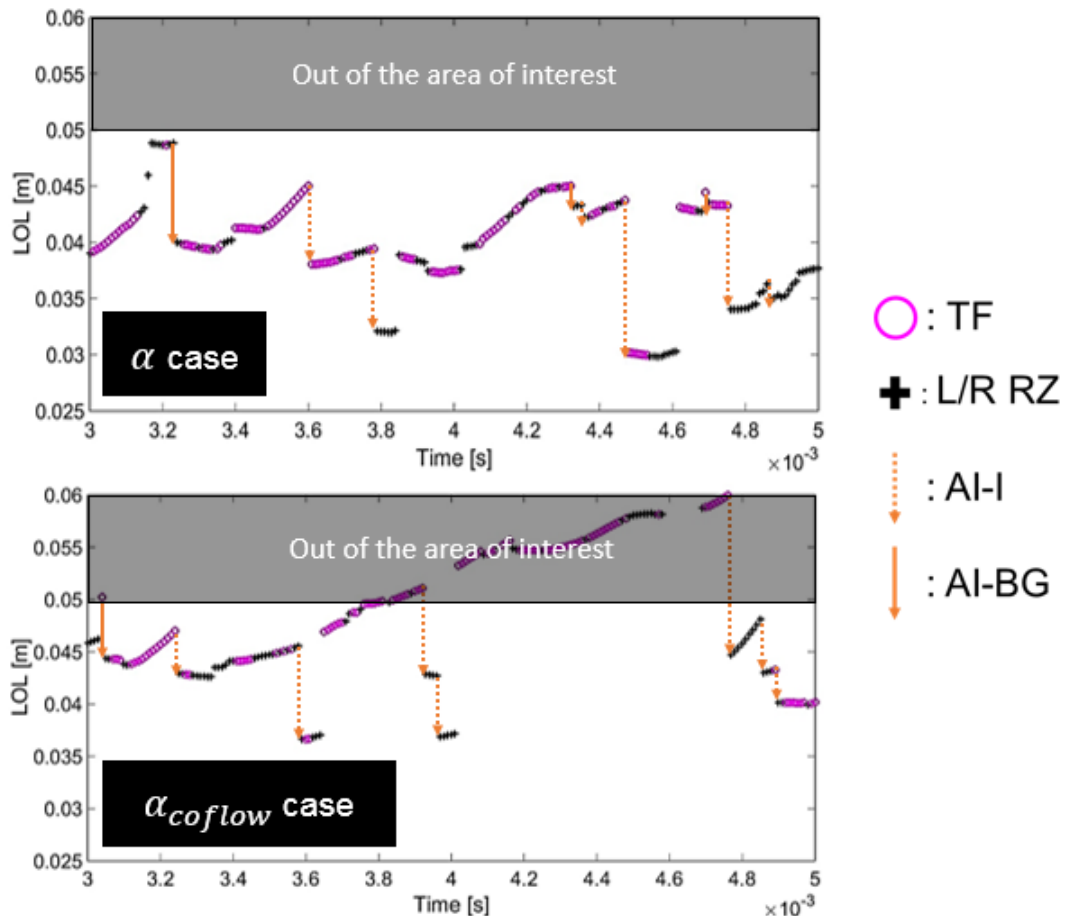


Figure C.2 – LOL time-tracking for cases α and α_{coflow} and for $R > 0$.

Appendix D

Setup of a "coarse DNS"

Performing multiple DNS, with a mesh resolution of $6\ \mu\text{m}$, was not possible because of the very high computational cost (120,000 CPU hours per simulated physical millisecond). Consequently, we chose to perform simulations named "coarse DNS" with a highest spatial resolution of $20\ \mu\text{m}$ in the area of interest (see Fig. 4.1 in Chapter 4). It leads to decrease the computational cost by approx. a factor 40.

The methodology to validate the "coarse DNS" consists in performing the same test conditions that studied in the experiments and the $6\ \mu\text{m}$ DNS: α test conditions. The "coarse DNS" has been run using the same numerical setup (excepted the mesh) and physical parameters than the $6\ \mu\text{m}$ DNS: same inlet profiles, initialization and simulated physical time. The only difference between the coarse and the $6\ \mu\text{m}$ DNS is an iso-factor applied on the cells of the mesh leading to reduce their size by a factor 0.3.

Following the same methodology than developed in Section 4.8.2, first a non-reactive simulation is performed to ensure that the mixing is well reproduced in the "coarse DNS". Therefore, time-averaged (between 2 and 10 ms) radial profiles of velocity, temperature and fuel mass fraction are obtained by post-processing instantaneous "coarse DNS". Fig. D.1 shows these radial profiles at 30 and 50 mm from the injector, from the coarse and $6\ \mu\text{m}$ DNS, but also profiles given by experimentally established correlations [55, 93]. Regarding the very small gap between the two simulations, it appears that the mesh change has a very weak influence on the time-averaged profiles. Therefore, the conclusions on the "coarse DNS" are the same than for the $6\ \mu\text{m}$ DNS: the imposed boundary conditions yielded satisfactory mean profiles in the area of interest where flame stabilization mechanisms were studied.

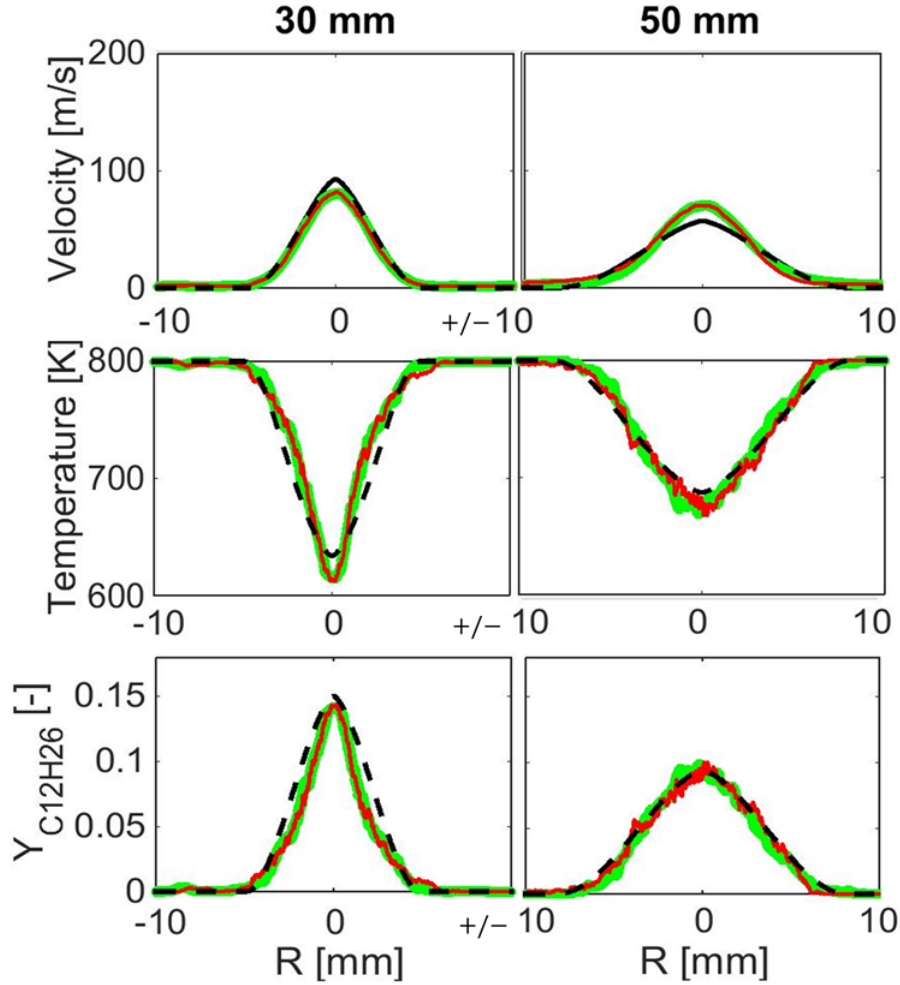


Figure D.1 – Radial profiles comparison between time-averaged non-reactive $6 \mu\text{m}$ DNS (thin red line), "coarse DNS" (thick green line) jet and a 1D spray model [55, 93] (dotted black line) for the α test conditions. Left column shows radial profiles at an axial distance of 30 mm from the injector. Right column shows radial profiles at 50 mm from the injector.

Second, a reactive simulation is run for 0 to 12 ms on the coarse mesh. Fig. D.2 shows averaged profiles of cool- (through CH_2O) and high-temperature (through OH and OH^*) flame, computed from the experimental data, $6 \mu\text{m}$ and coarse DNS. Note that the $6 \mu\text{m}$ DNS and the experimental images have already been described in Fig. 4.7, thus the reader can refer to Fig. 4.7 for more details on the construction of the averaged images.

Fig. D.2 is used to compare the structures of the cool- and high-temperature flame for the "coarse DNS" in comparison to the $6 \mu\text{m}$ DNS and experimental data. As for the $6 \mu\text{m}$ DNS, the "coarse DNS" fields of Y_{CH_2O} and Y_{OH} are time-averaged between 3 and 12 ms. The cool-flame structures between the two simulations are very similar. First, the upstream locations of the stabilized cool-flame, in both simulations, are similar to the experiments. Second, the CH_2O level in the center of the jet are lower in the simulations compared to the experiments. However, this difference is assumed to have a minor impact on the flame stabilization. Comparing the high-temperature flame between the two simulations, it appears that, some small differences exist: the bottom branch

(for $R < 0$) of the high-temperature flame in the "coarse DNS" is stabilized further downstream than the bottom branch of the $6 \mu\text{m}$ DNS. However, the overall structure of the high-temperature flame is fairly similar between the two simulations.

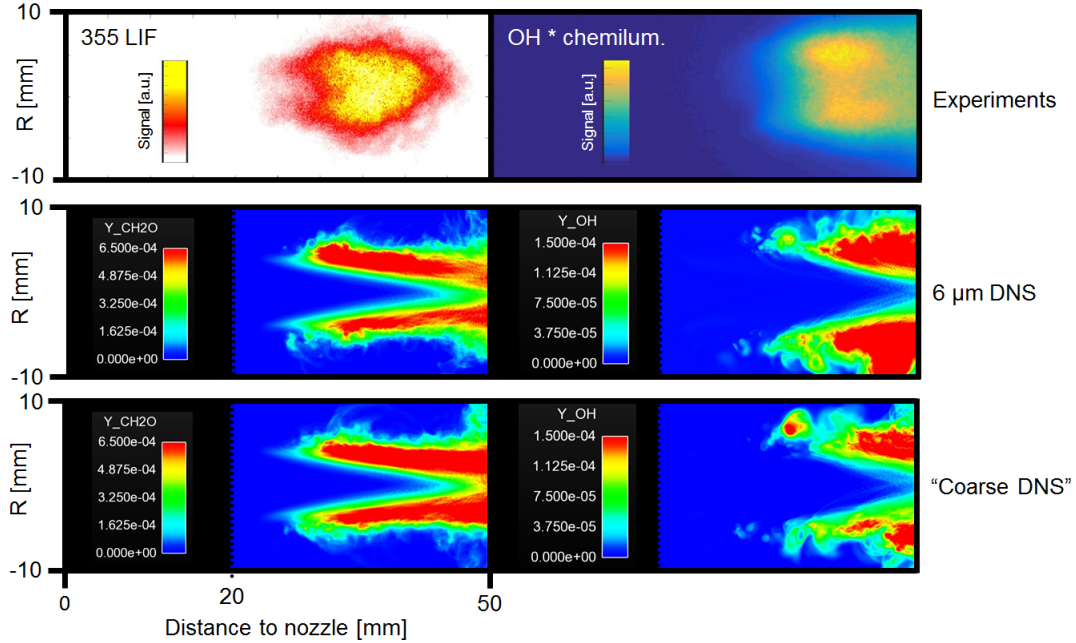


Figure D.2 – Averaged images for α test conditions. Top: Experimental average images of the high-temperature flame visualized by OH^* and the cool-flame visualized by CH_2O species. Middle and bottom: Time-averaged images of the cool- (through CH_2O) and high-temperature (through OH) flame computed on the mesh with a spatial resolution of $6 \mu\text{m}$ (middle) and $20 \mu\text{m}$ (bottom).

An instantaneous comparison between the "coarse DNS" and the $6 \mu\text{m}$ DNS is proposed in Fig. D.3. Both images show instantaneous temperature fields extracted at 3.26 ms for $R > 0$.

Observing the temperature fields, it clearly appears that, in both cases, high-temperature reservoirs are observed at the jet periphery. A qualitative representation of the turbulence structures can be observed through the stoichiometric line. The reference DNS shows smaller turbulent structures than the "coarse DNS". However, both simulations show small stoichiometric pockets being detached from the main jet. This observation is important, since these pockets are favorable to isolate auto-ignition, which is one of the four reaction zone topologies contributing to the flame stabilization.

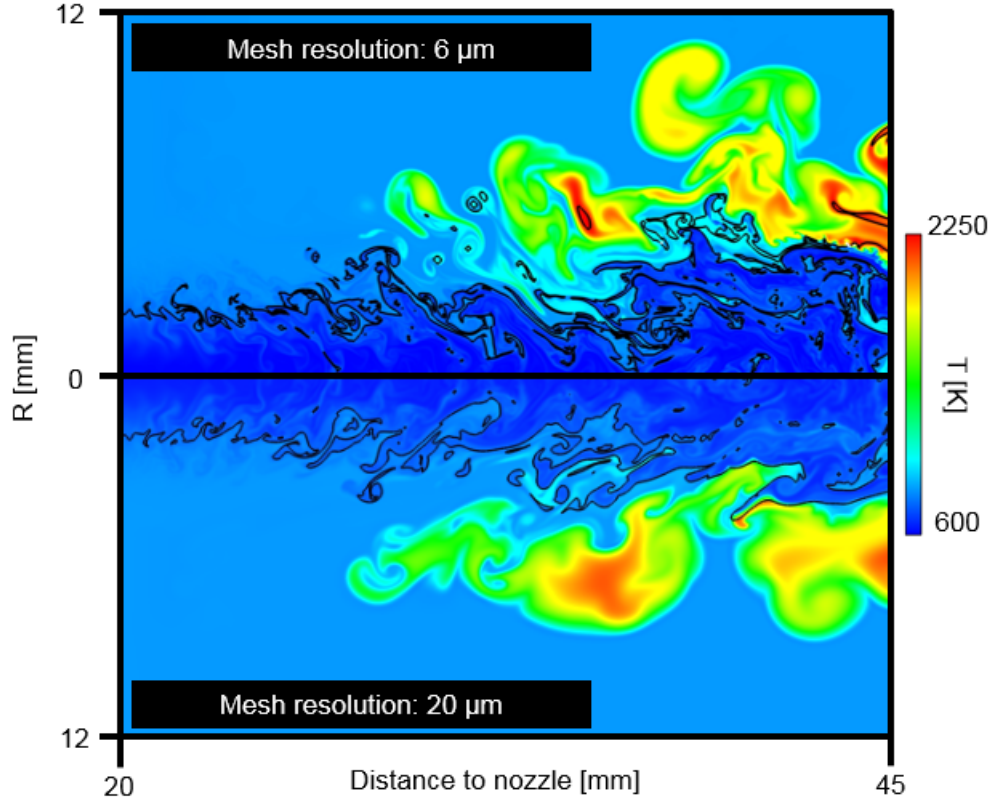


Figure D.3 – Instantaneous temperature fields for α test conditions, for a mesh resolution of $6 \mu\text{m}$ (top image) and $20 \mu\text{m}$ (bottom image), both of these images are displayed at 3.26 ms ASI for $R > 0$. The black line represents the stoichiometric line. (The bottom image has been rotated to provide a symmetrical comparison with the top image).

The four reaction zone topologies identified in Chapter 4 are also identified in the "coarse DNS". Focusing on the auto-ignition events, 56 % of the auto-ignition are assisted by burnt gases on the coarse mesh, against 69 % on the $6\mu\text{m}$ DNS. During the downstream evolution of the lift-off, 48 % of the reaction zones are triple flames in the "coarse DNS", against 45 % in the $6\mu\text{m}$ DNS.

In conclusion, the averaged and instantaneous structures of the cool- and high-temperature flames are similar, using a fine or a coarse mesh. Moreover, the proportion of triple flames, lean/rich reaction zones, isolated auto-ignition and auto-ignition assisted by burnt gases are also similar in both cases.

Therefore, even if small differences exist between the two simulations, we assume that the "coarse DNS" is able to reproduce the stabilization mechanisms observed in the reference DNS and in the experiments.

As a result, the simulations run on the coarse mesh can be used to simulate the α test conditions.

List of Figures

1.1	Relative evolution (1993 reference) of the regulatory emissions for Diesel vehicles in Europe from 1993 to 2015 for 4 pollutants: nitrogen oxides NO_x , carbon monoxide CO, the sum of nitrogen oxides NO_x and HC unburned hydrocarbons and finally the particles [4].	8
1.2	Four-stroke cycle Diesel engine [5].	9
1.3	Diesel spray combustion where the injection pressure is 700 bar inside a constant volume combustion chamber at 1100 K [6].	9
1.4	Illustration of the different physical phenomena occurring during Diesel spray combustion. Figure adapted from [7].	11
1.5	Illustration of the lift-off length (LOL) using broadband luminosity technique in constant volume combustion chamber extracted from [12].	12
1.6	Soot production as a function of the inverse of the equivalence ratio at the lift-off $1/\Phi_{LOL}$ for a Diesel spray in a constant volume vessel and for different ambient temperatures, densities and injection pressure. Figure adapted from [13].	13
2.1	Temporal evolution of temperature (black solid line) and heat release (red dotted line) for a n-dodecane/air mixture computed in 0D homogeneous constant pressure reactor. Figure adapted from [18].	18
2.2	Auto-ignition delay τ_{AI} of various fuels in a 0D constant pressure reactor. Figure adapted from [22].	19
2.3	Schematic of a conceptual combustion model describing from the injection to the stabilized diffusion combustion [24].	21
2.4	Schematic of a conceptual combustion model during the stabilized diffusion combustion [23].	22
2.5	Hypothetical shape of a premixed flame (left) and experimental verification of the hypothetical stabilization mechanism. Figures adapted from [27].	23
2.6	Flame wrinkling by turbulence where A and A_T are displayed. Figure adapted from [25].	24
2.7	Triple flames structure by [25] (top) and triple flames visualization in a laminar flow by [35] (bottom).	24
2.8	Top: contour lines of the reaction rate showing a triple flame with stream lines. Bottom: ratio u/S_L^0 as a function of the axial coordinate on the stoichiometric line. Figure adapted from [37].	26
2.9	Flame stabilization by critical scalar dissipation rate according to Peters et al. [42].	27

2.10	Nondimensional scalar dissipation rate as a function of the ratio of the lift-off height (h) to the jet diameter (d) for a turbulent methane diffusion flame. Figure adapted from [42].	28
2.11	Flame stabilization by recirculation of burnt gases according to Broadwell et al.[46]. Figure adapted from Karami et al. [47].	29
2.12	Illustration of a turbulent gaseous diffusion flame (left) and a Diesel spray flame (right).	30
2.13	LOL variations versus ambient temperature (left) [1], injection velocity (middle) [1] and oxygen concentration (right) [2].	30
2.14	LOL for three fuels and ambient densities. Labels are given by the symbol used for each fuel. The experimental conditions were: 180 μm orifice, 1380 bar pressure drop, fuel at 373 K, and 21 % ambient oxygen [15].	33
2.15	Stabilization of the flame-front by auto-ignition and flame propagation [61].	34
2.16	Typical OH chemiluminescence single-shot showing a separated ignition spot [61].	35
2.17	Cool-flame chemiluminescence images shortly before auto-ignition. The fuel is given on the lower left corner, and on the right side the auto-ignition delay is displayed. Quasi-steady LOL is shown as a vertical dashed white line [15].	36
2.18	The color shows the edge-flames through heat release rate fields, the solid line indicates the z_{st} contour, the star marker indicates the flame base position and the square markers indicates the closer distance to the injector of the cool-flame [67].	37
2.19	Qualitative regime diagram for the stabilization mechanisms as the boundary temperature and inlet velocity vary. The left cartoon is a zoom of a flame topology during the "kinetic" stabilization mode while the right cartoon shows an edge-flame during the "multi-mode" stabilization. The meaning of the acronyms is: RB: Rich Branch, LB: Lean Branch, RPF: Rich Premixed Flame, LPF: Lean Premixed Flame, NPF: Non-Premixed Flame. Figure adapted from [69].	38
2.20	"Initial domain configuration. Black shading pattern shows high vorticity regions. Grey/blue shading in top of figure represents the fuel and the white shading in the bottom represents the oxidiser." [65].	40
2.21	Heat release rate for a fixed window in the domain. The dashed line is z_{st} . Figure adapted from [75].	40
2.22	Left (adapted figure from [65]): computational domain including specification of the boundary condition. Right (figure from [18]): "volumetric rendering of H_2O_2 mass fraction, $Y_{H_2O_2}$ at $t = 0.45$ ms. The green color corresponds to $Y_{H_2O_2} = 10^{-3}$, and the red color to $Y_{H_2O_2} = 3 \times 10^{-3}$ ".	41
2.23	Turbulent DME lifted jet flame showing a low-temperature heat release marker, $Y_{CH_3OCH_2O_2}$ and a high-temperature flame marker Y_{OH} [76].	42
2.24	Chemiluminescence image sequence with laser ignition at 3.9 ms [14].	43
2.25	Schematic of a lifted spray flame under Diesel conditions (center), and different theories for the stabilization. Authors associated to the flame stabilization theories are noted in bold character above the illustrations. The flame cartoons is adapted from [47]	45

3.1	Experimental setup for simultaneous schlieren, 355 LIF and broadband chemiluminescence images with forced laser ignition.	49
3.2	Average formaldehyde cloud from 355 LIF at 100 mJ (top image) and 5 mJ (middle image), normalized average 355 LIF profiles integrated radially (bottom image).	52
3.3	Instantaneous frames from OH* and broadband chemiluminescence at 30 kfps for the α test condition. The time is expressed in terms of time ASI.	54
3.4	Superposition of an instantaneous frame from simultaneous schlieren imaging (30kfps) on an iso-contour of 355 LIF (6kfps, green line) and broadband chemiluminescence (30kfps, red line) for the α condition. The two red crosses show the location where the ignition laser is focused.	55
3.5	Left: LOL time tracking using OH* chemiluminescence imaging for ambient temperatures of 800 K and 850 K, respectively named α and α' conditions. Events A are shown as red rectangles and evolutions B as red lines for the α conditions. Right: snapshot of OH* images illustrating event A and evolution B.	58
3.6	Broadband chemiluminescence image sequence after the laser ignition (3000 μ s ASI) at 26 mm from the injector. The laser propagation is top to bottom.	60
3.7	Broadband chemiluminescence (red, first and third columns) and 355 LIF (green, second and fourth columns) image sequence after the laser ignition (3000 μ s ASI) at 26 mm from the injector, for condition α . The two dotted lines show the LOL just after the laser ignition (left line) and the average position of the “natural” LOL.	61
3.8	Ensemble and time averaged images of high-speed 355 LIF 500 μ s before (first pair of images) and after (second pair of images) laser ignition. Bottom plots: ensemble averaged of high-speed 355 LIF integrated over R for different timings.	62
3.9	Averaged high-energy 355 LIF image (first column), instantaneous high-energy 355 LIF profiles integrated over R (second column), instantaneous LOL evolution after laser ignition (at 17 mm and 3000 μ s) performed by OH* measurement (third column) for different injection events. The horizontal dotted blue line stands for the rising of HCHO signal at 22 mm from the injector. The two dotted vertical red lines delimit the three different stages observed after a forced laser ignition.	63
3.10	Instantaneous LOL tracking performed by OH* measurement (60 kfps) for the α , β , γ and δ test conditions and for laser ignition focused at 17 mm from the injector. The LOL tracking is performed by broadband chemiluminescence (30 kfps) for laser ignition at 26 mm (α test condition). When laser ignition occurs inside the formaldehyde cloud the LOL evolution are displayed with dotted lines, otherwise the LOL evolutions are plotted in solid lines.	65

4.1	Top: Superposition of the gas envelope of the spray (Schlieren imaging) on an iso-contour of the formaldehyde cloud (green line, high-speed 355 LIF), and the high-temperature flame (yellow line, broadband chemiluminescence). This image was obtained from the experimental setup presented in [82]. Bottom: Computational domain showing the used tetrahedral grid which is refined in the area of interest to capture combustion phenomena.	71
4.2	All of the graphs show radial profiles imposed at the inlet boundary condition. (a): Axial flow velocity (U_X) and axial velocity fluctuation (U_{RMS}), (b): temperature, (c): n-dodecane mass fraction.	72
4.3	Comparison between the reference mechanism of Yao et al. (solid black lines, [95]) the ARC model derived in the work (dotted red line), and experimental data (symbols, [22, 112, 113]). Left: laminar flame speeds, right: ignition delay times.	75
4.4	Instantaneous temperature profile of the stabilized flame (above the injector: $R < 0$) showing a triple flame. The bottom image is a zoom around the lift-off found in the upper image. The black line represents the stoichiometric line. The white line shows $4 \times 10^{11} W/m^3$ iso-contour of heat release rate.	78
4.5	(a) and (a'): two different instantaneous views illustrating a rich reaction zone (a) and a lean reaction zone (a') after an auto-ignition event. (b) and (b'): time sequence showing triple flames leaving the stoichiometric line. The black line represents the stoichiometric line. The white line shows the contour of heat release rate of $4 \times 10^{11} W/m^3$	79
4.6	DNS fields at 3.53 ms After the Start of Injection (ASI). Top image: mixture fraction field with an iso-line of temperature at 1900 K (black line). Bottom image: formaldehyde field with an iso-line of OH mass fraction at 1.5×10^{-4} in white.	80
4.7	(a): Average images of the high-temperature flame visualized by OH^* and OH species. (b): Average images of the cool-flame visualized by CH_2O species. The experimental data are generated using the experimental setup presented in [82].	82
4.8	LOL time-tracking with the detection of Triple Flames (TF), Lean/Rich Reaction Zones (L/R RZ), Isolated Auto-Ignitions (AI-I) and Auto-Ignitions Assisted by Burnt Gases (AI-BG) at the lift-off for $R > 0$	83
4.9	(a): auto-ignition event, also named Event A, occurring at t_1 . (b): downstream evolution, between t_0 and t_1 , also named Evolution B.	84
4.10	Image sequence illustrating an isolated auto-ignition (AI-I) at the lift-off. The black line represents the stoichiometric line and the white line shows the contour of heat release rate of $4 \times 10^{11} W/m^3$ (top images). The three bottom plots show OH and CH_2O mass fraction profiles along the red dotted line (measuring 1 mm long) shown on the top image sequence.	85
4.11	Image sequence leading to an AI-BG event. The black line represents the stoichiometric line. The white line shows $4 \times 10^{11} W/m^3$ iso-contour of heat release rate.	86

4.12	Instantaneous temperature fields showing Evolution B between 3.03 and 3.26 ms ASI. Black line: stoichiometric line. The triple flames detected at the lift-off are zoomed, and displayed on the right of the images. Iso-lines of heat release rate between $3.7 \times 10^{11} W/m^3$ and $4.3 \times 10^{11} W/m^3$ are displayed in red on the zoomed images.	87
4.13	(a): cartoon of a triple flame propagating along z_{st} . The red solid line represents the $\dot{\omega}_{T,crit} = 4 \times 10^{11} W/m^3$ iso-line. The red arrow shows the triple flame propagation direction (θ_{TF}) while the green arrow shows the flow direction (θ_{flow}). (b): histograms of θ_{TF}^+ and θ_{TF}^- . (c): histograms of $\theta_{TF,flow}^+$ and $\theta_{TF,flow}^-$ (right).	88
4.14	Both graphics have been constructed from triple flames data at the lift-off for $R > 0$ and $R < 0$. (a): Histogram of the ratio $U_{X,flow,LO}/S_a$. (b): symbols show $U_{X,flow,LO}/S_a$ as a function of $U_{X,flow,LO}$, while the black curve displays $U_{X,flow,LO}/(U_{X,flow,LO} - 1.5)$ as a function of $U_{X,flow,LO}$	90
4.15	Sketch illustrating the conceptual model of flame stabilization under Diesel condition derived from optical diagnostics and DNS.	91
4.16	Radial profiles comparison between time-average non-reactive DNS jet and a 1D spray model [55, 93]. Left column shows radial profiles at an axial distance of 30 mm from the injector. Right column shows radial profiles at 50 mm from the injector.	95
4.17	Illustration of a 1D flame stabilized by auto-ignition.	96
4.18	Grid convergence for 1D premixed flames at the stoichiometric mixture fraction. Temperature (top) and heat release rate (bottom) profiles are plotted for a spatial resolution varying between 1 and 7 μm	98
5.1	Peak optical thickness (KL) values from the averaged axial profiles of KL measured for each set of conditions considered, versus the inverse of the averaged equivalence ratio at the lift-off. The legend gives the range of experimental conditions considered. Adapted figure from [13]. A red star indicating the case chosen for illustration, the corresponding arbitrary value of equivalence ratio fluctuations related to LOL fluctuations and an area of corresponding soot production are added for illustration to the original figure.	101
5.2	Schematic representation of the Lift-off length as a function of time.	102
5.3	Averaged axial flow velocity in the center of the jet ($U_{X;R=0}$) as a function of the axial position (X) for the α test condition, computed with a 1D spray model [55, 93]. The LOL is also displayed in red to illustrate the assumption that the velocity at the lift off follows the same trend.	103
5.4	LOL time evolution using OH* chemiluminescence imaging. Test conditions are: $P_{inj} = 150 MPa$, $Prct_{O_2} = 15\%$, $T_{amb} = 800K$ and $\rho_{amb} = 22.8 kg/m^3$	106
5.5	Plot of the experimental and theoretical magnitude of the LOL fluctuations according to ambient temperature (T_{amb}), oxygen concentration ($Prct_{O_2}$) and injection pressure (P_{inj}) variations.	109

A.1	The two top images show heat release rate fields for two different instants ($t^* = t/\tau_{MR}$ defined in Section 2.3.4) where the dashed black lines are z_{st} . The plot labeled from A to F represents the evaluation of the diffusion term (D), reaction term (R) and χ along lines indicated on the top figures. Figure has adapted from [64].	118
A.2	Ratio of the diffusion term to the reaction rate of CO_2 after a forced laser ignition [80].	119
A.3	Left: "Illustration of instantaneous flow field represented by iso-surfaces of vorticity magnitude at 300,000 1/s colored by the enclosed temperature scale. The flame shape and location within the combustion chamber is illustrated by the red iso-surface of a representative value of heat release rate." Right: "(a) Iso-contours of the instantaneous field of α delineating the combustion modes. (b) Bar chart quantifying the fraction of H_2 fuel consumption (reaction rate) due to each mode." [129].	120
A.4	The propagation regime is given for a premixed propagation flame at the stoichiometry z_{st} (left plot) and auto-ignition flame is at the most reactive mixture fraction z_{mr} (right plot) [101].	121
A.5	Snapshots of (a) heat release rate, (b) temperature, (c) mean temperature field, (d) mean AI (Auto-Ignition) index field, (e) instantaneous AI index field + most reactive mixture fraction (z_{mr}) iso-lines, and (f) instantaneous FI (Flame Index) field + stoichiometric mixture fraction (z_{st}) iso-lines. Insets A and B show the local contribution of $R8$ and $R6$ to HO_2 consumption [101].	122
B.1	Qualitative regime diagram for the flame stabilization as the most reactive mixture fraction ($\tau_{AI,mr}$) and the axial flow velocity on the stoichiometric line (U_{st}) vary. The triple flame image is extracted from [25], the Cabra flame from [131], the burner flame stabilized from [68], while the n-dodecane spray flame image is obtained with the experimental setup presented in Section 3.2.2.	123
C.1	Instantaneous temperature fields for case α and α_{coflow} , both of these images are displayed at 3.26 ms ASI for $R > 0$. The black line represents the stoichiometric line. (The bottom image has been rotated to provide a symmetrical comparison with the top image).	127
C.2	LOL time-tracking for cases α and α_{coflow} and for $R > 0$	128
D.1	Radial profiles comparison between time-averaged non-reactive 6 μm DNS (thin red line), "coarse DNS" (thick green line) jet and a 1D spray model [55, 93] (dotted black line) for the α test conditions. Left column shows radial profiles at an axial distance of 30 mm from the injector. Right column shows radial profiles at 50 mm from the injector.	130

D.2	Averaged images for α test conditions. Top: Experimental average images of the high-temperature flame visualized by OH^* and the cool-flame visualized by CH_2O species. Middle and bottom: Time-averaged images of the cool- (through CH_2O) and high-temperature (through OH) flame computed on the mesh with a spatial resolution of $6 \mu\text{m}$ (middle) and $20 \mu\text{m}$ (bottom).	131
D.3	Instantaneous temperature fields for α test conditions, for a mesh resolution of $6 \mu\text{m}$ (top image) and $20 \mu\text{m}$ (bottom image), both of these images are displayed at 3.26 ms ASI for $R > 0$. The black line represents the stoichiometric line. (The bottom image has been rotated to provide a symmetrical comparison with the top image).	132

List of Tables

2.1	Comparison of the coefficients predicting the time-averaged LOL between experiments and simulations (RANS). The experiments assumed a flame stabilization by premixed flame at the flame base while the RANS estimated the LOL by flame extinction.	34
3.1	Operating condition.	48
3.2	The different test conditions. The parameters that change compared to the reference case α are in bold characters.	49
3.3	Laser and imaging parameters.	50
3.4	LOL and LOL_{HCHO} averages for the different test conditions.	56
3.5	Statistical analysis of the three different stages identified for laser ignition at 17 mm from the injector. Standard deviations are noted in parenthesis.	64
4.1	Initial species mass fractions in the vessel.	73
4.2	Summary of the reduced mechanism (28 ARC): transported (left) and Quasi Steady State (QSS) (right) species.	74
4.3	1D premixed flame initial conditions.	96
4.4	1D premixed flame characteristics.	97
5.1	High-speed OH* chemiluminescence optical setup.	106
5.2	Test conditions.	107
5.3	Number of realizations for the different test conditions performed.	107

Bibliography

- [1] D.L. Siebers, B. Higgins, Flame Lift-Off on Direct-Injection Diesel Sprays Under Quiescent Conditions, SAE Technical Paper 2001-01-0530 (2001). (Cit. on pp. 2, 30, 31, 53, 99, 103).
- [2] D.L. Siebers, B. Higgins, L.M. Pickett, Flame Lift-Off on Direct-Injection Diesel Fuel Jets: Oxygen Concentration Effects, SAE Technical Paper 2002-01-0890 (2002). (Cit. on pp. 2, 30–32, 34, 99, 103).
- [3] A. Nel, Air Pollution-Related Illness: Effects of Particles, *Science* 308 (2005) 804-806. (Cit. on p. 7).
- [4] J. Tillou, Développement d'une modélisation basée sur la tabulation des schémas cinétiques complexes pour la simulation aux grandes échelles de l'auto-inflammation et de la combustion turbulente non-pré mélangé dans les moteurs à pistons, PhD (2013). (Cit. on p. 8).
- [5] Diesel Engine Registry Website: <https://dieselengineregistry.wordpress.com/2-stroke-vs-4-stroke-engines/> (cit. on p. 9).
- [6] L. Yossapong, Diesel Spray at 700bar Inj inside constant volume combustion chamber (CVCC) of 1100K. Photron Fastcam SA-X2- 10,000 fps (1024x1024 pixels), Department of Mechanical Engineering King Mongkut's University of Technology Thonburi, 22 May, 2015 (cit. on p. 9).
- [7] G. Theotokatos, The CFD Development of Non-premixed Dual Fuel Combustion Diesel Engine injected by High-pressure Gas in the Cylinder Chamber, ARCHIE-WeSt Webiste. (Cit. on p. 11).
- [8] F. Payri, V. Bermúdez, R. Payri, F. J. Salvador, The influence of cavitation on the internal flow and the spray characteristics in diesel injection nozzles, *Fuel* 83 (2004) 419-431. (Cit. on p. 11).
- [9] F. R. Westlye, M. Battistoni, S. A. Skeen, J. Manin, L. M. Pickett, A. Ivarsson, Penetration and combustion characterization of cavitating and non-cavitating fuel injectors under diesel engine conditions, SAE Technical Paper 2016-04-05 (2016). (Cit. on p. 11).
- [10] L. He, F. Ruiz, Effect of cavitation on flow and turbulence in plain orifices for high-speed atomization. *Atom Sprays* 1995;5:569–84. (Cit. on p. 11).
- [11] C. Soteriou, R. Andrews, M. Smith, Direct injection diesel sprays and the effect of cavitation and hydraulic flip on atomization. SAE Paper 950080; 1995. (Cit. on p. 11).

-
- [12] M. Huo, S. Lin, H. Liu, C-F. F. Lee, Study on the spray and combustion characteristics of water-emulsified diesel, *Fuel* **123** (2014) 218-229. (Cit. on p. 12).
- [13] L. M. Picketta and D. L. Siebers, Soot in diesel fuel jets: Effects of ambient temperature, ambient density, and injection pressure, *Combust. Flame* **138** (2004) 114-135. (Cit. on pp. 12, 13, 99, 101).
- [14] L.M. Pickett, S. Kook, H. Persson, Ö. Andersson, Diesel fuel jet lift-off stabilization in the presence of laser-induced plasma ignition, *Proc. Combust. Inst.* **32** (2009) 2793-2800. (Cit. on pp. 12, 14, 42-44, 47, 48, 54, 55, 59, 68, 69, 79, 84, 92, 111, 113).
- [15] L.M. Pickett, D.L. Siebers, C.A. Idicheria, Relationship between ignition processes and the lift-off length of diesel fuel jets, *SAE Technical Paper 2005-01-3843* (2005). (Cit. on pp. 12, 19, 32, 33, 35, 36, 42, 44, 79, 103).
- [16] R. Venugopal, J. Abraham, A Review of Fundamental Studies Relevant to Flame Lift-off in Diesel Jets, *SAE Technical Paper 2007-01-0134* (2007). (Cit. on pp. 13, 29, 41, 46).
- [17] L. M. Pickett, ECN available at <http://www.sandia.gov/ecn/> 2015 (cit. on pp. 13, 39, 48, 105, 110).
- [18] G. Borghesi, A. Krisman, T. Lu, J.H. Chen, Direct numerical simulation of a temporally evolving air/n-dodecane jet at low-temperature diesel-relevant conditions, *Combust. Flame* **195** (2018) 183-202. (Cit. on pp. 18, 35, 40, 41, 68, 73, 84, 86, 88, 96, 119).
- [19] M. Jansons, A. Brar, F. Estefanous, R. Florea, D. Taraza, N. Henein, W. Bryzik, Experimental Investigation of Single and Two-Stage Ignition in a Diesel Engine, *SAE Technical Paper 2008-04-14* (2008). (Cit. on p. 18).
- [20] C. K. Westbrook, Y. Mizobuchi, T. Poinso, P. J. Smith, Computational combustion, *Proc. Combust. Inst.* **30** (2005) 125-157. (Cit. on p. 18).
- [21] L-M. Malbec, E. W. Eagle, M. P. B. Musculus, P. Schihl, Influence of Injection Duration and Ambient Temperature on the Ignition Delay in a 2.34L Optical Diesel Engine, *SAE Technical Paper 2015-09-01* (2015). (Cit. on p. 18).
- [22] U. Pfahl, K. Fieweger, G. Adomeit, Self-ignition of diesel-relevant hydrocarbon-air mixtures under engine conditions, *Symp. (Int.) Combust.* **26** (1996) 781-789. (Cit. on pp. 19, 75).
- [23] J.E. Dec, A Conceptual Model of DI Diesel Combustion Based on Laser-Sheet Imaging, *SAE Technical Paper 970873* (1997). (Cit. on pp. 19, 22, 70).
- [24] G. Bruneaux, Combustion structure of free and wall-impinging diesel jets by simultaneous laser-induced fluorescence of formaldehyde, polyaromatic hydrocarbons, and hydroxides, *Int. J. Eng. Res.* **9** (3) (2008) 249-265. (Cit. on pp. 19-21, 50, 51).

-
- [25] T. Poinso and D. Veynante, *Theoretical and Numerical Combustion*, Third Edition, 2005. (Cit. on pp. 21, 23, 24, 97, 123, 124).
- [26] K. Wohl, N.M. Kapp, C. Gazley, The stability of open flames, *Symp. (Int.) Combust.* **3** (1948) 3–21. (Cit. on p. 21).
- [27] L. Vanquickenborne, A. Van Tiggelen, The stabilization mechanism of lifted diffusion flames, *Combust. Flame* **10** (1966) 59–69. (Cit. on pp. 22, 23).
- [28] T. Gautam, Lift-off Heights and Visible Lengths of Vertical Turbulent Jet Diffusion Flames in Still Air, *Combust. Sci. Technol.* **41** (1984) 17-29. (Cit. on p. 22).
- [29] C.J. Lawn, Lifted flames on fuel jets in co-flowing air, *Prog. Energy Combust. Sci.* **35** (2009) 1–30. (Cit. on pp. 23, 28, 44).
- [30] K. K. Kuo, *Principles of combustion*, Book published in 2005. DOI 10.1007/s00162-006-0039-5 (cit. on p. 23).
- [31] J. H. Chen and I. G. Im, Correlation of flame speed with stretch in turbulent premixed methane/air flames, *Symp. (Int.) Combust.* **27** (1998) 819-826. (Cit. on p. 23).
- [32] S. Daniele, P. Jansohn, K. Boulouchos, Turbulent flame speed for syngas at gas turbine relevant conditions, *Proc. Combust. Inst.* **33** (2011) 2937-2944. (Cit. on p. 23).
- [33] C. R. Kaplan, S. W. Beak, E. S. Oran, J. L. Ellzey, Dynamics of a Strongly Radiating Unsteady Ethylene Jet Diffusion Flame, *Combust. Flame* **96** (1994) 1-21. (Cit. on p. 23).
- [34] M. Namazian, R. W. Schefer, J. Kelly, Scalar dissipation measurements in the developing region of a jet, *Combust. Flame* **74** (1988) 147-160. (Cit. on p. 23).
- [35] P.N. Kioni, B. Rogg, K. Bray, A. Liñán, Flame spread in laminar mixing layers, *Combust. Flame* **95** (1993) 276-290. (Cit. on pp. 24, 25, 89).
- [36] H. Phillips, Flame in a buoyant methane layer, *Symp. (Int.) Combust.* **10** (1965) 1277-1283. (Cit. on pp. 25, 89).
- [37] G.R. Ruetsch, L. Vervisch, A. Liñán, Effects of heat release on triple flames, *Phys. Fluids* **7** (1995) 1447-1454 (cit. on pp. 25, 26, 77, 89).
- [38] P. Domingo, L. Vervisch, Triple flames and partially premixed combustion in autoignition of non-premixed turbulent mixtures, *Symp. (Int.) Combust.* **26** (1996) 233-240. (Cit. on pp. 25, 89).
- [39] M. Chen, M. Herrmann, N. Peters, Flamelet modeling of lifted turbulent methane/air and propane/air jet diffusion flames, *Proc. Combust. Inst.* **32** (2000) 167-174. (Cit. on p. 25).
- [40] K.M. Lyons, Toward an understanding of the stabilization mechanisms of lifted turbulent jet flames, *Prog. Energy Combust. Sci.* **33** (2007) 211–231. (Cit. on pp. 25, 44).

-
- [41] S. Karami, E. R. Hawkes, M. Talei, J. H. Chen, Edge flame structure in a turbulent lifted flame: A direct numerical simulation study, *Combust. Flame* 169 (2016) 110-128. (Cit. on p. 25).
- [42] N. Peters, F.A. Williams, Liftoff characteristics of turbulent jet diffusion flames, *AIAA J.* 21 (1983) 423-429. (Cit. on pp. 26-28).
- [43] A. Liñán, The asymptotic structure of counterflow diffusion flames for large activation energies, *Acta Astronautica* 1 (1974) 1007-1039. (Cit. on p. 26).
- [44] D.A. Everest, D.A. Feikema, J.F. Driscoll, Images of the strained flammable layer used to study the liftoff of turbulent jet flames, *Symp. (Int.) Combust.* 26 (1996) 129-136. (Cit. on p. 28).
- [45] R.W. Schefer, M. Namazian, E. Filtopoulos, J. Kelly, Temporal evolution of turbulence/chemistry interactions in lifted, turbulent-jet flames, *Symp. (Int.) Combust.* 25 (1994) 1223-1231. (Cit. on p. 28).
- [46] J.E. Broadwell, W.J. Dahm, M.G. Mungal, Blowout of turbulent diffusion flames, *Symp. (Int.) Combust.* 20 (1985) 303-310. (Cit. on pp. 28, 29).
- [47] S. Karami, E.R. Hawkes, M. Talei, J.H. Chen, Mechanisms of flame stabilisation at low lifted height in a turbulent lifted slot-jet flame, *J. Fluid Mech.* 777 (2015) 633-689. (Cit. on pp. 29, 44, 45).
- [48] T. Ito, T. Kitamura, M. Ueda, T. Matsumoto, J. Senda, H. Fujimoto, Effects of flame lift-off and flame temperature on soot formation in oxygenated fuel sprays, *SAE Technical Paper 2003-01-0073* (2003). (Cit. on p. 30).
- [49] W. Zhang, J-P. Tian, K. Nishida, Effects of Nozzle Hole Diameter and Injection Pressure on Flame Lift-Off and Soot Formation in D.I. Diesel Combustion, *SAE Technical Paper 2011-08-30* (2011). (Cit. on p. 30).
- [50] N. Peters, *Turbulent Combustion*, Cambridge University Press, 2000. (Cit. on pp. 31, 124).
- [51] M. Metghalchi and J. C. Keck, Burning velocities of mixtures of air with methanol, isooctane, and indolene at high pressure and temperature, *Combust. Flame* 48 (1982) 191-210. (Cit. on p. 31).
- [52] B. Higgins, D.L. Siebers, Measurement of the flame Lift-Off location on DI diesel sprays using OH chemiluminescence, *SAE Technical Paper 2001-01-0918* (2001). (Cit. on pp. 31, 32, 53).
- [53] J. B. Heywood, *Internal combustion engine fundamentals*, Book published in 1988, ISBN: 978-0-07-028637-5. (Cit. on p. 31).
- [54] E. N. Balles and J. B. Heywood, *Fuel-Air Mixing and Diesel Combustion in a Rapid Compression Machine*, *SAE Transactions* (1988). DOI 10.4271/880206 (cit. on p. 32).

- [55] J. Naber, D.L. Siebers, Effects of gas density and vaporization on penetration and dispersion of diesel sprays, SAE Technical Paper 960034 (1996). (Cit. on pp. 32, 59, 65, 94, 95, 102, 103, 124, 129, 130).
- [56] G. Dugger, D. Simon, M. Gerstein, Basic Considerations in the Combustion of Hydrocarbon Fuels with Air, (1959) NACA report 1300, chapitre Laminar Flame Propagation, p. 321-356. (Cit. on p. 32).
- [57] C. J. Mueller, W.J. Pitz, L. M. Pickett, G. C. Martin, D. L. Siebers, C. K. Westbrook, Effects of oxygenates on soot processes in DI diesel engines: experiments and numerical simulations, SAE Technical Paper 2003-01-1791 (2003). (Cit. on p. 32).
- [58] M.P.B Musculus, J.E. Dec, D.R. Tree, Effects of fuel parameters and diffusion flame lift-off on soot formation in a heavy-duty DI diesel engine, SAE Technical Paper 2002-01-0889 (2002). (Cit. on p. 32).
- [59] L.M. Pickett, D.L. Siebers, Fuel effects on soot processes of fuel jets at DI diesel conditions, SAE Technical Paper 2003-01-3080 (2003). (Cit. on p. 32).
- [60] R. Venugopal and J. Abraham, A numerical investigation of flame lift-off in diesel Jets, Combust. Sci. Technol. 179 (2007) 2599–2618. (Cit. on pp. 33, 34, 99).
- [61] C. Pauls, G. Grünefeld, S. Vogel, N. Peters, Combined simulation and OH-chemiluminescence measurements of the combustion process using different fuels under diesel-engine like conditions, SAE Technical Paper, 2007-01-0020 (2007). (Cit. on pp. 34, 35, 42, 44, 79).
- [62] R.N. Dahms, G.A. Paczko, S.A. Skeen, L.M. Pickett, Understanding the ignition mechanism of high-pressure spray flames, Proc. Combust. Inst. 36 (2017) 2615–2623. (Cit. on pp. 35, 96, 119).
- [63] D.K. Dalakoti, A. Krisman, B. Savard, A. Wehrfritz, H. Wang, M.S. Day, J.B Bell, E.R. Hawkes, Structure and propagation of two-dimensional, partially premixed, laminar flames in diesel engine conditions, Proc. Combust. Inst. (2018). DOI 10.1016/j.proci.2018.06.169 (cit. on pp. 35, 39).
- [64] A. Krisman, E.R. Hawkes, M. Talei, A. Bhagatwala, J.H. Chen, Characterisation of two-stage ignition in diesel engine-relevant thermochemical conditions using direct numerical simulation, Combust. Flame 172 (2016) 326-341. (Cit. on pp. 35, 39, 41, 68, 73, 86, 117–119).
- [65] A. Krisman, E.R. Hawkes, M. Talei, A. Bhagatwala, J.H. Chen, A direct numerical simulation of cool-flame affected auto-ignition in diesel engine-relevant conditions, Proc. Combust. Inst. 36 (2017) 3567-3575. (Cit. on pp. 35, 40, 41, 68, 73, 86).
- [66] A. Krisman, E.R. Hawkes, J.H. Chen, The structure and propagation of laminar flames under autoignitive conditions, Combust. Flame 188 (2018) 399-411. (Cit. on pp. 35, 75, 95).

- [67] A. Krisman, E.R. Hawkes, M. Talei, A. Bhagatwala, J.H. Chen, Poly-brachial structures in dimethyl ether edge-flames at negative temperature coefficient conditions, *Proc. Combust. Inst.* **35** (2015) 999-1006. (Cit. on pp. 36-39, 41, 44, 86, 117).
- [68] S. Deng, P. Zhao, M.E. Mueller, C.K. Law, Autoignition-affected stabilization of laminar nonpremixed DME/air coflow flames, *Combust. Flame* **162** (2015) 3437-3445. (Cit. on pp. 37-39, 123).
- [69] S. Deng, P. Zhao, M.E. Mueller, C.K. Law, Stabilization of laminar nonpremixed DME/air coflow flames at elevated temperatures and pressures, *Combust. Flame* **162** (2015) 4471-4478. (Cit. on pp. 37-39, 124).
- [70] T. F. Lu, C. S. Yoo, J. H. Chen, C. K. Law, Three-dimensional direct numerical simulation of a turbulent lifted hydrogen jet flame in heated coflow: A chemical explosive mode analysis, *J. Fluid Mech.* **652** (2010) 45-64. (Cit. on pp. 38, 119).
- [71] R. Shan, C. S. Yoo, J. H. Chen, T. Lu, Computational diagnostics for n-heptane flames with chemical explosive mode analysis, *Combust. Flame* **159** (2012) 3119-3127. (Cit. on pp. 38, 119).
- [72] H. Pitsch, M. Chen, N. Peters, Unsteady flamelet modeling of turbulent hydrogen-air diffusion flames, *Symp. (Int.) Combust.* **27** (1998) 1057-1064. (Cit. on p. 38).
- [73] H. G. Im, J. H. Chen, Effects of flow strain on triple flame propagation, *Combust. Flame* **126** (2001) 1384-1392. (Cit. on p. 39).
- [74] J. Boulanger, L. Vervisch, J. Reveillon, S. Ghosal, Effects of heat release in laminar diffusion flames lifted on round jets, *Combust. Flame* **134** (2003) 355-368. (Cit. on p. 39).
- [75] A. Krisman, E.R. Hawkes, J.H. Chen, Two-stage auto-ignition and edge flames in a high pressure turbulent jet, *J. Fluid Mech.* **824** (2017) 5-41. (Cit. on pp. 39, 40, 68, 73, 86, 117, 119).
- [76] Y. Minamoto, J.H. Chen, DNS of a turbulent lifted DME jet flame, *Combust. Flame* **169** (2016) 38-50. (Cit. on pp. 41, 42, 68, 86, 88).
- [77] D-H. Shin, E.S. Richardson, V. Aparece-Scutariu, Y. Minamoto, J.H. Chen, Fluid age-based analysis of a lifted turbulent DME jet flame DNS, *Proc. Combust. Inst.* (2018). DOI 10.1016/j.proci.2018.06.126 (cit. on p. 41).
- [78] L. Gomet, V. Robin, A. Mura, Influence of Residence and Scalar Mixing Time Scales in Non-Premixed Combustion in Supersonic Turbulent Flows, *Combust. Sci. Technol.* **184** (2012) 1471-1501. (Cit. on p. 41).
- [79] N. Enjalbert, P. Domingo, L. Vervisch, Mixing time-history effects in Large Eddy Simulation of non-premixed turbulent flames: Flow-Controlled Chemistry Tabulation, *Combust. Flame* **159** (2012) 336-352. (Cit. on p. 41).

-
- [80] C. Gong, M. Jangi, X.-S. Bai, Diesel flame lift-off stabilization in the presence of laser-ignition, *Combust. Theor. Model.* **19** (2015) 696-713. (Cit. on pp. 43, 44, 119).
- [81] W.M. Pitts, Assessment of theories for the behavior and blowout of lifted turbulent jet diffusion flames, *Symp. (Int.) Combust.* **22** (1989) 809–816. (Cit. on p. 44).
- [82] F. Tagliante, L-M. Malbec, G. Bruneaux, L. M. Pickett, C. Angelberger, Experimental study of the stabilization mechanism of a lifted Diesel –type flame using combined optical diagnostics and laser-induced plasma ignition, *Combust. Flame* **197** (2018) 215-226. (Cit. on pp. 47, 67–69, 71, 76, 79, 81–83).
- [83] D. Verhoeven, J.-L. Vanhemelryck, T. Baritaud, Macroscopic and ignition characteristics of high-pressure sprays of single-component fuels, *SAE Technical Paper 981069* (1998). (Cit. on p. 48).
- [84] Panigrahi and Muralidhar Schlieren and Shadowgraph Methods in Heat and Mass Transfer (2012). (Cit. on p. 50).
- [85] L.M. Pickett, C.L. Genzale, G. Bruneaux, L.-M. Malbec, L. Hermant, C. Christiansen, J. Schramm, Comparison of diesel spray combustion in different high-temperature, high-pressure facilities, *SAE Int. J. Engines* **3** (2010) 156–181. (Cit. on p. 50).
- [86] J.M. García -Oliver, L.-M. Malbec, H.B. Toda, G. Bruneaux, A study on the interaction between local flow and flame structure for mixing-controlled diesel sprays, *Combust. Flame* **179** (2017) 157-171. (Cit. on pp. 50, 51, 79).
- [87] R. Payri, F.J. Salvador, J.Manin, A. Viera, Diesel ignition delay and lift-off length through different methodologies using a multi-hole injector, *Appl. Energy* **162** (2016) 541-550. (Cit. on p. 53).
- [88] N. Maes, M. Meijer, N. Dam, B. Somers, H. Baya Toda, G. Bruneaux, S.A. Skeen, L.M. Pickett, J. Manin, Characterization of Spray A flame structure for parametric variations in ECN constant-volume vessels using chemiluminescence and laser-induced fluorescence, *Combust. Flame* **174** (2016) 138-151. (Cit. on pp. 53, 79, 81).
- [89] Idex optics and photonics, Gaussian beam optics. (Cit. on p. 54).
- [90] C.L. Genzale, L.M. Pickett, A.A. Hoops, J.M. Headrick, Laser ignition of multi-injection gasoline sprays, *SAE Technical Paper 2011-01-0659* (2011). (Cit. on p. 54).
- [91] P.M. Lillo, L.M. Pickett, H. Persson, O. Andersson, S. Kook, Diesel spray ignition detection and spatial/temporal correction, *SAE Int. J. Engines* **5** (2012) 1330–1346. (Cit. on p. 55).
- [92] S.A. Skeen, J. Manin, L.M. Pickett, Simultaneous formaldehyde PLIF and high-speed schlieren imaging for ignition visualization in high-pressure spray flames, *Proc. Combust. Inst.* **35** (2015) 3167–3174. (Cit. on p. 55).

- [93] M.P.B Musculus, K. Kattke, Entrainment waves in diesel jets, *SAE Int. J. Engines* 2 (2009) 1170–1193. (Cit. on pp. 59, 65, 94, 95, 102, 103, 124, 129, 130).
- [94] D. G. Goodwin, H. K. Moffat, R. L. Speth, 2015, URL: <http://www.cantera.org>. (Cit. on pp. 59, 75, 120).
- [95] T. Yao, Y. Pei, B.-J. Zhong, S. Som, T. Lu, K.H. Luo, A compact skeletal mechanism for n -dodecane with optimized semi-global low-temperature chemistry for diesel engine simulations, *Fuel* 191 (2017) 339-349. (Cit. on pp. 59, 73, 75).
- [96] F. Tagliante, T. Poinso, L. M. Pickett, P. Pepiot, L-M. Malbec, G. Bruneaux, C. Angelberger, A conceptual model of the flame stabilization mechanisms for a lifted Diesel-type flame based on direct numerical simulation and experiments, *Combust. Flame* 201 (2019) 65-77. (Cit. on p. 67).
- [97] B. Franzelli, E. Riber, M. Sanjosé, T. Poinso, A two-step chemical scheme for kerosene-air premixed flames, *Combust. Flame* 157 (2010) 1364-1373. (Cit. on p. 68).
- [98] B. Franzelli, E. Riber, L. Gicquel, T. Poinso, Large Eddy Simulation of combustion instabilities in a lean partially premixed swirled flame, *Combust. Flame* 159 (2012) 621-637. (Cit. on p. 68).
- [99] P.Pepiot, Automatic strategies to model transportation fuel surrogates (Doctoral dissertation, Stanford University 2008). (Cit. on pp. 68, 73).
- [100] P. Pepiot-Desjardins and H. Pitsch, An efficient error-propagation-based reduction method for large chemical kinetic mechanisms, *Combust. Flame* 154 (2008) 67-81. (Cit. on pp. 68, 73).
- [101] O. Schulz, T. Jaravel, T. Poinso, B. Cuenot, N. Noiray, A criterion to distinguish auto-ignition and propagation applied to a lifted methane–air jet flame, *Proc. Combust. Inst.* 36 (2017) 1637-1644. (Cit. on pp. 68, 120–122, 124).
- [102] O. Schulz, N. Noiray, Autoignition flame dynamics in sequential combustors, *Combust. Flame* 192 (2018) 86-100. (Cit. on p. 68).
- [103] T. Jaravel, E. Riber, B. Cuenot, G. Bulat, Large Eddy Simulation of an industrial gas turbine combustor using reduced chemistry with accurate pollutant prediction, *Proc. Combust. Inst.* 36 (2017) 3817-3825. (Cit. on p. 68).
- [104] R. Payri, J. García-Oliver, M. Bardi, J. Manin, Fuel temperature influence on diesel sprays in inert and reacting conditions, *Appl. Therm. Eng.* 38 (2012) 185-195. (Cit. on p. 69).
- [105] V.Moureau, G. Lartigue, Y. Sommerer, C. Angelberger, O. Colin, T. Poinso, Numerical methods for unsteady compressible multi-component reacting flows on fixed and moving grids, *J. Comput. Phys.* 202 (2005) 710-736. (Cit. on p. 70).

-
- [106] P.D. Lax , B. Wendroff, Difference schemes for hyperbolic equations with high order of accuracy, *Commun. Pure Appl. Math.* 17 (1964) 381–398. (Cit. on p. 70).
- [107] T. Poinso , S. Lele , Boundary conditions for direct simulations of compressible viscous flows, *J. Comput. Phys.* 101 (1992) 104-129. (Cit. on pp. 72, 93).
- [108] A. Smirnov, S. Shi, I. Celik, Random flow generation technique for large eddy simulations and particle-dynamics modeling, *J. Fluids Eng.* 123 (2001) 359-371. (Cit. on p. 72).
- [109] T. Passot and A. Pouquet, Numerical simulation of compressible homogeneous flows in the turbulent regime, *J. Fluid Mech.* 181 (1987) 441-466. (Cit. on p. 72).
- [110] S. M. Sarathy, C. K. Westbrook, M. Mehl, W. J. Pitz, C. Togbe, P. Dagaut, H. Wang, M. A. Oehlschlaeger, U. Niemann, K. Seshadri, P. S. Veloo, C. Ji, F. N. Egolfopoulos, T. Lu, Comprehensive chemical kinetic modeling of the oxidation of 2-methylalkanes from C7 to C20, *Combust. Flame* 158 (2011) 2338-2357. (Cit. on p. 73).
- [111] T. Løv, D. Nilsson, F. Mauss, Automatic reduction procedure for chemical mechanisms applied to premixed methane/air flames, *Proc. Combust. Inst.* 28 (2000) 1809-1815. (Cit. on p. 74).
- [112] C. Ji, E. Enoch, Y. L. Wang, H. Wang, F. N. Egolfopoulos, Propagation and extinction of premixed C5-C12 n-alkane flames, *Combust. Flame* 157 (2010) 277-287. (Cit. on p. 75).
- [113] S. S. Vasu, D. F. Davidson, Z. Hong, V. Vasudevan, R. K. Hanson, N-Dodecane oxidation at high-pressures: Measurements of ignition delay times and OH concentration time-histories, *Proc. Combust. Inst.* 32 (2009) 173-180. (Cit. on p. 75).
- [114] R. W. Bilger, S.H. Stårner, R. J. Kee, On reduced mechanisms for methane air combustion in nonpremixed flames, *Combust. Flame* 80 (1990) 135-149. (Cit. on p. 75).
- [115] J. Hirschfelder , C. Curtiss , D.E. Campbell , The theory of flames and detonations, *Symp. (Int.) Combust.* 4 (1953) 190–211. (Cit. on p. 75).
- [116] L. Muñiz, M.G. Mungal, Instantaneous flame-stabilization velocities in lifted-jet diffusion flames, *Combust. Flame* 111 (1997) 16-31. (Cit. on pp. 77, 89).
- [117] K. M. Pang, M. Jangi, X-S. Bai, J. Schramm, J. H. Walther, P. Glarborg, Effects of ambient pressure on ignition and flame characteristics in diesel spray combustion, *Fuel* 237 (2019) 676-685. (Cit. on p. 78).
- [118] M. EidiAttarZade, S. Tabejamaat, M. Mani, M. Farshchi, Numerical Study of Ignition Process in Turbulent Shear-less Methane-air Mixing Layer, *Flow Turbul. Combust.* 99 (2017) 411-436. (Cit. on p. 91).

-
- [119] C. Chartier, U. Aronsson, Ö. Andersson, R. Egnell, B. Johansson, Influence of jet–jet interactions on the lift-off length in an optical heavy-duty DI diesel engine, *Fuel* 112 (2013) 311-318. (Cit. on pp. 93, 115).
- [120] A. M. Rusly, M. K. Le, S. Kook, E. R. Hawkes, The shortening of lift-off length associated with jet–wall and jet-jet interaction in a small-bore optical diesel engine, *Fuel* 125 (2014) 1-14. (Cit. on pp. 93, 115).
- [121] M. Bardi, G. Bruneaux, A. Nicolle, O. Colin, Experimental Methodology for the Understanding of Soot-Fuel Relationship in Diesel Combustion: Fuel Characterization and Surrogate Validation, SAE Technical Paper 2017-03-23 (2017). (Cit. on pp. 99, 105).
- [122] L-M. Malbec, J. Egúsqiza, G. Bruneaux, M. Meijer, Characterization of a Set of ECN Spray A Injectors: Nozzle to Nozzle Variations and Effect on Spray Characteristics, SAE Technical Paper 2013-24-0037 (2013). (Cit. on pp. 103, 124).
- [123] B. Michele, G. Bruneaux, L-M. Malbec, Study of ECN Injectors' Behavior Repeatability with Focus on Aging Effect and Soot Fluctuations, SAE Technical Paper 2016-01-0845 (2016). (Cit. on p. 103).
- [124] J. Pareja, A. Johchi, T. Li, A. Dreizler, B. Böhm, A study of the spatial and temporal evolution of auto-ignition kernels using time-resolved tomographic OH-LIF, *Proc. Combust.* (2018). DOI 10.1016/j.proci.2018.06.028 (cit. on p. 113).
- [125] H. Yamashita, M. Shimada, T. Takeno, A numerical study on flame stability at the transition point of jet diffusion flames, *Symp. (Int.) Combust.* 26 (1996) 27-34. (Cit. on p. 116).
- [126] J. H. Chen, E. R. Hawkes, R. Sankaran, S. D. Mason, H. G. Im, Direct numerical simulation of ignition front propagation in a constant volume with temperature inhomogeneities, *Combust. Flame* 145 (2006) 128-144. (Cit. on p. 117).
- [127] C. S. Yoo and H. G. Im, Transient soot dynamics in turbulent non-premixed ethylene–air counterflow flames, *Proc. Combust. Inst.* 31 (2007) 701-708. (Cit. on p. 117).
- [128] R. L. Gordon, A. R. Masri, S. B. Pope, G. M. Goldin, Transport budgets in turbulent lifted flames of methane autoigniting in a vitiated co-flow, *Combust. Flame* 151 (2007) 495-511. (Cit. on p. 117).
- [129] K. Aditya, A. Gruber, C. Xu, T. Lu, A. Krisman, M. R. Bothien, J. H. Chen, Direct numerical simulation of flame stabilization assisted by autoignition in a reheat gas turbine combustor, *Proc. Combust. Inst.* (2018). DOI 10.1016/j.proci.2018.06.084 (cit. on pp. 117, 119, 120).
- [130] C. S. Yoo, R. Sankaran, J. H. Chen, Three-dimensional direct numerical simulation of a turbulent lifted hydrogen jet flame in heated coflow: Flame stabilization and structure, *J. Fluid Mech.* 640 (2009) 453-481. (Cit. on p. 120).

- [131] R. Cabra, J-Y. Chen, R.W Dibble, A.N Karpetis, R. S. Barlow, Lifted methane-air jet flames in a vitiated coflow, *Combust. Flame* **143** (2005) **491-506**. (Cit. on pp. 123, 124).